Development of Micromegas-like gaseous detectors using a pixel readout chip as collecting anode

ACADEMISCH PROEFSCHRIFT

ter verkrijging van de graad van doctor
aan de Universiteit van Amsterdam
op gezag van de Rector Magnificus
prof. dr. D.C. van den Boom
ten overstaan van een door het college voor promoties ingestelde
commissie, in het openbaar te verdedigen in de Agnietenkapel
op donderdag 15 januari 2009 om 12.00 uur

door

Maximilien Alexandre Chefdeville

geboren te Nice, Frankrijk

Promotor ....prof. dr. J. Schmitz
Copromotor ....dr. P. Colas
Copromotor ....dr. ir. H. van der Graaf

Faculteit der Natuurwetenschappen, Wiskunde en Informatica

Thèse de doctorat
de l'Université d'Amsterdam
en cotutelle avec
l'Université Paris Sud XI
(Ecole Doctorale Environnement et Rayonnement, Orsay)

préparée à NIKHEF, Amsterdam et au CEA/Irfu, Saclay

Doctorat de l'Université Paris Sud XI
Spécialité : Physique

par

Maximilien CHEFDEVILLE

Développement de détecteurs Micromegas utilisant des puces pixelisées comme anodes collectrices

Directeurs de thèse :

Jurriaan SCHMITZ/Paul COLAS/Harry van der GRAAF

Date de soutenance prévue pour le 15 janvier 2009 à Amsterdam
devant la commission d'examen composée de :

M. Jan TIMMERMANS	Rapporteur
M. Daniel FOURNIER	Rapporteur
M. Stan BENTVELSEN	Examinateur
Md. Els KOFFEMAN	Examinateur
M. Paul KOOIJMAN	Examinateur
M. Frank LINDE	Examinateur

à Marthe et Albert Noto

Contents

Introduction

Particle physics

Particle physics is a branch of physics that studies the elementary constituents of matter and radiation and the interactions between them with the aim of more unity and simplicity to the apparent complexity of the universe. It looks at extremely small objects (or particles) which obey the laws of quantum mechanics and exhibit a dual particle/wave behaviour. The wavelength λ of such a particle then relates to its momentum p according to:

$$\lambda = h/p \tag{1}$$

where h is the Plank constant. When a particle is accelerated, its wavelength can be reduced to the typical size of an atom or below. The particle can hence be used to probe the structure of matter at very small scales. In practice, this is realized by directing a beam of high energy particles towards a fixed target or another beam and looking at the result of the collisions with adequate detectors (for this reason, particle physics is also called high energy physics). Accelerators and detectors are hence comparable to microscopes with a separation power given by the energy of the accelerated particles. They are since several decades the principal experimental tool of particle physicists.

Types of particles

Particles are classified according to their internal angular momentum (or spin). Half-integral spin particles follow Fermi-Dirac statistics and are thus called fermions. They are the building blocks of matter and can be sorted in two categories: the leptons which can be observed free (*e.g.* the electron and the neutrinos) and the quarks which only appear in double or triple combinations called hadrons. The quarks carry a kind of charge called "colour" that can take three values.

1^{st} generation	2^{nd} generation	3^{rd} generation
e	μ	τ
0.511	105.6	1776.8
ν_{e}	ν_μ	ν_τ
$< 2.2 \cdot 10^{-6}$	$< 170 \cdot 10^{-3}$	< 15.5
u	c	t
1.5–2.3	1160-1340	169100-173300
d	s	b
3.5–6.0	70-130	4130–4370

Table 1: *Elementary fermions known in nature and their masses in MeV/c^2.*

The known fermions in nature are grouped in three generations of two quarks and two leptons (see Table 1). The first generation consists of the lightest *up* and *down* quarks (u,d), the electron e and the uncharged electron neutrino ν_{e}. All stable matter is made from those particles. This pattern is repeated twice, with the *strange* and *charm* quarks (s,c), the muon μ and muon neutrino ν_μ and in the third generation, the *bottom* and *top* quarks (b,t), the tau τ and tau neutrino ν_τ. In comparison with the fermion masses of the first generation, those particles are much heavier and unstable: after a certain life-time they decay into lighter fermions. The total number of known fermions in nature is 24 (plus the same number of particles with opposite electric charge called anti-particles).

Integral spin particles follow Bose-Einstein statistics and are termed bosons. Bosons are the carriers of the four fundamental forces and are exchanged during an interaction between two fermions. For instance, two electrically charged particles can exchange a photon which is the carrier of the electromagnetic force. Similarly, the weak force is mediated by the massive W^+, W^- and Z^0 bosons. The strong force acts on the quarks which are "coloured"-charged particles and is transmitted by the gluons. The different types of interactions can hence be described in a unified way as the exchange of a boson. In the case of gravity, an hypothetical particle called the graviton would propagate the interaction, this particle has not yet been observed. The known bosons in nature are listed in Table 2.

The matter particles and the force carriers are described by relativistic quan-

boson	force	electric charge (e)	mass (GeV/c^2)
γ (photon)	electromagnetic	0	0
W^+, W^-	weak	± 1	80.2
Z^0	weak	0	91.2
8 gluons	strong	0	0

Table 2: *Elementary bosons known in nature and some of their properties.*

tum field theory in a model called the Standard Model. In the past forty years, this model has been the subject of an impressive experimental program. So-far, measurements agreed with its predictions to a great level of precision. Yet, the Standard Model describes the particles as if they were massless which is in complete contradiction with the experimental observations. To solve this inconsistency, a mechanism which would generate the masses was introduced in the model. It is called the Higgs mechanism and implies the existence of a new particle: the Higgs boson. This particle has not yet been discovered and is the subject of intense research at current accelerators.

Accelerators

The fermions of the second and third generation are unstable but can be produced in collisions of particles with a sufficient energy and studied. Such collisions occur for instance in the interactions of cosmic rays with the atmosphere nuclei but can also be more conveniently realized in a laboratory experiment with an accelerator.

The main figure of merit of an accelerator is the energy that it can transfer to the beam particles and that is then available for the production of new particles. The first accelerators would guide a beam towards a fixed target surrounded by detectors (so-called fixed target experiment). In this case most of the beam energy goes into propelling the centre-of-mass forward and only a small fraction of it is useful. With the development of circular accelerators in the sixties, particles of two beams traveling in opposite directions could be brought into collision in a very small region of space. The maximum energy available at the collision, called the centre-of-mass energy, is the sum of the energy of the two beams. The centre-of-mass energy has increased exponentially from a few GeV in the seventies to the TeV range in the nineties. In 2009, collisions of protons and anti-protons up to an energy of 14 TeV should be realized at the CERN Large Hadron Collider (LHC).

A particle beam consists of closely spaced bunches of a very large number of particles. Upon collision, two bunches are smashed against each other and interactions between the individual particles may occur. The rate of occurrence R of a particular interaction (or process) depends on the process cross-section σ, the bunch collision frequency f, the number of particles N_1 and N_2 per bunch in each beams and on the transversal size A of the beams:

$$R = f\frac{N_1 N_2}{A} \cdot \sigma = \mathcal{L} \cdot \sigma \tag{2}$$

where $\mathcal{L}$ is called the luminosity and is a property of the accelerator. Current accelerators are intended for studying rare processes and therefore have a high luminosity. This implies very high collision rates (*e.g.* the beams will cross at a frequency of 40 MHz at LHC) and fast, precise and radiation hard detectors.

Detectors

Detectors are used to measure the position and the energy of the produced particles. They combine a sensor (solid, liquid or gaseous) where a signal is produced upon the passage of a particle with a readout part which takes care that the information is available to the external world. The first detectors were read out by eye or with a camera (*e.g.* nuclear emulsion, cloud chamber, spark and bubble chamber) and were successfully applied for cosmic ray studies and in low rate fixed-target experiments. Due to a long recovery time, however, they are unable to cope with high collision rates.

A dramatic improvement of the detector rate capability was initiated in the sixties by the development of microelectronics. It was possible to read out the detectors electronically and hence much faster. Also, the measured signals would be available in a digital form which is convenient for data processing and storage. Following Moore's law, the ever-smaller size of integrated circuits enabled the fabrication of detectors with a growing number of readout channels. This resulted in improved spatial resolution, rate capability, radiation hardness but at the price of increased complexity, size and cost.

Scope of the thesis

This thesis reports on the fabrication and test of a new gaseous detector with a very large number of readout channels. This detector is intended for measuring the tracks of charged particles with an unprecedented sensitivity to single electrons of almost hundred percents. It combines a metal grid for signal amplification called the Micromegas with a pixel readout chip as signal collecting anode and is dubbed GridPix.

GridPix is a potential candidate for a sub-detector at a future electron linear collider foreseen to work in parallel with the LHC around 2020–2030. This collider is called the International Linear Collider (ILC) and the motivations for its construction are presented in Chapter 1 together with the detector concepts proposed so far.

Chapter 2 and 3 cover the basics of gaseous detectors, namely the drift and multiplication of electrons in gas under external electric and magnetic fields and the primary ionization. The main electronically read out gas detectors are surveyed in Chapter 4 which ends with a presentation of GridPix.

The tracking capability of GridPix is best exploited if the Micromegas is integrated on the pixel chip. This integrated grid is called InGrid and is precisely fabricated by wafer post-processing. The various steps of the fabrication process of InGrid on bare silicon wafers are detailed in Chapter 5.

InGrid should show a similar performance to Micromegas. For this purpose, several InGrids were fabricated on bare wafers and tested. Measurements of electron collection efficiency, gain and energy resolution in various gas mixtures are reported in Chapter 6. Gain fluctuations partly determine the sensitivity of GridPix to ionizing radiation and also affect the performance of other Micromegas-based detectors. This subject was investigated and simulation results will be shown. The ion backflow is an important issue at a high luminosity collider like ILC and was measured for several detector geometries. The measurements are presented in Chapter 7 and confronted to the ILC performance goal.

Studies of the response of the complete detector formed by an InGrid and a TimePix pixel chip to X-rays and cosmic particles are detailed in Chapter 8 and 9. In particular, the efficiency for detecting single electrons and the point resolution in the pixel plane are determined and the implications for a GridPix detector at ILC are discussed.

Chapter 1

The International Linear Collider

The International Linear Collider ILC is an electron positron collider foreseen to continue around 2025 the study of particle physics in the TeV energy range initiated by the actual Tevatron and soon by the LHC colliders. This chapter gives a short description of the design and parameters of the ILC and its main physics goals. The performance requirements and technology options for the subdetectors are presented with the three detector concepts.

1.1 The ILC accelerator

1.1.1 Accelerator baseline design

ILC will collide bunches of electrons and positrons up to a centre-of-mass energy of 500 GeV at a peak luminosity of $2{\cdot}10^{34}$ cm^{-2}s^{-1}. With a total length of $\sim$ 31 km, the ILC will consist of two sources of electrons and positrons with 80 % and 50 % polarization respectively, two damping rings to reduce the emittance of the beams, two 11 km long linear accelerators and a beam delivery system to focus the beams to their final sizes and to bring them into collision [1]. The linear accelerators will be based on 1.3 GHz 1 m long superconducting radio frequency (SCRF) accelerating cavities which will provide an average gradient of 31.5 MeV/m [2]. Each linac will consist of approximately 8550 cavities and will accelerate the beam particles up to 250 GeV with an energy spread less than 0.1 %. After a few years of operation at 500 GeV centre-of-mass energy, the machine could be upgraded to 1 TeV by increasing the number of accelerating cavities along the linacs and the accelerating gradient.

1.1.2 Beam parameters

The ILC will operate in a pulsed mode: 0.95 ms long bunch trains of electrons and positrons will collide every 200 ms, each bunch containing some $2{\cdot}10^{10}$ particles. The number of bunches per pulse can be tuned between roughly 1000 and 5400. At a value of 2820 bunches per pulse, bunch collisions will occur every 337 ns. At the interaction point (IP) the bunches will have r.m.s. vertical and horizontal sizes of 5.7 nm and 640 nm respectively and an r.m.s. length of 300 μm.

1.2 Physics goals

1.2.1 Introduction

The ILC will be a unique tool to study the mechanisms of elementary particle mass generation and electroweak symmetry breaking by precisely measuring the properties of the Higgs boson, if the latter exists. The Standard Model (SM) gives predictions on all its properties but its mass. Therefore, disagreements between measurements and expectations will indicate that the SM is the low energy approximation of a more fundamental theory that is still to be established. Similarly, the precision on several previously measured parameters of the SM, as gauge bosons masses, couplings and mixing angles will be improved, providing more stringent tests of the SM predictions. If discrepancies between the model predictions and measurements are found, various SM extensions like supersymmetric models, extra-dimension models and other alternative scenarios may be put to the test and unexpected discoveries may be made. In the following sections, I briefly present the expected properties of the Higgs boson and how they could be measured at the ILC. Also, a short section is devoted to supersymmetry.

1.2.2 The Higgs boson in the Standard Model

The Higgs mechanism, which implies the existence of the Higgs boson, is one pillar of the Standard Model because it explains the mass of elementary particles [3, 4]. According to the Higgs mechanism, the mass of elementary particles results from the interaction between the particles and the Higgs field: the stronger the coupling to the Higgs boson, the larger the mass. The Higgs boson spin J, parity P and charge conjugation C quantum number are given by $J^{PC} = 0^{++}$. The only free parameter of the model is the Higgs mass M_{H} itself which, from direct searches [5, 6] and theoretical constraints [7, 8] should lie in the range of 115–700 GeV. The Higgs boson is unstable and should therefore decay in various ways according to probabilities called decay branching ratios. The Higgs boson decay branching ratios depend on its mass M_{H}. Below $\sim$ 140 GeV, it decays mainly into $b\bar{b}$ pairs (80 %) and less often into $c\bar{c}$, $\tau^{+}\tau^{-}$ and gluon $g\bar{g}$ pairs. At higher M_{H}, it almost merely decays into WW and ZZ pairs with the ratio $\frac{2}{3}$ and $\frac{1}{3}$ respectively [9, 10].

1.2.3 Higgs mass measurement at the ILC

The main Higgs boson production channels in e^+e^- collisions are the so-called Higgs-strahlung process ($e^+e^- \rightarrow ZH$) where the electron and positron produce a virtual Z boson that then radiates a Higgs boson [11, 12] and the W-fusion process ($e^+e^- \rightarrow \nu\overline{\nu}H$) where the electron and positron turn into neutrinos via the emission of two W bosons which produce a Higgs [13, 14]. At a centre-of-mass of 500 GeV, the luminosity is such that samples of 3–4$\cdot 10^4$ events should take place in both the Higgs-strahlung and W-fusion channels [15] within the first four years of operation of the ILC.

In the Higgs-strahlung process, the Z boson is mono-energetic and the Higgs mass can thus be measured in a model independent way, assuming that the initial energies of the two beams are precisely known. The Z boson decays mostly into quark pairs (70 %) and less often into lepton pairs. When the Z decays into a muon pair, a very clear signature is available even if the Higgs decays invisibly (Figure 1.1).

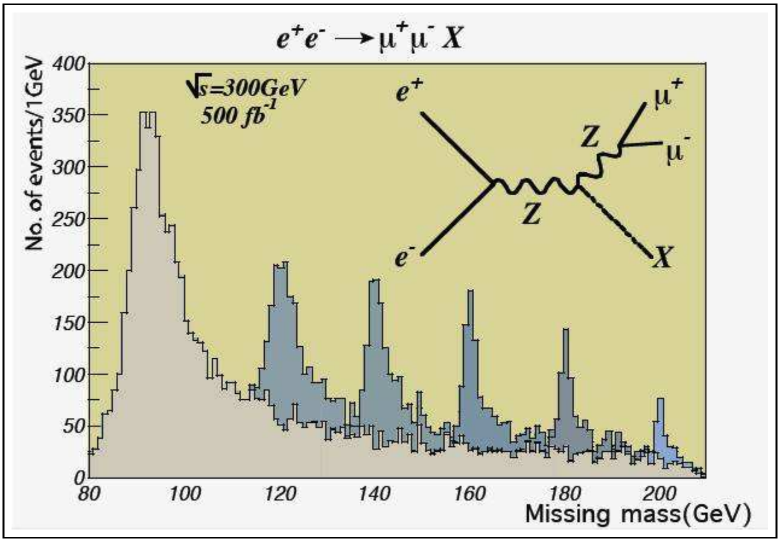

Figure 1.1: *Distributions of the $\mu^+\mu^-$ recoil mass in $e^+e^- \rightarrow \mu^+\mu^- X$ for various Higgs boson masses [16]. Eventually only one peak should be measured, the position of which will depend on the mass.*

Other production channels with smaller cross-sections are the Z-fusion process ($e^+e^- \rightarrow e^+e^-H$), associated production with top quarks ($e^+e^- \rightarrow t\overline{t}H$) and double production channels like $e^+e^- \rightarrow \nu\overline{\nu}HH$ and $e^+e^- \rightarrow ZHH$. Production cross-sections as a function of the Higgs boson mass can be found in [17].

1.2.4 Higgs couplings measurements at the ILC

If the Higgs boson is lighter than 140 GeV, it will decay predominantly into $b\bar{b}$ and less often into $c\bar{c}$, $\tau^+\tau^-$ and $g\bar{g}$. The relative couplings of the Higgs to these fermions can be determined by measuring the corresponding branching ratios. The Higgs boson couplings to W and Z bosons can be measured through Higgs-strahlung and fusion processes while its coupling to top quarks is measured when it is produced with a top quark pair.

If the Higgs boson is responsible for the mass of the particles, it should also generate its own mass through a self-interaction. Decisive tests of this prediction can be realized at the ILC where the trilinear coupling of the Higgs boson λ_{HHH} could be determined by a measurement of the double Higgs-strahlung cross-section $\sigma(e^+e^- \to HHZ)$. For $M_{\mathrm{H}} = 120$ GeV, an accuracy on λ_{HHH} of about 22 % should be obtained at 500 GeV centre-of-mass energy with an integrated luminosity of 1 ab^{-1} [18]. These measurements should confirm the basic SM prediction that the couplings are proportional to the particle masses and will thus be crucial for assessing the mass generation mechanism of the Standard Model.

1.2.5 Probing Supersymmetry at the ILC

In the Standard Model the Higgs boson mass can be formally expressed as an infinite series of terms called radiative corrections. One problem of the SM is that these corrections become larger and larger and the series diverges. The mass therefore can not be calculated. By predicting that every particle would have a partner with a spin difference of $\frac{1}{2}$ [19, 20], Supersymmetry prevents the divergence of the series because the contributions from SM particles are canceled by the contributions from their supersymmetric partners [21, 22].

Supersymmetry implies the existence of many new particles among which are several Higgs bosons [23]. It also accounts for the observed lack of mass in the universe by predicting the existence of an electrically neutral weakly interacting particle (so-called dark matter candidate): the lightest supersymmetric particle [24]. The expected masses of some supersymmetric particles are light enough to allow their production at the ILC. Thanks to the unique features of the ILC (*e.g.* tunable centre-of-mass energy for threshold scans, beam polarization to select given physics channels), their properties could be studied in great detail.

1.3 Sub-detectors at the ILC

Collisions between energetic electrons and positrons will produce short-lived particles which will rapidly decay sometimes through several reactions, into particles with longer life-times. The latter will travel over macroscopic distances and their properties can be measured with adequate detectors to study the initial reaction. The typical structure of a colliding beam experiment is illustrated in Figure 1.2.

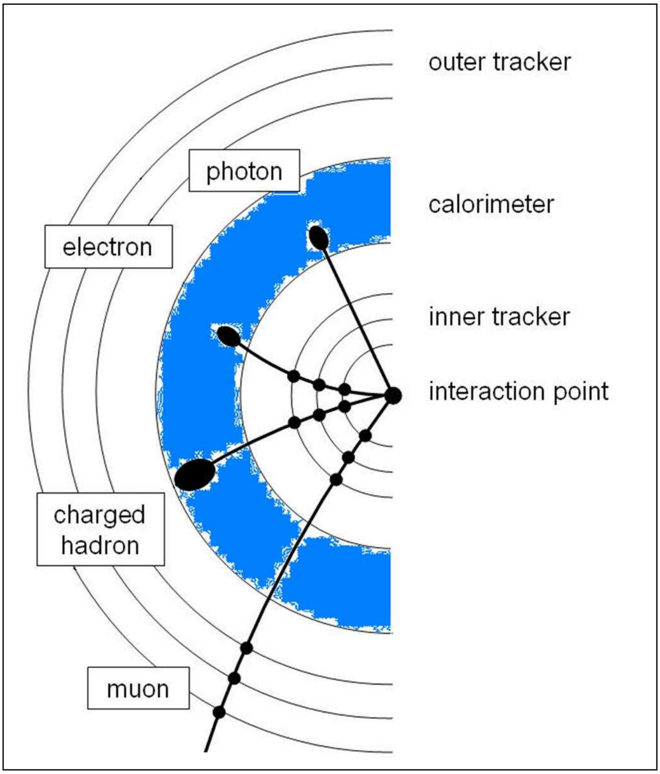

Figure 1.2: *View of the sub-detector arrangement around the interaction point of a colliding beam experiment in a plane perpendicular to the beams (the solenoid which generates the magnetic field is not shown). The signatures of some highly energetic particles in the trackers and the calorimeters are indicated.*

1.3.1 The vertex detector

The vertex detector determines the space points where the particles are produced. While particles with very short life-times decay close to the interaction point (IP), those with longer life-times can travel several millimeters before decaying. For this reason, not all tracks extrapolate to the interaction point but rather to a few decay vertices. Identification of heavy particle decay vertices and measurement of the masses of their charged decay products tag their flavor. The vertex detector can thus identify with a certain efficiency the flavor of quarks produced at the IP.

Although the ILC collision rates will be relatively low, large backgrounds of e^+e^- pairs from the bremsstrahlung photons emitted by the particle beams are expected (some 100 hits/mm^2/bunch train in the first layer of the vertex detector). This large occupancy calls for very fast readout technology, beyond state of the art of traditional pixel detectors. The choice of technology is driven by many criteria (precision, layer thickness, granularity, material budget, radiation hardness, alignment preservation, resistance to electromagnetic interference) and is still debated [25]. It is accepted, however, that the detector should have some 10^9 pixels with size below $20 \times 20\ \mu\mathrm{m}^2$ and a layer thickness equivalent to 0.1 % X_0.

1.3.2 The main tracker

The main tracker determines the momentum of charged particles by measuring their track curvatures in a uniform magnetic field of known strength. At the ILC, both a silicon tracker [26, 27] and a Time Projection Chamber [28, 29] have been proposed to meet the challenging momentum resolution of

$$\frac{\sigma_{p_\mathrm{t}}}{p_\mathrm{t}^2} \sim 5 \cdot 10^{-5}(\mathrm{GeV/c})^{-1} \tag{1.1}$$

The TPC would use a large volume of gas where numerous 3D points are measured (some 100–200 for tracks with high transverse momentum) while keeping passive material to minimum. Thanks to its high pattern recognition capability (the charge pattern is projected onto the end plate) it is robust for tracking in environments of high multiplicity and large backgrounds. Also, the measurement of energy loss dE/dx along the tracks can be used for particle identification purposes. More details on TPCs are given in section 4.4.

The silicon tracker would be made of barrels and disks of silicon strip detectors. Strip detectors are fast and provide a few direct and precise measurements of hits along the tracks but have the disadvantage of introducing dead material that can result in multiple scattering and parasitic interactions. Nevertheless, a silicon tracker would be useful to maintain good tracking performance for particles emitted with a small angle with respect to the beam direction. For those particles, a TPC would be less precise as a smaller number of hits would be measured on the endplate.

The main tracker will be placed inside the coil of a solenoid which will provide a uniform field of a few Teslas. For the TPC a diameter of 3–4 m, a total length of 4 m and a field of 3–4 T are foreseen. The silicon tracker would be more compact and compensate its smaller dimensions (2.5 m diameter, 3 m long) by a higher field of 5 T.

1.3.3 Technology options for the TPC

The high particle rates encountered during the e^+e^- collisions make Micro Pattern Gas Detectors (so-called MPGDs) such as GEMs and Micromegas more suitable than traditional wire based amplification structures. The electric field configuration of these gas gain grids suppresses the E × B effects encountered in the vicinity of the wires. They also permit almost full collection of the ions from the amplification by the grids, reducing drift field distortions by the ion space charge.

The main option concerning the segmentation of the readout plane is the use of charge collecting pads of a few mm^2. Even though the pad width is large with respect to the grid hole pitch, excellent point resolutions can be achieved by spreading the signal on several pads and estimating the cluster position as the centre-of-gravity of the signals on the pads. This spreading effect is natural with GEMs because of the 1–2 mm distance between the pad plane and the first GEM bottom electrode [30]. Micromegas structures require the coating of the pad plane with a resistive layer to spread transversally the initially narrow charge distribution [31]. A second option is the use of pixels which in the case of Micromegas fully exploits the granularity of the grid. The pixel option should permit the off-line identification and suppression of δ-rays and will provide a few very precise "end" points for tracks traversing the end-plate (cf. chapter 4).

1.3.4 Calorimetry

Measurement of the particle energy can be performed by full absorption of the particle in a sensitive material and is handled by calorimeters. In order to stop particles with GeV energies, calorimeters are made of high Z materials like lead or iron. A particle penetrating a calorimeter will interact with the atoms of the material, producing a cascade of particles called a shower. The particle energy is determined by measuring the total energy of the shower particles. Because of the different properties of $e^\pm$, γ and hadrons, one generally builds two calorimeters each specialized in the absorption of these two types of radiation. The absorption of $e^\pm$ and γ is taken care of by a high-Z material electromagnetic calorimeter. Hadrons are much more penetrating and make wider showers than $e^\pm$ and γ, for this reason the hadronic calorimeter is made of small interaction length materials.Due to a property of the strong force, when a quark pair produced in an e^+e^- collision fragments, new quarks and gluons emerge from the colour field of the initial pair. This results in "jets" of hadronic particles emitted in opposite directions. When measuring the energy of the initial pair, one has to measure the energy of the particles contained in the two jets.

At the ILC, the calorimeters should have large angular coverage and excellent jet energy resolution ($\sigma_E/E = 3$ % at 100 GeV). The approach followed to meet this goal is based on the Particle Flow (PF) concept. The latter relies on the fact that for charged relativistic particles, the momentum (and thus the energy) measurement from the tracker is more precise than the one provided by the calorimeter. Therefore the energy of a jet is more accurately measured if the hits from individual charged particles are isolated and their energy deposits replaced by the information from the tracker. This approach calls for finely segmented and compact calorimeters with single particle shower imaging capability.

A second approach is based on the separation of electromagnetic and hadronic contents within showers by means of dual readout of scintillation and Cerenkov lights [32]. Properly recombined, the two components exhibit less fluctuations than each component alone resulting in improved energy resolution.

1.3.5 Detector concepts

Four detector concepts have so far emerged with the common design characteristics of a pixelated vertex detector, a high momentum resolution tracking system and highly segmented electromagnetic and hadronic calorimeters placed inside the coil of a 3 to 5 T solenoid. Recently, two rather similar concepts merged into one. At the time of writing, the three detector concepts are:

- the Silicon Detector SiD with its full Si tracking system and Particle Flow oriented calorimetry [33];
- the International Linear Collider Detector ILD with a TPC as main tracker and Particle Flow oriented calorimetry. ILD is actually the merging of the initial concepts GLD [34] and LDC [35];
- the 4th concept with its dual readout calorimetric system and innovative magnet system [36].

The TPC of the ILD concept would have an inner and outer radius of 30–45 and 160–200 cm and a half-length of 210–230 cm. The key parameters of the detector concepts can be found in [25].

Chapter 2

Charge transport and electron multiplication in gas

The basic working principle of electronically read out gas detectors is the primary ionization of the gas molecules, the drift and multiplication of the primary electrons and the detection of the amplified signals. This chapter treats the transport of electrons and ions in gas and the multiplication of electrons while primary ionization is presented in the next chapter.

2.1 Brief description of gas

Gaseous detectors used for track measurements are generally operated at normal pressure and temperature ($P = 1$ atm and $T = 293$ K). The number of molecules per unit volume n at those conditions can be estimated using the ideal gas law:

$$n = \frac{P}{k_{\mathrm{B}}T} \tag{2.1}$$

where k_{B} is Boltzmann's constant. From 2.1 n is equal to $2.687 \cdot 10^{19}$ cm^{-3} which corresponds to an average molecular spacing of 3.4 nm. It is called the Loschmidt number and is used to translate the cross-section σ for a given process into a mean free path λ:

$$\lambda = (n\sigma)^{-1} \tag{2.2}$$

As an example, the cross-sections σ_{s} for elastic scattering of thermal electrons (0.04 eV) off various noble gas atoms and the corresponding mean free paths are listed in Table 2.1. At thermal energies the mean free path between collisions is much larger than the molecular spacing.

Atom	He	Ne	Ar	Kr	Xe
$\sigma_\mathrm{s} \cdot 10^{16}$ (cm^2)	6	5	3	10	70
λ_s (μm)	0.7	0.8	1.3	0.4	0.06

Table 2.1: *Cross section [37] and corresponding mean free path for elastic scattering of thermal electrons off various noble gas atoms.*

The kinetic energy of molecules in a gas in thermodynamic equilibrium follows Maxwell's distribution [38] which gives the number of molecules with energies between E and $E+\mathrm{d}E$:

$$p(E)dE = N\frac{2}{(\pi)^{1/2}(k_\mathrm{B}T)^{3/2}}\sqrt{E}\exp\left(-\frac{E}{k_\mathrm{B}T}\right)dE \tag{2.3}$$

where T is the absolute temperature and N the total number of molecules in the gas. Writing m the mass of a molecule, the velocity distribution can be calculated from 2.3:

$$p(v)dv = N\left(\frac{2}{\pi}\right)^{1/2}\left(\frac{m}{k_\mathrm{B}T}\right)^{3/2} v^2\exp\left(-\frac{mv^2}{2k_\mathrm{B}T}\right)dv \tag{2.4}$$

The mean energy of a gas molecule at normal conditions depends only on the temperature and is equal to $3/2k_\mathrm{B}T$, this is 0.04 eV at 293 K. This energy is due to the thermal agitation and corresponds to an average velocity:

$$v = \sqrt{\frac{3k_\mathrm{B}T}{m}} \tag{2.5}$$

If some electrons and ions present in the gas are in thermal equilibrium with the gas molecules, their velocity distributions are also Maxwellian. In this case, Equation 2.5 predicts average velocities of about 10 cm/μs and 10^{-2} cm/μs respectively.

When a uniform electric field is applied, the instantaneous velocities of charged particles will pick up, in between collisions, an extra component along the field direction. On the macroscopic scale, the charged particles move along the field direction at an average velocity v_d called the drift velocity. Also, their energies do not follow the Maxwell's distribution anymore. Although an approximate velocity distribution valid at low fields was proposed by Druyvesteyn [39], there is no exact distribution at arbitrary fields. Nevertheless, simple equations can be used to coarsely understand the motion of electrons and ions under the influence of external electric and magnetic fields.

2.2 The Langevin formula

The velocity vector $\overrightarrow{v}$ of a particle of mass m and charge e moving in an electric field $\overrightarrow{E}$ and a magnetic field $\overrightarrow{B}$ obeys the following equation of motion:

$$m\frac{d\overrightarrow{v}}{dt} = e(\overrightarrow{E} + \overrightarrow{v} \times \overrightarrow{B}) \tag{2.6}$$

To model the slowing down of the drifting particles by the gas molecules, one introduces in Equation 2.6 a friction force $\overrightarrow{f}$ = -$K\overrightarrow{v}$. Historically, this approach was undertaken by P. Langevin [40, 41] to describe the motion of Brownian particles. So, one has:

$$m\frac{d\overrightarrow{v}}{dt} = e(\overrightarrow{E} + \overrightarrow{v} \times \overrightarrow{B}) - K\overrightarrow{v} \tag{2.7}$$

Noting that $\tau = m/K$ has the dimension of a characteristic time, the term on the left of Equation 2.7 can be dropped for $t \gg \tau$. In this case, the velocity vector is constant and equal to the drift velocity vector $\overrightarrow{v_{\mathrm{d}}}$ which obeys:

$$\frac{\overrightarrow{v_{\mathrm{d}}}}{\tau} - \frac{e}{m}\overrightarrow{v_{\mathrm{d}}} \times \overrightarrow{B} = \frac{e}{m}\overrightarrow{E} \tag{2.8}$$

In terms of the cyclotron frequency $\omega = (e/m)B$, the solution can be written as:

$$\overrightarrow{v_{\mathrm{d}}} = \frac{e}{m}\tau E \frac{1}{1+\omega^2\tau^2}(\overrightarrow{u_E} + \omega\tau(\overrightarrow{u_E} \times \overrightarrow{u_B}) + \omega^2\tau^2(\overrightarrow{u_E} \cdot \overrightarrow{u_B})\overrightarrow{u_B}) \tag{2.9}$$

where $\overrightarrow{u_E}$ and $\overrightarrow{u_B}$ are the unit vectors in the directions of the fields.
Equation 2.9 is the Langevin formula. It shows that for arbitrary oriented electric and magnetic fields, the drift velocity vector has components along the directions of $\overrightarrow{E}$, $\overrightarrow{B}$ and $\overrightarrow{E} \times \overrightarrow{B}$. The magnitudes of those components depend on the dimensionless parameter $\omega\tau$. The angle between the drift velocity and the electric field is called the Lorentz angle α_{L} [42].

When no magnetic field is applied, $\omega\tau = 0$ and the drift velocity vector points in the direction of the electric field:

$$\overrightarrow{v_{\mathrm{d}}} = \frac{e}{m}\tau\overrightarrow{E} = \mu\overrightarrow{E} \tag{2.10}$$

where μ, called the scalar mobility, is a function of the gas, the field and the drifting particle. In the presence of a magnetic field, the magnitude of $\overrightarrow{v_{\mathrm{d}}}$ is reduced by a factor:

$$\frac{v_{\mathrm{d}}(\omega)}{v_{\mathrm{d}}(0)} = \left(\frac{1+\omega^2\tau^2\cos\phi}{1+\omega^2\tau^2}\right)^{1/2} \tag{2.11}$$

where ϕ is the angle between $\overrightarrow{E}$ and $\overrightarrow{B}$. Equation 2.11 predicts that the drift velocity is unaffected by a magnetic field if the latter is oriented parallel to the electric field.

2.3 The microscopic theory

In the previous section, a frictional force was used to account for the slowing down of the drifting particles by the gas molecules. After a characteristic time τ, the “friction” of the gas molecules balances the acceleration from the field and the drift velocity emerges as an asymptotic value of the velocity. I now adopt a more detailed approach which includes the gas number density, the scattering cross-section and the fractional energy loss. It will be shown how these microscopic quantities relate to the drift velocity and the diffusion coefficients. The detailed derivation of the equations presented in this section can be found in [43].

2.3.1 Drift velocity of electrons

When no external fields are applied, a free electron in a gas has a thermal kinetic energy equal to $(3/2)k_{\mathrm{B}}T$ and a randomly oriented instantaneous velocity u. Under the influence of an electric field E, the electron picks up in between two collisions an extra velocity v equal to the acceleration along the field multiplied by the time between the two collisions. Calling Δt the mean free time between collisions, the average extra velocity (or drift velocity) can be expressed as:

$$\overrightarrow{v_{\mathrm{d}}} = (e/m)\Delta t \cdot \overrightarrow{E} \tag{2.12}$$

Comparing Equations 2.10 and 2.12, the characteristic time τ defined in the macroscopic picture corresponds actually to the mean free time between collision Δt. In the following Δt will be referred to as τ.

If one considers the balance between the energy gained from the field and the energy lost in collisions, approximate expressions for the drift velocity and instantaneous velocity can be derived:

$$v_{\mathrm{d}}^2(\epsilon) = \frac{eE}{mn\sigma_{\mathrm{s}}(\epsilon)}\sqrt{\frac{f(\epsilon)}{2}} \tag{2.13}$$

$$u^2(\epsilon) = \frac{eE}{mn\sigma_{\mathrm{s}}(\epsilon)}\sqrt{\frac{2}{f(\epsilon)}} \tag{2.14}$$

where $\sigma_{\mathrm{s}}(\epsilon)$ and $f(\epsilon)$ are the electron elastic scattering cross-section and the mean fraction of energy lost by an electron in an elastic collision. These are a function of the electron energy ϵ and the gas molecule electronic structure.

It was early discovered and explained that for heavy noble gases (Ar, Kr and Xe) and light molecular gases (*e.g.* CO_2 and CH_4), σ_{s} exhibits a dip around a few tenths of eV [44, 45]. This dip is due to an interference between diffusion states and bound states of the electrons at energies such that the de Broglie wavelength of the incident electron wave function is comparable to the atomic size. This is the Ramsauer effect.

Larger drift velocities are obtained if the electron energy remains close to the elastic cross-section minimum during the drift. In pure noble gases, the electron energy can only be dissipated through excitation and ionization. The thresholds of these inelastic collisions are several eV high, therefore most of the collisions are elastic and the mean fractional energy loss is very small ($f \rightarrow 0$). In this case, the electron energy quickly rises above the Ramsauer minimum and the drift velocity is small. The gases where the electron energy is high are called hot gases.
Molecular gases, on the other hand, have rotational and vibrational levels available at a few hundredth of eV. The mean fractional energy loss is thus much larger than in noble gases, resulting in a lower electron energy (so-called cool gases).

The electron drift velocity therefore depends critically on the exact gas composition. Even small additions of a molecular gas to a noble gas dramatically changes the energy distribution and thus the drift velocity. As an example, the trend of the drift velocity with the electric field in various Ar/CO_2 mixtures is illustrated in Figure 2.1.

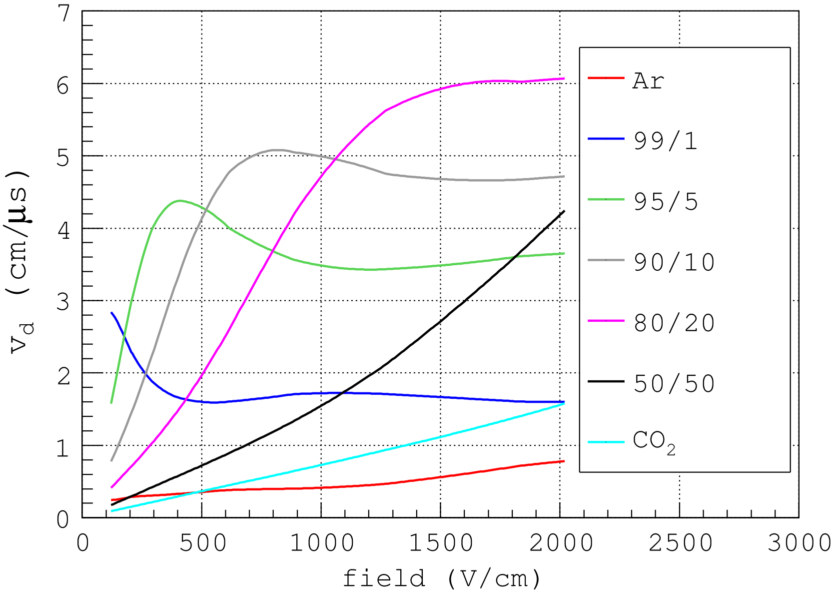

Figure 2.1: *Trend of the drift velocity with electric field as calculated by the program MAGBOLTZ in various Ar/CO_2 gas mixtures and in pure gases [37].*

2.3.2 The mobility of ions

The drift of ions differs from that of electrons because of their larger masses. If one approximates the collision partners by hard spheres of mass M_1 and M_2, the mean fractional energy loss f of the impinging particle of mass M_1 is given by:

$$f = \frac{2M_1M_2}{(M_1+M_2)^2} \tag{2.15}$$

which yields $f \sim 1/2$ when the collision partners have roughly the same mass (*e.g.* in the case of ion-atom collisions) and $f \sim 10^{-3}$ for electron-atom collisions ($M_1 \ll M_2$) [38]. Ions acquire over one mean free path an amount of energy comparable to that acquired by electrons. Due to their large mean fractional energy loss, however, half of this energy is lost in the next collision. Ion energies are thus thermal over a wide range of electric fields. It can be shown [43] that singly charged thermal ions have a constant mobility and a drift velocity given by:

$$v_\mathrm{d} = \frac{e}{N\sigma_\mathrm{s}}\left(\frac{1}{M_1}+\frac{1}{M_2}\right)^{1/2}\left(\frac{1}{3k_\mathrm{B}T}\right)^{1/2} E = \mu \cdot E \tag{2.16}$$

where μ is the ion mobility in the gas and σ_s is the scattering cross-section of ions off gas molecules (valid for a singly charged ion). At thermal energies, the cross-section varies little with energy and the drift velocity is proportional to the field strength. Actually Equation 2.16 is also valid for electrons which are thermal up to a few V/cm in argon and a few kV/cm in CO_2 [46].

In practice, ions drift in mixtures of two or more constituents and the mobility in the gas mixture follows Blanc's law (valid for thermal ions):

$$\frac{1}{\mu} = \frac{1}{N}\sum \frac{N_\mathrm{i}}{\mu_\mathrm{i}} \tag{2.17}$$

where N_i are the number densities of the different gas species in presence and μ_i the ion mobility in each of the pure gas. The validity of Equation 2.17 has been established in several binary Ar-based gas mixtures [47]. In those mixtures, ion mobilities between 0.6 and 2.0 $\mathrm{Vs/cm^2}$ were measured, corresponding to drift velocities between 0.7 and $2{\cdot}10^{-3}$ cm/μs at 1 kV/cm.

Above a certain field, ions pick up over one mean free path an energy comparable to the thermal energy and their drift velocity deviates from Equation 2.16. At such high fields, the mobility depends on the field strength and if one neglects the thermal motion, the velocity obeys [43]:

$$v_\mathrm{d} = \left(\frac{eE}{M_1N\sigma_\mathrm{s}}\right)^{1/2}\frac{M_1}{M_2}\left(1+\frac{M_1}{M_2}\right)^{1/2} \tag{2.18}$$

which shows that if the cross-section σ_s varies little with the field, the drift velocity goes like the square root of the field strength. An illustration of the two limiting behaviours of ions in low and high fields can be found in [48] for $\mathrm{He^+}$, $\mathrm{Ne^+}$ and $\mathrm{Ar^+}$ ions drifting in their parent gas.

2.3.3 Diffusion of electrons and ions

A charged particle drifting under the influence of external fields scatters off the gas molecules and does not follow precisely the field lines. A point-like cloud of such particles spreads out and along the field lines. These processes are called transverse and longitudinal diffusion respectively and their magnitudes differ for electrons and ions.

After a collision, ions retain their direction of motion to some extend because their mass is comparable to the mass of the gas molecules. They diffuse little at the typical drift fields encountered in gas detectors (a few to several hundred volts per centimeter). Electrons, oppositely, scatter almost isotropically and their direction of motion is randomized after each collision.

Let's first assume the diffusion to be the same in all directions and consider a point-like cloud of charge let to drift along the z direction at $t_0 = 0$ from $z = 0$. The particle current is conserved during the drift and obeys a continuity equation in which enters the particle density distribution. It can be shown that after a time t, the density distribution is a three-dimensional Gaussian function centered at $(0,0,v_\mathrm{d}t)$. At a distance r from the cloud center, the density $n(r)$ is given by:

$$n(r) = \left(\frac{1}{4\pi D_\mathrm{c}t}\right)^{3/2} \exp\left(\frac{-r^2}{4D_\mathrm{c}t}\right) \tag{2.19}$$

with a mean squared deviation $\sigma_\mathrm{i}^2 = 2D_\mathrm{c}t$ in any direction "i" and D_c the diffusion constant that enters the continuity equation. In the microscopic picture, σ_i^2 can be calculated assuming exponentially distributed distances between collisions and isotropic scattering. Using the average energy of the drifting particles $\epsilon = (1/2)mu^2$ and their mobility $\mu = (e/m)\tau$, one obtains:

$$\sigma_\mathrm{i}^2 = 2\left(\frac{2\epsilon\mu}{3e}\right)t \tag{2.20}$$

where the part in brackets identifies with the diffusion constant D_c. The average time elapsed during the drift of the cloud over a distance L is $t = L/(\mu E)$ and Equation 2.20 can be written as:

$$\sigma_\mathrm{i} = D\sqrt{L} \tag{2.21}$$

where D is the diffusion coefficient:

$$D = \sqrt{\frac{2D_\mathrm{c}}{\mu E}} = \sqrt{\frac{4\epsilon}{3eE}} \tag{2.22}$$

The diffusion sets a limit to the accuracy of track measurement and it is desirable to have σ_i^2 as low as possible, that is: low electron energies at high drift fields (Equation 2.22). This is best realized in cold gases or cold gas mixtures. In the thermal limit, the energy is proportional to the temperature: $\epsilon = (3/2)k_\mathrm{B}T$.

The diffusion is then a decreasing function of the field and is not dependent on the gas:

$$D = \sqrt{\frac{2k_{\mathrm{B}}T}{eE}} \tag{2.23}$$

which gives $D \sim 230$ and 70 μm/$\sqrt{cm}$ at 100 V/cm and 1 kV/cm respectively. This formula is valid for electrons drifting in cold gases and for ions. In CO_2, electrons are thermal up to 1–2 kV/cm with a diffusion coefficient of 80 μm/$\sqrt{cm}$ at 1 kV/cm [46]. As for electrons, the field at which ions depart from thermal behaviour depends on the gas. In Xe/CS_2 for instance, the ion drift velocity is proportional to the field up to 22 kV/cm [49]. In pure He, Ne and Ar, the proportionality is progressively lost above fields of 7.5, 10.5 and 18 kV/cm respectively [48].

A more accurate picture of the diffusion mechanism emerged in 1967 when Wagner *et* al. [50] measured that the diffusion of a cloud of electrons along the field is different from the one in the direction normal to the field (so-called electric anisotropy). As a result, we distinguish between longitudinal and transverse diffusions and split Equation 2.21 in two parts:

$$\sigma_{\mathrm{t}} = D_{\mathrm{t}}\sqrt{L} \tag{2.24}$$

$$\sigma_{\mathrm{l}} = D_{\mathrm{l}}\sqrt{L} \tag{2.25}$$

where D_{t} and D_{l} are respectively the transverse and longitudinal diffusion coefficients often expressed in units of μm/$\sqrt{cm}$. Common values of D_{t} and D_{l} for electrons at drift fields below 1 kV/cm lie between 200 and 600 μm/$\sqrt{cm}$.

When a magnetic field is also applied, the electrons follow helicoidal trajectories in the direction of $\overrightarrow{B}$ while drifting in the direction of the electric field. If one neglects the electric anisotropy, the same treatment used in the derivation of Equation 2.20 shows that the diffusion in the plane perpendicular to the magnetic field is reduced by a factor:

$$\frac{D_{\mathrm{t}}(\omega)}{D_{\mathrm{t}}(0)} = \frac{1}{1+\omega^2\tau^2} \tag{2.26}$$

whereas the longitudinal diffusion coefficient is unaffected. In some gas detectors, electrons drift over large distances (up to two meters in a TPC (cf. chapter 4)) and this effect is used to reduce the transverse diffusion coefficient by a large factor (*e.g.* up to 30 in Ar/CH_4 95/5 at 40 V/cm and 4 T). Beside using a high magnetic field to obtain a large ω value, the gas mixture can be optimized to maximize the time between collision τ. In the general case of combined electric and magnetic anisotropies with randomly oriented E and B fields, the diffusion is described by a 3×3 tensor [43].

2.4 Electron multiplication in gas

2.4.1 Introduction

The primary charge generated by ionizing radiations in the gas volume is collected on electrodes by means of an electric field (sometimes combined with a magnetic field) that attracts the electrons towards the anode and the ions towards the cathode. The electrodes are connected to sensitive electronics for signal processing. The number of primary electrons from X-rays or minimum ionizing particles is too small to be detected by the electronics and has to be increased in the gas by electron multiplication. The multiplication factor is called the gas gain and generally assumes values between 10^3 and 10^5.

At a given gas pressure, the gain is determined mainly by the gas composition and the electric field strength. The impact of these two variables on the various ionization mechanisms is discussed in the three following sections.

2.4.2 Ionization by electrons

Electron multiplication is based on the mechanism of electron avalanche. At increasing electric fields, the energy distribution of the drifting electrons extends beyond the thresholds of inelastic collisions, resulting in excitation and ionization of the gas molecules. In the case of an ionization, one electron produces an electron-ion pair and the two electrons, in turn, can cause further ionizations. The number of electrons hence grows with time until all electrons are collected at the anode.

At a given field, the mean energy of the avalanche electrons is higher in hot gases than in cold gases. It would hence be expected that the largest gains are obtained in noble gases. This is not true in practice because the multiplication process in these gases is not stable.

2.4.3 The role of photons

The cross-sections for ionization and excitation have roughly the same order of magnitude at electron energies beyond the inelastic thresholds. Therefore, a comparable number of ionizations and excitations occur. In noble gases, the excited states return to the ground state via the emission of photons [51]. Because excitation mainly concerns outer shell electrons, a direct transition to the ground state results in the emission of a photon with an energy in the UV range [52]. De-excitation sometimes involves more than one transition and the energies of the emitted photons are lower, typically in the IR region. Oppositely, molecular gases have several excitation levels (vibration, rotation) with non-radiative relaxation modes. Also, they have a tendency to break into lighter fragments under impact of energetic electrons [53].

IR photons are not sufficiently energetic to impact on the avalanche development. This is not the case of the UV photons which can release new electrons from the gas molecules or from the detector electrodes by the photo-electric effect [54]. The new electrons initiate secondary avalanches, leading to detector instability and eventually to detector breakdown. The fate of the UV photons is thus very important for the detector stability and partly determines the maximum gas gain. It is desirable to stop them as early as possible. Molecular gases have absorption bands in the UV range [55, 56] and are well suited for this task. They are generally mixed with noble gases to stabilize the avalanche process (so-called quenching gases or quenchers). Extensive studies of various quenchers mixed with Ar, Kr and Xe are reported in [57, 58].

2.4.4 The Penning effect

The Penning effect is the ionization of a gas B by an excited state of a gas A^*:

$$A^* + B \rightarrow A + B^+ + e^- \tag{2.27}$$

where the ionization potential of B is lower than the excitation potential of A. In principle A and B may be of the same gas species, however, studies reporting on the Penning effect concern mixtures of two noble gases or of one noble gas and a molecular gas.

Beside increasing the primary ionization yield, the Penning effect enhances also the gas gain (cf. chapter 3). Extensive measurements of gas gain in several Ar-based and Xe-based Penning mixtures performed with a wire counter are reported in [59, 60, 61]. Also, gain measurements performed with a Micromegas detector in Ar-based Penning and regular gas mixtures (*i.e.* mixtures with no Penning effect) are reported in [62].

2.4.5 Gas discharges

The multiplication factor can not be increased at will. Above gains of several hundred thousand, the electron charge enhances the electric field at the front of the avalanche [53]. As a result, electrons and photons are produced at an increasing rate, resulting in instabilities in the multiplication process. If the photons are too numerous, they are not all quenched and secondary avalanches contribute to the formation of a plasma filament, called a streamer [43]. If the latter grows up to the point where the detector electrodes are connected, a conductive path is created in the gas and the detector capacity discharges.

An empirical limit on the maximum charge that can be tolerated in the avalanche before breakdown was formulated by Raether [63] and corresponds to an avalanche size of approximately 10^8 electrons (so-called Raether limit).

2.4.6 The Townsend coefficient

We present here and in the following sections, quantities relevant to the description of the avalanche development. It is assumed that the only ionization mechanism is ionization by electron impact. Moreover, recombination, attachment, photo-ionization, Penning and space charge effects are neglected.

The probability for an electron of energy ϵ to create an ion pair depends on the ionization cross-section $\sigma_{\mathrm{i}}(\epsilon)$ (the index “i” stands for ionization). Under the assumption that the ionizing collisions are independent, the mean free path for ionization λ_{i} relates to the cross-section:

$$\lambda_{\mathrm{i}}(\epsilon) = (n\sigma_{\mathrm{i}}(\epsilon))^{-1} \tag{2.28}$$

The mean number of ionizations per unit length is called the Townsend coefficient and is defined as:

$$\alpha(\epsilon) = 1/\lambda_{\mathrm{i}}(\epsilon) \tag{2.29}$$

In practice, it is more useful to know the Townsend coefficient at a given value of the electric field E and $\alpha(\epsilon)$ should be averaged over the electron energy distribution $p(E,\epsilon)$:

$$\alpha(E) = \int_0^\infty p(E,\epsilon)\alpha(\epsilon)d\epsilon \tag{2.30}$$

where $p(\mathrm{E},\epsilon)$ is normalized to unity. The analytical form of $p(E,\epsilon)$ in high fields is not known and one relies on measurements or numerical calculations for a determination of $\alpha(E)$. A couple of parametrizations of the dependence of the Townsend coefficient on the electric field have been proposed, valid in certain ranges of field [64]. One common parametrization that can be used for both cylindrical and parallel-plate detector geometries up to electric fields of about 50 kV/cm, was given by Rose and Korff [65]:

$$\alpha/P = \mathcal{A} \cdot \mathrm{e}^{-\mathcal{B}P/E} \tag{2.31}$$

with P the pressure and $\mathcal{A}$ and $\mathcal{B}$ two coefficients which depend on the gas.

2.4.7 The multiplication factor

The multiplication factor, or gain, can be calculated from the Townsend coefficient. Let $N(x)$ be the number of electrons present in the avalanche after a drift over a distance x along the field $E(x)$. After a path dx, the increase of the number of electrons is proportional to $N(x)$ and dx:

$$dN = N(x)\alpha(E(x))dx \tag{2.32}$$

with $\alpha(E(x))$ the Townsend coefficient at the field experienced by the electrons over the path *dx*. After a distance $\Delta x = x_1$-x_0, the avalanche size is obtained by integrating Equation 2.32:

$$N(\Delta x) = N_0 \cdot \exp\left(\int_{x_0}^{x_1} \alpha(E(x))dx\right) \tag{2.33}$$

where N_0 is the number of electrons at x_0.
The gain in an arbitrary field configuration can be simply expressed as:

$$G(\Delta x) = N(\Delta x)/N_0 = \exp\left(\int_{x_0}^{x_1} \alpha(E(x))dx\right) \tag{2.34}$$

where the integral is performed over the drift path of the electron that initiates the avalanche. In the case of a uniform field 2.34 reduces to:

$$G(\Delta x) = e^{\alpha \Delta x} \tag{2.35}$$

Using 2.35, the Raether limit of 10^8 electrons corresponds to $\alpha\Delta\mathrm{x} \sim 20$.

2.4.8 Gain fluctuations

The avalanche process is governed by probabilities and therefore the final size of an avalanche started by a single electron fluctuates. The avalanche size distribution, also called single electron response or gain distribution, impacts on many important detector properties. A few examples are given below.

The efficiency for detecting the passage of a particle through the gas is partly determined by the electronic noise level and the gain distribution. Only signals whose heights are significantly higher than the noise level are detected. This is of particular importance when the segmentation of the readout plane is high (*e.g.* pixel readout) as the charge induced on a pixel results from the multiplication of a single primary electron only.

The measurement of energy deposits of a few keV is realized by multiplication of the primary electrons. The precision of this measurement (or energy resolution) is mainly governed by the fluctuations in the primary number of electrons and the gain fluctuations. Therefore, the smaller the gain fluctuations, the more precise the energy deposit measurement.

When measuring the track of a charged particle with a detector whose anode is segmented in rows of pads of a few mm^2, signals from the multiplication of several primary electrons are induced on the same pad (cf. chapter 4). The position of the track along each pad row is calculated as the centre-of-gravity of the signals induced on the pads of each row. Ideally, the signal detected on each pad would be proportional to the number of primary electrons that arrived at this pad. Gain fluctuations, however, disturb the proportionality and therefore reduce the track reconstruction precision.

2.4.9 Gain fluctuations at moderate uniform fields

At fields of a few tens of kV/cm, the mean free path for ionization is large compared to the distance over which an electron of almost no energy gets in thermal equilibrium with the gas. At such fields, the probability per unit path length for a drifting electron to ionize a gas molecule does not depend on the previous history of the electron. It is constant throughout the electron drift. In this case, the size N (in number of electrons) of avalanches initiated by single electrons follows an exponential distribution [66, 67]:

$$p_N = \frac{1}{\overline{N}} \cdot \exp\left(-\frac{N}{\overline{N}}\right) \tag{2.36}$$

where $\overline{N}$ is the average avalanche size or gain, given by Equation 2.35. This distribution indicates that the most probable avalanche size is small but that large fluctuations occur (100 % r.m.s.). The distribution 2.36 was observed at low electric fields [68, 69]. Fluctuations in electronegative gases were investigated by Legler [70, 71]. He found a distribution more complicated than Equation 2.36 but still with a maximum at small N.

2.4.10 Gain fluctuations at high uniform fields

At high fields, an electron of almost no energy has to travel a distance x_0 comparable to the ionization mean free path $\lambda_\mathrm{i} = 1/\alpha$ before any ionization. The ionization probability per unit length is not constant but depends on the previous history of the electron. This situation applies to the electrons ejected from a gas molecule with almost no energy and also to the electrons that have lost almost all their energy in an inelastic collision. In the latter case, the abrupt change in energy is referred to as the relaxation of the electron energy distribution. The distinction between moderate and high fields can be made using the relaxation parameter:

$$\chi = \alpha x_0 \tag{2.37}$$

where x_0 is the threshold distance mentioned above and α^{-1} the mean free path for ionization. At moderate fields $x_0 \ll \alpha$ and $\chi \sim 0$ while at higher fields χ tends to 1. The distance x_0 can be expressed in terms of the energy U_0 gained by an electron during its acceleration by the field:

$$x_0 = U_0/E \tag{2.38}$$

where U_0 is often approximated to the ionization potential of the gas U_i. The shape of the gain distribution was observed to depend on the value of χ [63, 72]. For $\chi \sim 0$ the gain fluctuations are well described by the exponential distribution. When the electric field is increased, χ approaches 1 and the most probable gain shifts towards the mean gain.

The relaxation of the electron energy distribution was modeled by Legler [70, 73] using a modified Townsend coefficient a_0. The latter depends on the distance ξ that the electron has traveled since its last inelastic collision or birth:

$$a(\xi) = \begin{cases} 0 & \text{for } \xi < x_0 \\ a_0 & \text{for } \xi \geq x_0 \end{cases} \tag{2.39}$$

where

$$a_0 = \frac{\alpha}{2e^{-\chi} - 1} \tag{2.40}$$

and α is the Townsend coefficient. Although Legler was unable to derive the analytical form of the gain distribution, he found a very good agreement between measured single electron spectra and his model predictions.

Using Legler's model, Alkhazov derived an analytical expression for the relative variance of the gain distribution [74, 75], valid in arbitrary electric field configurations. He showed that in a uniform field, the gain relative variance b can be calculated as:

$$b = \frac{4e^{-2\chi} - 4e^{-\chi} + 1}{4e^{-\chi} - 2e^{-2\chi} - 1} \tag{2.41}$$

which predicts that b decreases with the field and assumes a value between 0.5–0.7 at 50–100 kV/cm in most gases.

2.4.11 The Polya distribution

A popular form of the gain distribution which was introduced by Byrne [76] is known as the Polya distribution (or Negative Binomial Distribution). Its derivation [43] assumes that the ionization probability per unit path length depends on the current size of the avalanche N through a dimensionless parameter b:

$$\frac{\partial p_{\mathrm{i}}}{\partial x} = \alpha\left(b + \frac{1-b}{N}\right) \tag{2.42}$$

The probability quickly reaches a constant value when N increases. This reflects the fact that the final size of the avalanche depends mainly on its early stages.

The dependence on N can be explained as follows. If the first ionization occurs after the electron has traveled a distance larger than the mean free path for ionization, the ionization probability per unit path length increases. Oppositely, fluctuations at larger N in the early stages of the avalanche will reduce the rate of development in the latter stages. The net effect is a reduction of the gain fluctuations. Using $m = b^{-1}$, the Polya distribution can be written as:

$$p(m, N) = \frac{m^m}{\Gamma(m)} \frac{1}{\overline{N}} \left(\frac{N}{\overline{N}}\right)^{m-1} \exp\left(-m\frac{N}{\overline{N}}\right) \tag{2.43}$$

It has a maximum at $\overline{N}(m\text{-}1)/m$ and its relative variance (equal to b) was found to decrease with the relaxation parameter χ [77].

The Polya distribution treats electrons starting the avalanche differently than the ones subsequently produced and therefore misses a clear physical interpretation. Yet, it fits the measurements of single electron response in parallel-plate detectors remarkably well [78, 79]. Also, measurements of very good energy resolution with detectors of different geometries can only be explained if the gain fluctuations are Polya-like [80, 81].

2.5 Signal development

During the electron multiplication process, a large number of electron-ion pairs are created in the gas. Electrons and ions are separated by the field and move towards their respective electrodes. The motion of electrons and ions in the gas induces charge on the electrodes. In typical operating conditions, most of the electrons are created a few microns away from the anode and their drift velocities are 2–3 orders of magnitude higher than those of ions. As a result, electrons are collected in a few ns and the signal is mainly due to the ion drift.

The charge induced onto an electrode corresponds to a current flowing between this electrode and ground. In a medium with perfect conductors and insulators, the current $i(t)$ induced by a moving charge q onto an electrode can be calculated by means of the Shockley-Ramo theorem [82, 83]:

$$i(t) = q\frac{\overrightarrow{v_\mathrm{d}}(t) \cdot \overrightarrow{E_\mathrm{w}}}{V_\mathrm{w}} \tag{2.44}$$

where $\overrightarrow{v_\mathrm{d}}(t)$, $\overrightarrow{E_\mathrm{w}}$ and V_w are the charge drift velocity and the weighting field and potential respectively. The weighting field and potential can be calculated by setting the voltage of the electrode of interest at 1 and all others at 0. After the moving charge has been collected, the total charge Q induced on the electrode is given by:

$$Q = \int_0^{\Delta t} i(t)dt = q\Delta V_\mathrm{w} \tag{2.45}$$

where ΔV_w is the weighting potential difference across which the charge has drifted. When resistive elements are present in the medium, the signal induction is more complex and the conductivity and permittivity of these elements have to be considered. Extended theorems for signals inductions in such configurations can be found in [84, 85].

Chapter 3

Ionization of gas by photons and charged particles

In high energy physics experiments, gaseous trackers are intended for measuring the tracks of relativistic charged particles. These particles exchange virtual photons with the gas molecules, resulting in excitation and ionization of the molecules. In the latter case, electrons may be released in the gas with some kinetic energy. As a result, the total ionization is due to the virtual photons and these electrons. I first treat the interaction of photons with matter and the ionization statistics of electrons with an energy up to a few thousand eV. Gas ionization by relativistic charged particles is then presented.

3.1 Interaction of photons with matter

A photon traveling through a material (solid, liquid or gas) can undergo three different interactions depending on its energy [42, 53]:

- The photo-electric effect where the photon is absorbed by an atomic electron which is then ejected with a part of the photon energy.
- Compton scattering where part of the photon energy is transfered to an atomic electron. In this process the photon is deflected and its wavelength increases.
- Pair production where the photon traversing the electromagnetic field of a nucleus materializes into an electron-positron pair.

The cross-sections for these interactions depend on the photon energy and on the atomic number and the density of the material. In gases with an atomic number larger than 4, the cross-section for the photo-electric effect dominates up to energies of several tens of keV. Above this, Compton scattering takes over. Pair production occurs for a photon energy higher than 2 electron masses ($\sim$ 1 MeV) and quickly surpasses the other processes.

3.1.1 Attenuation coefficient

The propagation of photons through matter is described by the attenuation coefficient. Let's consider a mono-energetic beam of photons traveling in the x direction and penetrating a given medium at position x_0. If the beam contains $N(x_0)$ photons at x_0, the number of photons that will have interacted with the medium atoms after a distance dx is proportional to the distance dx and the initial number of photon $N(x_0)$. If any photon undergoing an interaction is removed from the beam, $N(x)$ obeys:

$$dN = N(x_0 + dx) - N(x_0) = -\mu_\mathrm{t} N(x_0) dx \tag{3.1}$$

where μ_t is the total attenuation coefficient and depends on the total cross-section σ_t and the material number density n:

$$\mu_\mathrm{t} = \sigma_\mathrm{t} n = \sum_\mathrm{k} \sigma_\mathrm{k} n = \sum_\mathrm{k} \mu_\mathrm{k} \tag{3.2}$$

where σ_k is the cross-section for the individual processes indexed by "k" and μ_k is the corresponding attenuation coefficient. The number density of the medium relates to its mass density ρ:

$$n = n_\mathrm{A} \rho / A \tag{3.3}$$

with $n_\mathrm{A} = 6.02 \cdot 10^{23}$ mol^{-1}, the Avogadro constant and A the mass of a mole of medium element. From Equation 3.1, the beam attenuation along x is:

$$N(x) = N(x_0) \cdot \exp(-\mu_\mathrm{t} x) \tag{3.4}$$

which shows that over a distance $\lambda_\mathrm{t} = 1/\mu_\mathrm{t}$ (called the total mean free path), the number of photons in the beam is reduced by a factor $e \sim 2.7$. A mean free path λ_k can be defined for every interaction of kind "k":

$$\lambda_\mathrm{t} = 1/\mu_\mathrm{t} = 1/\sum_\mathrm{k} \mu_\mathrm{k} = 1/\sum_\mathrm{k} (1/\lambda_\mathrm{k}) = \left(\prod_\mathrm{k} \lambda_\mathrm{k}\right) / \sum_\mathrm{k} \left(\prod_{\mathrm{i} \neq \mathrm{k}} \lambda_\mathrm{i}\right) \tag{3.5}$$

The mass attenuation coefficient μ_t/ρ is also commonly used. The energy dependence of the mean free path for the photo-electric effect and Compton scattering on He, Ar and Xe atoms is illustrated in Figure 3.1.

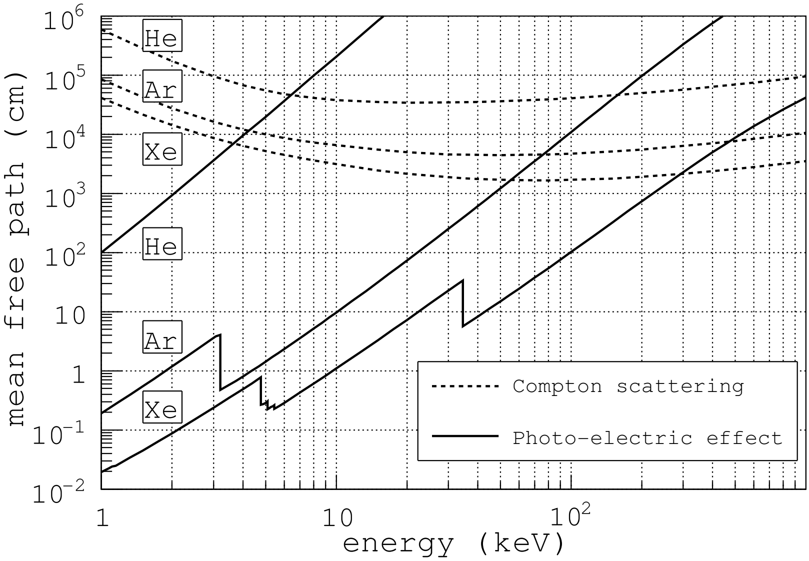

Figure 3.1: *Mean free paths for the photo-electric effect and Compton scattering in He, Ar and Xe at normal conditions. The mean free paths are calculated using gas mass densities from [43] and mass attenuation coefficients from [86].*

3.1.2 The photo-electric effect

The photo-electric effect is the absorption of a photon of energy E_0 by an atomic electron followed by the emission of the electron (so-called photo-electron) with a kinetic energy equal to:

$$E = E_0 - E_{\text{shell}} \tag{3.6}$$

with E_{shell} the energy of the shell the electron belongs to. Because the photon energy is completely absorbed, the photo-electric effect must involve a third collision partner to take the recoil momentum: the nucleus.

When the photon energy increases above the energy of a shell, the electrons of this shell become available for the photo-electric effect and the cross-section sharply rises (so-called shell edges). This can be seen, in Figure 3.1, as a sudden decrease of the mean free path at *e.g.* 3.2 keV in Ar. The total cross-section for the photo-electric effect is the sum of the cross-sections for the photo-electric effect on the various shells energetically allowed. At energies higher than the K-shell energy (so-called K-edge), the cross-section for absorption in the K-shell is about 80 % of the total cross-section because of the proximity of the third collision partner [87].

In the non-relativistic limit ($E_0 \ll m_\mathrm{e}\mathrm{c}^2$) and at photon energies higher than the energy of the K-shell, the cross-section for the photo-electric effect is [42]:

$$\sigma_\mathrm{pe}(E) = 4\alpha^4\sqrt{2}Z^5\frac{8\pi r_\mathrm{e}^3}{3}\left(\frac{m_\mathrm{e}c^2}{E_0}\right)^{7/2} \tag{3.7}$$

where α is the fine structure constant, r_e the classical radius of the electron, m_e the electron mass, Z the atomic number of the material and E_0 the photon energy. This formula, valid up to energies of roughly 500 keV, shows a very strong dependence of the cross-section on the number of electrons in the medium atom Z. This accounts for the much larger value of the mean free path for the photo-electric effect in He compared to, for instance, Ar.

The emission of a photo-electron leaves a vacancy in the shell it belonged to. This vacancy can be filled by two mechanisms [53].

- Fluorescence: the vacancy is filled by an electron from an outer shell and the energy difference is liberated in the form of an X-ray of characteristic energy. The most probable fluorescence transitions are indicated in Figure 3.2.
- Auger transition: the vacancy is also filled by an electron from an outer shell but the energy difference is transfered to an electron of the same atom. If the energy is larger than the binding energy of this electron, the latter is ejected from the atom (so-called Auger electron).

  Auger transitions are classified as XYZ with X the shell of the original vacancy, Y the shell of the electron that fills the vacancy and Z the shell from which the Auger electron is ejected [88].

  In the case of one initial vacancy, an Auger transition leaves the gas atom (or molecule) in a doubly ionized state.

In both processes, a vacancy is replaced by another vacancy and the complete atomic relaxation can involve more than one transition [89]. The fraction of de-excitation through fluorescence is called the fluorescence yield and is an increasing function of the number of electrons [90]. It is negligible in helium where a photo-electron is always accompanied by an Auger electron. In argon, the K-shell fluorescence yield is equal to 13.5 % while the one of the L-shell is negligible [91].

3.1.3 The Compton effect

The Compton effect is the incoherent scattering of a photon off an atomic electron: the photon is not sensitive to the atomic structure and scatters off the electron as if it were free. The coherent scattering off the atom as a whole is called Rayleigh scattering and is of no direct interest for particle detection as no energy is transfered to the medium [93]. Oppositely, a Compton scattered photon transfers some energy to an atomic electron (so-called Compton electron) and its wavelength shifts by:

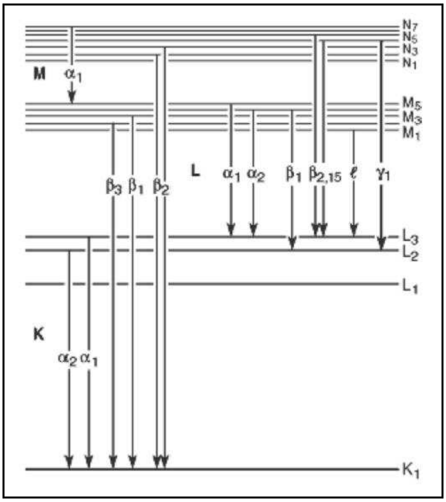

Figure 3.2: *Transitions that give rise to the strongest fluorescence lines [92].*

$$\Delta\lambda = \frac{h}{m_\mathrm{e}c}(1-\cos\theta) \tag{3.8}$$

where h is the Planck constant and θ the angle between the initial and final wave vector of the photon. If the transfered energy is larger than the electron binding energy, the electron is ejected from the atom. The maximum transfered energy is given by:

$$\Delta E_\mathrm{max} = E \cdot \frac{2E/(m_\mathrm{e}c^2)}{1+2E/(m_\mathrm{e}c^2)} \tag{3.9}$$

The total and differential cross-sections for Compton scattering can be found in [93]. For photons less energetic than X-rays, the cross-section is independent of the photon energy and the transfered energy becomes negligible (so-called Thomson scattering).

3.2 Absorption in gas of electrons with energies in the keV range

The interaction of an X-ray in gas results in the emission of a photo-electron, sometimes accompanied by one or more Auger electrons. These electrons (called fast electrons in the following) have energies in the keV range and are generally fully absorbed in the gas. They lose their energy through inelastic collisions with the molecules, producing a certain number of primary electron/ion pairs and excited molecules. At energies higher than a few tens of eV, the number of primary electrons is proportional to the absorbed energy. The energy can thus be measured through the number of produced electrons and the relation between the two quantities is important and explained in the following sections.

3.2.1 The mean energy per ion pair in pure gases

A fast electron stopped in the gas loses its energy in discrete amounts through inelastic collisions with the gas molecules. The collisions with noble gas atoms mainly result in electronic level excitations and ionizations, while for more complex molecules (*e.g.* CO_2, CH_4 and heavier organic gases), excitations of vibrational and rotational levels are also possible. Therefore, the electron energy E_0 is not all invested in ionization and the number of primary electrons N_e depends on the gas mixture. Experimentally, it obeys the following equation:

$$N_\mathrm{e} = E_0/W \tag{3.10}$$

where W is the mean energy per ion pair and is derived from measurements. The value of W is governed by the cross-sections for the various inelastic collisions and the corresponding energy losses. It thus depends on the gas composition and the electron energy [94, 95].

In a given gas, W is constant for electron energies above a few keV and slightly increases at lower energies [96]. The dependence of W on the gas composition is complex. In pure gases it generally decreases with the ionization potential U_i and rises with the number of non-ionizing "channels" of the gas molecules (*e.g.* excitation, rotational and vibrational levels). For this reason, the value of W is about 20–30 eV in both noble gases (like Ar, Kr and Xe) and hydrocarbons. The high ionization potentials of He and Ne (24.6 and 21.6 eV respectively) account for the large values of W in those gases (41 and 36 eV). The case of CO_2 is also interesting: despite its relatively low ionization potential (13.8 eV), the very large number of vibrational and rotational levels results in a high W value of 34 eV.

Values of W and U_i for pure gases can be found in [97, 98] and [95]. The ratio W/U_i indicates what fraction of the primary energy is invested into ionization. It is approximately 60 % in pure gases. In molecular gases, the number of non-ionizing channels is larger and W/U_i is about 40 %.

3.2.2 The Fano factor in pure gases

The outcome of each collision between an electron and a gas molecule is governed by probabilities and the number of primary electrons resulting from the absorption of an energy E_0 fluctuates. In the case of independent ionizing collisions, the number of primary electrons N_e would follow Poisson statistics with a variance equal to N_e. The number of ionizing collisions, however, is constrained by the initial energy of the fast electron: $N_\mathrm{e} \leq E_0/U_i$. The process is therefore not Poissonian and N_e exhibits a reduced variance [93].

The reduction of the variance is accounted for by the Fano factor F [99]:

$$\sigma^2_{N_\mathrm{e}} = F \cdot N_\mathrm{e} \tag{3.11}$$

The Fano factor indicates the magnitude of the fluctuations of the number of electrons: the smaller it is, the smaller the variance. Alike W, F depends on the gas mixture and the electron energy [100]. The Fano factor of electrons lies between 0.15–0.2 in noble gases and 0.2–0.4 in molecular gases (Table 3.1). A compilation of measurements suggests that it decreases with the ratio U_i/W [101].

Fano showed [99] that if the ratios of the cross-sections for inelastic collisions are independent on the electron energy, the Fano factor is given by:

$$F = (1/\overline{N})\overline{(N - (E/W))^2} \tag{3.12}$$

where N is the number of electrons resulting from an inelastic collision and E the energy lost in this impact; the average is carried out over the different collisions. Fano distinguished between three types of inelastic collisions, depending of the energy loss.

- Excitations (e): the energy loss is smaller than the ionization potential of the gas. The fast electron loses an energy equal to the excitation potential and no electrons are produced.

- Ionization of first type (i1): the energy loss lies between U_i and $2U_\mathrm{i}$. The emitted electron has insufficient energy to ionize the gas. In his model, Fano assumes this energy to be constant although it should vary from one collision to the other.

- Ionization of second type (i2): the energy loss is larger than twice U_i. The emitted electron has sufficient energy to ionize the gas. As the electron kinetic energy can be utilized again, the effective energy lost by the fast electron is U_i.

Finally Fano arrived to:

$$F = \left(\sum_\mathrm{k}^{\mathrm{e}} \sigma_\mathrm{k} \left(\frac{E_\mathrm{k}}{W} \right)^2 + \sum_\mathrm{k}^{\mathrm{i1}} \sigma_\mathrm{k} \left(1 - \frac{E_\mathrm{k}}{W} \right)^2 + \sum_\mathrm{k}^{\mathrm{i2}} \sigma_\mathrm{k} \left(1 - \frac{U_\mathrm{i}}{W} \right)^2 \right) \Big/ \sum_\mathrm{k}^{\mathrm{i1,i2}} \sigma_\mathrm{k} \tag{3.13}$$

from which he evaluated F to lie between 1/3 and 1/2. Despite the crude assumption of his model, namely that electrons produced with energy in excess of U_i have the same collision probabilities as those of the fast electron, he found the correct order of magnitude.

3.2.3 Regular and Penning gas mixtures

The values of W and F in a mixture of gases depend on the occurrence of the Penning effect (cf. section 2.4.4). In regular mixtures, no Penning transfers occur between the two gases and the total ionization yield is given by the super imposed ionization of each gas. The ionization yield in Penning mixtures is generally higher: in addition to the direct ionization of each gas species, some extra ionization is produced through Penning transfers. Binary mixtures exhibiting a strong Penning effect are mixtures of a noble gas and a small concentration (a few percents at most) of another noble gas or a molecular gas.

3.2.4 *W* and *F* in regular gas mixtures

In a regular gas mixture, the number of primary electrons N_e can be calculated as a weighted average of N_e in the pure gases. The weights are determined by the relative concentrations C and ionization cross-sections σ. For a mixture of two gases A and B, the value W_{AB} should thus obey:

$$\frac{1}{W_{\mathrm{AB}}} = \frac{C_{\mathrm{A}}\sigma_{\mathrm{A}}}{W_{\mathrm{A}}} + \frac{C_{\mathrm{B}}\sigma_{\mathrm{B}}}{W_{\mathrm{B}}} \tag{3.14}$$

where $\sigma_{\mathrm{A}}+\sigma_{\mathrm{B}} = 1$. The latter equation can be written as:

$$W_{\mathrm{AB}} = \frac{W_{\mathrm{A}}W_{\mathrm{B}}}{C_{\mathrm{A}}\sigma_{\mathrm{A}}W_{\mathrm{B}} + C_{\mathrm{B}}\sigma_{\mathrm{B}}W_{\mathrm{A}}} \tag{3.15}$$

In a mixture of more than two gases, Equation 3.15 can be generalized:

$$W_{\mathrm{mix}} = \left(\prod_{\mathrm{k}} W_{\mathrm{k}}\right) / \sum_{\mathrm{k}} \left(C_{\mathrm{k}}\sigma_{\mathrm{k}} \prod_{\mathrm{i}\neq\mathrm{k}} W_{\mathrm{i}}\right) \tag{3.16}$$

where $\sum \sigma_{\mathrm{k}} = 1$. The Fano factor in some binary regular mixtures was found to lie between the values of the two species, suggesting that it could also be obtained from a weighted average [102, 103].

3.2.5 *W* and *F* in Penning gas mixtures

The total ionization yield in a Penning mixture is due to the contribution from direct ionization of the gas species plus the contribution of the Penning transfers. The value of W is thus lower than the one predicted by Equation 3.16 [95]. As an example, the ratio U_{i}/W in a mixture of argon with 0.5 % of acetylene was measured to be as high as 80 % while it is equal to 60 and 40 % in the two pure gases [104].

The possibility to decrease the Fano factor in Penning mixtures was first considered by Vorob'ev *et al.* who predicted that Fano factors as small as 0.05 could be achieved at very small admixture concentrations [74, 105]. Alkhazov *et al.* measured a Fano factor between 0.05 and 0.09 for alpha particles in various Penning mixtures with admixture fractions below 1 % [104, 106]. This can be explained by a reduction of the possible outcomes of the inelastic collisions. At small admixture concentrations, most of the energy is invested in ionization and excitation of the main gas. If all the excited states of the main gas participate in Penning transfers, the number of primary electrons is almost maximum and fluctuates very little. In other words, U_i/W tends to 1 and F to 0. In avalanche-based gas detectors, however, the gas mixture consists of a rare gas and at least 5 % of a quencher and such small Fano factors can not be obtained. Measured values of F in pure gases and mixtures lie between 0.1–0.4 and are listed in Table 3.1.

3.2.6 Range of fast electrons in gas

The range of fast electrons is of concern when measuring the tracks of relativistic charged particles which, in a small fraction of ionizing collisions, knock out energetic electrons from the gas molecules (so-called δ-rays). These electrons are stopped over a distance of several millimeters to a few centimeters and can produce large ionization clusters far from the particle trajectories. Eventually, this may cause an error when reconstructing the particle tracks. Fast electrons of a given energy scatter almost randomly about their initial direction but cover on average a distance R_p, called the practical range. A parametrization of the dependence of R_p (in g/cm^2) on the electron energy E (in MeV) is given by:

$$R_\mathrm{p}(E) = 0.71E^{1.72} \tag{3.17}$$

and is valid for energies up to a few hundred keV [118].

3.3 Ionization by relativistic charged particles

Gas ionization by relativistic charged particles is a complex subject and its full treatment is beyond the scope of this thesis. Only the main aspects will be introduced here and the reader is referred to [43] for a detailed treatment.

3.3.1 Ionization mechanisms

A relativistic charged particle traversing a gas exchanges with the molecules a copious number of low-energy virtual photons. These photons are mostly absorbed in the outer shells of the molecules, resulting in excitation and sometimes ionization [119, 120]. After emission of the photo-electrons, the excited neutral and charged molecules de-excite through fluorescence, Auger transitions and if possible Penning transfers. As a result, only a certain fraction of the total ionization comes from the molecules encountered by the charged particle. This fraction is called the primary ionization. Oppositely, secondary ionization is produced by the primary electrons (photo-electrons and Auger electrons), the fluorescence photons and by Penning transfers.

Gas	F	E_0 (keV)-particle	method	ref.
He	0.17	β	C.	[106]
Ne	0.17		C.	[106]
Ar	0.17		C.	[106]
	0.22	α	I.C.	[107]
	0.23 ± 0.05	5.9 (^{55}Fe) - γ	P.S.	[108]
	0.20 ± 0.02	5305 (^{210}Po) - α	I.C.	[109]
	$\leq0.40\pm0.03$	1 .49 (K$_\alpha$ Al) - γ	P.S.	[110]
Kr	$\leq0.19\pm0.02$	1.49 (K$_\alpha$ Al) - γ	P.S.	[110]
Xe	$\leq0.15\pm0.03$	1.49 (K$_\alpha$ Al) - γ	P.S.	[110]
	≤0.15	1.49 (K$_\alpha$ Al) - γ	P.S.	[110]
	0.170 ± 0.007	1.49 (K$_\alpha$ Al) - γ	P.S.	[111]
	0.13 ± 0.01	5.9 (^{55}Fe) - γ	P.S.	[112]
CH_4	0.26	1.49 (K$_\alpha$ Al) - γ	D.	[113]
C_2H_6	0.28	1.49 (K$_\alpha$ Al) - γ	D.	[113]
C_2H_6	0.250 ± 0.010	1.49 (K$_\alpha$ Al) - γ	E.C.	[114]
C_3H_8	0.25	1.49 (K$_\alpha$ Al) - γ	D.	[113]
iC_4H_{10}	0.26	1.49 (K$_\alpha$ Al) - γ	D.	[113]
iC_4H_{10}	0.255 ± 0.009	1.25 (K$_\alpha$ Mg) - γ	E.C.	[114]
C_5H_{12}	0.27	1.49 (K$_\alpha$ Al) - γ	D.	[113]
C_6H_{14}	0.26	1.49 (K$_\alpha$ Al) - γ	D.	[113]
C_2H_2	0.31	1.49 (K$_\alpha$ Al) - γ	D.	[113]
CO_2	0.33	1.49 (K$_\alpha$ Al) - γ	D.	[113]
Ar/CH_4 90/10	0.14	0.26 and 2.82 - β		[115]
Ar/CH_4 90/10	0.18 ± 0.01	5305 (^{210}Po) - α	I.C.	[116]
Ar/CH_4 90/10	0.31 ± 0.10	2.6 keV (^{37}Ar) - γ	D.	[117]
Ar/CH_4 90/10	0.21 ± 0.10	5.9 keV (^{55}Fe) - γ	D.	[117]
Ar/C_2H_6 20/80	0.250 ± 0.010	1.49 (K$_\alpha$ Al) - γ	E.C.	[114]
Ar/iC_4H_{10} 20/80	0.250 ± 0.010	1.25 (K$_\alpha$ Mg) - γ	E.C.	[114]
Ar/DME 20/80	0.315 ± 0.015	1.25 (K$_\alpha$ Mg) - γ	E.C.	[114]
Ar/C_2H_2 99.5/0.5	0.09	$5.68\cdot10^3$ (^{224}Ra) - α	I.C.	[104]
Ar/CH_4 99.2/0.8	0.19	$5.68\cdot10^3$ (^{224}Ra) - α	I.C.	[104]

Table 3.1: *Measured and calculated Fano factors in several pure gases and gas mixtures. The type and energy of the ionizing radiation is also quoted. The technique used for the measurement is indicated in column five: C. refers to calculations, P.S. to proportional scintillation, I.C. to ionization chamber, D. to deconvolution and E.C. to electron counting. These techniques are explained in more detail in chapter 8.*

3.3.2 The Bethe and Bloch formula

The total ionization density along the track of a relativistic charged particle is proportional to the mean energy loss through electromagnetic interactions per unit length dE/dx. The dE/dx can be parametrized by the Bethe and Bloch formula [121] which is valid for particles other than electrons:

$$dE/dx = -4\pi N_{\mathrm{A}}\rho \frac{Z}{A}\frac{e^4}{m_{\mathrm{e}}c^2} z^2 \frac{1}{\beta^2}\left\{\ln \frac{2m_{\mathrm{e}}c^2}{I}\beta^2\gamma^2 - 2\beta^2 - \frac{\delta(\beta)}{2}\right\} \tag{3.18}$$

where $\beta = v/c$ is the particle velocity in units of c, $m_{\mathrm{e}}c^2$ the electron rest mass and $\gamma = (1\text{-}\beta^2)^{-1/2}$ the relativistic factor. The dependence of the energy loss on the gas composition is accounted for through the effective atomic number Z/A, the gas density ρ and the mean excitation potential I. The dependence on the particle kind and velocity enters the formula through the charge z and the velocity β. The term $\delta(\beta)/2$ is responsible for the saturation of the energy loss at high energy.

According to Equation 3.18, the energy loss initially decreases like $1/\beta^2$ and goes through a minimum at $\beta \sim 3.2$. Particles with energies close to this minimum are called minimum ionizing particles or MIPs. At higher velocities, the field of the incoming particle becomes stronger and spreads across the medium. Moreover, the maximum energy transfer increases too and the energy loss per unit length rises again (so-called relativistic rise region). At larger values of $\beta\gamma$, the medium becomes polarized by the particle field which is shielded by the polarization field. The energy loss saturates and reaches the so-called Fermi plateau. The dependence of the dE/dx on the particle momentum and type is illustrated in Figure 3.3. Over certain momentum ranges, the energy loss depends significantly on the particle type and can be used for particle identification purposes [43, 122].

3.3.3 Primary ionization statistics

The energy lost by a relativistic charged particle at every impact with a gas molecule is very small with respect to its total energy and the ionization cross-section is constant. Thus, the number of ionizing collisions over a given distance can be described by Poisson statistics [53] and the distance l between two successive ionizing collisions obeys the following distribution:

$$p(l) = 1/\lambda_{\mathrm{p}} \cdot e^{-l/\lambda_{\mathrm{p}}} \tag{3.19}$$

where λ_{p} is the ionization mean free path. The primary ionization density n_{p} is equal to $1/\lambda_{\mathrm{p}}$ and depends on the type of charged particle, the particle velocity and the gas mixture. For MIPs n_{p} assumes values between 5 and 90 electrons per cm depending on the gas mixture [43].

3.3.4 Secondary ionization statistics

The number and localization of the secondary electrons depend on the distribution of the discrete energy transfers ΔE from the particle to the gas electrons. At small ΔE, this distribution is a complex function of the electronic structure of the gas molecules, the particle energy and the type of particle. When the energy transfer is larger than the highest atomic binding energy, the orbiting electrons can be considered free and the distribution behaves like ΔE^{-2} (Rutherford scattering). This means that although the distribution drops fast, it has a long tail: large energy transfers are rare but do occur. The secondary ionization has large fluctuations and the total ionization can thus be several times larger than the primary ionization. The total electron density n_t for MIPs ranges from 10 to 300 electron/ion pairs per cm depending on the gas mixture [43].

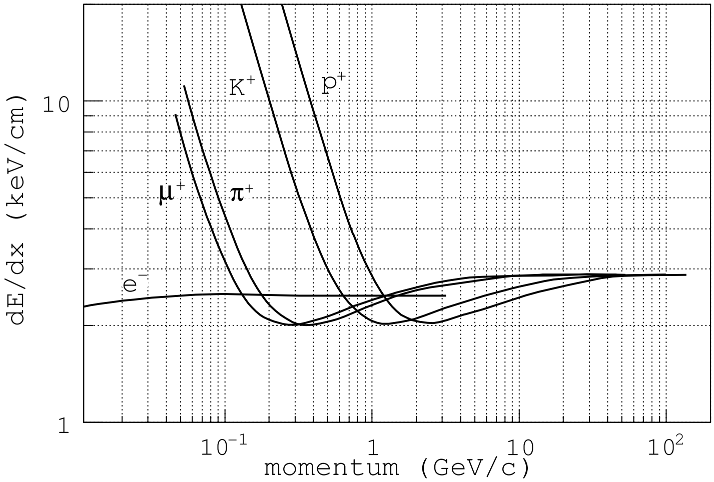

Figure 3.3: *Mean energy loss per unit length dE/dx in argon at normal conditions as a function of the momentum for various particles as calculated by the HEED program [119].*

3.3.5 Ionization clustering

For most of the primary ionizing collisions, the energy transfers are small. As a result, the secondary ionization is produced close to the primary collisions and the total ionization along the particle tracks appears in clusters. The cluster size distribution gives the probability p_k that a cluster contains k electrons and is used to account for the various energy transfers. Few measurements of p_k have been performed so far [123] and one often relies on computer calculated distributions. One popular program that simulates the energy loss of fast charged particles in gas is the HEED program [119].

Chapter 4

Gaseous trackers

Gaseous trackers are intended for reconstructing the trajectories of charged particles and measuring their momenta. The trajectories are interpolated by measuring the positions of the primary electrons produced along the tracks and the momenta are derived from the curvature of the tracks in a magnetic field of known strength.

In this chapter, I introduce and explain the operation principle of various gas detectors, from the wire tube to recent pixelated micro-scale detectors. The last section is devoted to the measurement of the momentum of charged particles in colliding beam experiments.

4.1 The wire tube

4.1.1 Principle of operation

The wire tube is a metal cylinder of a few centimeters diameter containing a mixture of gas. A conductive wire is stretched along its axis and connected to a readout circuitry outside the gas volume. The wire is raised to a positive voltage of a few hundred volts while the cylinder wall remains at ground. Assuming a cylinder of infinite length, the electric field $E(r)$ at a distance r from the wire axis is:

$$\overrightarrow{E(r)} = \frac{V_0}{\ln(b/a)} \frac{1}{r} \overrightarrow{u_r} = \frac{CV_0}{2\pi\epsilon_0} \frac{1}{r} \overrightarrow{u_r} \tag{4.1}$$

where V_0 is the wire voltage, C the detector capacity per unit length, a and b the wire and cathode radii and $\overrightarrow{u_r}$ the unit vector in cylindrical coordinates.

A charged particle traversing the gas volume produces some primary electron-ion pairs which are separated by the electric field: ions drift towards the cathode wall while the electrons drift towards the wire. When entering the high field region in the vicinity of the wire, the primary electrons become sufficiently energetic to release electrons from the gas molecules. Hence, each primary electron initiates an avalanche which grows until all electrons have hit the wire surface. Because of diffusion of the electrons in the gas, the avalanche has a certain spatial extension. In typical operating conditions, the avalanche develops on one side of the wire (Figure 4.1 (a)).

The avalanche electrons are collected on the wire surface after a few nanoseconds, leaving a drop-shaped cloud of positive ions that slowly drifts to the cathode in several tenths of ms. During part of the ion drift time, the wire field (and thus the gain) is locally reduced by the ion space charge. In this region, the detector is temporarily insensitive to new incoming primary electrons.

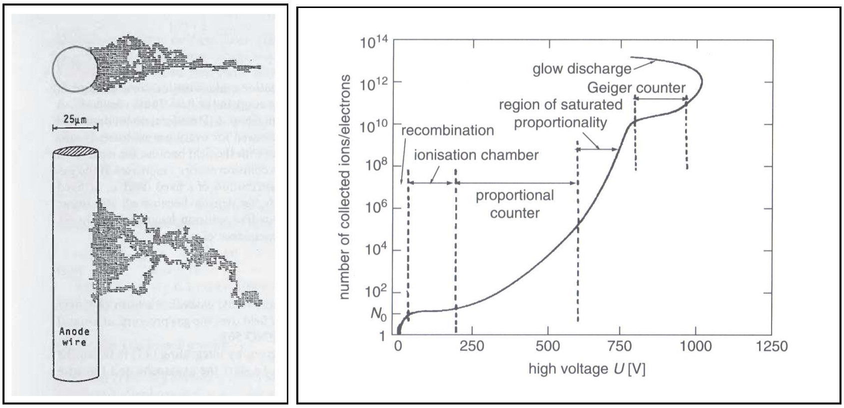

(a) (b)

Figure 4.1: *Two-dimensional displays of the electron density of an avalanche as calculated by a Monte Carlo simulation (a) [124]. Total number of collected electrons as a function of wire voltage in a wire tube irradiated with electrons (b) [87].*

4.1.2 Modes of operation

The motion of electrons and ions in the gas gives rise to an electric signal on the electrodes which can be detected by an external electronic circuit. For a given gas and type of impinging particle, the magnitude of the induced signals depends mainly on the field strength (or the wire voltage) and one distinguishes various modes of operation. These modes are illustrated in Figure 4.1 (b) where the total number of collected electrons produced upon irradiation of the tube to electrons are plotted against wire voltage in a given gas mixture. Several regions corresponding to the various modes of operation can be distinguished.

- Below voltages of a few volts, the electric field is too low to separate efficiently the electron-ion pairs, some of which thus recombine. When the voltage is increased, recombination diminishes and the signal increases. Above a certain voltage, all the primary charge is collected and the detector works in the ionization chamber mode.

- Gas amplification takes place in the third region and the signal grows exponentially with the voltage. The interesting property of this region (not apparent in Figure 4.1 (b)) is that the amplified signal is proportional to the number of primary electrons. With sensitive electronics connected at the wire end, the wire tube can be used to measure the energy loss of a charged particle traversing the gas volume or the total energy of a particle stopped in the gas. The detector is referred to as the proportional wire tube.
- At higher voltages, the proportionality is progressively lost because the wire field at the front of the avalanche is enhanced by the field of the electrons, resulting in an increased production rate of photons and electrons. The signal rises super-exponentially with the voltage and becomes independent of the primary charge (limited proportionality or streamer region).
- When the voltage is increased further, any electron avalanche evolves in a spark: a conductive path is created in the gas between the wire and the cathode resulting in the discharge of the detector capacity. The detector operates in the so-called Geiger mode: large signals are obtained but at the price of long dead times (a few milliseconds). In this region the signal is the same no matter the primary number of electrons and the detector can only be used for counting.

A single wire tube has essentially no segmentation, however, when stacking several tubes together, tracks of charged particles traversing the tube array can be reconstructed from the signals induced on the wires. This principle is used for instance in the muon spectrometer of the ATLAS experiment [125] and is illustrated in Figure 4.2. In order to have a small distance between the wires, arrays of proportional tubes with a few millimeters radii, called straw-tube detectors, were built. It was also proposed to bring the wires inside the same gas volume or chamber; this detector is called the Multi Wire Proportional Chamber or MWPC.

4.2 The Multi Wire Proportional Chamber

4.2.1 Definition and electrostatic configuration

The MWPC consists of several wires placed in a common gas chamber. The wires are stretched parallel and at equal distance from each other, in between two parallel planes kept at ground potential (Figure 4.3). Let's consider an infinite planar set of infinitely long parallel wires of radius a extending along the z-axis. The wires are placed at $y = 0$ and separated by a distance p along the x-axis. Two grounded planes are placed at $y = h$ and $y = -h$.

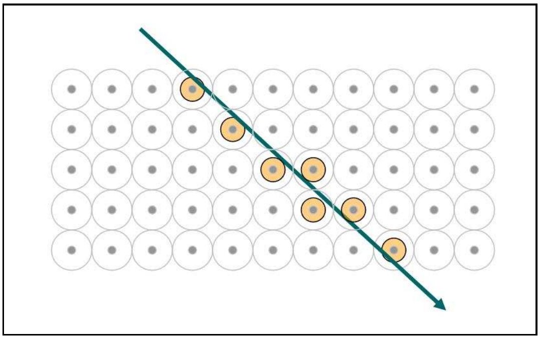

Figure 4.2: *Cross-section of an array of wire tubes traversed by a charged particle. The track is reconstructed from the ionization produced in the tubes.*

With $V = V_0$ on the wires [53], the electric field is given by:

$$E(x,y) = \frac{CV_0}{2\epsilon_0 p}\left(1+\tan^2\frac{\pi x}{p}\tanh^2\frac{\pi y}{p}\right)^{1/2}\left(\tan^2\frac{\pi x}{p}+\tanh^2\frac{\pi y}{p}\right)^{-1/2} \quad (4.2)$$

where the capacity per unit length C is equal to:

$$C = \frac{2\pi\epsilon_0}{\pi h/p - \ln(2\pi a/p)} \quad (4.3)$$

The electric field configuration is illustrated in Figure 4.3 where the field lines are drawn. MWPC of several meter square areas can be built, providing large detection areas for ionizing radiations. Typical dimensions of large area MWPCs are 2 mm wire spacing, 20 μm wire diameter and 6 mm between the cathode and the wire planes.

4.2.2 Tracking capabilities

MWPCs are intended for measuring track points of particles traversing the gas volume perpendicular to the wire plane (along the y-axis). If the signals are read out from the wires only, the ionization from a particle traveling along the y-axis is often collected onto one wire, providing a coordinate along the x-axis with a precision σ_x of the order of $p/\sqrt{12}$ where p is the wire pitch. As the y position of the chamber is known, the coordinate along the y-axis is determined with an accuracy σ_y of about $2h/\sqrt{12}$, where h is the wire-cathode distance.

In this configuration, a single MWPC provides no information along the wire (*i.e.* z-direction). This limitation can be overcome by stacking several chambers with different wire orientations or by segmenting the cathode plane in individual electrodes. The case of a segmentation into pads will be dealt with in section 4.4 and I present here the case of a segmentation into strips.

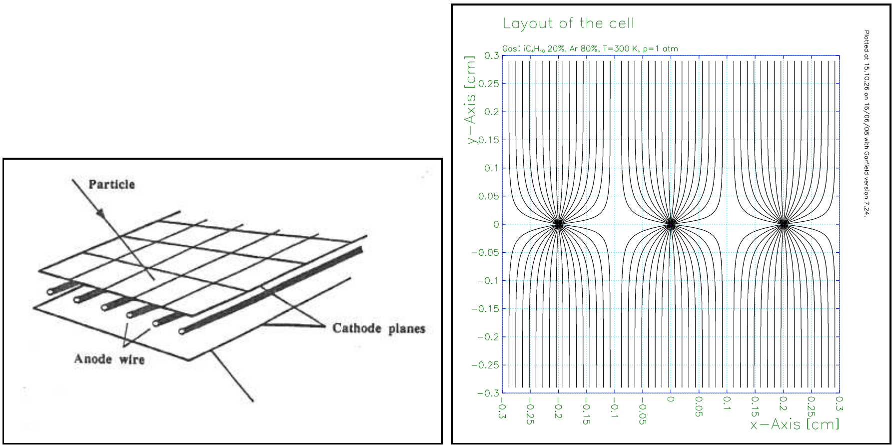

(a) (b)

Figure 4.3: *Layout (a) and field lines (b) of a Multi Wire Proportional Chamber.*

While drifting to the cathode plane, ions from the electron avalanches induce charge on this plane. The induced charge distribution on the cathode plane is approximately gaussian with a width given by the distance h between the wire and the plane [43]. Advantage can be taken of this broad distribution if the cathode plane is segmented into metal strips (or wires) running perpendicular to the anode wire direction. When the width and pitch of the strips are carefully adjusted to the distribution width, the drifting ions induce a signal on 3 to 5 strips. The position of the avalanche along an anode wire can then be inferred by measuring the centre-of-gravity of the cathode signals.

Cathode readout MWPCs yield excellent spatial resolution along the wires, typically of the order of 50 μm [126]. On the other hand, they require a large number of electronic channels and are more complex to build than chambers with continuous cathode planes.

4.3 The drift chamber

The drift chamber has a design similar to that of a MWPC and aims at measuring the drift distances of the primary electrons produced by a particle traversing the detector volume perpendicular to the wire planes. This measurement requires the time of passage of the particle (provided by an external trigger), a well-known (preferably linear) relation between the drift distance Δd and the drift time Δt and finally fast electronics to measure precisely the arrival times of the electrons.

The linear relation between Δd and Δt is fulfilled if the drift velocity is constant over the drift volume. This is not the case of MWPCs where the electric field around the wires is varying (Equation 4.2 shows that the field even vanishes between two wires), however, the field homogeneity can be improved if field-shaping wires (so-called field wires) are placed in between anode wires (so-called sensing wires). Also, the gas mixture can be chosen for a minimum dependence of the drift velocity on field variations.

Several planes of wires can be combined in a single gas volume if the cathode planes are replaced by field wires. A typical layout of a "drift cell" is sketched in Figure 4.4 where the drift paths of primary electrons and ions are drawn.

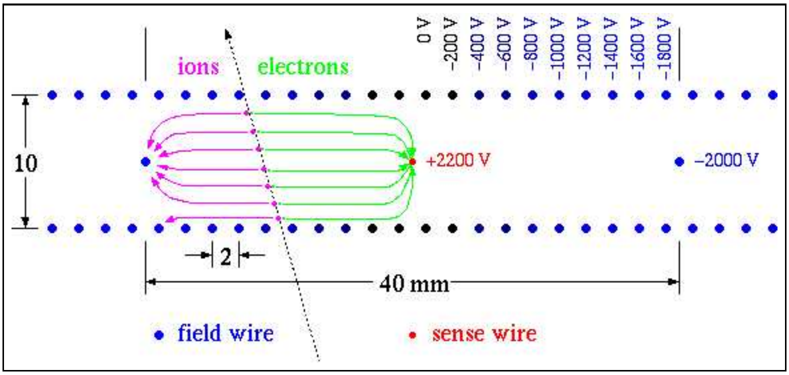

Figure 4.4: *Layout of a drift chamber "cell" where a sensing wire is placed in the center of an array of field-shaping wires.*

The spatial resolution of drift chambers depends mainly on the arrival time measurement precision, the electron longitudinal and transverse diffusion in the gas (generally smaller than 50 μm) and the homogeneity of the field. Drift chambers of cylindrical geometry have also been built to measure the tracks of particles produced in the collisions of two particle beams. An overview of these detectors can be found in [42].

4.4 The Time Projection Chamber

4.4.1 Operating principle

The Time Projection Chamber (or TPC) is based on the drift chamber principle of determining the track position along the field direction by measuring the time of drift of the primary electrons. It is a large cylindrical chamber generally separated in two drift regions of equal volume by means of a central high voltage plane. The chamber is closed by two endcaps, segmented into sectors of concentric pad rows.

By means of circular conductive strips set at linearly decreasing voltages around the cylindrical field cage, a uniform axial electric field is created with opposite directions in the two regions. For gas amplification purposes, arrays of anode and cathode wires are placed parallel to the pad planes. The chamber layout is illustrated in Figure 4.5.

Primary electrons produced along the track of a traversing particle drift along the field towards a pad plane. When approaching the anode wire plane, the electrons enter a high field region where they are multiplied. Some of the ions produced in the multiplication process drift in the direction of the pads on which signals are picked up. Hence, a pattern of hits is recorded and a two-dimensional projection of the track onto the pad plane is obtained. Due to the uniform field in the drift region, the electron drift velocity is constant and the third coordinate of the hits is determined from the arrival time of the signals at the pads.

A TPC is intended for measuring the momentum of charged particles from the curvature of the tracks in a uniform magnetic field of known strength. For this purpose, it is placed inside the coil of a solenoid. In most gas mixtures, when the magnetic field is oriented along the electric field, the electron transverse diffusion coefficient is reduced by large factors. This is very useful in TPCs where electrons drift over distances of several tens of centimeters or even meters.

4.4.2 Tracking capabilities

TPCs are a key element of the tracking system of several modern particle physics experiments ([127] and [128, 129]). They cover large volumes (diameters of a few meters and half lengths of one or two meters are common) and thus provide a large number of points along the tracks (~ 100 for high transverse momentum tracks). TPCs introduce little material along the particle trajectories, which keeps multiple scattering to a minimum. In addition, they allow very good pattern recognition as the tracks are projected onto the pad plane.

Like cathode readout MWPCs, the measurement of track points on the pad plane is realized by the centre-of-gravity method. A careful choice of the pad pitch and of the distance between the wire and pad planes allows a precise measurement of the avalanche average position. For this reason, the resolution in the pad plane $\sigma_{r\varphi}$ (where r is the radial position of an electron and φ its azimuthal angle) is not limited by the pad and wire configurations which can be optimized but mainly by the transverse diffusion in the gas. The resolution in the drift direction σ_z depends primarily on the longitudinal diffusion in the gas which, oppositely to the transverse diffusion, is not affected by the magnetic field.

4.4.3 Ion backflow

Ions produced in the avalanche drift either to the pads or to the drift region. The fraction of ions that reach the drift region is called the ion backflow fraction. If the backflowing ion density is large enough, the drift field can be disturbed by

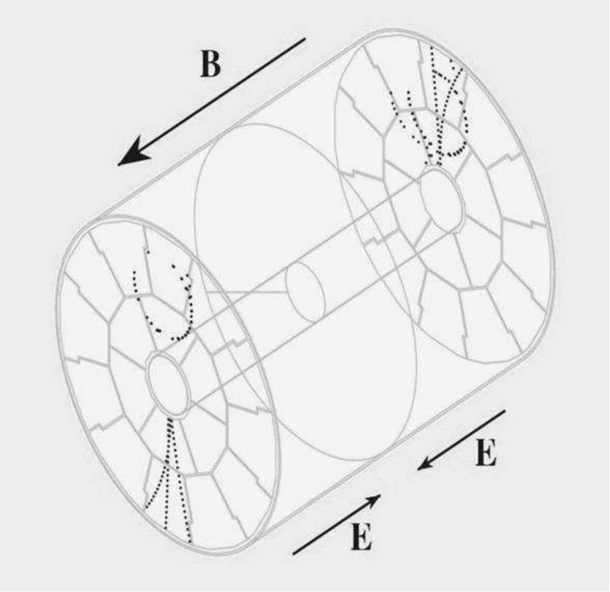

(a)

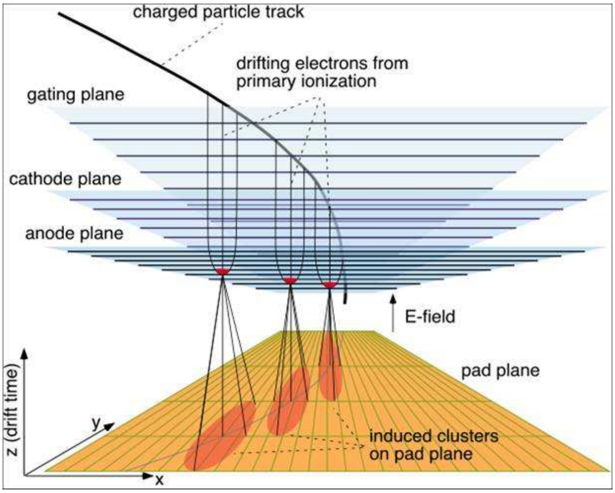

(b)

Figure 4.5: *Three-dimensional view of a TPC where the central plane and the endcap sectors are shown, together with the direction of the fields and some hits recorded on the pad plane (a). Each sector is segmented in pads above which planes of wires are placed for signal amplification and ion collection (b).*

the resulting space charge and the detector performance is locally altered. For this reason, TPCs based on wire amplification incorporate a third wire plane (so-called gating grid) placed in the drift region, a few centimeters from the cathode wire plane. By changing the voltages of the grid wires, the grid can be "opened" and let the primary electrons reach the anode wires or "closed" and collect the backflowing ions before they enter the drift region [43].
In colliding beam experiments, bunches of particles collide at a certain frequency. The use of a gating grid is possible if the time between two collisions is long enough for the grid to be opened and closed.

4.4.4 Rate capability

In wire-based detectors, the ions from the electron multiplication have to drift at least a few millimeters to reach the pad plane or the cathode wire plane. The time necessary to evacuate the ion charge is about 100 μs. During part of this time, the space charge locally reduces the electric field and the gain, resulting in some local detection inefficiencies. This effect is illustrated in Figure 4.6 where the gas gain of a MWPC is plotted against the incoming X-ray flux (or rate per unit area) from a copper target X-tube.

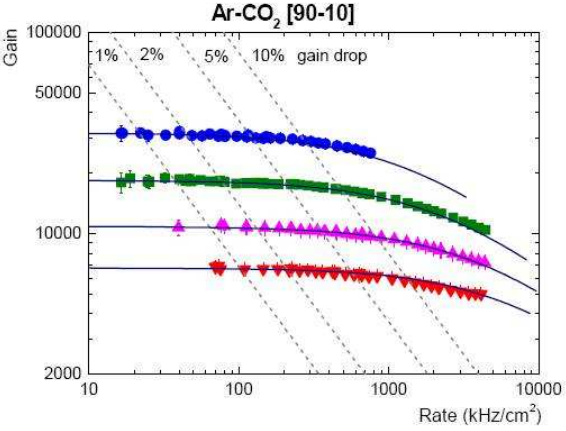

Figure 4.6: *Gas gain of a MWPC of 2 mm wire pitch and 6 mm gas thickness as a function of X-ray rate per unit area [130]. The curves are measured at various wire voltages, the smaller voltage yielding the smaller initial gain.*

At fluxes of 10^2–10^3 kHz/cm^2 MWPCs suffer from the accumulation of positive ions and are not suitable for high luminosity colliders where very high collision rates are expected (*e.g.* the collision rate at the interaction point of the ATLAS and CMS experiments at LHC will reach 40 MHz). New detector designs were invented to match these requirements.

4.5 Micro Pattern Gas Detectors

Micro Pattern Gas Detectors (MPGD) have electrode dimensions of the order of 100 μm. They are fabricated by means of printed-circuit-board techniques such as photolithography, etching and plating. These techniques offer design flexibility and a large variety of MPGDs have been developed so far. It is not our purpose to review them all here and only a short list with references is given below.

- The Micro Trench Gas Counter [131];
- the Micro Heightened Strips Counter (MHSC) also called Compteur à Trou (CAT) [132];
- the microdot gas avalanche chamber [133];
- the Micro-gap wire chamber [134];
- the Micro Wire Detector [135];
- the Micro PIxel Chamber (or μ-PIC) [136];
- the Field Gradient Lattice Detector (FGLD) [137];
- the Micro-CAT with Redundant Electrodes detector (CATER) [138];
- the WELL detector [139].

We will rather focus on the basic properties of the first MPGD built: the Micro Strip Gas Counter and on the most widely used Micro mesh gaseous detector (or Micromegas) and Gas Electron Multiplier (or GEM).

4.5.1 The Micro Strip Gas Counter

The first attempt to replace wires by micro-patterned structures was conducted by Oed in 1986 [140] with the Micro Strip Gas Counter (MSGC).

MSGCs are formed by printing metal strips onto a flat glass plate above which is placed a drift plane (Figure 4.7). The strip configuration consists in alternate anode and cathode strips separated by a few tens of microns. With proper voltages on the electrodes, a uniform drift field of a few hundred V/cm is generated in the region from the drift plane down to a short distance from the strip plane. The electron multiplication takes place close to the strips where the electric field increases up to several tens of kV/cm. The resulting field gradient focuses the primary electrons towards the anode strips (Figure 4.7 (b)).

MSGCs have many good properties also showed by more recent MPGDs. Most of all, the high granularity enables a precise measurement of the position of traversing particles (a spatial resolution of 30 μm is reported in [141]) and an operation at counting rates as high as 10^6 counts/mm^2/s [142].

Thanks to the particular shape of the electric field, most of the ions produced in the avalanche are collected on the neighbouring cathode strips rather than on the drift plane, providing fast signals (∼ 50–100 ns).
Finally, the precise control of the electrode dimensions provides good gain uniformity across the strip plane and hence an energy resolution close to the statistical limit, down to 4.6 % r.m.s. for 5.9 keV X-rays in Ar-based mixtures [143, 144].

It was observed, however, that the performance of MSGCs degrades under long-term irradiation. This issue relates to the charging up of the surface of the insulating substrate. During the development of an avalanche, some electrons and ions may reach by diffusion this surface, which progressively charges. As a result, very high fields can be generated at the substrate surface where the discharge probability locally increases. In case of discharges the thin electrodes can melt, precluding the operation of the detector. For more details on the performance and limitations of MSGCs, the reader is referred to [80, 145].

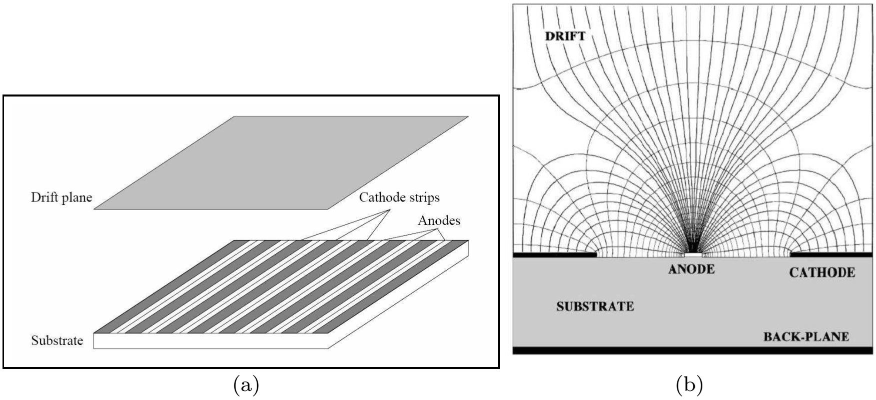

(a) (b)

Figure 4.7: *Layout (a) and electric field configuration (b) of the Micro Strip Gas Counter.*

4.5.2 The Micro Mesh Gaseous Detector

Micromegas is a parallel-plate detector invented by Giomataris *et al.* in 1995 [146]. It uses a thin metal grid to separate the drift region where the primary electrons are produced from the amplification region (50–100 μm thick) where they are multiplied. The grid has a hole pitch of 20 – 50 μm and is maintained above the anode plane by means of insulating pillars. High electric fields (40–80 kV/cm) are created in the amplification gap by applying some -400 V between the grid and the anode.

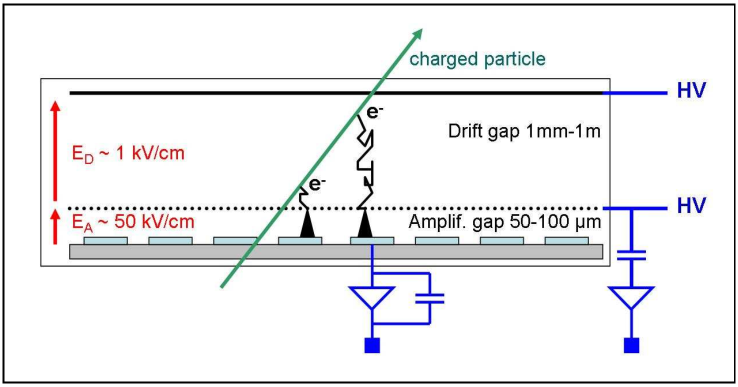

(a)

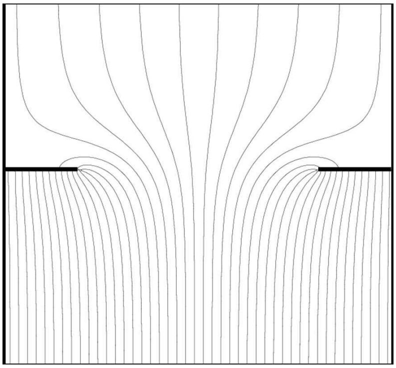

(b)

Figure 4.8: *Operating principle of a Micromegas detector (a). Field line configuration in the amplification region (b).*

The operating principle and the electric field configuration of Micromegas detectors are illustrated in Figure 4.8. Due to the field gradient at the entrance of the hole, the field lines are compressed resulting in a characteristic funnel shape. This ensures a good transmission of the electrons from the drift to the amplification region and a collection on the grid of more than 99 % of the ions produced in the avalanche [147].

For a given grid voltage and gas mixture, a flat maximum of the gas gain as a function of the amplification gap size is predicted [148]. The maximum should occur for gaps between 10 and 100 μm depending on the gas mixture. With a careful choice of the gas and the gap, the detector should be insensitive to small gap variations. This property, together with the uniform amplification field, explain the very good energy resolution of Micromegas detectors (5 % r.m.s. at 5.9 keV is reported in [149]).

Because of the small size of the amplification gap, electrons and ions produced in the gas amplification are collected in 1 ns and 30–100 ns respectively. This allows the operation of the detector up to very high rates. As an example, no drop of gas gain was observed at proton fluxes of $2{\cdot}10^9$ /mm^2/s [150].

Micromegas chambers are applied in several physics experiments. For instance, as a kaon beam spectrometer in KABES [151] and as an X-ray detector in CAST for axion search [152]. In the COMPASS fixed target experiment at CERN, twelve 40×40 cm^2 Micromegas chambers are part of the tracking system [153]. Application in the three TPCs of the near neutrino detector for the T2K experiment is reported in [154].

4.5.3 The Gas Electron Multiplier

The Gas Electron Multiplier (GEM) was introduced in 1996 by Sauli [155]. It is a composite grid consisting of two metal layers separated by a thin insulator which is etched with a regular matrix of holes (Figure 4.9 (a)). Typical detector dimensions are hole pitches of 100 μm, metal layer and insulator thicknesses of 5–10 μm and 50 μm respectively. When applying some -400 V across the metal layers, electrons entering the holes are multiplied.

GEM separates the gas volume in three regions: a low field region above the GEM where the primary charge is produced, a high field region inside the holes where the electrons are multiplied and a transfer region below the GEM where about 50 % of the avalanche electrons drift to the readout electrodes. The electric field configuration inside the holes is illustrated in Figure 4.9 (b). When approaching the hole along its axis, the field lines first compress due to the increase of field and de-focus at the exit of the hole.

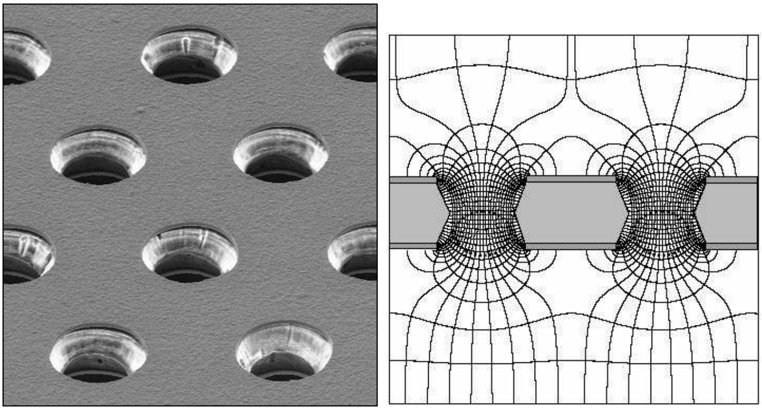
(a) (b)

Figure 4.9: *Photograph (a) and electric field configuration (b) of a GEM.*

The effective gas gain of a GEM foil is not very high [156] and one often cascades two or three GEMs [157, 158, 159]. Because of the electron transverse diffusion in between the GEMs and between the bottom GEM and the readout plane, the electron charge distribution is broad. With a readout plane segmented in pads of a few millimeters width, an electron avalanche induces signals on several pads. This effect is used to accurately measure the track cluster positions by the centre-of-gravity method in GEM-based TPCs [160]. Also, the signals induced on the pads are only caused by the electron motion and are therefore very fast [161].

GEM detectors have been used in the inner tracker of HERA-B in combination with MSGCs [162] and more recently in COMPASS [163]. At the Large Hadron Collider (LHC), they are part of the LHCb muon system [164] and used for triggering and tracking purposes in the TOTEM experiment [165]. They are also foreseen as UV-photon detectors for an upgrade of the PHENIX detector at the Relativistic Heavy Ion Collider in Brookhaven [166].

4.6 Pixel readout gas detectors

4.6.1 Concept and applications

The use of pixel readout chips as highly segmented anodes of Micro Pattern Gaseous Detectors offers a few tens of microns granularity and a low noise at the input of each channel. This permits the detection of single electrons with a potentially very good spatial resolution and a high efficiency with still the high rate capability of MPGDs. These features make pixelated gas detectors very attractive for several applications.

- TPC for the ILC. The high granularity could enhance the spatial resolution by improving the off-line identification/rejection of δ-rays. The high single electron sensitivity (larger than 90 % when combined with a Micromegas-based amplification stage) may also help in particle identification by improving the energy loss measurement (dE/dx by cluster of electron counting) [167].

- Vertex detection. With a drift gap of 1–2 mm, one has a light and very fast detector [168]. This innovative detector concept, dubbed Gas On Slimmed Silicon Pixels (or GOSSIP), would not suffer from certain limitations of Si pixel detectors like radiation damage. A vertex detector made of several thin GOSSIP layers could provide many precise points along the particle trajectories while keeping multiple scattering to a minimum.

- X-ray polarimetry. Few-keV photo-electron tracks can be resolved and the distribution of the common azimuthal angle can be used to measure the source polarization [169].

- Rare event detection. Low energy nuclear recoils from WIMP interactions leave localized energy deposits of a few keV in the gas which can be detected with a high efficiency [170]. This readout could also be applied to double beta decay experiments which put high constraints on the energy resolution. With single electron counting capability, a Fano-limited resolution could in principle be reached.

In the coming sections, we first present the Medipix2 and TimePix chips. During the last five years these chips were applied as the readout of triple GEM and Micromegas detectors [171, 172, 173]. The R&D activities on MPGD-based pixel detectors (so-called GridPix detectors) are then summarized, with a special emphasis on performance enhancement by means of wafer post-processing.

4.6.2 The Medipix2 chip

Medipix2 [174] is a pixel readout chip designed in 0.25 μm CMOS technology, segmented in a 14 × 14 mm^2 matrix of 256 × 256 pixels of 55 × 55 μm^2. Because of I/O pads, the total area is slightly larger (14 × 16 mm^2). The pixel circuitry includes a preamplifier-shaper, 2 discriminators, a 14 bit counter and communication logic. The Medipix2 chip is originally intended for single photon counting by means of an X-ray semiconductor sensor/converter bump bonded to the chip (Figure 4.10 (a)). Therefore, every pixel is covered with an octagonal bump bonding pad made of aluminium (Figure 4.10 (b)).

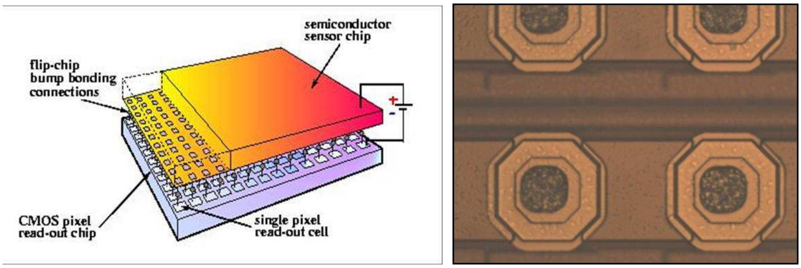

(a) (b)

Figure 4.10: *Drawing of a Medipix chip bump bonded to a semiconductor sensor (a). Magnified top view of part of the pixel matrix (b).*

For application in gas detectors, the chip is put inside the gas volume without the X-ray converter. Instead, dedicated amplification structures are placed above it. The charge from primary electron avalanches is collected onto the pixel pads and, if larger than a user-defined threshold, activates the pixel circuitry. The Medipix2 chip can be used to record projections of tracks onto the pixel plane, however, no information on the drift time of the electrons is recorded.

4.6.3 The TimePix chip

TimePix [175] is a pixel readout chip inspired from Medipix2 and intended for TPC applications. Its design was motivated by the need to measure the arrival time of the avalanches (or hits) at the pixels: instead of counting hits, the 14 bit counters of Medipix2 are used to count clock pulses during a certain duration.

TimePix can operate in 4 counting modes, the main of which are the charge counting mode (so-called Time-Over-Threshold or TOT mode) and the time counting mode (so-called TIME mode). In all modes, the pixel counter is triggered when a signal from the preamplifier crosses a user-defined threshold of the circuitry. In TOT mode, clock pulses are counted until the signal passes below the threshold and the total number of counts is a rising function of the input charge. In TIME mode, the counter is active during a certain duration (so-called shutter time) and the total number of counts indicates how much time before the end of the shutter window the signal crossed the threshold. More details on the operation of the TimePix chip will be given in chapter 8.

4.6.4 GridPix detectors

GridPix detectors combine a micro-patterned amplification stage with a pixel readout chip as charge collecting anode. The first GridPix detector was built in February 2003 when a Medipix2 chip was applied as the anode of a triple GEM structure. In 2004, a detector consisting of a Micromegas mesh placed above a Medipix2 chip was built. A cathode foil placed parallel above the mesh defined a drift volume of $14 \times 14 \times 14$ mm^3 which was flushed with a gas mixture of He/iC$_4$H$_{10}$ 80/20. At gas gains of roughly 10^4, single primary electrons produced by cosmic particles traversing the sensitive volume were detected at the pixels with a high efficiency [176]. In this way, two-dimensional projections of tracks onto the pixel plane were recorded (Figure 4.11).

The main limitations of the detector were a reduced life-time due to destructive gas discharges and spatial variations of efficiency due to a mismatch between the grid hole pitch and pixel pitch. Also, the third coordinate of the primary electrons could not be measured; this was then possible with the TimePix chip. Inspired from the functioning of Resistive Plate Chambers (so-called RPCs), it was proposed to solve the spark issue by using electrodes of high resistivity. This can be achieved by using a grid made of highly resistive materials or/and by depositing such materials on the chip. The alignment of the pixels and the grid hole can be ensured by fabricating the grid directly onto the chip by means of microelectronic fabrication techniques.

4.6.5 Wafer post-processing of pixel readout chips

Integrated circuits are originally devoted to information processing. With the recent developments in microelectronic techniques, however, extra functionalities

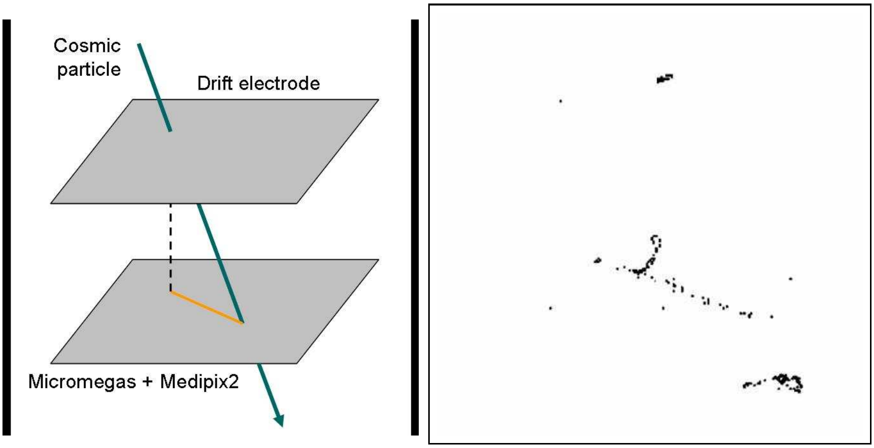

(a) (b)

Figure 4.11: *Drawing of a cosmic particle traversing the detector (a). Image recorded with the Medipix2/Micromegas detector showing the projected tracks of a cosmic particle and a δ-electron (b) in a He/iC_4H_{10} gas mixture.*

can be integrated on-chip by wafer post-processing [177]. These techniques can be used to equip wafers of pixel readout chips with resistive coatings for protection against gas discharges and with amplification structures.

InGrid, an integrated Micromegas

By means of wafer post-processing, the Micromegas grid can be integrated directly on top of silicon wafers [178]. The grid holes can be accurately aligned with the pixel pads and the pillars can fit in between the grid holes as their diameter can be shrunk to 30 μm. This fully suppresses the alignment issue, maximizes the detection efficiency and the fiducial detector area. This integrated grid is called InGrid, its fabrication process and performance are described in detail in this thesis. In the future, this technology should be applied to wafers of chips, permitting the mass production of integrated pixelated gas detectors.

SiProt, an amorphous silicon protection layer

When an electron avalanche grows very large, a discharge may occur and a considerable charge is dumped into some pixels. The increased temperature inside the pixels likely provokes the evaporation of the circuit components which damages the full chip. To protect the chip, a few microns thin continuous layer of hydrogenated amorphous Silicon (a-Si:H) of resistivity 10^{11} Ω.cm is deposited over the chip surface. Its main effect is a local reduction of the amplification field by the electron charge that remains on the resistive surface for a certain time.

In this way, the discharge stops at a certain stage and the charge dumped into the pixels is reduced. Also, the layer prevents the evaporation of the pixel components by the hot plasma of the discharge. This discharge protection is called SiProt and can be deposited in CMOS compatible conditions [179].

Multi-grid structures

The silicon protection layer does not reduce the sparking probability but quenches gas discharges at a certain stage. A possibility to reduce the sparking rate is to decrease the electric field by sharing the gain over two or more amplification stages. An example of such development is the TwinGrid which consists of two InGrids on each other (Figure 4.12 (b)).

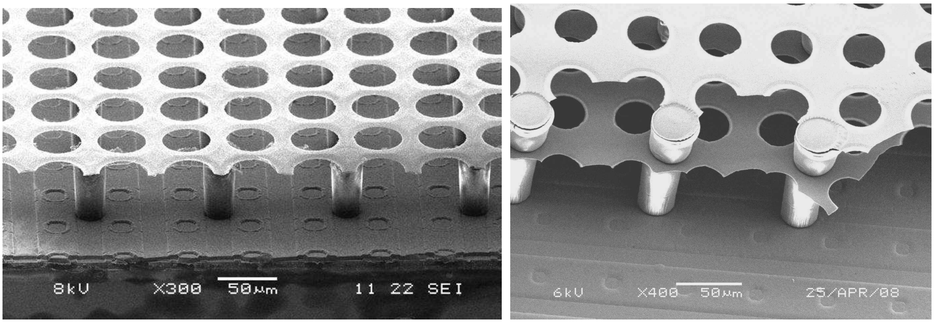

(a) (b)

Figure 4.12: *SEM pictures of an InGrid (a) and a TwinGrid (b) integrated on a SiProt equipped TimePix chip.*

Post-processed TimePix chip

Since 2006 a few TimePix chips have been equipped with SiProt and InGrid (Figure 4.12 (a)). The uniform detection efficiency resulting from the hole/pixel alignment and the reduction of dead areas are illustrated in Figure 4.13 where images recorded with Micromegas and InGrid equipped TimePix chips are shown.

The discharge probability increases with the primary charge density and therefore depends on the gas mixture. When a discharge occurs, however, the minimum SiProt thickness that provides protection depends on the charge stored in the grid and thus on the grid voltage [180]. It was observed that a TimePix chip covered with a 3 μm thin layer of aSi:H could operate during several months under high voltage in He/iC$_4$H$_{10}$ 77/23 before the voltage was switched off, while, at least 15 μm were required in Ar-based mixtures (Ar/iC$_4$H$_{10}$ 80/20, Ar/iC$_4$H$_{10}$ 95/5 and Ar/CO$_2$ 90/10).

Due to the SiProt layer, a single electron avalanche induces some signals on more than one pixel. The hit multiplicity increases which worsens the position measurement of the primary electrons. This effect was observed to be more pronounced with thicker aSi:H coating. As a result, the SiProt layer should be just thick enough to provide protection against sparks. The determination of the optimum thickness is an ongoing study.

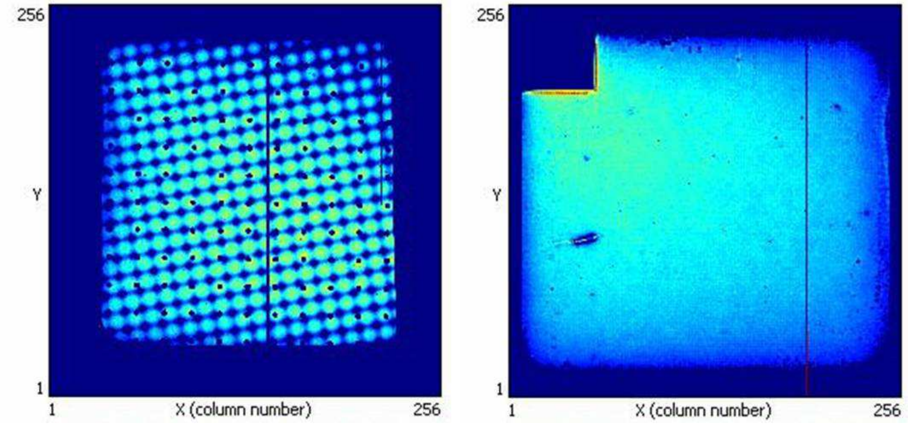

(a) (b)

Figure 4.13: *Integral images of* ^{55}*Fe quantum conversions in He/iC*$_4$*H*$_{10}$ *77/23 recorded with a standard Micromegas equipped TimePix chip (a) and an InGrid equipped TimePix chip (b). The top left corner of the InGrid equipped chip where no hits are recorded is used for contacting the grid. In the left image, note the periodic variation of detection efficiency and the dead areas due to the Micromegas pillars (black dots).*

4.7 Measurement of momentum with TPCs

A charged particle of charge e and momentum (p_r,p_φ,p_z) traversing the volume of a TPC is curved by the axial uniform magnetic field (0,0,B_z) and hence its trajectory is a helix. In the plane perpendicular to the magnetic field ($r\varphi$-plane), the projected trajectory is a circle segment of radius:

$$R = \frac{p_\mathrm{t}}{eB} \tag{4.4}$$

where $p_\mathrm{t} = (p_r^2 + p_\varphi^2)^{1/2}$ is the particle transverse momentum. Expressing the momentum in units of GeV/c, the radius in meters, the field in Tesla and the charge q in units of e, the transverse momentum can be conveniently written as:

$$p_\mathrm{t} \sim 0.3qBR \tag{4.5}$$

As illustrated in Figure 4.14, the radius R can be expressed as a function of the TPC outer radius L and the deflection angle in the $r\varphi$ plane Φ:

$$R = \frac{L}{2\sin\Phi} \tag{4.6}$$

which yields:

$$p_{\mathrm{t}} = \frac{eBL}{2\sin\Phi} \tag{4.7}$$

Often, the sagitta s of the projected track is used in place of Φ. For high-momentum tracks, the deflection angle is small ($s \ll L$) and Equation 4.7 becomes:

$$p_{\mathrm{t}} = \frac{eBL^2}{8s} \tag{4.8}$$

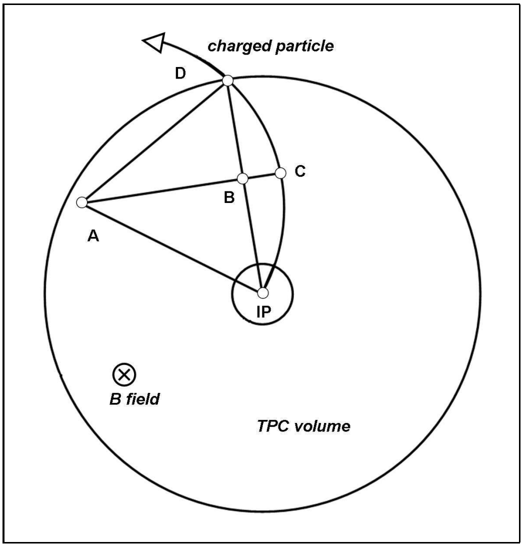

Figure 4.14: *Cross-section of a TPC traversed by a charged particle produced at the interaction point (IP). The sagitta is the distance $s = \overline{BC}$.*

For N_{p} equidistant points measured along the track and neglecting the contribution from multiple scattering, the momentum and sagitta relative resolutions σ_p/p and σ_s/s are equal [181]:

$$\frac{\sigma_{p_{\mathrm{t}}}}{p_{\mathrm{t}}} = \frac{\sigma_s}{s} = \sigma_{r\varphi}\frac{p_{\mathrm{t}}}{eBL^2}\sqrt{\frac{720}{N_{\mathrm{p}}+4}} \tag{4.9}$$

where $\sigma_{r\varphi}$ is the resolution in the $r\varphi$-plane. Finally, the particle total momentum is determined by the measurement of the polar angle Θ between the track and the direction of $\overrightarrow{B}$:

$$p = \frac{p_{\mathrm{t}}}{\sin\Theta} \tag{4.10}$$

where the precision on Θ depends on the resolution in the z-direction and the number of equidistant measured points [42]:

$$\frac{\sigma_\Theta}{\Theta} = \frac{\sigma_z}{z}\sqrt{\frac{12(N_{\mathrm{p}}-1)}{N_{\mathrm{p}}(N_{\mathrm{p}}+1)}} \tag{4.11}$$

4.8 Conclusion

I presented the working principle and performance of some gaseous tracking detectors used in high energy physics experiments. The development of these detectors has been motivated by physics goals which put ever growing constraints on spatial and time resolution, rate capability and long term irradiation behaviour.

We emphasized the important step realized with the invention of Micro Pattern Gas Detectors such as GEM and Micromegas. These gas gain grids have hole pitches of the order of 100 μm which confines the electron multiplication to a small volume. This, together with the fast ion collection, result in a rate capability three orders of magnitude higher than those of traditional MWPCs.

With pads, the segmentation of the readout plane is lower than the one of the amplification stage. By using pixel chips as collecting anodes, both segmentations match. In the case of Micromegas, each grid hole has its own readout channel and single primary electrons can be detected with an efficiency larger than 90 %. This promises very good tracking performance as almost all the information on the track is available.

The fabrication of Micromegas pixelated detectors benefits from the development of microelectronic techniques which can be used to integrate the amplification structures directly on the chips by wafer post-processing. Such integrated Micromegas are called InGrids and their fabrication is detailed in the next chapter.

Chapter 5

Fabrication of integrated Micromegas

I present in this chapter the fabrication of integrated Micromegas detectors called InGrids. Measurements of geometric parameters of several InGrids will be summarized, demonstrating that the dimensions of the grids can be controlled to a precision of a few microns. I will discuss the dimension and material limitations and briefly sketch the detector test procedure.

5.1 Introduction

InGrid is a Micromegas grid integrated on a silicon substrate by means of planar microfabrication techniques [182]. It is meant to enhance the performance of Micromegas-based pixel readout detectors. By means of a few post processing steps [177], wafers of pixel readout chips can be equipped with InGrids, paving the way to the mass production of Micromegas pixelated detectors.

The manufacturing techniques provide an accurate control of the grid geometry over areas of a few cm^2. The grid can fit any pixel readout chip, with the grid holes precisely aligned with the pixel input pads. Also, the grid-supporting structures (pillars or walls) can be placed in between the pads. Accordingly, the detection efficiency should be uniform across the detector surface and almost all the chip area is active. In addition, the grid dimensions can be optimized for low ion backflow and efficient electron collection and detection.

InGrids are fabricated on 100-mm wafers which act as dummy carriers. Several InGrids of various geometries are made on a single wafer in order to study the impact of the geometry on the operational characteristics. Later on, the process is meant to work on 200-mm and 300-mm wafers.

5.2 Fabrication process

5.2.1 Process flow

The steps of the fabrication process are detailed in the following sections. They consist in wafer cleaning and oxidation, deposition and patterning of the anode material, deposition and exposure of a thick photosensitive film, deposition and patterning of the grid material and finally removal of the photosensitive film through the grid holes. Some of these steps are depicted in Figure 5.1. For more informations on the various microfabrication techniques used throughout the process, the reader is referred to [182, 183].

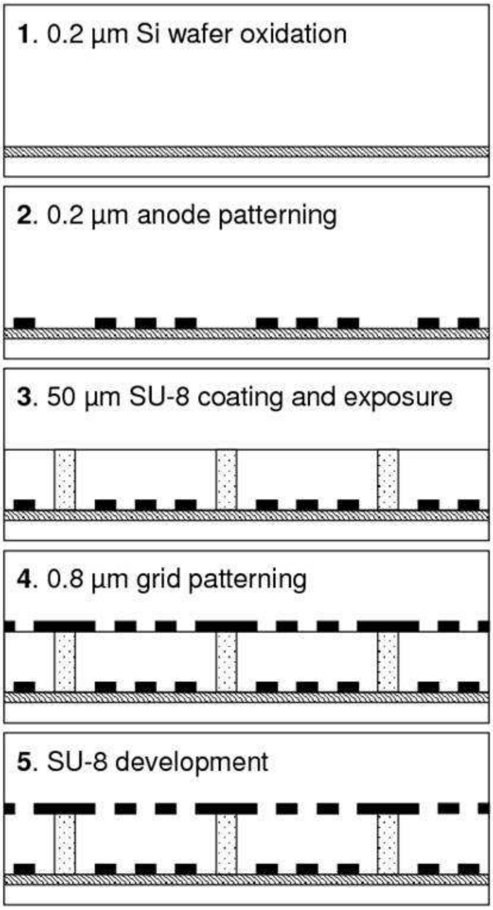

Figure 5.1: *Main steps of the InGrid fabrication.*

5.2.2 Wafer cleaning

During the growth of a silicon oxide layer, it is desirable that the oxidation proceeds uniformly across the wafer surface. For this reason, native oxide and any residual impurities and particles should be removed from the wafer surface prior to the oxidation. The types of impurities likely to exist at the wafer surface include organic compounds and metallic particles. These are generally residues of photoresist or metal films previously deposited on the wafer. At the beginning of the process, we expect a small contamination of these. On the other hand, native oxide forms upon exposure of the wafer to air (*e.g.* during storage, before the wafer is used). It should be removed if a uniform oxide layer is to be formed during the oxidation.

The cleaning is a sequential procedure to remove organic and metal residues as well as native oxide from the wafer surface. There are different types of cleaning procedures. When cleaning bare silicon wafers, a common wet chemical cleaning procedure consists in dipping the wafer in several acid baths. The first wafer bath is performed in a solution of fuming nitric acid which dissolves the organic compounds. Metallic impurities are removed when the wafer is immersed in a solution of boiling nitric acid. Finally, a solution of hydrofluoric acid is used to remove the native oxide from the wafer surface. After each acid bath, the wafer is rinsed in a solution of de-ionized water to prevent reactions between the different acids.

5.2.3 Wafer oxidation

The InGrids are fabricated on bare silicon wafers which act as dummy carriers. Due to impurities in the bulk, silicon wafers are slightly conducting and it is therefore desirable to electrically isolate the detector anode from the wafer bulk. This is realized by the deposition on the wafer of a layer of insulating material. Silicon oxide with a breakdown voltage of 10^7 V/cm is well suited for this purpose. We chose to grow a 200 nm thin layer of SiO_2 on the wafer surface by dry oxidation. The oxidation proceeds according to the overall reaction:

$$\mathrm{Si(solid)} + \mathrm{O_2(gas)} \rightarrow \mathrm{SiO_2} \tag{5.1}$$

Due to a much higher diffusivity of O_2 than Si in SiO_2, the reaction occurs at the Si-SiO_2 interface. At room temperature, however, the oxygen molecules are not sufficiently mobile to diffuse through the oxide. Reaction 5.1 effectively stops after a while and oxide thicknesses of about 25 Å are obtained. The oxidation can be continued by heating up the wafer, which increases the diffusivity of O_2 in SiO_2. This is realized inside a furnace which once closed, is flushed with oxygen gas. A batch of wafers is placed on a quartz carrier which is then introduced inside the furnace. At a temperature of 800 °C an oxide thickness of 200 nm is obtained after approximately 12 hours.

5.2.4 Anode deposition

The detector anode is a 200 nm thin layer of aluminium formed on the wafer surface by sputtering. The wafer is placed horizontally inside a plasma reactor below a target of the material to be deposited. The reactor is pumped down and flushed with an inert gas (Ar or N_2) which is ionized by a discharge. The positive ions of the plasma are accelerated towards the target by a uniform electric field. Upon impact of the ions, some atoms are released from the target and reach the wafer surface.

The sputtering system used provides deposition rates from 10–10^4 nm/min [184]. At the highest deposition rate, a 200 nm thin aluminium layer is formed in a few seconds. It is worth noting that during the deposition, the substrate receives energy from UV photons and electrons produced in the plasma as well as from the target atoms. When sputtering aluminium on substrates that are sensitive to UV light or heat, the substrate chemical properties may change.

5.2.5 Anode patterning

The sputtered Al layer extends all over the wafer surface and is patterned to individual regions by means of photolithography and wet etching techniques. Photolithography is the patterning of a photosensitive film, or photoresist, using light. The patterned film can subsequently be used as mask to treat specific wafer regions underneath (*e.g.* doping, sputtering, etching). Photolithography proceeds in four main steps some of which are illustrated in Figure 5.2 in the case of an etching process.

- Deposition by spin coating of a thin liquid photoresist which has high absorption coefficient in the UV domain. The photoresist is a mixture of a resin, a photoactive compound and a solvent. The latter controls the mechanical properties of the resin such as its viscosity.
- Evaporation of the solvent by heating up the photoresist (so-called softbake). This is realized by placing the wafer on a hot plate.
- Exposure to UV light through a mask, the photoresist chemical properties change in the exposed regions.
- Immersion of the wafer in a specific solution (so-called developer) where either the exposed or unexposed regions of the resist are dissolved, depending on its polarity. In this way a positive or negative image of the mask is printed in the resist.

We spin coat a 1.6 μm thin layer of positive photoresist over the Al covered wafer. This resist is produced by Fujifilm (OiR 907) and is referred to as 907 in the following. It is patterned to 12 square-shaped regions of 2 × 2 cm^2 (the wafer design is presented in section 5.3). The patterned film is then used as a mask

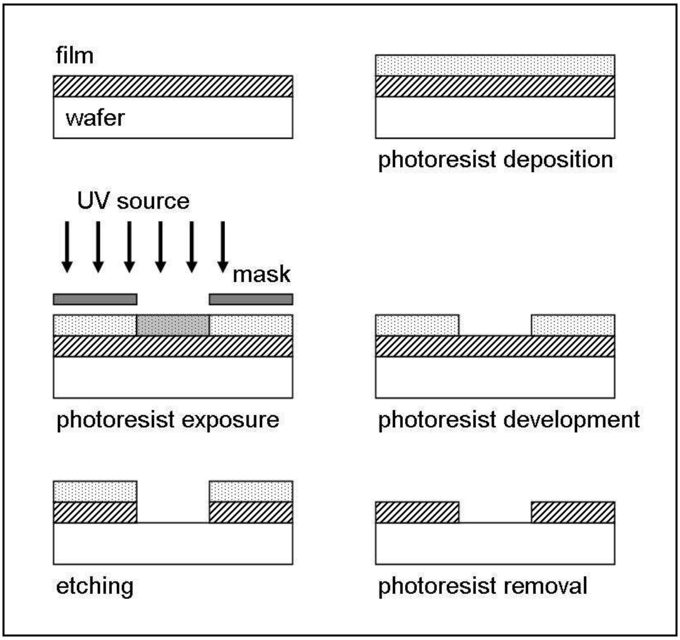

Figure 5.2: *Main steps of a photolithographic process used to etch specific regions of a film present on the wafer surface.*

to etch the Al layer in regions where the photoresist has been developed. The etching is done in a solution of phosphoric acid at a temperature of 60 °C at a rate of about 1.2 μm/min. After rinsing in de-ionized water, the photoresist is removed in a bath of fuming nitric acid. Eventually, one is left with a 100-mm diameter oxidized wafer onto which are printed 12 Al square-shaped regions of 2×2 cm^2.

5.2.6 Supporting structures deposition and exposure

A few tens of microns thick layer of SU-8 photoresist is deposited onto the wafer by spin coating. It is then exposed to UV light to define the grid-supporting structures: pillars or walls, outer dikes and grid contact pads. The dikes support the grid on its edges.

SU-8 is a negative tone, near-UV photoresist whose absorption spectrum peaks at 365 nm. Due to its high viscosity, structures with thicknesses up to 2000 μm can be patterned with large aspect ratios. These features make SU-8 a very attractive material for fabrication of MEMS and micro-sensors [185, 186]. Studies of the use of SU-8 for building radiation detectors are also reported in [187, 188].

SU-8 consists of a polymeric epoxy resin dissolved in an organic solvent to which is added a photosensitive salt. Upon exposure to UV light, the salt generates an acid which acts as a catalyst in the reaction between epoxy groups. On average, a single molecule has eight epoxy groups (hence the name SU-8) and this reaction results in a dense network of chemical bounds (so-called cross linking reaction). As this reaction is very slow at room temperature, the SU-8 film is heated up to accelerate the cross linking reaction (so-called post-exposure bake). After cross linking, the exposed regions are insoluble in the SU-8 developer.

The film is deposited on the wafer by spin coating and its thickness is chosen according to the desired InGrid amplification gap thickness, generally between 30 and 100 μm. Measurements of thickness variations across the wafer surface are reported in section 1.4.2. The film is soft-baked approximately 1 hour at 120 °C to evaporate the solvent and slowly cooled down to room temperature. During the soft-bake, important internal thermal stress is generated in the film. To release that stress, the wafer is left 24 hours at room temperature. Afterwards, the SU-8 film is exposed to UV light during a few tens of seconds, the precise exposure time being adjusted to the SU-8 thickness and the amount of photoacid generator present in the film. A post-exposure bake of 1 hour at 95 °C is performed to accelerate the cross linking reaction in the exposed SU-8 regions. Again, the resist is slowly cooled down to room temperature and 24 hours are awaited before resuming the process.

The SU-8 layer is not developed yet. Instead it is used as a sacrificial layer for the deposition of the grid metal layer. Pictures of SU-8 structures where the photoresist has been developed before the formation of the grid are shown in Figure 5.3.

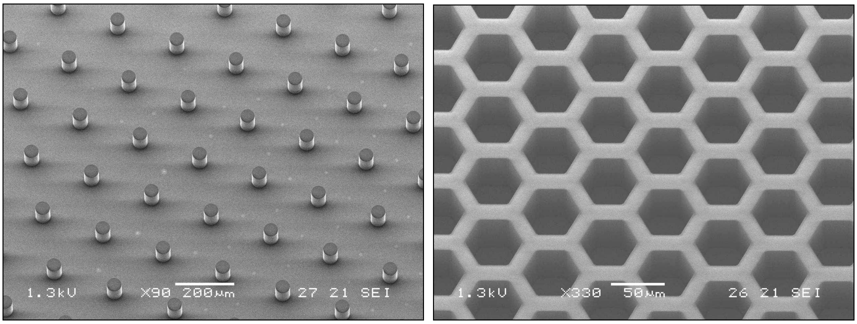

(a) (b)

Figure 5.3: *Pictures of pillars (a) and walls (b) supporting structures.*

5.2.7 Metal layer deposition

The grid is formed by sputtering on the SU-8 surface a thin layer of aluminium which is then shaped into a grid by wet etching. Aluminium exhibits low residual stress, it can be easily etched and shows good adhesion with SU-8 [189]. The sputtering of the aluminium layer on the SU-8 surface is realized in the reactor used for the anode deposition.

The grid thickness should be such that the grid is sufficiently rigid and does not bend when applying high voltage across the amplification gap. Standard Micromegas grids have thicknesses of at least 5 μm and one may want to start with such values. Unfortunately, the grid thickness can not be increased at will because the chemical properties of SU-8 are expected to change during the metal deposition. In particular, UV light produced in the glowing plasma may initiate the production of acid at the surface of the unexposed SU-8 regions. Therefore, local increases of temperature across the SU-8 film surface may initiate the cross linking reaction, preventing a complete development of the SU-8 unexposed regions. This increase can be due to the photons, electrons and target atoms striking the substrate and also by the heat-of-condensation of the depositing film [190].

For this reason, a 1 μm thin layer of 907 positive photoresist is deposited over the SU-8 and both resists are exposed simultaneously. The positive resist is developed prior to the metal sputtering such that the unexposed regions of SU-8 are, to some extent, protected against the UV light. The resist is later removed in the SU-8 developer. Also, the metal is sputtered in several short steps. Between each step, the wafer is brought out of the reactor to a loadlock where a flow of N_2 gas cools the substrate surface to room temperature. Repeating those steps a reasonable number of times, an aluminium thickness of about 1 μm is obtained.

5.2.8 Grid hole etching

The patterning of the aluminium layer to the desired grid geometry is realized by photolithography. The soft-bake, however, can not be performed. Despite the additional photoresist layer, some acid could have been produced during the sputtering and the SU-8 film should not be heated anymore. Instead, the wafer is left 3 hours at room temperature before exposure of the photoresist. The etching of the grid is performed in a solution of phosphoric acid at room temperature resulting in an etch time of roughly 40 minutes. The etch rate is slightly higher for holes with large hole diameters than for holes with smaller ones. Because the etching is stopped when the small holes are opened, the diameters of large holes generally exceed their design values. Measurements of hole diameter variations are reported in section 5.4.2.

5.2.9 Wafer dicing

It will be of interest to have at the same time in the test chamber InGrid detectors from different wafers. If, for instance, InGrids of different amplification gap thicknesses should be tested in a row, several wafers would have to fit in the chamber. The dimensions of the chamber, for practical reasons, can not match this requirement. Instead, the 12 InGrids are diced to individual wafer pieces of 2×2 cm^2, each InGrid being equipped with anode and grid contact pads. The dicing is performed prior to the SU-8 development, otherwise the InGrids would be easily damaged during the dicing.

5.2.10 SU-8 development

After dicing, one proceeds to the development, through the grid holes, of the unexposed regions of SU-8 and of the additional 907 positive resist. During the development, the adhesion of the grid onto the supporting structures is sometimes not sufficient and the grid peels off. Therefore the development should be stopped as soon as no SU-8 is seen flowing through the grid holes. Although SU-8 has its specific developer, acetone is preferred as it was observed that the development proceeds faster in this solution. According to the SU-8 processing rules, isopropanol is used to rinse the InGrid after the development.

Hence, individual InGrids are dipped in acetone until no SU-8 is seen flowing through the grid holes and rinsed with isopropanol. Sometimes, unexposed regions of SU-8 are not properly dissolved after rinsing and additional baths in both solutions are performed. The duration and the number of baths required for a complete development vary from wafer to wafer and were observed to depend strongly on the grid metal sputtering recipe. In particular, when the sputtering steps are too long or when the wafers are not vented sufficiently between these steps, several baths are performed.

This is interpreted as follows: during the aluminium deposition, the chemical properties of the SU-8 unexposed regions change from the SU-8/907 interface until a certain depth in the SU-8. The thickness and composition of this intermediate layer probably correlate to the temperature of the SU-8 surface and the number of absorbed photons, during the sputtering. If these are kept low enough, the intermediate layer is thin enough for acetone to break through and SU-8 is readily developed. On the other hand, if these are too high, that layer does not dissolve in acetone and no development takes place. A picture of a grid after SU-8 development is shown in Figure 5.4 (a).

5.2.11 Plasma cleaning

After the SU-8 development, residues of the interface layer are etched in a plasma reactor. A batch of InGrids is placed in a quartz carrier which is brought inside the reactor. The reactor is pumped down to pressure of a few millibars and filled

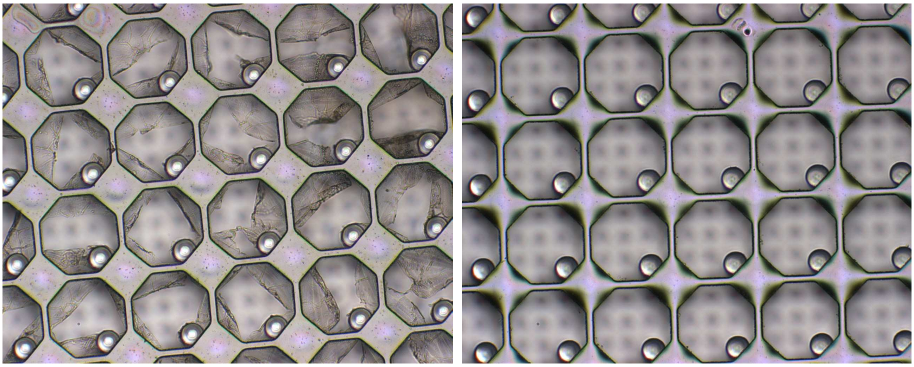
(a) (b)

Figure 5.4: *View of a grid after the development of the SU-8 layer (a). The residues of the interface layer around the holes are etched in a plasma reactor (b). The misalignment between the pillars and the grid was due to a loss of contact during the SU-8 development.*

with oxygen gas. The plasma is ignited by a discharge, producing electrons, ions and oxygen radicals. The radicals readily react with organic compounds and etch the residues of the SU-8 interface layer. The SU-8 supporting structures are also etched and therefore the process has to be carefully watched over. One proceeds in several short steps: after each step, the InGrids are brought out of the reactor for inspection. Additional steps are performed if necessary. A picture of a grid after cleaning in the plasma reactor is shown in Figure 5.4 (b).

5.3 InGrid wafer designs

Photolithography techniques permit an accurate control of the detector amplification gap thickness, hole pitch and diameter. It is interesting to study how the mechanical and operational characteristics of InGrid detectors depend on these geometrical parameters. Hence, four wafer designs were successively realized, all consisting in a large variety of geometries with various hole pitches and diameters.

One of the first designs contained 18 177 mm^2 round-shaped InGrids with various supporting structure dimensions. It was mainly intended to determine which pillar configurations would provide enough support. The latest design consists of 12 314 mm^2 InGrids of 4 different hole pitches (20, 32, 45 and 58 μm) with holes placed according to a square pattern. The hole diameters of InGrids of same pitch are roughly equal to 1/3, 1/2 and 2/3 of the pitch. Also, the layout of the 12 InGrids is such that the wafer is easily diced to individual prototypes. A pillar diameter of 30 μm is adopted. For InGrids with hole pitches of 45 and 58 μm, the pillars are placed in between the holes. The pillars are placed according to a square pattern and their pitch is adjusted to the hole pitch, between 90–128 μm.

5.4 Geometry uniformity

It was of interest to quantify how precisely the detector geometry can be controlled. In this section, I report on measurements of amplification gap thicknesses and grid hole diameters performed on InGrids from five wafers.

5.4.1 Amplification gap thicknesses

Gap thicknesses were determined by measuring step sizes between the wafer surface and the SU-8 dikes. Step sizes were measured by means of a Dektak [191]: a thin needle tip free to move vertically is dragged horizontally over the wafer surface and its vertical displacements reflect the topography underneath with an accuracy of a few tens of nanometers.

InGrids from the 5 wafers were placed below the Dektak tip, for each one the dike heights were measured on 4 different locations. All gap thicknesses exceeded by 10–20 % the expectations from the SU-8 deposition system, however, variations at the wafer level were below 5 % r.m.s.. At the grid level, gap variations below 1 % r.m.s. were measured.

The SU-8 layer is deposited by spin coating and its final thickness depends on the spin coater rotation speed and the photoresist viscosity. The latter relates to the fraction of solvent mixed with the photosensitive compound. When SU-8 is stored for several days in its container, some solvent evaporates, resulting in larger viscosities and therefore larger thicknesses. This explains the 10–20 % discrepancies between measured and expected thicknesses.

5.4.2 Hole diameters

Hole diameters were measured by means of a microscope with a precision of 0.5 μm. First, hole diameters of 5 InGrids from a same wafer were measured on 5 different locations across the grids. The diameter standard deviations were all below 1 μm. Secondly, differences between measured and design-on-mask hole diameters were determined for most InGrids of 3 wafers. In this case a single measurement per InGrid was realized. The measurements showed that the grid hole diameters exceed the design-on-mask values by 1 to 8 μm.

5.5 Processing considerations

5.5.1 Largest amplification gap thickness

The maximum thickness of the amplification gap depends on the aspect ratio of the SU-8 supporting structures. In the case of pillar-like structures, aspect ratios up to 4 are used. With a pillar diameter of 30 μm, the pillar heights should not exceed 120 μm. This is not problematic as there are no strong motivations to fabricate InGrids with gaps larger than 100 μm.

5.5.2 Distance between pillars

The distance between pillars is important for the adhesion of the grid on the pillars. Also, it determines the flatness of the grid: if the distance between pillars is too large the grid may bend towards the anode. The effect may be accentuated when negative voltage is applied to the grid (while the anode is connected to ground) as the electric force pulls the grid towards the anode. Accordingly, the amplification gap thickness may be higher close to the pillars than in between the pillars. For certain gap thicknesses, this should result in gain variations from hole to hole.

Although pillar pitches as large as 240 μm for a triangular pattern of 40 μm diameter pillars showed good operational characteristics [178], they could not be fabricated in a reliable way. In some cases, due to a poor adhesion, the grids peeled off locally or completely during the SU-8 development. We therefore adopted pillar pitches ranging from 90 to 128 μm (for a square pattern of 30 μm diameter pillars). These smaller pitches, together with some process improvements, showed increased fabrication yield.

5.5.3 Smallest hole diameter

The InGrid with the smallest hole diameter that could be fabricated and tested has a hole diameter of 10 μm. The etching of such small holes takes more time than that of larger holes. This is because the by-products of the reaction between the acid and the metal are less quickly removed from the aluminium surface and prevent fresh acid molecules to reach this surface. The etch rate can be increased by a constant stirring of the acid solution and one could in principle go to smaller diameters.

In typical working conditions of an InGrid detector, the mean free path of an electron in the gas is about a few microns. When approaching the grid, the probability that the electron hits the grid and is not detected increases when the hole diameter is reduced (see section 6.3.2 for experimental measurements). From the functional point of view, it is thus not worth going to hole diameters smaller than 10 μm.

5.5.4 Largest hole diameter

The largest hole diameter is limited by the hole pitch. On the functional side, holes with large diameters facilitate the passage of the electrons through the grid but degrade the electric field uniformity in the amplification region. If the field is not uniform at the entrance of the amplification region, the gain may depend on where the electrons enter the hole. This introduces additional gain fluctuations and therefore the hole diameter should not be too large, especially for small amplification gap thicknesses (see section 6.7.3 for simulation results).

5.5.5 Grid thickness and material

The grids are made of 1 μm of metal and are very fragile, the InGrid detectors are hence easily damaged during manipulation or testing. For instance, the resistance to gas discharges is poor as the metal locally vaporizes. That could be improved with the deposition of thicker layers and the use of conductive materials with a higher heat capacity.

So far, trials to sputter aluminium layers thicker than 1 μm resulted in wrinkles on the metal film surface and in an incomplete SU-8 development. Similar observations were made when trying to depose materials other than Al like TiW, Cu, aSi or Au. Other deposition techniques like evaporation or electroplating are being investigated but did not produce testable prototypes yet [192].

Another important aspect related to the grid thickness is the field shape in the vicinity of the hole edges. Due to the sharpness of the grid close to these edges, we expect there an electric field stronger than in the amplification region. Electrons entering the amplification region close to a hole edge may experience more ionizing collisions than an electron entering in the center. In those cases, the gain and the discharge probability may increase significantly there.

5.6 Detector testing

The 2 × 2 cm^2 individual InGrids are mounted on thin PCB boards for easier manipulation (Figure 5.5). The boards are 2 × 2.5 cm^2 and are equipped with two contacting pins to which are soldered the anode and grid HV wires. Two thin wires are used to connect the InGrid pads and the board pins and are silver-glued to these electrodes on both ends. The test chamber can house up to 6 InGrid carrying boards.

5.7 Conclusion

The techniques of photolithography, wet etching and sputtering permit a large variety of detector geometries to be fabricated with high precision. With SU-8 as a pillar material, amplification gap thicknesses from 30 to 100 μm can be realized with variations less than 1 % at the grid level. Hole diameters down to 10 μm could be controlled with a precision of 1 μm. This accurate control on the detector dimensions promises a very good gain uniformity across the grids.

The choice of grid material is driven by yield reasons. The sputtering of a 1 μm thin layer of Al on SU-8 does not prevent the subsequent development of this photoresist. This is unfortunately not the case when depositing thicker layers or materials of higher heat capacity which are desirable to improve the resistance of the grid against gas discharges. As a result, only InGrids made of Al were tested sofar. Measurements of their amplification properties are reported in the next chapter.

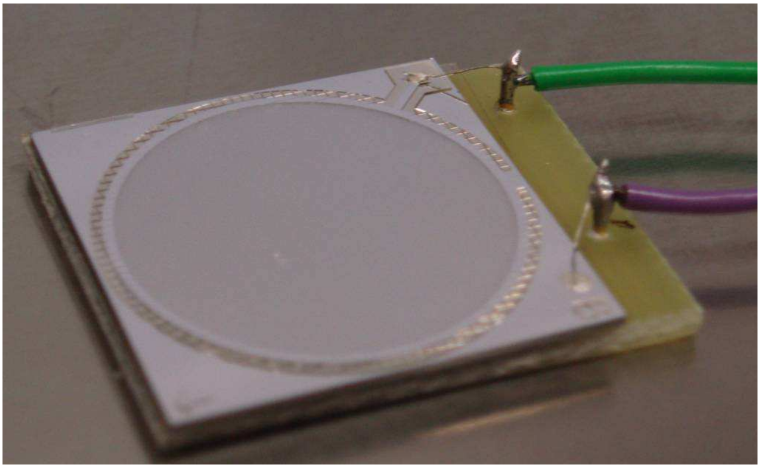

Figure 5.5: *A 2 cm diameter InGrid mounted on a board for test.*

Chapter 6

Amplification properties of InGrid detectors

GridPix detectors should show superior performance when equipped with an InGrid than with a standard Micromegas (*e.g.* no dead areas, uniform response across the detector area). Still, it is important to verify that the good amplification properties of standard Micromegas are maintained when the grid is fabricated by post-processing. In particular, gains of several thousand should be routinely achieved with an InGrid and the energy resolution should be close to the statistical limit. The latter case would imply small gain fluctuations and hence high single electron detection efficiency. These measurements were realized with an ^{55}Fe source in several gas mixtures and are reported in this chapter.

The experimental setup is presented first, followed by a detailed description of the absorption of ^{55}Fe quanta in argon-based mixtures. In section three, I explain how the gain and the energy resolution are determined from the measured spectra. The measurements are presented in the next section and are accompanied by simulation results. They will provide a sound basis for discussing the contribution of UV photons and Penning ionization to the measured gains and the various sources of gain fluctuations in InGrid detectors. I will then draw conclusions on the choice of grid geometry, gas filling and amplification fields of GridPix detectors.

6.1 Experimental setup

6.1.1 Prototypes and test chamber

The InGrids are fabricated on 100-mm diameter wafers. The wafers are diced to single InGrids which are then mounted on 2×2.5 cm^2 boards. Up to six boards can be placed inside the test chamber.

The chamber consists of a 15 × 22 cm^2 aluminium base plate and a cover. A sensitive volume and drift gap is created by placing a cathode foil at a distance of 4 mm from the chamber base plate. The foil is held in a 10 cm diameter frame and fixed parallel to the base plate by means of insulating spacers (Figure 6.1 (a)). The cover is a 2 cm thick metal frame onto which is glued a kapton gas seal. The kapton foil is the detector window. By means of feedthroughs, connections are made from outside the chamber to the cathode, grids and anodes. A metal shielding box contains a preamplifier and some RC-filters. Grids and cathode are connected to high voltage supplies through the RC-filters and the anodes are set at ground potential (Figure 6.1 (b)).

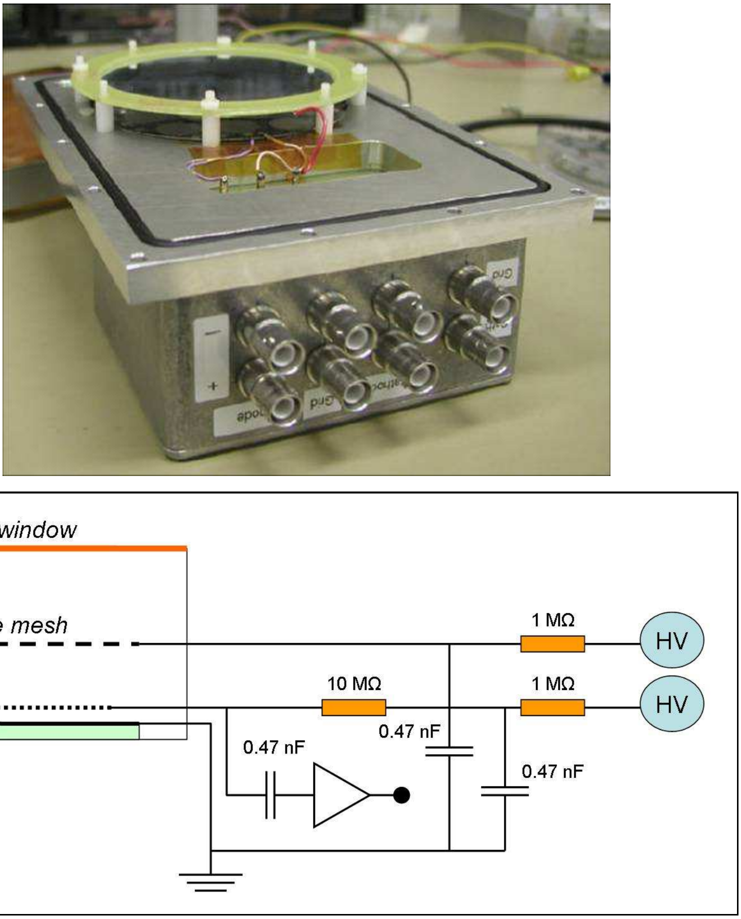

Figure 6.1: *Test chamber with the gas cover removed (a) and readout circuitry (b).*

6.1.2 Signal readout and electronic calibration

Signals are read out from the grid and directed to a low-noise charge-sensitive preamplifier (800 electrons ENC, 1 μs integration time). The integration time is larger than the time it takes to complete the grid charge signal (50–100 ns) and therefore the height of the preamplifier pulse should be proportional to the avalanche charge. Further amplification is realized by an Ortec amplifier with a gain of 8 [193]. Its output is connected to a PC-controlled Amptek portable Multi Channel Analyzer (called MCA) for spectrum display and analysis [194].

The calibration constant of the electronic chain (preamplifier-amplifier-MCA) will be very important to derive the gain from the measured signals. It is determined by injecting a known amount of charge on a test capacity C_i connected to the preamplifier input. For this purpose, a pulse generator was used. The capacity C_i was measured to be 12.0 ± 0.6 pF and the test pulse height V_i could be measured on an oscilloscope with a 5 % accuracy. The MCA operates in two ranges of input pulse voltage. For this reason, two calibrations were made and a linear function was fitted to the measured points:

$$P = SQ_\mathrm{i} + P_0 \tag{6.1}$$

where $Q_\mathrm{i} = C_\mathrm{i} V_\mathrm{i}$ is the input charge, S the calibration constant and P_0 the possible offset are the fit parameters.

6.1.3 Radiation source

The measurements are performed using an ^{55}Fe source. The ^{55}Fe isotope decays into Mn by electron capture. The excited Mn atoms then emit fluorescence photons of 5.90 keV (Mn K_α) and 6.49 keV (Mn K_β) in the ratio 8.5:1 [195]. A 15 mm thick collimator with a 3 mm diameter hole is placed above the detector window to irradiate 30 % of the InGrid area. Before reaching the sensitive volume of the detector, the 5.90 and 6.49 keV photons traverse, successively, 15 mm of air (collimator), 50 μm of kapton (detector window), 16 mm of the chamber gas (gap between the window and the cathode) and a 20 μm thick stainless steel cathode mesh. The total photon absorption coefficient in these materials is higher at 5.90 keV than that at 6.49 keV. The ratio between the number of 5.90 keV and 6.49 keV photons that stop in the sensitive volume of the detector is, therefore, smaller than 8.5:1. It will be calculated in section 6.2.3.

6.1.4 Gas system

The measurements are performed in mixtures of Ar/CH_4 90/10 (so-called P10), Ar/$i$$C_4H_{10}$ and Ar/CO_2. In the last two mixtures, the gas relative fractions are set by adjusting the flow rates with mass controllers with a 0.5 % precision. The P10 mixture was available from a pre-mixed bottle. All mixtures were flushed through the chamber at flow rates of 0.5 to 5 l/h.

6.2 ^{55}Fe spectrum in argon-based mixtures

6.2.1 Interaction of ^{55}Fe quanta in the gas mixtures used for test

An ^{55}Fe quantum can interact in the gas by the photo-electric effect and Compton scattering, pair production being impossible at these energies. The mean free paths for these processes at 5900 and 6492 eV in the various gases used (Ar, CO_2, CH_4, iC_4H_{10}) are listed in Table 6.1. The mean free paths for Compton scattering are two and three orders of magnitude larger than those for the photo-electric effect in CO_2, iC_4H_{10}, CH_4 and Ar respectively. We therefore assume that the photons convert in the gas by the photo-electric effect only.

The probabilities, in those four gases, that a photon converts by the photo-electric effect in the 4 mm drift gap of the detector, are quoted in the last column of Table 6.1. Clearly, the conversion probability is the highest in Ar. We checked that it is still the case in Ar-based mixtures with quencher fractions smaller than 20 %. As a result, in the mixtures that will be used ^{55}Fe quanta interact mainly by the photo-electric effect on argon atoms.

The photo-electric effect results in the emission of a photo-electron. Afterwards some Auger electrons and/or fluorescence photons are also emitted, the energies of which depend on the various electronic transitions involved in the de-excitation of the atom. The complete spectrum of electrons and photons is very complicated. I present here a simplified version where only the principal transitions are taken into account.

6.2.2 Energies of the photo-electrons and Auger electrons

The photo-electrons

The energy of a photo-electron is given by the photon energy minus the energy of the shell where the photon is absorbed (Equation 3.6). In an argon atom, electrons are distributed among the K-shell, the three L-shells (L_1, L_2 and L_3) and the three M-shells (M_1, M_2 and M_3). The binding energies of electrons from those shells are listed in Table 6.2.

In argon, a 5900 eV photon can be absorbed by the photo-electric effect by electrons from the M, L and K shells. The total cross-section for the photo-electric effect at 5900 eV is equal to $0.176 \cdot 10^{-19}$ cm^2. The contributions from the photo-ionizations of the L and M shells should be small.

As an indication, sub-shell cross-sections were calculated at 8048 eV (K_α line of Cu) by [198] and are listed in Table 6.3, together with the total cross-section for the photo-electric effect taken from [86]. At 8048 eV, the sub-shells contribute to 9 % to the total photo-electric cross-section and this contribution can be expected to remain small at 5900 and 6492 eV.

	$\lambda^{\mathrm{p.e.}}_{\alpha}$ (cm) $\lambda^{\mathrm{p.e.}}_{\beta}$ (cm)	$\lambda^{\mathrm{c.s.}}_{\alpha}$ (cm) $\lambda^{\mathrm{c.s.}}_{\beta}$ (cm)	$\lambda^{\mathrm{t}}_{\alpha}$ (cm) $\lambda^{\mathrm{t}}_{\beta}$ (cm)	$\mathsf{P}^{\mathrm{p.e.}}_{\alpha}$ (%) $\mathsf{P}^{\mathrm{p.e.}}_{\beta}$ (%)
Air	33.46	8064.52	33.32	
	44.80	7331.38	44.56	
Kapton	$4.29 \cdot 10^{-2}$	6.40	$4.27 \cdot 10^{-2}$	
	$5.82 \cdot 10^{-2}$	6.07	$5.73 \cdot 10^{-2}$	
Fe	$1.46 \cdot 10^{-3}$	2.16	$1.46 \cdot 10^{-3}$	
	$1.92 \cdot 10^{-3}$	2.00	$1.92 \cdot 10^{-3}$	
Ar	2.08	8153.81	2.08	17.49
	2.70	7643.51	2.70	13.77
CO_2	21.22	4951.48	21.13	1.87
	28.53	4676.39	28.37	1.39
$i C_4H_{10}$	65.16	4073.49	64.11	0.61
	88.32	3913.74	86.41	0.45
CH_4	166.73	8468.83	163.59	0.24
	225.47	8169.93	219.41	0.18

Table 6.1: *Mean free paths for the photo-electric effect ($\lambda^{\mathrm{p.e.}}$), Compton scattering ($\lambda^{\mathrm{c.s.}}$) and total absorption (λ^{t}) at normal conditions, in the various elements of the detector. The indexes α and β refer to the energy of the K_α and K_β quanta emitted by the ^{55}Fe source. The mean free paths are calculated using the gas mass densities and the mass attenuation coefficients taken from [43] and [86] respectively. In the last column, the probability that a photon entering the drift gap of the detector converts by the photo-electric effect within 4 mm is quoted.*

One can also estimate this contribution by extrapolation of the cross-section trend below the K-edge, up to ^{55}Fe quantum energies, neglecting the increase due to the K-shell. At 5900 eV, we find that the sub-shells should contribute to 11 % to the total cross-section which is consistent with the somewhat lower values found at 8048 eV.

As a conclusion, this contribution is small and we ignore the absorption of ^{55}Fe quanta by electrons from the L and M shells. Photo-electrons with energies of 2694 eV and 3286 eV for K_α and K_β photons respectively are emitted in the gas. This leaves a vacancy in the K-shell which is filled through two competing mechanisms: fluorescence and Auger transitions. These two processes have relative probabilities of 0.135 and 0.865 [199].

Shell	K	L_1	L_2	L_3	M_1	M_2	M_3
Energy (eV)	3205.9	326.3	250.6	248.4	29.3	15.9	15.7

Table 6.2: *Binding energies of the electrons of an argon atom [196, 197].*

	total	L_1	$L_{2,3}$	M_1	$M_{2,3}$
$\sigma_{\text{p.e.}}$ (cm^2)	$0.76{\cdot}10^{-20}$	$0.47{\cdot}10^{-21}$	$0.13{\cdot}10^{-21}$	$0.59{\cdot}10^{-22}$	$0.19{\cdot}10^{-22}$

Table 6.3: *Cross-sections for the photo-ionization of the various sub-shells of an argon atom at a photon energy of 8048 eV taken from [198]. The total cross-section for the photo-electric effect is taken from [86].*

Fluorescence transitions

The main fluorescence lines of argon atoms with a vacancy in the K-shell are the K_{α_1}, K_{α_2}, K_{β_1} and K_{β_3} lines [92] and are listed in Table 6.4.

line	transition	energy (eV)	relative intensity
K_{α_1}	$L_3 \rightarrow K$	2957	7.30
K_{α_2}	$L_2 \rightarrow K$	2955	3.60
K_{β_1}	$M_3 \rightarrow K$	3190	0.58
K_{β_3}	$M_2 \rightarrow K$	3190	0.30

Table 6.4: *Main fluorescence lines of argon atoms with a vacancy in the K-shell [92].*

A vacancy in the K-shell is therefore filled almost only by an electron from the L_2 or the L_3 shell. This results in the emission of a photon of 2957 eV (or 2955 eV) and a vacancy in the L_3-shell (or in the L_2 shell). The mean free path for total absorption at these energies in pure argon is close to 3.2 cm. This distance is larger than the dimensions of the sensitive volume of our detector and thus the fluorescence photons have a large probability to escape from detection.

Auger transitions

An argon atom contains 18 electrons that fill completely the K and L shells and partly the M shells. The possible Auger transitions are therefore KLL, KLM, LLM and LMM (cf. section 3.1.2). These transitions result each in an Auger electron spectrum of several lines depending on which of the L-shell and M-shell electrons are involved (see [89] for the KLL and KLM spectra, [200] for the LMM spectrum and [201] for the LLM spectrum). The energy of the most intense lines are quoted in Table 6.5. In an Auger transition, an electron is emitted and a new vacancy is created in the atom. Auger transitions often occur in cascade resulting in multiply-charged positive ions. The final Auger electron spectrum is therefore complex and I will detail the principal Auger cascades only.

transition	$KL_{2,3}L_{2,3}$	$KL_1L_{2,3}$	$KL_{2,3}M$	$L_1L_{2,3}M$	$L_{2,3}MM$
energy (eV)	2660	2574	2923	47	203

Table 6.5: *Main Auger electron energies taken from [89, 200, 201].*

A list of the Auger decay cascades of an argon atom with a K-hole produced by the photo-electric effect can be found in [199]. The main cascades are:

1. $KL_{2,3}L_{2,3}$ with 69.5 % probability.

   This creates two new vacancies in the L_2-shell or L_3-shell which are both filled through $L_{2,3}MM$ transitions. The cascade results in an Ar^{4+} ion and the emission of one electron of 2660 eV and two electrons of 203 eV.

2. $KL_1L_{2,3}$ with 15.1 % probability.

   This creates two vacancies in the L-shells which are filled in 93.4 % of the cases through an $L_{2,3}MM$ and an $L_1L_{2,3}M$ transition. In the last case, the $L_{2,3}$ vacancy is filled through an $L_{2,3}MM$ transition. An Ar^{5+} ion is produced and four electrons are emitted with energies of 2574, 203, 47 and 203 eV.

3. $KL_{2,3}M$ with 10.1 % probability.

   The resulting $L_{2,3}$ vacancy is filled through an $L_{2,3}MM$ transition. The resulting ion is Ar^{3+} and the two Auger electrons have an energy of 2923 and 203 eV.

The main energy deposits are thus: 3066, 3027 and 3126 eV with the relative probabilities of 0.75, 0.15 and 0.10.
In the case where the K-shell vacancy was filled through a $K_{\alpha 1}$ fluorescence transition, the resulting L_3 vacancy is filled by an $L_{2,3}MM$ Auger transition as the fluorescence yield of the L-shell is negligible [91].

Final energy spectrum

In conclusion, the energy spectrum of the electrons from the K_α photo-electric conversions results from the following process chains.

1. Photo-electric effect on the K-shell with emission of a 2694 eV photo-electron, followed in 13.5 % of the cases by an escaping photon and an Auger electron of 203 eV.

   The total energy deposit is 2897 eV and the corresponding line is called the escape peak of argon.

2. Photo-electric effect on the K-shell with emission of a 2694 eV photo-electron, followed in 86.5 % of the cases by Auger cascades resulting in three main lines at 3066, 3027 and 3126 eV with relative intensities of 0.75, 0.15 and 0.10.

   The total energy deposits are 5760, 5721 and 5820 eV respectively and the three corresponding lines form the photo-peak of argon. The average energy is 5760 eV.

These four lines are accompanied by four additional lines (592 eV higher) from the conversions of the K_β quanta. The final spectrum is sketched in Figure 6.2, assuming a ratio between K_α and K_β conversion of 5. This ratio will be important for fitting the measured spectra and its calculation is detailed in the next section.

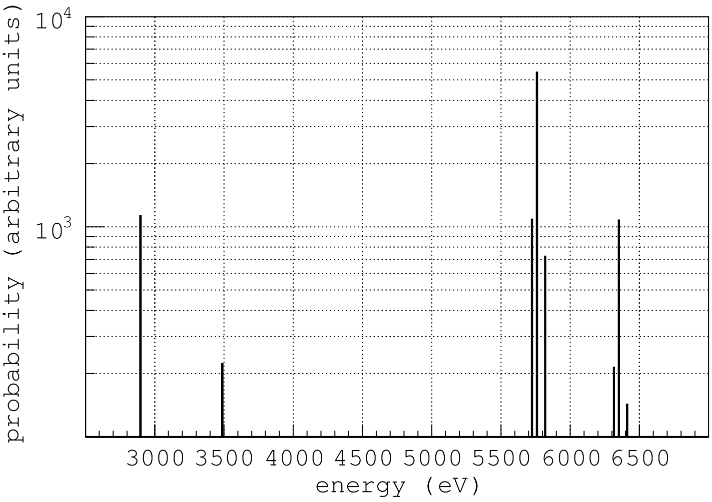

Figure 6.2: *Expected main lines of the ^{55}Fe spectrum in argon.*

6.2.3 Ratio between the number of K$_\alpha$ and K$_\beta$ photon conversions by the photo-electric effect

The ratio between the number of K$_\alpha$ and K$_\beta$ photo-electric conversions depends on the absorption in the various materials traversed from the source to the sensitive volume.
Let's call N^0_α and N^0_β the number of 5900 and 6492 eV photons emitted by the source per unit time. The ratio $r_0 = N^0_\alpha / N^0_\beta$ is equal to 8.5/1. With $\lambda^{\mathrm{t}}_\alpha$ and $\lambda^{\mathrm{t}}_\beta$ the mean free paths for total absorption in a given material, the ratio r after a distance d in this material becomes:

$$r(d) = \frac{N_\alpha(d)}{N_\beta(d)} = r_0 \cdot \exp\left(-d\frac{\lambda^{\mathrm{t}}_\beta - \lambda^{\mathrm{t}}_\alpha}{\lambda^{\mathrm{t}}_\beta \cdot \lambda^{\mathrm{t}}_\alpha}\right) = r_0 \cdot A \tag{6.2}$$

where the factor A depends on the material, its number density and the traversed distance d. The photons traverse, from the source to the bottom of the cathode mesh, 15 mm of air, 50 μm of kapton, 16 mm of the chamber gas and 20 μm of a stainless steel (cathode mesh). For each of these materials, a factor A enters Equation 6.2:

$$r_1 = r_0 \cdot A(\mathrm{air}) \cdot A(\mathrm{kapton}) \cdot A(\mathrm{gas}) \cdot A(\mathrm{stainless\ steel}) \tag{6.3}$$

The mean free paths for total absorption at 5900 and 6492 eV in those materials are listed in Table 6.1. They are used to calculate the various factors in Equation 6.3:

$$r_1 = r_0 \cdot 0.989 \cdot 0.9706 \cdot 0.838 \cdot 0.720 \tag{6.4}$$

where A(gas) was calculated for 16 mm of argon and A(stainless steel) for 20 μm iron, considering the 44 % optical transparency of the mesh. The product of the factors is 0.58 and yields a ratio $r_1 = 5.0$. Using this figure, the ratio between the number of K$_\alpha$ and K$_\beta$ conversions (by the photo-electric effect) in the drift gap is:

$$r_2 = \frac{\int_0^{D_{\mathrm{g}}} N_\alpha(x)dx}{\int_0^{D_{\mathrm{g}}} N_\beta(x)dx} \tag{6.5}$$

where D_{g} is the drift gap thickness and $N_\alpha(x)dx$ and $N_\beta(x)dx$ the number of 5900 and 6492 eV photons that convert per unit time, between x and $x+dx$. Using the ratio r_1:

$$r_2 = r_1 \cdot \frac{\lambda^{\mathrm{p.e.}}_\alpha}{\lambda^{\mathrm{p.e.}}_\beta} \cdot \frac{1-\exp(-D_{\mathrm{g}}/\lambda^{\mathrm{p.e.}}_\alpha)}{1-\exp(-D_{\mathrm{g}}/\lambda^{\mathrm{p.e.}}_\beta)} = 5.0 \cdot 0.9800 \tag{6.6}$$

where $\lambda^{\mathrm{p.e.}}_\alpha$ and $\lambda^{\mathrm{p.e.}}_\beta$ are the mean free paths for the photo-electric effect in the gas. With a drift gap of 4 mm the ratio r_2 in argon is equal to 4.9. In the mixtures that will be used r_2 shows variations smaller than 2%.

6.2.4 Number of primary electrons and total number of electrons

Number of primary electrons

The number of primary electrons N_p resulting from the full absorption of a photoelectron or an Auger electron of energy E_0 in the keV range is distributed according to a gaussian distribution [113]. The distribution mean N_p and variance $\sigma^2_{N_\mathrm{p}}$ are given by:

$$N_\mathrm{p} = E_0/W \tag{6.7}$$

$$\sigma^2_{N_\mathrm{p}} = E_0 F/W \tag{6.8}$$

In the case of an ^{55}Fe quantum photo-electric conversion in argon, one photoelectron and at least one Auger electron are produced and the number of primary electrons is given by:

$$N_\mathrm{p} = \sum_\mathrm{k} E_\mathrm{k}/W(E_\mathrm{k}) \tag{6.9}$$

where the sum is carried over the number of electrons emitted from the atom. Neglecting the dependence of W on the initial energy, Equation 6.9 applied to the K_α line of the escape peak reduces to:

$$N_\mathrm{p} = (2694 + 203)/W = 2897/W \tag{6.10}$$

and the variance of N_p:

$$\sigma^2_{N_\mathrm{p}} = \sum_\mathrm{k} E_\mathrm{k} \cdot F(E_\mathrm{k})/W(E_\mathrm{k}) \tag{6.11}$$

finally yields:

$$\sigma^2_{N_\mathrm{p}} = (2694 + 203) \cdot F/W = 2897 \cdot F/W \tag{6.12}$$

Similarly, the mean and variance of the number of primary electrons from K_α events in the photo-peak is calculated by assuming a line at 5760 eV. The values of W and F that will be used for fitting the measured spectra are listed in Table 6.6. Except in $\mathrm{Ar}/i\mathrm{C_4H_{10}}$ 95/5, the values of W in gas mixtures are calculated using a weighted average of the values in the pure gases (cf. Equation 3.15). As a result, an error of 5 % is assumed on W (and on N_p). The Fano factor in $\mathrm{Ar/CO_2}$ mixtures is also calculated as an average while in all $\mathrm{Ar}/i\mathrm{C_4H_{10}}$ mixtures, a value of 0.21 measured with a GridPix TPC in a 95/5 mixture is used (cf. chapter 8).

Gas mixture	W (eV)	N_p (5760 eV)	F
Ar	26.4	218	0.16
CO_2	33.2	173	0.33
iC_4H_{10}	23.0	250	0.26
Ar/iC_4H_{10} 99/1	26.36	218	
Ar/iC_4H_{10} 97.5/2.5	26.30	219	
Ar/iC_4H_{10} 95/5	25.00	228	0.21
Ar/iC_4H_{10} 90/10	26.02	221	
Ar/iC_4H_{10} 80/20	25.64	225	
Ar/CO_2 95/5	26.67	216	0.17
Ar/CO_2 90/10	26.95	213	0.18
Ar/CO_2 80/20	27.53	209	0.20

Table 6.6: *Mean energy per ion pair W, number of primary electrons* N_p *at 5760 eV and Fano factor F in the various mixtures used for test. W and F are taken from literature (cf. chapter 3) except for the Ar/*iC_4H_{10} *95/5 mixture for which measurements with a GridPix TPC are used (cf. chapter 8).*

Total number of electrons

The distribution of the number of electrons produced in a single avalanche is generally parametrized by the exponential or the Polya distribution. The distribution mean and relative variance are noted G and b respectively. When the number of primary electrons initiating an avalanche is larger than a few tens, the central limit theorem predicts that the total number of electrons N_t after multiplication is normally distributed. If all N_p primary electrons are multiplied, the distribution mean N_t and variance $\sigma^2_{N_\mathrm{t}}$ are given by:

$$N_\mathrm{t} = GE_0/W \tag{6.13}$$

$$\sigma^2_{N_\mathrm{t}} = G^2E_0(F+b)/W \tag{6.14}$$

which can be applied to the energy deposits from ^{55}Fe photo-electric conversions if G and b do not depend on the initial energies of the photo-electron and the Auger electrons. For energy deposits in the keV range and gains of 10^3–10^4 this assumption is certainly reasonable as no gain saturation should occur. The mean and variance of N_t from the four energy deposits (2897, 3489, 5760 and 6352 eV) are listed in Table 6.7.

Energy deposit (eV)	N_t	$\sigma^2_{N_\mathrm{t}}$	h
$E_\alpha^{\mathrm{e.p.}} = 2897$	$2897G/W$	$2897G^2(F+b)/W$	0.135
$E_\beta^{\mathrm{e.p.}} = 3489$	$3489G/W$	$3489G^2(F+b)/W$	0.027
$E_\alpha^{\mathrm{p.p.}} = 5760$	$5760G/W$	$5760G^2(F+b)/W$	1
$E_\beta^{\mathrm{p.p.}} = 6352$	$6352G/W$	$6352G^2(F+b)/W$	0.2

Table 6.7: *Mean, variance and integral of the distributions of the total number of electrons from the four energy deposits.*

6.2.5 Spectrum on the Multi Channel Analyzer

The motion of electrons and ions produced in the avalanches induces on the grid a signal which is measured by the preamplifier. The latter produces a voltage pulse with a height proportional to N_t which is further amplified. The amplified pulse is then digitized by the MCA, which converts proportionally the signal height into a number of ADC counts. The distribution of the number of ADC counts is generally displayed on a histogram. A given number of N_p electrons, all multiplied in the amplification region, corresponds to a certain peak position P on that histogram:

$$P = S \cdot eN_\mathrm{t} + P_0 = S \cdot (eN_\mathrm{p}G) + P_0 \tag{6.15}$$

where S and P_0 are the calibration constants of the electronics that enter Equation 6.1. The detector gain and energy resolution will be determined by fitting the photo-peak by two gaussian functions and a linear function that accounts for the background. Noting x the channel number of the MCA, the fit function has eight parameters and can be written as:

$$f = \frac{h_\alpha}{\sqrt{2\pi}\sigma_\alpha} \exp\left(-\frac{1}{2}\left(\frac{x-\mu_\alpha}{\sigma_\alpha}\right)^2\right) + \frac{h_\beta}{\sqrt{2\pi}\sigma_\beta} \exp\left(-\frac{1}{2}\left(\frac{x-\mu_\beta}{\sigma_\beta}\right)^2\right) + ax + b \tag{6.16}$$

where μ_α, μ_β, σ_α, σ_β and h_α, h_β are the peak positions, standard deviations and integrals of the K_α and K_β lines respectively. The number of parameters of f can be reduced by expressing the K_β line parameters as a function of those of the K_α line. For instance $h_\beta = h_\alpha/r_2$. Also, from Table 6.7 the following relations are obtained:

$$\mu_\beta = \mu_\alpha \cdot 6352/5760 \tag{6.17}$$

$$\sigma_\beta = \sigma_\alpha \cdot \sqrt{6352/5760} \tag{6.18}$$

Hence, the number of parameters of the fit function 6.16 reduces to five.

6.3 Electron collection efficiency

The gain is measured as the ratio between the total number of electrons after amplification and the number of primary electrons. For a precise measurement, it is thus important that the largest fraction of primary electrons participate to the signal. Before the gain study I therefore discuss the electron collection efficiency and measure, among different InGrids, which ones show the best collection efficiency.

6.3.1 Definition

The collection efficiency is the probability that a primary electron produced in the drift region reaches the amplification region. If the electrons would follow precisely the field lines the collection efficiency would depend only on the grid geometry and electrode voltages. A two-dimensional drawing of the field lines from the cathode is shown in Figure 6.3.

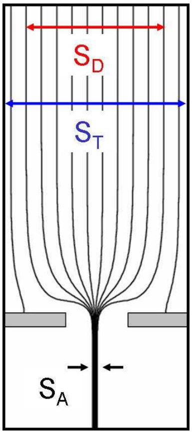

Figure 6.3: *Two-dimensional view of the field lines from the cathode in the vicinity of a grid hole. S_D and S_A refer to the area of the funnel in planes parallel to the grid plane. S_T is the area of a periodic cell.*

Using the notations of Figure 6.3, the collection efficiency in the limit of no diffusion can be approximated to:

$$\eta_0 = S_D/S_T \tag{6.19}$$

which is true when the drift gap is several times larger than the grid hole diameter. In this case, Gauss' law can be used to express the ratio S_D/S_A as:

$$S_D/S_A = E_A/E_D = FR \tag{6.20}$$

with *FR* the field ratio (this equation is derived in chapter 7). Equation 6.20 predicts that when *FR* increases, S_{D} and hence η_0 increase while S_{A} decreases. Above a certain field ratio which depends on the grid geometry, S_{D} is almost equal to S_{T} and the collection efficiency should be close to one. In practice, even if all field lines from the cathode reach the anode, some electrons may not enter the amplification region:

- electrons can be attached by some electronegative molecules from contamination which become negatively-charged ions. Those would drift very slowly and reach the amplification region a long time after the multiplication of the other primary electrons. An attached electron, hence, does not participate to the signal. Because of the small distances over which electrons drift in the test chamber (at most 4 mm), attachment will not be considered;

- electrons can be collected outside the grid area if the range of the photoelectrons and Auger electrons is larger than the dimensions of the sensitive volume. The practical range of a 3 keV electron is about 300 μm in argon at normal conditions (Equation 3.17). With the collimation used, the resulting primary ionization is produced above the center of the grid;

- due to the potential difference between the chamber base plate and the grid, field non-uniformity is expected close to the grid edges. In particular, some field lines that should arrive at the grid edges eventually end on the base plate. The distance from the grid center at which the electron collection would be affected by this effect depends on the drift gap, the grid diameter and the potential difference across the gap. With a drift gap of 4 mm and a grid diameter of 20 mm, two-dimensional field calculations showed that the drift field is uniform in the region of interest;

- electrons can be collected at the grid because of transverse diffusion. The probability that this occurs depends on the three-dimensional field (which can not be precisely calculated) and the diffusion. Still, when the drift field is reduced, one may expect a larger electron diffusion in the field gradient region above the grid because from one to several kV/cm, the diffusion is a decreasing function of the field.

Finally, the collection efficiency of the detectors should be governed by two mechanisms that have opposite effects: the electric focusing and the transverse diffusion.

6.3.2 Measurements with various grid geometries

The peak position for arbitrary electron collection efficiency can be expressed from Equation 6.15 as:

$$P = S \cdot (eN_{\mathrm{p}}\eta G) + P_0 \tag{6.21}$$

Because the gain is not known in advance (it is actually measured using this equation, assuming $\eta = 1$), it is not possible to measure the absolute value of the collection efficiency with our setup. Therefore, only relative variations of collection efficiency will be shown. The measurements are performed with InGrids of about 90 μm amplification gap thicknesses and various hole pitches and diameters. In a mixture of Ar/iC$_4$H$_{10}$ 95/5 and at a grid voltage of -368 V (E_A = 41 kV/cm), the position of the photo-peak was measured as a function of the drift field. In Figure 6.4, the peak position is plotted against the field ratio.

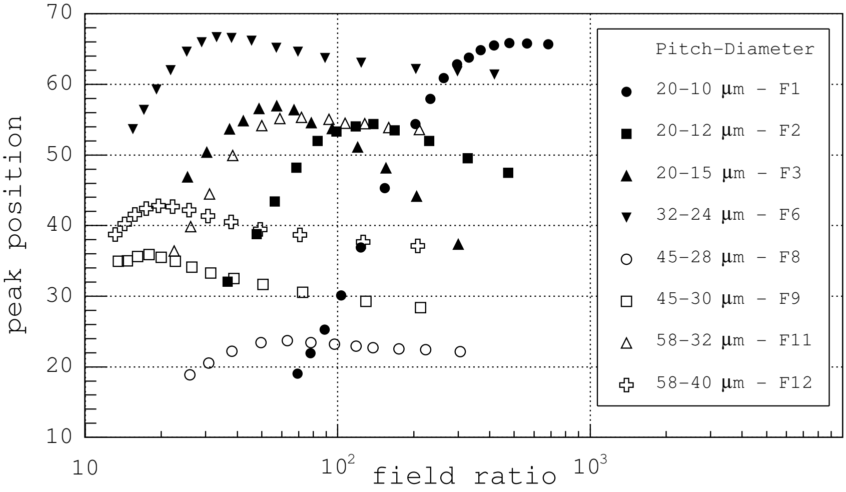

Figure 6.4: *Peak position and field ratio measured with InGrids of various hole pitches and diameters in Ar/iC$_4$H$_{10}$ 95/5 at an amplification field of 41 kV/cm.*

We make the following observations:

- at a given field ratio, the peak position varies significantly from one InGrid to the other. These differences can be explained by gap size and hence gain variations (gap size relative variations across the area of a 100 mm wafer of 5 % were reported in chapter 5) and also by the variations of the collection efficiency;
- for all InGrids, the peak position first increases, reaches a maximum at a field ratio FR^M and then drops. The values of FR^M are listed in Table 6.8 and vary with the grid geometry. At a given hole pitch, FR^M increases when the diameter is reduced; this is well illustrated with InGrids F1, F2 and F3. Also, the decrease of the peak position at field ratios above FR^M depends on the grid geometry.

  We think that the peak position variations below FR^M are dominated by the variations of η_0. Above FR^M, η_0 may be close to one and the peak position variations could be due to an increased electron transverse diffusion or, according to Equation 6.21, to a reduction of the gain. In the latter case, the collection efficiency would be constant.

A qualitative study of the variation of the gain and the collection efficiency with the drift field was carried out with the two-dimensional model of the field presented in [81]. The simulation results indicate that the gain drops at low drift fields, especially for geometries where the diameter is large w.r.t. to the gap. Furthermore, no effect of the diffusion on the collection was observed, suggesting that the signal variations for field ratios larger than FR^{M} would reflect the gain variations.

Accordingly, the value of FR^{M} should indicate the maximum drift field above which the collection efficiency decreases. In a TPC, the collection efficiency should be as high as possible to obtain the maximum information on the particle tracks. Also, the drift field is set in order to have the largest drift velocity and the lowest electron diffusion. A high value of FR^{M} would therefore bring additional constraints and it should be as low as possible.

InGrid	F1	F2	F3	F6	F8	F9	F11	F12
p (μm)	20	20	20	32	45	45	58	58
t (%)	19	28	43	41	30	35	24	37
FR^{M}	480	140	60	33	60	15	70	20

Table 6.8: *Field ratio FR^{M} at which the peak position is the highest as measured with InGrids of various geometries in Ar/iC_4H_{10} 95/5. The hole pitch p and the grid optical transparency t are also quoted.*

6.3.3 Measurements in various gas mixtures

At field ratios larger than 70 InGrid F11 exhibits a small dependence of the peak position on the drift field. It has thus probably a good collection efficiency. Its gain and energy resolution will be measured in the following gas mixtures: Ar/$i\mathrm{C}_4\mathrm{H}_{10}$ 80/20, 90/10, 95/5, 97.5/2.5, 99/1 and Ar/CO_2 80/20, 90/10, 95/5. Prior to this, we look at the collection efficiency in those mixtures. Pure argon will also be used: in order to reduce the concentration of impurities to the minimum, the chamber was flushed some 30 hours at a rate of 6 l/h before starting the measurements; which corresponds to 100 times the chamber volume.

Because of the large effect of the gas composition on the gas gain, the grid voltage is adjusted in each mixture so as to obtain signals of similar heights. As a result, the drift and amplification fields at a given field ratio vary from one mixture to the other. The measurements are shown in Figure 6.5.

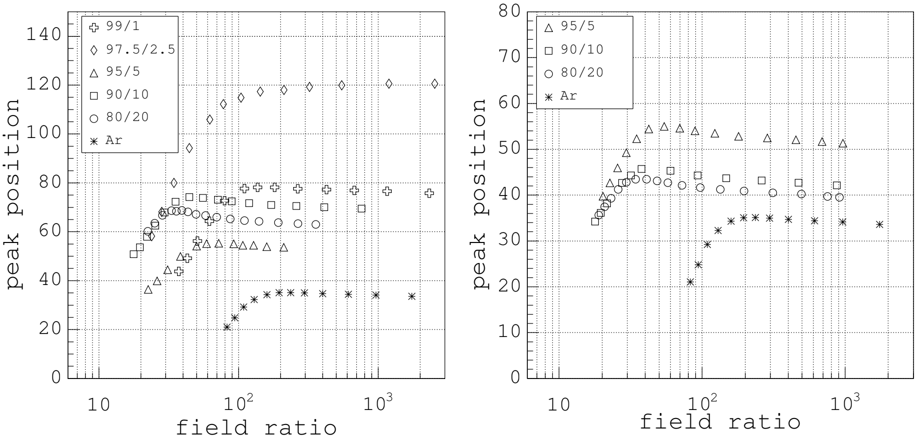

Figure 6.5: *Peak position and field ratio measured in Ar/*iC_4H_{10} *(a) and Ar/*CO_2 *(b) gas mixtures. The grid voltage is different from one mixture to the other.*

The values of FR^{M} are listed in Table 6.9. We observe that FR^{M} decreases when for a given quencher gas the quencher concentration increases. This can be explained by a reduction of the electron diffusion coefficients at larger quencher concentrations. Also, at equal quencher concentrations, FR^{M} is similar in Ar/CO_2 and Ar/iC_4H_{10} mixtures. This is expected because in the mixtures used, the diffusion coefficients at fields above a few kV/cm depend little on the quencher gas but mainly on the quencher concentration.

Ar	Ar/iC_4H_{10}					Ar/CO_2		
	99/1	97.5/2.5	95/5	90/10	80/20	95/5	90/10	80/20
196	110	211	72	44	33	54	38	26

Table 6.9: *Field ratio* FR^{M} *at which the maximum of the peak position is reached in various Ar-based mixtures.*

6.3.4 Discussion of the results

For the first time, the dependence of the collection efficiency of Micromegas-like detectors on the grid geometry was studied. In Ar/iC_4H_{10} 95/5, deviations from the expected standard Micromegas response were observed (no clear plateau of the peak position was measured).

In particular, the collection of the 20 μm hole pitch InGrids appears problematic: at a small hole diameter of 10 μm FR^{M} is very large while at a larger hole diameter of 15 μm, the signal severely drops above FR^{M}. In a TPC, a high value of FR^{M} would put additional constraints on the drift field and therefore such geometries should be avoided. For hole pitches larger than 32 μm, the situation improves: FR^{M} lies between 20 and 60 which allows operation at larger drift fields, up to 2000 and 700 V/cm respectively. Also, the signal drop at field ratios larger than FR^{M} is less severe and could be due to a drop of gain only.

An effect of the gas mixture on the collection efficiency was observed at low quencher fractions. In Ar/iC$_4$H$_{10}$ mixtures and for one tested geometry, this effect is significant for fractions below 5%.

6.4 Measurements of gas gain in various gas mixtures

6.4.1 Measurements

The measurements of the gain of InGrid F11 as a function the amplification field E are shown in Figure 6.6. The measurements are corrected for pressure variations.

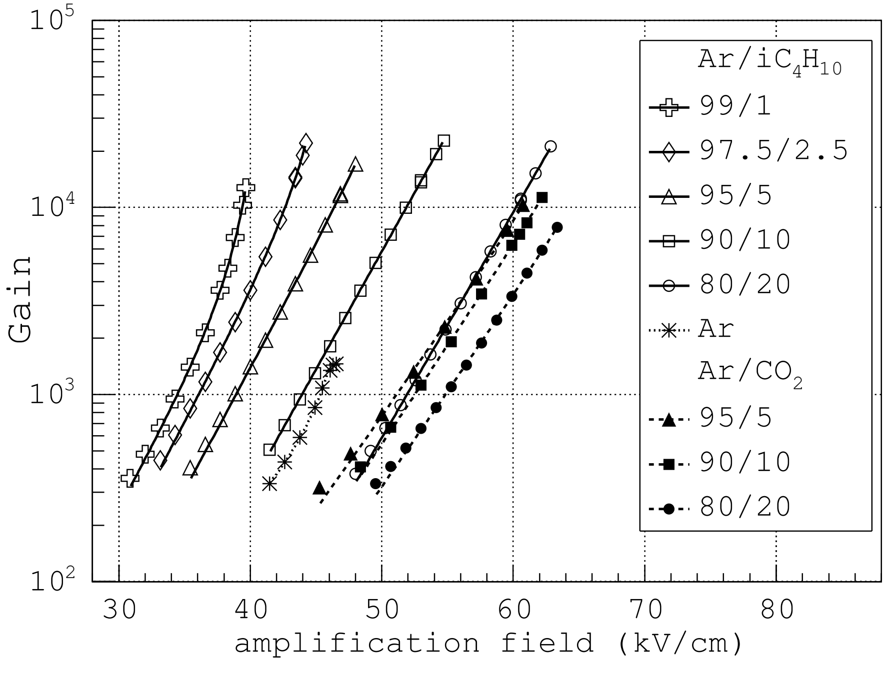

Figure 6.6: *Gain and amplification field in some argon-based mixtures. The amplification gap size is equal to 86 μm.*

In all mixtures, the drift field is set such as to obtain a field ratio larger than FR^{M} and the grid voltage is increased until discharges occur. We make the following observations:

- in most gas mixtures, the gain is an exponential function of E. Also, the field required for a given gain changes from one mixture to the other. It appears that higher gains and maximum gains before sparking are obtained in Ar/$i\mathrm{C}_4\mathrm{H}_{10}$ mixtures than in Ar/CO_2 mixtures;

- at a given field strength, the gain decreases with the quencher fraction. The reduction of the energy of the avalanche electrons at larger quencher fractions is predicted by MAGBOLTZ in those mixtures and is a plausible explanation for our observations.

  Also, the gain is smaller in pure argon than in Ar/$i\mathrm{C}_4\mathrm{H}_{10}$ up to isobutane fractions of 10 % while in the three Ar/CO_2 mixtures used, the gain is always lower than in pure argon;

- the gain curves measured in pure Ar and in mixtures with quencher fractions up to 5 % exhibit, at gains close to the maximum gain, a deviation from the exponential behaviour.

  A well-accepted explanation for this over-exponential behaviour is that a small fraction of the UV photons produced in the avalanche releases a few photo-electrons from the detector material (in our case the grid), producing secondary avalanches [202]. The multiplication process hence consists of a primary avalanche accompanied by successor avalanches. The mechanism of avalanche feeding by photo-electrons is called the photon feedback and will be discussed in more detail in the next section.

  In the over-exponential region, the spark rate increases. Sparks are identified as a sudden spike of current on the grid power supply current monitor.

The increase of gain at lower quencher fractions and the over-exponential behaviour in poorly quenched mixtures are in agreement with previous measurements done with a standard Micromegas [62] and a wire counter [202]. The relative positions of the gain curves measured with InGrid are also consistent with Micromegas measurements although the field required to obtain a given gain is 20 kV/cm smaller in the case of InGrid. This can be explained by different gap sizes, grid thicknesses and gas pressures.

Another important difference lies in the maximum gains: those of InGrid in Ar/$i\mathrm{C}_4\mathrm{H}_{10}$ mixtures are smaller by factors of 2 to 5 (depending on the isobutane fraction) than those of Micromegas. The processing of InGrid is such that the grid has sharp corners at the hole edges. These are not present in the case of Micromegas which is made with different techniques (electroforming or woven mesh [146, 203]). High fields can be generated in the vicinity of these corners,

increasing the discharge probability and thus limiting the maximum gain. The sharp edges could be suppressed with a different InGrid processing; this is an object of further study [192].
Nevertheless, for a GridPix detector a gain of 10^4 should be sufficient to achieve a single electron detection efficiency of 90 % at least. We are therefore satisfied with the measured performance.

In the over-exponential region, the spark rate increases and precludes the operation of the detector above a certain gain. Although pixel chips can be protected against gas discharges (cf. SiProt, chapter 4), parts of the grid metal may be vaporized. Operation of a GridPix detector in this region should hence be avoided. If the instabilities are indeed caused by the photon feedback, a significant fraction of the gain should be due to secondary avalanches. This is assessed in the next section.

6.4.2 Effect of UV photons on the gas gain

The interpretation of the gain deviation from exponential behaviour in terms of photon feedback is supported by the fact that the over-exponential rise occurs at lower gains when the quencher fraction is decreased.
To estimate the impact of photon feedback on the gain, we follow the approach described in [42] and used by [202, 204]. Calling G_0 the gain that would be obtained without feedback and γ the probability per avalanche electron to produce a photo-electron, the total gain G can be written as the following sum:

$$G = G_0 + (G_0\gamma)G_0 + (G_0\gamma G_0\gamma)G_0 + \cdots = \sum_{\mathrm{k}=0}^{\infty} G_0^{\mathrm{k}+1}\gamma^{\mathrm{k}} \tag{6.22}$$

which, for $\gamma \ll 1$, converges to

$$G = \frac{G_0}{1 - \gamma G_0} \tag{6.23}$$

The product γG_0 is equal to the average number of electrons released from the grid by photons produced in the first avalanche. The probability γ (also called secondary Townsend coefficient) is a function of the gas composition, the electric field and the detector geometry. Its dependence on the field should not be very strong as even though the number of photons (and hence of photo-electrons) increases with the field, so is the number of avalanche electrons. As a result, we neglect the dependence of γ on the field and use Equation 6.23 to fit the gain curves. The dependence of the gain on the field being contained in G_0:

$$G_0 = A \cdot \exp(BE) \tag{6.24}$$

where A and B are together with γ the fit parameters, they are listed in Table 6.10.

It is observed that A and B decrease with the quencher concentration. Although B depends weakly on the gas (0.22–0.29 cm/kV in the mixtures), A varies significantly between $1.11{\cdot}10^{-1}$ in Ar/iC$_4$H$_{10}$ 99/1 and $9.77{\cdot}10^{-3}$ in Ar/CO$_2$ 80/20. The parameter γ is equal to $3{\cdot}10^{-3}$ in argon and decreases to 10^{-5} in Ar/iC$_4$H$_{10}$ 95/5 and below for larger fractions. Except for the Ar/iC$_4$H$_{10}$ 90/10 gain curve which is accurately described by an exponential function ($\gamma \sim 0$), it decreases with the quencher fraction, as expected.

Gas mixture	$\boldsymbol{A}$	$\boldsymbol{B}$ (cm/kV)	γ
Ar/$\boldsymbol{i}$C$_4$H$_{10}$			
80/20	$7.62{\cdot}10^{-4}$	$2.71{\cdot}10^{-1}$	$4.12{\cdot}10^{-6}$
90/10	$2.69{\cdot}10^{-3}$	$2.92{\cdot}10^{-1}$	$6.68{\cdot}10^{-11}$
95/5	$1.38{\cdot}10^{-2}$	$2.88{\cdot}10^{-1}$	$1.37{\cdot}10^{-5}$
97.5/2.5	$2.21{\cdot}10^{-2}$	$2.96{\cdot}10^{-1}$	$4.69{\cdot}10^{-5}$
99/1	$5.97{\cdot}10^{-2}$	$2.77{\cdot}10^{-1}$	$2.04{\cdot}10^{-4}$
Ar	2.35	$1.02{\cdot}10^{-1}$	$3.10{\cdot}10^{-3}$
Ar/CO$_2$			
80/20	$1.86{\cdot}10^{-3}$	$2.41{\cdot}10^{-1}$	$9.19{\cdot}10^{-5}$
90/10	$4.29{\cdot}10^{-3}$	$2.35{\cdot}10^{-1}$	$1.52{\cdot}10^{-5}$
95/5	$1.38{\cdot}10^{-2}$	$2.19{\cdot}10^{-1}$	$2.74{\cdot}10^{-5}$

Table 6.10: *Fit parameters A, B and γ.*

The contribution of photons to the total gain is calculated as:

$$\Delta G/G = \frac{G - G_0}{G} = \gamma G_0 \tag{6.25}$$

with G the total gain and G_0 the gain without photon feedback given by Equation 6.24. This contribution is plotted as a function of the gain in Figure 6.7. Up to the maximum gains, it stands below 10 % in Ar/iC$_4$H$_{10}$ 90/10 and 80/20 and in Ar/CO$_2$ 80/20. Similar contributions in gas mixtures with lower quencher fractions can also be obtained but at lower gains.

6.4.3 Monte Carlo calculation of the gain

Introduction

The gain without photon feedback G_0 can be compared to the predictions of the MAGBOLTZ program [37]. MAGBOLTZ contains the cross-sections for electron elastic and inelastic collisions in several gases from thermal energies up to several tens of eV. It simulates in detail the electron drift and calculates the drift velocity, the diffusion coefficients, the attachment and Townsend coefficients, the electron energy distribution and the various collision frequencies. Hence, it is

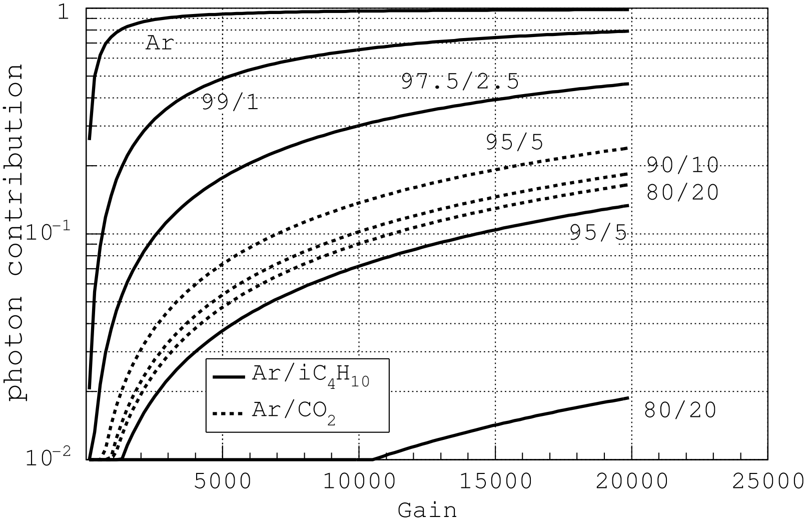

Figure 6.7: *Photon contribution to the measured gain as derived from Equation 6.25.*

possible to quantify the fraction of ionization from each gas species. Likewise, the excitation frequencies of the various levels of the gas species are accessible. On the other hand, MAGBOLTZ does not predict the fate of the excited states (*e.g.* fluorescence and Penning transfers).

If discrepancies between measured gains (without photon feedback) and calculated gains are observed, Penning ionizations should occur in the gas mixture. At the same electric field, higher gains should be reached in Penning than in regular mixtures and the grid voltage required for a given detection efficiency should be smaller in the first case. Because it is preferred to operate the detector at a low voltage (*e.g.* to minimize the possible damages of the detector components by discharges), the operation of a GridPix detector should be safer in Penning mixtures. In the following I will identify among the mixtures used, which present the strongest Penning effect.

Gain calculation

The gain at a given value of the electric field E is calculated as the integral of the Townsend coefficient over the gap size g:

$$G_{\mathrm{sim}}(E) = \exp\bigg(\alpha_{\mathrm{sim}}(E) \cdot g\bigg) \tag{6.26}$$

where α_{sim} is corrected for possible attachment losses in the amplification region. The calculated gains in the Ar/CO$_2$ and the Ar/iC$_4$H$_{10}$ mixtures are shown in

Figure 6.8 and 6.9 respectively. The measured gains corrected for the photon contribution G_0 and the calculated gains with full Penning transfers are also plotted. In a given mixture, the gain with full Penning transfer is obtained when all energetically allowed excited states are assumed to de-excite through ionization. This calculation requires the excited and ionization spectra of the gas species (taken from MAGBOLTZ) and is inspired from [205].

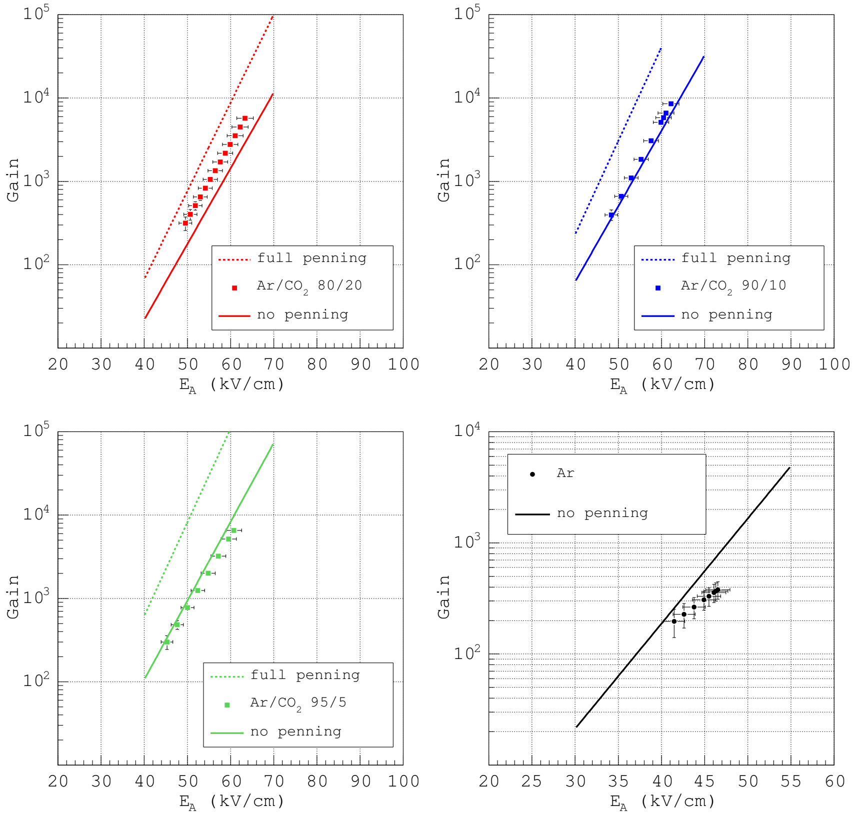

Figure 6.8: *Measured and calculated gains without and with full Penning transfers in Ar/CO_2 mixtures and in pure Ar. The measurements are corrected for the photon contribution using Equation 6.24.*

A good agreement is observed in Ar/CO_2 90/10 and 95/5 while in all other mixtures, especially in the Ar/iC_4H_{10} ones, MAGBOLTZ predictions are too small. The difference between the measured and the calculated gains could be attributed to Penning ionizations which are not taken into account by MAGBOLTZ. Our measurements would then suggest that a mild Penning effect takes place in Ar/CO_2 80/20 and that its impact on the gain is less pronounced at smaller

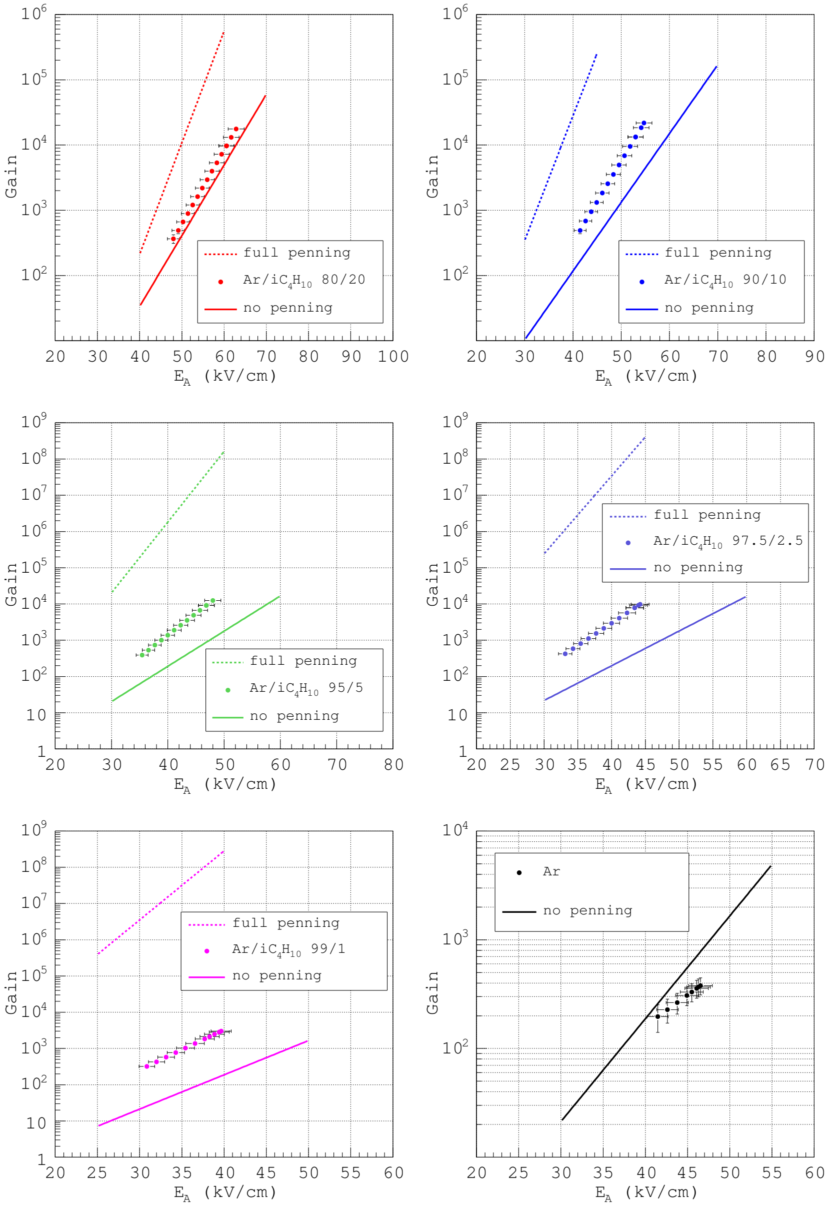

Figure 6.9: *Measured and calculated gains without and with full Penning transfers in Ar/iC_4H_{10} mixtures and in pure Argon. The measurements are corrected for the photon contribution using Equation 6.24.*

quencher concentration. Also, all Ar/iC$_4$H$_{10}$ mixtures seem to be affected by the Penning effect, especially those of low isobutane concentrations.

The gain curve in pure argon does not compare well with the simulation which predicts larger gains and a steeper slope. Due to the limited range of field at which the detector could operate, the fit parameters are affected by a large error, resulting in an over-estimated contribution of the photon feedback.

Contribution of Penning effect to the Townsend coefficient

If we assume that the differences between MAGBOLTZ calculated gains and measured gains (without photon feedback) are only due to the Penning effect, the contribution from Penning ionizations to the Townsend coefficient can be estimated using the ratio:

$$\frac{\Delta\alpha}{\alpha} = \frac{\alpha_0 - \alpha_{\text{sim}}}{\alpha_{\text{sim}}} \tag{6.27}$$

with α_0 the Townsend coefficient derived from the gain G_0 and α_{sim} that from MAGBOLTZ. This ratio is equal to the relative increase of the mean number of ionization per centimeter due to the Penning effect. Its trend is illustrated in Figure 6.10 for the gas mixtures in which $G_0 \geq G_{\text{sim}}$.

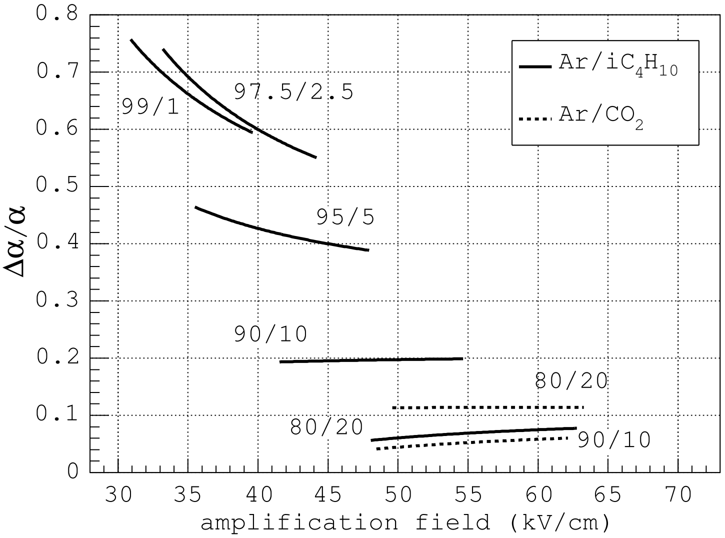

Figure 6.10: *Relative increase of the Townsend coefficient due to the Penning effect as calculated by Equation 6.27.*

Under our assumption, the Penning effect in Ar/iC$_4$H$_{10}$ mixtures is more important at low quencher fractions. The corresponding relative increase of the

Townsend coefficient varries from 5 % in the 80/20 mixture up to 60–70 % in the 97.5/2.5 and 99/1 mixtures. An opposite trend is observed in Ar/CO_2 mixtures where this contribution is equal to 5 and 10 % in the 90/10 and 80/20 mixtures.

Ar/iC_4H_{10} mixtures with small quencher fractions are thus well suited to achieve high gains at low grid voltages. Yet, this fraction has to be large enough to keep photon feedback to a small level. In this respect, an optimum mixture would be Ar/iC_4H_{10} 95/5.

6.5 Measurements of gas gain with various gaps

6.5.1 Introduction

It is predicted that for a given grid voltage and gas mixture, the gain of Micromegas detectors reaches a maximum for an amplification gap between 10–100 μm [148]. A reduction of gap at constant grid voltage results in an increased electric field but in a smaller distance along which the avalanche can develop. For gaps of a few millimeters, the first effect dominates and the gain increases at smaller gaps. Yet, when the gap size becomes of the same order as the distances between ionizations, the high field does not compensate for the small available distance and eventually the gain should drop.

If the gap is adjusted to this particular value, the gain would then be relatively insensitive to local gap variations, resulting in a good gain uniformity across the grid surface. This effect is attractive for large area Micromegas (*e.g.* 30×30 cm^2). The amplification gap of InGrids can be controlled to a 1 μm precision, however, if wrinkles form on the grid surface during the fabrication, the uniformity can be locally disturbed. In a GridPix detector, the detection efficiency would eventually vary across the detector surface. Therefore, it is wise (and easy) to fabricate InGrids with this particular gap size. This gap should depend mainly on the gas mixture and slightly on the grid voltage [148] but no systematic study was carried out before. The particular value of this gap is a useful information for all Micromegas-like detectors and is estimated in a P10 mixture.

6.5.2 Measurements

The dependence of the gas gain on the amplification gap thickness was investigated with three prototypes. The detector geometrical parameters are listed in Table 6.11.

The position of the photo-peak from ^{55}Fe conversions is first measured as a function of the field ratio to estimate above which field ratio the collection efficiency is the highest. The trend of the peak position with the field ratio is shown in Figure 6.11 (a) for the three detectors. As expected, a strong dependence of FR^{M} on the grid geometry is observed (Table 6.11).

For each InGrid, the peak position is then measured as a function of the grid voltage and a constant drift field. The drift field is set in order to obtain at each

InGrid	gap (μm)	pitch (μm)	diameter (μm)	FR^{M}
4	57.6 ± 3.0	32.0	18.9 ± 0.5	232
5	45.3 ± 3.0	32.0	15.5 ± 0.5	50
6	68.1 ± 3.0	32.0	22.9 ± 0.5	18

Table 6.11: *Geometrical parameters of the InGrids used for test.*

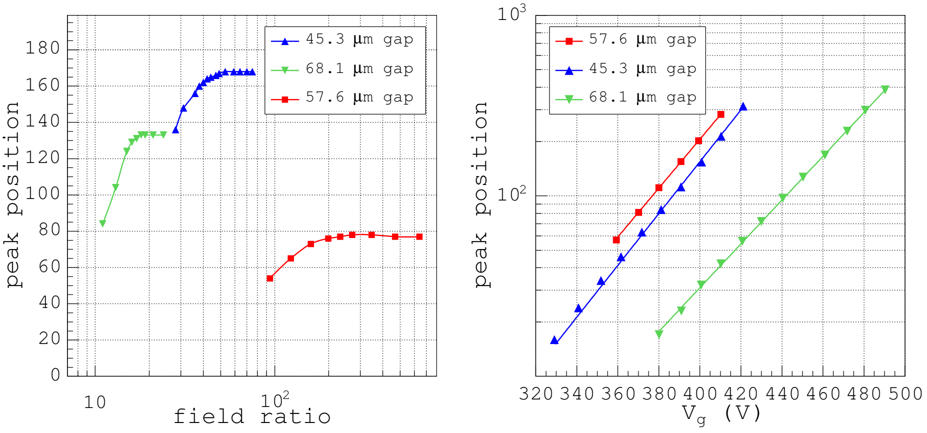

(a) (b)

Figure 6.11: ^{55}*Fe peak position as a function of field ratio (a) and grid voltage (b) measured with detectors of different gap sizes.*

grid voltage a field ratio higher than FR^{M}. At such field ratios, we assume that the peak position is a direct indication of the gain.

The measurements are shown in Figure 6.11 (b) where one observes that the 57.6 μm gap detector exhibits the highest gain. The dependence of the gain with the gap is illustrated in Figure 6.12 where the peak position as measured at a grid voltage of -390 V is plotted against the gap.

The peak position goes through a maximum for a gap between 45.3 and 57.6 μm. The value of this gap is estimated by fitting a parabola to the three points. The hole diameter, however, varies from one detector to the other which also affects the gain and the peak position. For this reason, the peak positions measured with the 45.3 and 68.1 μm gap detectors are corrected for diameter variations using the two-dimensional model of the field presented in [81]. The fit parameters indicate that the gain should be maximum for a gap of about 53 μm.

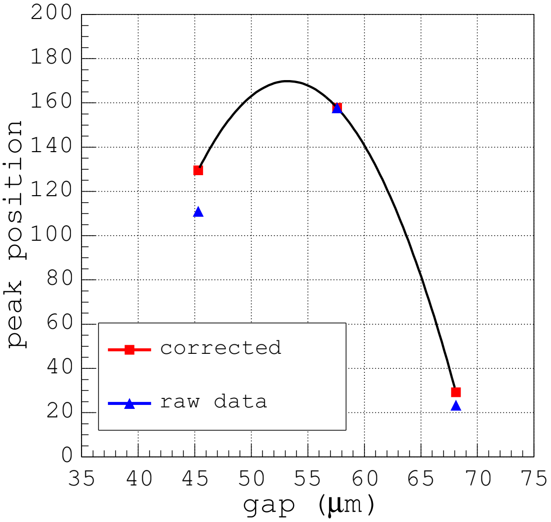

Figure 6.12: *Peak position, corrected for hole diameter variations, at a grid voltage of -390 V for three gap sizes. The data point at 57 µm is used as reference and is not corrected for diameter variations.*

6.5.3 Discussion

Simulation results tend to show that the optimum gap size depends mainly on the carrier gas [206] and hence our finding should be applicable to other Ar-based mixtures. In any case, this study could easily be repeated in other mixtures and with an improved precision if more prototypes of different gaps are available.

In view of a large pixel readout TPC, a few tens of thousand chips should be equipped with a SiProt and an InGrid. If each InGrid should be independently biased the number of power supplies will be unrealistically large (much larger than in a wire-based or Micromegas-based TPC). It will therefore be necessary to put several grids (of slightly different gaps) in parallel. In such a case, the gain compensation effect will help maintaining a uniform detection efficiency across the endplate.

6.6 Energy resolution

6.6.1 Definition

The energy resolution is a measure of how precisely the energy of a radiation stopped in the detector can be determined. Ideally, for a given amount of energy deposited in the gas, the final pulse height read out from the detector would be a delta function. In practice, the energy measurement involves a few processes (*e.g.* gas ionization, electron drift and multiplication, signal readout) which contribute to the pulse height fluctuations. The energy resolution is defined as the relative r.m.s. of the pulse height distribution. Assuming primary and avalanche fluctuations only, it can be expressed directly from the distribution of the total number of electrons N_t (Equations 6.13 and 6.14):

$$R = \frac{\sigma_{N_\mathrm{t}}}{N_\mathrm{t}} = \sqrt{\frac{F+b}{N_\mathrm{p}}} = \sqrt{\frac{W}{E_0}(F+b)} \tag{6.28}$$

Equation 6.28 gives the lower limit of the energy resolution in gas detectors based on electron multiplication. Using typical values of $F = 0.2$, $W = 25$ eV and $b = 0.5$, the minimum resolution at 5.9 keV is 5–6 % RMS. In practice, other sources of fluctuations of N_t may worsen the resolution. For instance: local variations of the gain across the detector surface (due to variations of the amplification gap thickness or the hole diameter), pressure and temperature variations in time which affect the gain and primary electron loss in the field gradient region above the grid due to a limited collection efficiency. With the InGrid fabrication techniques, the gain variations across the grid surface should be very small. During the time it takes to record an ^{55}Fe spectrum (few minutes), pressure and temperature variations can be safely ignored. Concerning the last point, at high field ratios the electron loss on the grid is probably small.

6.6.2 Measurements in various gas mixtures

The energy resolution is determined from the ^{55}Fe spectra used for the gain measurements using the following formula:

$$R = \frac{\sigma_P}{P - P_0} \tag{6.29}$$

where P is the peak position and P_0 the offset. The trend of the resolution as a function of the gain in Ar/CO$_2$ and Ar/iC$_4$H$_{10}$ mixtures is shown in Figure 6.13.

In a given gas mixture, the Fano factor is constant and the trend of the energy resolution should be a direct indication of the gain fluctuations. In all mixtures, the resolution degrades with the gain:

- in Ar/iC$_4$H$_{10}$ mixtures with quencher fractions larger than 2.5 % and in Ar/CO$_2$ mixtures, the degradation is progressive from 5–6 % at gains below 10^3 to 8–9 % at gains of about 10^4;
- in Ar/iC$_4$H$_{10}$ 99/1 the degradation is more abrupt and the resolution exceeds 8 % at a gain of $2{\cdot}10^3$. The resolution is worse in pure argon, reaching 8 % at a gain of 800;
- at equal quencher fractions, the resolution in Ar/CO$_2$ and Ar/iC$_4$H$_{10}$ mixtures is similar.

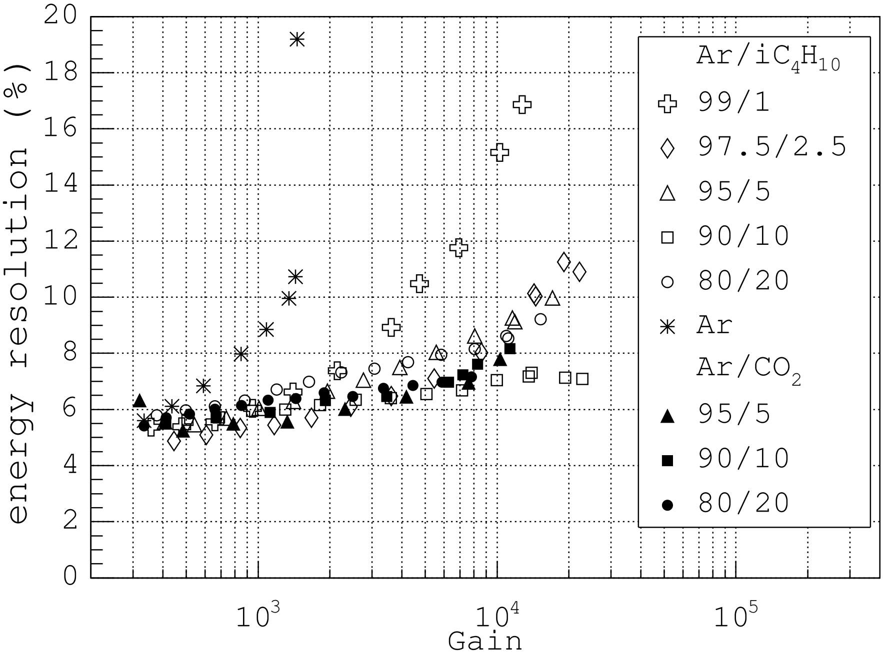

Figure 6.13: *Energy resolution at 5.9 keV and gain in argon-based mixtures.*

The measurements suggest a strong correlation between the gain fluctuations and the quenching of UV photons produced in the avalanche. This statement is assessed in section 6.7 where a simple model of avalanche development with photon feedback is presented.

In mixtures with at least 5 % of quencher gas, the resolution varies between 5 % at gains of a few hundred and 9 % at a gain of 10^4. This roughly translates in gain relative variations of 85–125 % r.m.s. and suggests a transition from a Polya-like to the exponential gain distribution. It will be shown in the simulation section that only the tail of the distribution is affected at high gains. The main feature of the Polya, namely the small probability for weak signals, is maintained. Accordingly, the detection efficiency should benefit from those increased fluctuations at large signals as long as the spark rate is kept at an acceptable level.

Before the fabrication of the 90 μm prototypes, a very good energy resolution of 5.2 % r.m.s. was measured with a 59 μm gap InGrid operated at a gain of $2.5{\cdot}10^3$ in a P10 mixture. The results were reported in [81] and we only show here the measured ^{55}Fe spectrum (Figure 6.14).

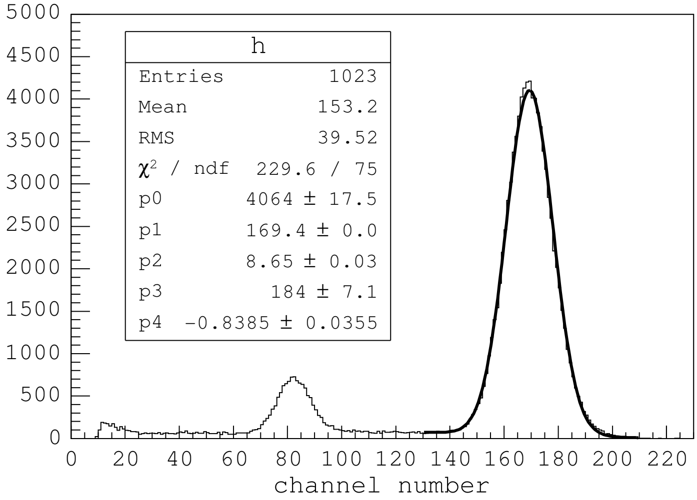

Figure 6.14: ^{55}*Fe spectrum recorded in a P10 mixture. The* K_β *line was strongly absorbed by a 10* μ*m thin Cr foil. The parameters of a gaussian* (p_0–p_2) *and a linear* (p_3, p_4) *function were adjusted to the photo-peak.*

6.7 Simulation of gain fluctuations

6.7.1 Causes of fluctuations

We distinguish between the gain fluctuations at the hole scale and at the grid scale. At the hole scale, three main causes of gain fluctuations can be identified.

- Intrinsic gain fluctuations due to the stochastic nature of the avalanche mechanism.
- Field non-uniformity which is responsible for the variation of the gain as a function of the entrance position of the electron in a grid hole.
- Photon feedback which should extend the tail of the gain distribution.

At the grid scale:

- the grid geometry and eventually the gain distribution may vary from one hole to the other.

InGrids should be affected very little by geometry non-uniformity because the gap size and hole diameter are accurately controlled. I will therefore focus on the variations at the hole scale. A simulation that would integrate the three mentioned effects all together is beyond the scope of this thesis and they will be treated separately. This approach should nevertheless be admissible to estimate their respective contribution to the gain fluctuations.

6.7.2 Intrinsic avalanche gain fluctuations

Gain relative r.m.s.

The Legler model presented in chapter 2 can be used to predict the dependence of the relative gain variations on the field and the gas. Neglecting photon feedback and space-charge effects, the gain relative variance b in a uniform field can be shown to obey Equation 2.41:

$$b = \frac{4e^{-2\chi} - 4e^{-\chi} + 1}{4e^{-\chi} - 2e^{-2\chi} - 1} \tag{6.30}$$

where the parameter χ is given by:

$$\chi = \alpha x_0 = \alpha \frac{U_0}{E} \tag{6.31}$$

The Townsend coefficient is taken from the measured gains corrected for the effect of photon feedback: $\ln(G_0)/g$. In the Legler model, the parameter x_0 is the minimum distance to be traveled by an electron of zero energy before any ionization and hence U_0 is approximated to the gas ionization potential U_i. Yet, in Penning mixtures U_0 should be lower than U_i because the potential of the Penning-allowed excited states are smaller than U_i. As a result, the value of U_0 will be slightly varied between 10 and 15 eV. Over this range, Equation 2.41 predicts that the value of $\sqrt{b}$ lies between 50 and 70 % in all mixtures and depends mainly on U_i, the smaller value being attained for 15 eV. For a given gas and a fixed U_0, the variation of χ (and hence of b) over the experimental range of fields is trifling.

For a direct comparison with the measurements, the energy resolution at 5900 eV is calculated from b using W and F from Table 6.6. The minimum and maximum energy resolution obtained in Ar/iC$_4$H$_{10}$ and Ar/CO$_2$ 80/20 are shown in Figure 6.15 together with some measurements. Although the Legler model is unable to reproduce the measured trend, it gives a good estimate of the energy resolution and hence of the magnitude of the gain fluctuations.

Shape of the gain distribution

The shape of the gain distribution is an important input to predict the single electron detection efficiency of GridPix detectors. In this section, this shape is investigated with a one-dimensional simulation of the avalanche development. The simulation parameters are the gap size g, the distance x_0 and the ionization coefficient a_0 defined in Equation 2.40 which is proportional to the electron ionization probability.

It will be interesting to vary χ over a large range to appreciate its impact of the gain fluctuations. For this purpose, it is preferred to use the Townsend coefficient calculated by MAGBOLTZ rather than the one derived from the measurements, the latter is known over a limited range of fields only. Because MAGBOLTZ does

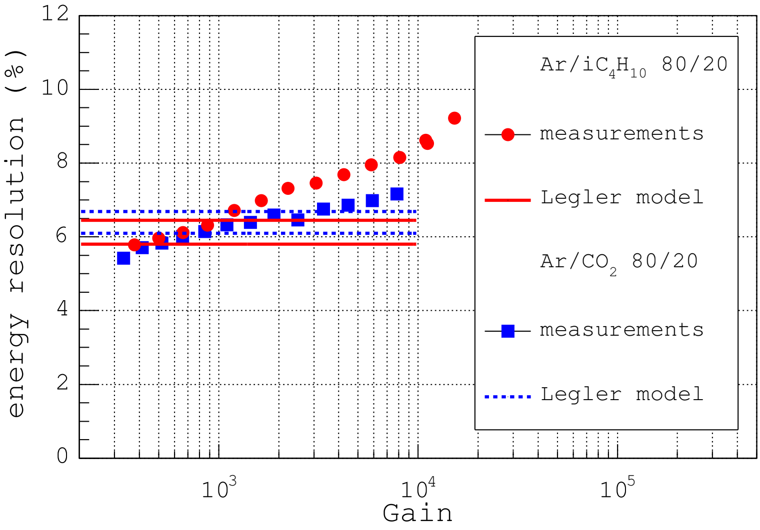

Figure 6.15: *Measured energy resolution at 5900 eV as a function of gain. The simulated lines are calculated for* $U_0 = 10$ *eV and* $U_0 = 15$ *eV, the smaller resolution in a given gas mixture being attained for 15 eV. In the Legler model* U_0 *is approximated to the ionization potential of the mixture. Due to the Penning effect it may decrease down to the lowest Penning-wise excitation potential and the final resolution in a given mixture should lie between the two lines.*

not account for the Penning effect, the simulation parameters are those of an Ar/CO_2 95/5 mixture where this effect was measured to be negligible. Also, in a regular mixture, U_0 should be close to U_i and is set to 15 eV. The simulation of the avalanche development proceeds as follows:

1. one electron is released at $x = 0$;
2. the electron is drifted over a distance x_0, over that distance its ionization probability is zero;
3. at x_0 the ionization probability per unit path length is equal to a_0. The distance to the ionization location x_i is randomly drawn from an exponential distribution of mean $1/a_0$. At this position, a secondary electron is created;
4. steps 2 and 3 are repeated until the electron arrives at the anode;
5. steps 2 to 4 are repeated for all secondary electrons.

This procedure was repeated a few thousand times at different values of the electric field and for different gaps.

When normalized to the mean gain, the gain distributions do not depend on the gap size but only on the parameter χ. Some normalized distributions are shown in Figure 6.16 for various values of χ. The relative variance of the distribution predicted by Equation 2.41 is compared to the one derived from a fit of the Polya function. Similar values are obtained as can be seen in Table 6.12. Because no ionization occurs over the distance x_0, the maximum gain $G_{\max}$ is equal to $\exp(g/x_0)$. As a result, the Polya function which has an exponential tail, fits worse the distributions close to the maximum gains.

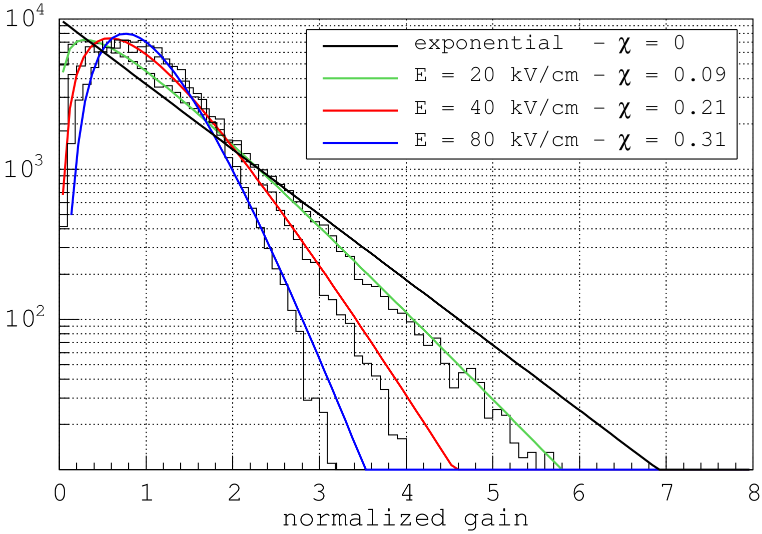

Figure 6.16: *Single electron gain distributions (histograms) in Ar/CO$_2$ 95/5 calculated at various values of the electric field using the Legler model. The Polya function (lines) is fitted to each distribution. The exponential limit of χ = 0 is also shown.*

At 20 kV/cm, $\chi \sim 0.1$ which means that x_0 is roughly one tenth of the mean distance between ionization ($1/\alpha$). The relaxation effect is mild and the ionization probability is almost constant through the electron drift. Nevertheless, even at such low electric field, the single electron response departs from an exponential distribution, with a maximum of two tenth of the mean gain. When the field increases, the maximum of the distribution slides up while the maximum normalized gain decreases. The gain relative r.m.s. reduces down to 50 % at 80 kV/cm.

Discussion

The exponential distribution does not suit the simulated gain distributions, even at low values of field where it was thought to apply well [43]. The distributions are better described by the Polya function which accounts for the maximum at gains

E (kV/cm)	χ	gain rms (%)	
		Polya fit	Equation 2.41
20	0.09	85	83
40	0.21	65	63
80	0.31	49	50

Table 6.12: *Relaxation parameter χ and calculated relative gain r.m.s. at various fields in Ar/CO_2 95/5.*

close to the mean gain. Our model suggests that the gain fluctuations reduce at high electric fields and hence that for a given gain, detectors with a small amplification gap should be preferred. For GridPix detectors, the reduced gain fluctuations would impact on the detection efficiency as illustrated in Figure 6.17. This conclusion should also be valid in other gas mixtures because the Legler model predictions depend very little on the gas composition but mainly on the parameter χ.

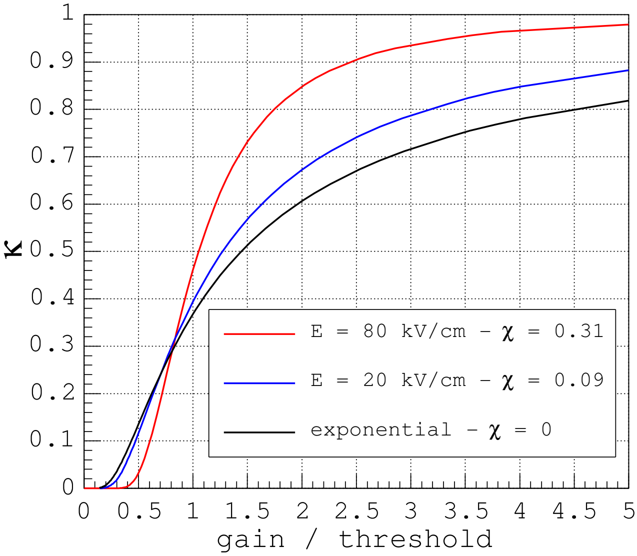

Figure 6.17: *Calculated trend of the detection efficiency κ with the ratio of the gain and the pixel threshold for different shapes of the gain distribution. The exponential limit of χ = 0 is also shown.*

6.7.3 Field uniformity

For a given grid thickness, the amplification field uniformity depends on the hole diameter and the gap size. The field is uniform when the diameter is small with respect to the gap size. At larger diameters, the field in the center of the hole becomes less than that on the edges. Accordingly, the average gain decreases towards the center and its variance over the hole may contribute to the overall gain fluctuations.

The gain dependence on the electron entrance position in the hole was studied for different grid geometries by means of the two-dimensional model of the field presented in [81]. Geometries with 50, 75 and 100 μm gap and various hole diameters were investigated. The hole pitch was 100 μm and the diameters were varied between 10 and 82 μm. The grid voltage and drift field were kept at -400 V and 500 V/cm respectively. The gas parameters are those computed by MAGBOLTZ in Ar/iC$_4$H$_{10}$ 95/5. In this mixture, the computed Townsend coefficients are lower than the measured ones, yet, in our experimental conditions α is proportional to the field and mainly the trend of α with the field matters. The measured trends being only slightly steeper than those predicted by MAGBOLTZ, the simulation results should be valid for all the mixtures used.

Electrons are released one by one at a distance above the grid where the field is uniform and tracked until they hit an electrode. The gains, calculated as the integrals of the effective Townsend coefficient along the drift lines, and the positions at which the electrons cross the grid plane are recorded. The gain relative r.m.s. σ_G/G is calculated from the trend of the gain with the distance from the center of the hole $G(r)$. For instance, the gain variance is given by:

$$\sigma_G^2 = \overline{G^2} - \overline{G}^2 = \frac{1}{d}\int_{-d/2}^{d/2} G(r)^2 p(r) dr - \left(\frac{1}{d}\int_{-d/2}^{d/2} G(r) p(r) dr\right)^2 \tag{6.32}$$

where $p(r)$ is the electron entrance distribution that we take to be uniform across the hole due to a lack of knowledge. The results are shown in Figure 6.18 where the gain r.m.s. is plotted against the ratio of the gap to the diameter g/d.

We observe that the gain variations over the hole decrease with the ratio g/d as the field uniformity improves. When the gap and diameter are equal, the resulting gain variation is of about 30 % r.m.s. while it drops below 5 % for $g/d \geq 4$. This study does not take into account the focusing of the electron towards the center of the hole. This should reduce the gain fluctuations and hence, the obtained gain variations are upper limits. Still, the condition $g/d \geq 4$ is useful as a design rule.

Maximum gains at constant grid voltage are achieved with gaps of 50–55 μm. With such a gap, the field should be sufficiently uniform if the hole diameter is smaller than 12–14 μm. From the measured trends of the peak position with the field ratio with 90 μm gap InGrids, it appears that the collection efficiency suffers from such small holes. Yet, large field ratios are more easily achieved with smaller gaps which finally may improve the collection efficiency.

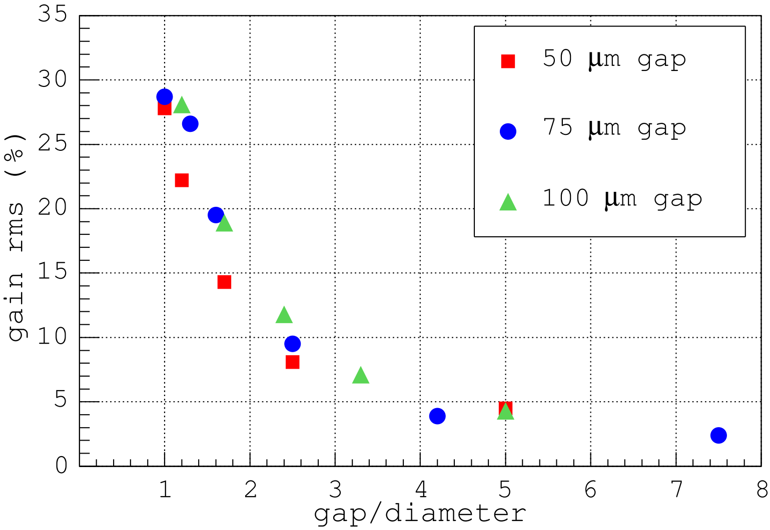

Figure 6.18: *Trend of the gain relative r.m.s. with the ratio of the amplification gap to the hole diameter calculated for geometries of different gap.*

6.7.4 Photon feedback

Introduction

The gain statistics without photons was studied with the Legler model. In this section I estimate the impact of photon-induced secondary avalanches on the gain distribution. A complete simulation of the photon feedback would require the knowledge of the following points.

- The distribution of the distances between inelastic collisions. In the case of excitation of the gas molecules, the photon spectrum should be known (emission probabilities and energies).
- The mean free path for total absorption and ionization of the emitted photon on the various detector materials (gas, pillars, grid).
- The geometry of the grid and the pillars.
- The quantum yield (for the photo-electric effect) of the grid at the energies of the emitted photons.

These points and the model hypothesis are discussed below.

Distance between inelastic collisions

The mean distance between electron ionizations λ_i is derived from the measured gain without photons G_0. For simplicity I take $\chi = 0$: the ionization probability is constant over the electron drift and the distances between consecutive ionizations are exponentially distributed.

Quencher gases have mainly non-radiative de-excitation modes and I hence assume that the photons are only emitted by the argon atoms. The emission of a UV photon results from a direct transition of the atom from an excited state to the ground state. Considering the main levels of the argon atom (S, P and D), the energy of the emitted photons should lie between 11–14 eV [205]. For simplicity I assume a single energy at 12 eV. Alike ionizing collisions, the distribution of the distances between the emission locations of the photons is taken to be exponential. The mean distance λ_p is a parameter of the model.

Photon absorption

The absorption of UV photons by gas impurities or argon atoms is not considered. Moreover, quencher gases have a large cross-section for photo-absorption and most of the photon/quencher interactions should be non-ionizing. I hence neglect the photo-ionization of the quencher molecules. Eventually, UV photons are either absorbed at the grid, the pillars or by the quencher. The photon mean free path for absorption λ_a is a parameter of the model.

Detector geometry and quantum yield

The pillar and grid geometries are those of InGrid F11 which was used for the gain and the energy resolution measurements. Because of the low atomic number of SU8 molecules the quantum yield (for the photo-electric effect) of the pillars should be negligible. Accordingly, photo-electrons are only released from the grid. The quantum yield Q of the grid is a parameter of the model.

Simulation steps

Photon feedback is a three-dimensional process and the simulation takes into account the pillar and grid geometries. For simplicity, however, the electron transverse diffusion is neglected and the avalanches develop along a vertical axis parallel to the grid hole axis (z-axis). The grid xy-plane is at $z = 0$ and the anode plane at $z = g$. For a given set (λ_i, λ_p, λ_a, Q) of the model parameters, the simulation proceeds as follows:

1. one starts with one electron at $z = 0$ in the center of a grid hole;

2. the electron is drifted over a distance z_t randomly drawn from an exponential distribution of mean λ_t:

$$1/\lambda_{\rm t} = 1/\lambda_{\rm i} + 1/\lambda_{\rm p} \tag{6.33}$$

At $z = z_{\rm t}$, the relative probabilities for ionization and photon emission are calculated as $\lambda_{\rm t}/\lambda_{\rm i}$ and $\lambda_{\rm t}/\lambda_{\rm p}$. The outcome of the collision is decided by drawing a random number r distributed between 0 and 1;

3. if $\mathrm{r} \leq \lambda_{\rm t}/\lambda_{\rm i}$, a new electron is created at $z_{\rm t}$;

4. if $\mathrm{r} > \lambda_{\rm t}/\lambda_{\rm i}$, a photon is emitted in a direction randomly chosen over 4π. If the photon is emitted in the 2π solid angle in the direction of the anode or in the direction of a pillar, it is abandoned.

   When emitted in the direction of the grid, the distance that the photon would travel before absorption in the gas is drawn from an exponential distribution of mean $\lambda_{\rm a}$. If this distance is smaller than the distance to the grid, the photon is absorbed in the gas, otherwise at the grid.

   The probability of releasing a photo-electron from the grid is equal to the quantum yield Q. If $\mathrm{r} \leq Q$ where r is uniformly distributed between 0 and 1, an electron is created at $z = 0$ and at the (x,y) position where the trajectory crosses the grid;

5. steps 2 to 4 are repeated until the initial electron arrives at the anode;

6. steps 2 to 5 are repeated for all secondary electrons.

In a given gas mixture and at a given value of the electric field, the mean distance between electron ionizations is derived from the measured gain corrected for photon feedback G_0:

$$\lambda_{\rm i} = 1/\alpha = g/\ln(G_0) \tag{6.34}$$

For given values of $\lambda_{\rm i}$ and Q, the mean distance between photon emission $\lambda_{\rm p}$ is adjusted so as to reproduce the measured gain $G = G_0/(1\text{-}\gamma G_0)$. The simulation is hence repeated until the mean of the calculated gain distribution is close to the measured gain.

Model results, impact of $\lambda_{\rm p}$, $\lambda_{\rm a}$ and Q

I first investigated the dependence of the gain distribution on the parameters $\lambda_{\rm p}$, $\lambda_{\rm a}$ and Q for a given gas at a given field (*i.e.* $\lambda_{\rm i}$ and G are fixed). The gain distribution was calculated for several values of those parameters.
The conclusion is that any set of $(\lambda_{\rm p},\lambda_{\rm a},Q)$ that yields a similar mean gain also yields a similar gain r.m.s. because the mean number of photo-electrons released from the grid $N^0_{\rm pe}$ during the first avalanche is similar. This number is equal to γG_0. In other words, an increased production rate of photons (smaller $\lambda_{\rm p}$) has a similar effect on the gain distribution than a reduced mean free path $\lambda_{\rm a}$ or a

reduced quantum yield Q. As a result, the individual choice of (λ_p,λ_a,Q) is not crucial as soon as the measured gain is reproduced by the simulation.

Model results, impact of λ_i and G

In a second time, I investigated the dependence of the gain distribution on the gas mixture, using various values of the gain parameters λ_i and G. Now, (λ_p,λ_a,Q) are kept constant such that the simulated gain is equal to G. The gain now varies from one simulated distribution to the other, still any set of (λ_i,G) that yields a similar mean number of photo-electrons also yields a similar gain relative r.m.s..

Model results, single electron response

These two observations strongly suggest that the effect of the photon feedback on the gain fluctuations can be accounted for by a single parameter: the number of photo-electrons produced in the first avalanche $N^0_\mathrm{pe} = \gamma G_0$. Single electron gain distributions are shown in Figure 6.19 for various values of N^0_pe. For easier comparison, the distributions are normalized such as to have a mean value of 1 and an integral of 1. The distribution tail extends to larger gains when N_pe increases, resulting in larger gain fluctuations. In case of negligible photon feedback ($N_\mathrm{pe} = 0$), the simulated gain distribution is an exponential because the relaxation effect was not taken into account ($\chi = 0$).

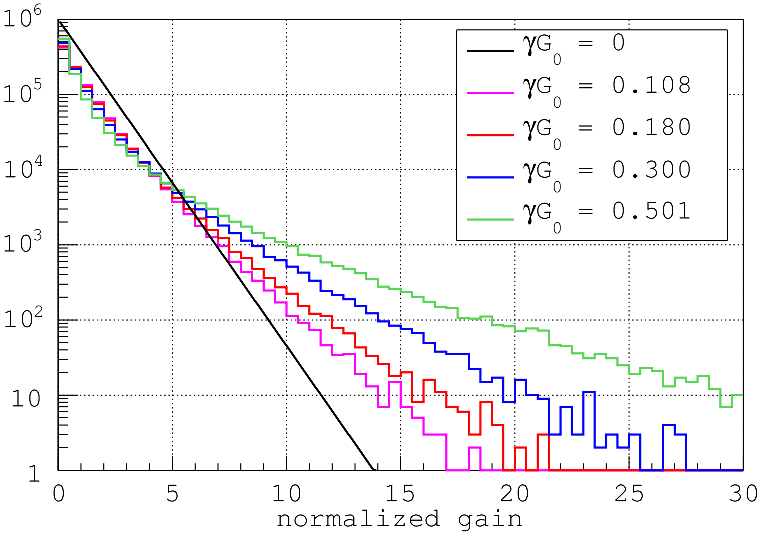

Figure 6.19: *Calculated single electron gain distributions for various values of the mean number of photo-electrons produced in the first avalanche* $N_\mathrm{pe} = \gamma G_0$*. The distribution with no photon feedback and with* $\chi = 0$ *is a decreasing exponential and is also shown.*

Comparison to measurements

The simulation predictions are compared with measurements of energy resolution at 5.90 keV performed in various gas mixtures. From the measured resolutions, single electron gain relative r.m.s. are determined using Equation 6.28 assuming a Fano factor of 0.3 and 220 primary electrons. The exact values of F and N_{p} are not crucial as the simulation only predicts the trend of the gain variations with γG_0.

The variations of the gain r.m.s. as a function of γG_0 in argon and poorly quenched mixtures are shown in Figure 6.20, together with the simulated trend. As expected, the absolute values depart from the predictions but, considering the many assumptions of our model, the gain r.m.s. variations agree very well with the simulated trend.

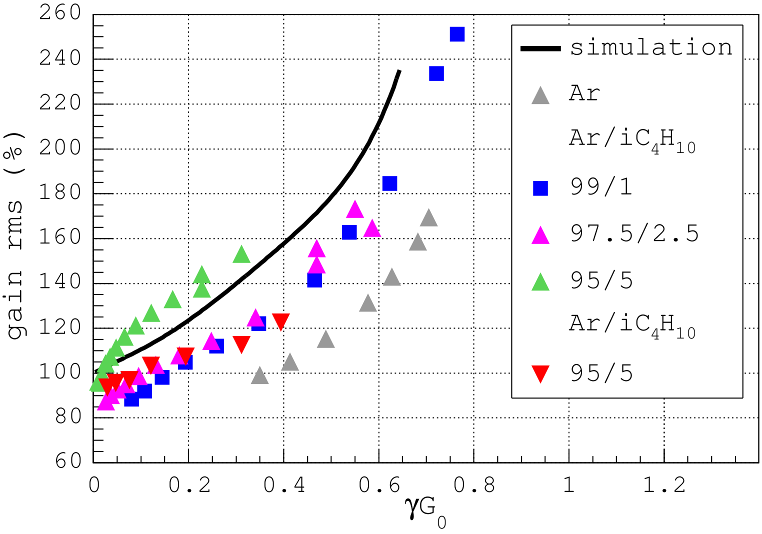

Figure 6.20: *Gain r.m.s. and mean number of photo-electrons produced in the first avalanche* $N_{\mathrm{pe}} = \gamma G_0$*. The points are deduced from measurements of energy resolution at 5.9 keV and follow the simulated trend.*

6.7.5 Summary

We estimated the contribution from various sources to the gain fluctuations of Micromegas-like detectors.

- In high uniform fields and in mixtures of a noble and quencher gases, the single electron response depends little on the gas composition and mainly on the field strength. At the typical fields of Micromegas-like detectors, the gain distribution is satisfactorily described by the Polya distribution with a relative r.m.s. of 50–70 %.
- The gain variations from field non-uniformity depend on the ratio g/d and should be at most 5 % when $g/d \geq 4$.
- The impact of photons feedback on the gain fluctuations can be simply modeled by means of the number of photo-electrons liberated from the grid in the first avalanche N^0_{pe}. When $N^0_{\mathrm{pe}} = 0$, the gain distribution can be predicted by the Legler model. When N^0_{pe} increases, the distribution tail gets longer and the gain r.m.s. increases from 100 % at $N^0_{\mathrm{pe}} = 0$ up to 180 % at $N^0_{\mathrm{pe}} = 0.5$. These values should be smaller if the relaxation effect is taken into account ($\chi > 0$).

6.8 Conclusion

Measurements of the amplification properties of InGrid detectors in Ar/CO_2 and Ar/iC_4H_{10} mixtures were reported and are in good agreement with similar measurements with standard Micromegas.

At a given grid voltage, the signal drops above a certain drift field due to a loss of electrons on the grid. That drift field depends on the grid geometry and lies between 700–2000 V/cm for most tested geometries. These values are larger than the typical drift fields encountered in TPCs of a few meters lengths and are therefore not an inconvenient.

Maximum gains between 10^4 and $2{\cdot}10^4$ were reached depending on the gas mixture. In principle, these are sufficient to reach a single electron detection efficiency of at least 90 % in all tested mixtures. Still, due to the photon feedback, mixtures with quencher fractions lower than 5 % are more prone to sparking and should be avoided.

A strong Penning effect is suspected to take place in Ar/iC_4H_{10} mixtures, especially at low quencher fractions. Hence, a given detection efficiency would be reached at a lower grid voltage in Ar/iC_4H_{10} mixtures than in Ar/CO_2 ones where the Penning effect is less effective. The chance that the grid is damaged by a discharge increases with the grid voltage and therefore Ar/iC_4H_{10} mixtures are preferred in this respect. Eventually, a mixture of Ar/iC_4H_{10} 95/5 should be well suited to benefit from the Penning effect while providing enough quenching of the photons.

The gain of Micromegas-like detectors exhibits, for a given grid voltage, a maximum as a function of the gap thickness. The value of this gap should depend mainly on the carrier gas and was measured to be close to 53 μm in an Ar/CH$_4$ 90/10 mixture. GridPix detectors should be fabricated with such a gap size to reduce the gain sensitivity to possible gap variations.

The energy resolution is similar in the gas mixtures used and depends mainly on the gain. It is close to 6 % r.m.s. (for 5.9 keV X-rays) at a gain of 10^3 and degrades at larger gain because of photon feedback. The degradation is more abrupt in mixtures with poor quenching.

Gain fluctuations partly determine the single electron efficiency of pixel readout gas detectors and modeling results on this subject were presented. They indicate that the gain distribution is Polya-like: small signals are rare and the detection efficiency is better than what is expected from an exponential distribution. The tail of the distribution should be longer than that of the Polya if the photons are not properly quenched. Photon feedback should actually improve the detection efficiency but at the price of an increased spark probability.

Chapter 7

Ion backflow properties of InGrid detectors

I report in this chapter on measurements of the ion backflow fraction of integrated Micromegas detectors performed in a P10 gas mixture. I first recall the issues related to the ion backflow in TPCs and discuss the performance of MWPCs and MPGDs in this respect. A detailed account on the ion backflow properties of Micromegas-like detectors is given next. In particular, a simple model of the field and the avalanche development is proposed. The measurements are then presented and confronted to the model predictions.

7.1 Introduction

The ion backflow is the drift of the positive ions produced in the avalanche, from the amplification region to the cathode plane. In TPCs operated at high particle rates the space charge of the backflowing ions may modify the electron drift by locally disturbing the electric field. The number of backflowing ions should therefore be kept below a certain value.

The field line configuration of wire-based TPCs in the vicinity of the sense wires is such that roughly half of the ions produced in an avalanche drifts to the cathode pad plane. To prevent the other half from drifting to the central plane, such TPCs incorporate a gating grid which collects the ions before they enter the drift region. This technique was applied for instance in the TPCs of the ALEPH, DELPHI and STAR experiments [207, 128, 208].

GEM and Micromegas are grids with hole pitches of a few tens of microns. Due to the field gradient between the drift and the amplification region and the periodic hole pattern, the field lines from the cathode plane are compressed in the vicinity of the grid holes and form a funnel of a few microns width in the amplification region. As a result, an electron approaching the grid is focused towards the center of a hole and produces an avalanche which develops inside the funnel. Due to transverse diffusion, the avalanche also develops outside the funnel. Yet, the avalanche transverse extension is larger than the funnel size and only a small fraction of the ions drifts back to the cathode plane. The backflow fraction of GEM and Micromegas is therefore smaller than that of wire-based TPCs.

In the case of multi-GEM detectors, measurements performed with triple and four GEMs have shown backflow fractions of two per mil and below one per mil respectively [209, 210]. In typical biasing conditions, Micromegas detectors exhibit a backflow fraction of the order of one percent. With a well-chosen grid geometry and at low drift fields, this fraction can be easily lowered to the per mil level [147].

Although the ion backflow has been studied with standard Micromegas, it is still very interesting to measure it with InGrids for the following reasons. First, because of the thinner grid, the field in the vicinity of the InGrid holes may be different which eventually may result in different ion backflow properties. Secondly, the freedom in the choice of hole pitch, diameter and gap size can be exploited to investigate in detail the relation between the backflow fraction and the InGrid geometry. Also, it provides a good test for a model.

7.2 Backflow fraction of Micromegas detectors

7.2.1 Ion backflow fraction without ion diffusion

The ion backflow fraction can be defined as:

$$BF = \frac{N_{\mathrm{b}}}{N_{\mathrm{t}}} \tag{7.1}$$

where N_{t} is the average total number of ions produced in an electron avalanche and N_{b} the average number of backflowing ions. The simplest way to obtain N_{b} is to assume that ions do not diffuse and follow precisely the field lines. This assumption is essential to treat the backflow phenomenon as purely geometric. Neglecting ion diffusion, Equation 7.1 can be expressed as:

$$BF = \frac{\int_{V_{\mathrm{b}}} f(x,y,z)\mathrm{d}V}{\int f(x,y,z)\mathrm{d}V} \tag{7.2}$$

where $f(x,y,z)$ is the density distribution of the ions in the amplification region and depends on the avalanche development. The volume V_{b} is such that any ion produced inside this volume will eventually be collected at the central plane. The integral over V_{b} is therefore equal to the number of backflowing ions. The integral of the denominator is performed over all space and is equal to the total number of ions N_{t}. Accordingly the backflow fraction depends on the field configuration and the spatial development of the avalanche.

7.2.2 Field configuration

Due to the field gradient in the vicinity of the grid holes, the field lines compress at the entrance of the amplification region. A cross-section of the periodic pattern of funnel-shaped field lines is shown in Figure 7.1 (a) where the trajectories of some ions produced at the anode are drawn. The trajectories that join the anode to the cathode define the volume V_{b} of Equation 7.2: V_{b} is the volume contained inside the funnels.

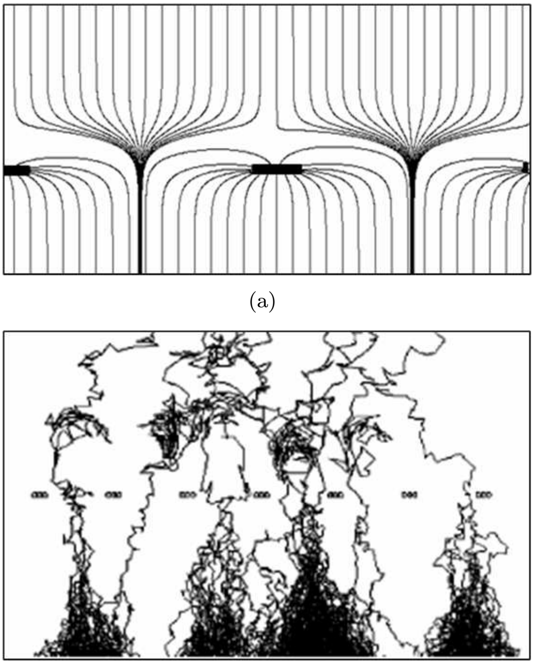

(a)

(b)

Figure 7.1: *Drift lines of ions produced at the anode (the diffusion is neglected) (a). Avalanche development calculated by the program GARFIELD (b) [206].*

The volume V_{b} can be expressed as a function of the fields and the grid hole pitch. We first consider the flux of the electric field through the volume contained inside one funnel of field lines. According to Gauss' law:

$$\int_{S_{\mathrm{D}}} \vec{E} \cdot \vec{dS} + \int_{S_{\mathrm{A}}} \vec{E} \cdot \vec{dS} = 0 \tag{7.3}$$

where S_D and S_A are the funnel cross-section areas at the cathode and at the anode. Close to these electrodes, the amplification field and the drift field are uniform and Equation 7.3 reduces to:

$$E_\mathrm{D} S_\mathrm{D} - E_\mathrm{A} S_\mathrm{A} = 0 \tag{7.4}$$

In terms of the field ratio *FR*, the funnel cross-section area at the anode is:

$$S_\mathrm{A} = S_\mathrm{D}/FR \tag{7.5}$$

If the field ratio is large enough, all field lines leaving the cathode enter the amplification region and S_D is maximum. In those conditions and for a square pattern of hole, S_D is equal to the square of the hole pitch p and S_A is given by:

$$S_\mathrm{A} = p^2/FR \tag{7.6}$$

If we assume that the amplification field is uniform throughout the amplification region, the funnel cross-section area in this region is constant. This is not true close to the grid where the field decreases and the funnel cross-section area gets larger. A small fraction of the total number of ions, however, is created in this region and the field there should impact very little on the integral of the numerator of Equation 7.2. Assuming too that the funnel cross-section in the amplification region is circular, S_A is contained inside a circle of radius:

$$R = \left(\frac{S_\mathrm{A}}{\pi}\right)^{1/2} = \left(\frac{p^2}{FR}\frac{1}{\pi}\right)^{1/2} \tag{7.7}$$

The shape of the funnel cross-section depends on the hole pattern which, for all tested InGrid geometries, is square. The program MAXWELL3D was used to calculate the three-dimensional field of a geometry of square hole pattern [211]. It was then checked that the funnel cross-section in the amplification region is indeed circular.

As a conclusion the funnel in the amplification region is a cylinder of height g (the gap size) and of radius given by Equation 7.7. The volume V_b in the amplification region is composed of an array of such cylinders.

7.2.3 Avalanche development

An electron avalanche is a stochastic process: the avalanche development of two primary electrons entering the amplification region at the center of a hole will be different. This means that the final avalanche size and the spatial distribution of electron–ion pairs vary from one avalanche to the other. The average size and ion spatial distribution, yet, can be described by an analytical formula.

In this chapter the magnetic field is not taken into account because its influence on the ion backflow in Micromegas detectors was measured to be negligible [147]. If one neglects the role of photons, insulating pillars, space charge effects and

assumes a uniform electric field throughout the amplification region, any avalanche grows exponentially towards the anode along the hole axis (z-axis) and expands laterally and longitudinally because of the electron diffusion (Figure 7.1 (b)).
In the region where the avalanche develops, the funnel cross-section area is constant. Because the ion diffusion is neglected, the number of backflowing ions does not depend on the distance from the anode at which they are created. Accordingly, the electron longitudinal diffusion does not affect the number of ions inside the funnel and is ignored in the following.

We work in a cylindrical frame with origin at the center of the hole and consider an avalanche initiated by a single electron that crosses the grid plane at a distance r_0 from the center of the hole. At a distance z_0 from the grid plane, the normalized ion density distribution in the $r\varphi$-plane is the following gaussian function:

$$f_{r_0}(r) = \frac{1}{2\pi\sigma_{\mathrm{t}}^2} \cdot \exp\left(-\frac{1}{2}\left(\frac{r-r_0}{\sigma_{\mathrm{t}}}\right)^2\right) \tag{7.8}$$

where σ_{t} is given by the diffusion: $\sigma_{\mathrm{t}} = D_{\mathrm{t}}\sqrt{z_0}$. Taking into account the exponential development of the avalanche along the hole axis, the three-dimensional distribution can be written as:

$$f_{r_0}(r,z) = \frac{C}{2\pi D_{\mathrm{t}}^2 z} \cdot \exp\left(-\frac{1}{2}\left(\frac{r-r_0}{D_{\mathrm{t}}}\right)^2 \frac{1}{z}\right) \cdot (\exp(\alpha z) - 1) \tag{7.9}$$

where α is the Townsend coefficient and C is a normalization constant such that the integral of f_{r_0} over all space is equal to the total number of ions $N_{\mathrm{t}} = \exp(\alpha z)$. A two-dimensional and one-dimensional view of the distribution are shown in Figure 7.2.

The collected primary electrons cross the grid plane with a certain distribution $g(r_0,\varphi)$ and the average ion density distribution is:

$$F(r,z) = \int_0^{2\pi} \int_{-d/2}^{d/2} g(r_0,\varphi) f_{r_0}(r,z) \mathrm{d}r_0 (r_0 \mathrm{d}\varphi) \tag{7.10}$$

where d is the hole diameter. The distribution $g(r_0,\varphi)$ depends on the shape of the field lines (field ratio and grid geometry) and the electron diffusion in the region where the field lines are compressed. It is not precisely known and therefore we use a delta function peaked at the center of the hole.

As a conclusion, the average ion density distribution is approximated by Equation 7.9 with $r_0 = 0$. In what follows, the index r_0 is not useful and is dropped.

7.2.4 Backflow fraction, grid geometry and fields

The ion backflow fraction can now be expressed as the three-dimensional integral of function 7.9 over the volume V_{b} which is composed of an array of cylinders of height g and radius R:

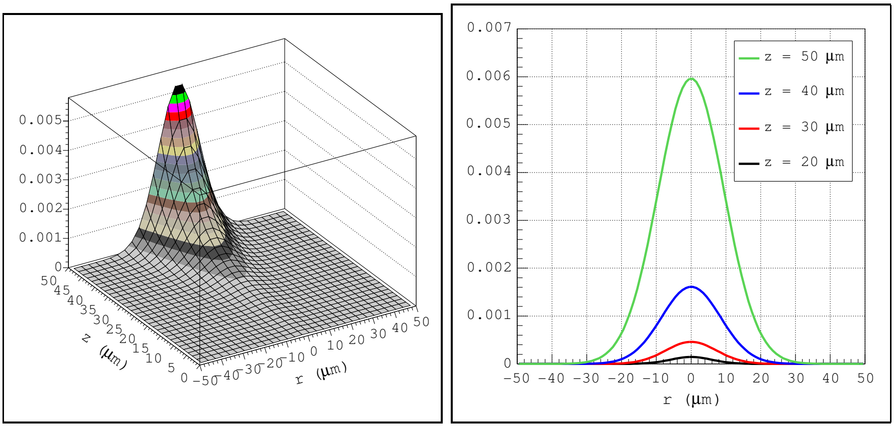

(a) (b)

Figure 7.2: *Ion density distribution normalized to one, in the rz-plane (a) and in the r-plane at various distances from the anode (b). The distribution is calculated with* $r_0 = 0$ *and for a gap size of 50* μ*m and a field of 80 kV/cm in P10 (*α *= 1530 cm*$^{-1}$*,* D_t *= 134* $\mu\mathrm{m}/\sqrt{\mathrm{cm}}$*).*

$$BF = \frac{1}{N_\mathrm{t}} \sum_{\mathrm{funnels}} \int_0^{2\pi} \int_0^{g} \int_0^{R} f(r,z) \cdot \mathrm{d}r\mathrm{d}z(r\mathrm{d}\varphi) \tag{7.11}$$

which, because of the cylindrical symmetry, reduces to:

$$BF = \frac{2\pi}{N_\mathrm{t}} \sum_{\mathrm{funnels}} \int_0^{g} \int_0^{R} f(r,z) \cdot r\mathrm{d}r\mathrm{d}z \tag{7.12}$$

The number of funnels over which the integral is performed should in principle be infinite. Still, for practical calculations, it can be restricted to a certain number that depends on the transverse spread of the avalanche.
The total number of ions is:

$$N_\mathrm{t} = 2\pi \int_0^{g} \int_0^{+\infty} f(r,z) \cdot r\mathrm{d}r\mathrm{d}z \tag{7.13}$$

From Equations 7.11 to 7.13, the following predictions can be drawn:

1. when the transverse spread of the avalanche is small w.r.t. the hole pitch, the avalanche develops below one hole only. At field ratios such that the funnel radius is small w.r.t. the avalanche spread, the integral of Equation 7.12 in the $r\varphi$-plane can be replaced by a product. In the two-dimensional limit (neglecting the longitudinal development):

$$BF \propto \left(\frac{R}{\sigma_{\mathrm{t}}}\right)^2 \tag{7.14}$$

Using Equation 7.7 one obtains:

$$BF \propto \frac{1}{FR}\left(\frac{p}{\sigma_{\mathrm{t}}}\right)^2 \tag{7.15}$$

This approximate equation predicts that BF decreases with the field ratio FR and with p^2 as both relate to the funnel radius. Also, the $1/\sigma_{\mathrm{t}}^2$ dependence of BF can be explained by the fact that the number of ions inside the funnel decreases with the avalanche width squared;

2. when the transverse spread becomes comparable with the hole pitch, some ions should drift through the neighboring holes. Even if less ions would drift through the central hole, more would do so through the surrounding ones. Hence, the backflow fraction should still decrease with the field ratio but should become much less sensitive to σ_{t}/p. Numerical calculations in the two-dimensional limit have shown that, in fact, the total number of backflowing ions remains the same and BF becomes independent of σ_{t}/p. This is predicted for values of σ_{t}/p larger than 0.5 [147].

These predictions will be confronted to the measurements in the next section.

7.3 Backflow fraction measurements

7.3.1 Goal and constraints

Considering the InGrid detector under irradiation, if there are no electron or ion losses in the drift region, the backflow fraction can be measured as:

$$BF = \frac{I_{\mathrm{C}} - I_{\mathrm{P}}}{I_{\mathrm{A}}} \tag{7.16}$$

where

- I_{C} is the current that flows between the ground and the cathode, it is proportional to the number of ions collected on the cathode and is referred to as the cathode current;

- I_{P} is equal to the cathode current without amplification, it is proportional to the number of primary ions collected on the cathode and is referred to as the primary current;

- I_A is the current that flows between the anode and the ground, it is proportional to the number of electrons collected on the anode. It is referred to as the anode current.

The numerator and denominator of Equation 7.16 should respectively be proportional to the number of backflowing ions and to the total number of ions produced in the amplification. Accordingly, the measurement of the backflow fraction requires:

- a radiation source strong enough for primary currents to be measured. We therefore used an X-ray tube;

- a high detector gain G and a precise cathode current monitor. At a field ratio of several hundred, a backflow fraction BF of a few per mil is expected and the difference I_C-I_P = $I_P(G{\cdot}BF\text{-}1)$ is small.

However these points are hard to satisfy with an InGrid detector because the grid area is small (3.14 cm^2) and the grid can easily be damaged by sparks:

- the 1 μm thin aluminum grid can be locally vaporized during a gas discharge. A high gas gain and an intense X-ray flux should hence be avoided in order to keep the discharge probability to a minimum;

- the diameters of the cathode and the grid are 10 and 2 cm respectively (see section 7.3.2) which restricts the X-ray energy to some 10 keV. The range of electrons of higher energies would be too large for the primary ionization to be fully collected on the grid. This also implies that the X-ray beam should be collimated to a few mm^2 area;

- above a certain ion density in the drift region, space charge effects can worsen the field uniformity. As a result, electrons can be directed outside the grid area. Also, backflowing ions can recombine with the primary electrons.

  These effects are observed as a saturation of the anode current while raising the detector gain and depend on the primary electron density (X-ray tube current and voltage), the backflowing ion density (gas gain and backflow fraction) and the ion drift velocity (drift field).

Eventually, the measurements should be performed at low gas gains with a mild energy low intensity collimated photon source. In those conditions, currents of tens of nanoamperes and picoamperes are flowing between anode and ground and cathode and ground respectively, which calls for a precise monitoring of the cathode current.

7.3.2 Experimental set-up

The measurements are performed using an X-ray tube delivering photons of energies up to 12 keV at a variable intensity [212]. The photons are collimated to a 4 mm diameter beam by means of a 18 mm thick perforated metal plate placed on the 5 μm thin mylar window of the detector (Figure 7.3).
A 20 mm diameter InGrid (built on a 20 × 20 mm^2 square Si substrate) is placed on the chamber baseplate and surrounded by a guard ring electrode. That electrode is meant to extend the grid potential beyond the grid edges in order to improve the field uniformity in the drift region and hence the electron collection efficiency. The InGrid is equipped with two bond pads for contacting the anode and the grid. Finally, a 1 cm drift gap is defined by placing a 10 cm diameter stainless steel cathode mesh 1 cm above the grid.

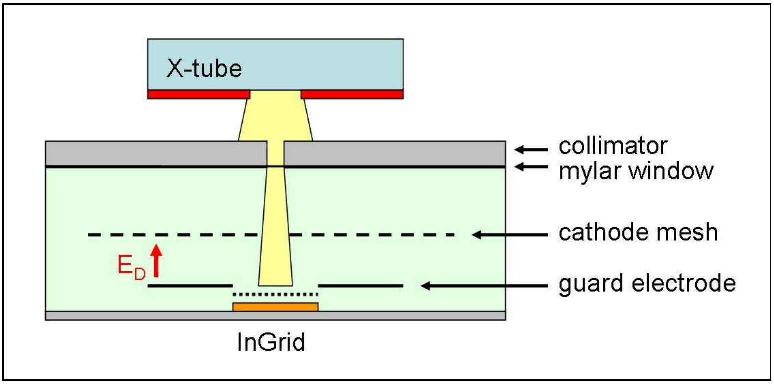

Figure 7.3: *Drawing of the experimental setup.*

The ion currents are calculated by measuring the voltage drops across resistors placed in series with the electrodes. In order to minimize the current flowing through the voltmeters (and make a precise measurement), the latter should have an input impedance much larger than the resistance they are connected to. Hence, a 100 MΩ input impedance TENMA voltmeter [213] is placed in parallel with a 10 MΩ resistor connected to the anode. Also, a 1 GΩ input impedance PREMA voltmeter [214] is used for the two 45 MΩ resistors placed in series with the cathode (Figure 7.4). The anode and cathode currents measured this way are under-estimated by 10 % and are corrected for this error.

The detector was initially biased with negative high voltage on the cathode and the grid, the anode connected to ground. In this configuration, the cathode current was changing with time. This instability was explained as an additional contribution to the cathode current from ions created between the detector window and the cathode. This problem was solved by setting the cathode to ground potential and the grid and anode to positive high voltages. Beside this, two RC-

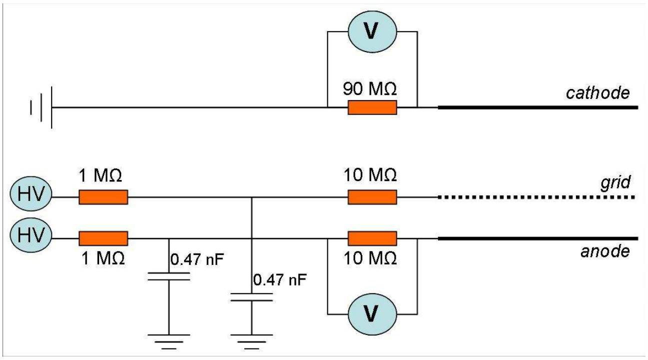

Figure 7.4: *Readout circuitry of the test chamber.*

filters are placed between the HV supplies and the grid and anode (Figure 7.4).

All the measurements are performed in a P10 mixture available from a premixed bottle.

7.3.3 Detectors and operating conditions

Several InGrids of three different amplification gap sizes (45, 58 and 70 μm) and of various hole pitches (20, 32, 45 and 58 μm) and diameters were fabricated.

The detector gains are kept low, between 200 and 400, in order to reduce the ion density in the drift region and the discharge probability. InGrids of equal gap sizes are operated at the same voltage differences between the grid and the anode, and thus, at approximately equal gains.

The operating conditions and the gas parameters are listed in Table 7.1; the measured geometrical parameters appear in Table 7.2.

g (μm)	ΔV (V)	E_A (kV/cm)	D_t ($\mu\mathrm{m}/\sqrt{cm}$)	σ_t (μm)	α (1/cm)	G
45	325	72.2	140.6	9.4	1327	390
58	350	60.4	152.4	11.6	1013	360
70	360	51.4	163.8	13.7	773	220

Table 7.1: *Amplification gap thickness g, voltage across the gap ΔV, amplification field E_A. The transverse diffusion coefficient D_t and the Townsend coefficient α (from MAGBOLTZ) are used to calculate the expected electron diffusion σ_t across the gap and the gas gain G.*

g (μm)	InGrid	p (μm)	d (μm)	σ_t/p
45	F2	20	12	0.47
	F6	32	23	0.30
	F9	45	32	0.21
	F10	58	21	0.16
58	F1	20	9	0.58
	F4	32	15	0.36
	F9	45	34	0.26
	F10	58	22	0.20
70	F5	32	18	0.43
	F9	45	32	0.30
	F10	58	22	0.24

Table 7.2: *Geometrical parameters of the various InGrids used for test. The ratio of the expected electron transverse diffusion in the amplification gap and the hole pitch is quoted in the last column.*

7.3.4 Measurements

The backflow fraction was measured at field ratios in the range of 10^2–10^3, which corresponds to drift fields between 700 and 50 V/cm. The trends of the backflow fraction with the field ratio are shown in Figure 7.5 (a), (c) and (e) for InGrids of various geometries. As expected the backflow fraction is a decreasing function of the field ratio. At field ratios close to 10^3, backflow fractions between one and a few per mil are measured. At such high field ratios, the product of the gain and the backflow fraction should be smaller than one. Hence, for some avalanches, all ions should be collected at the grid.

In order to test the validity of Equation 7.15, the following function is fitted to the measured trends:

$$BF = p_0/FR \tag{7.17}$$

where p_0 is the fit parameter. The functions are drawn in the left plots of Figure 7.5. The best fits are obtained for the measurements from the 45 and 58 μm gap InGrids of pitch 20 to 45 μm. A rough agreement is observed for all of the 58 μm pitch InGrids as well as with the three 70 μm gap InGrids.

To assess the dependence of the backflow fraction on the ratio σ_t/p, the values of BF extrapolated to a field ratio of 100 are plotted for a given pitch at

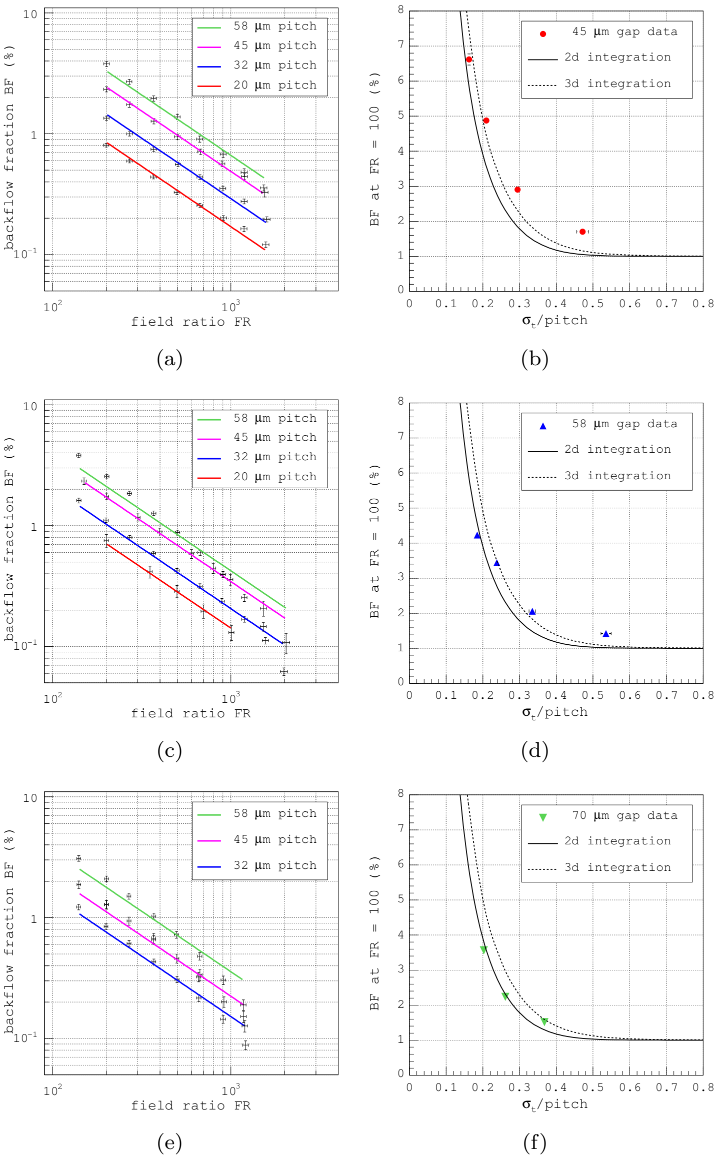

Figure 7.5: *Left plots: backflow fraction and field ratio as measured with 45 µm (a), 58 µm (c) and 70 µm (e) gap InGrids. Right plots: backflow fraction extrapolated at a field ratio of 100 and σ_t/p ratio for the three gaps (b,d,f).*

various values of σ_t in Figure 7.5 (b), (d) and (f). In each plot, the trends obtained from the numerical integration of the 2D and 3D ion density distributions (Equation 7.11) are also shown.

The measured and calculated trends are compatible for hole pitches down to 32 μm, the data points lying in between the two lines. The measurements from InGrids of 20 μm pitch, however, are slightly larger than the model predictions. Still, the discrepancies remain below one percent.

As mentioned in section 7.2.4, it is predicted that the backflow fraction at a given field ratio should reach a constant value for $\sigma_t/p > 0.5$. This is supported by our results, summarized in Figure 7.6, although more measurements with InGrids of smaller hole pitches or larger gap sizes would be needed for a definitive assessment.

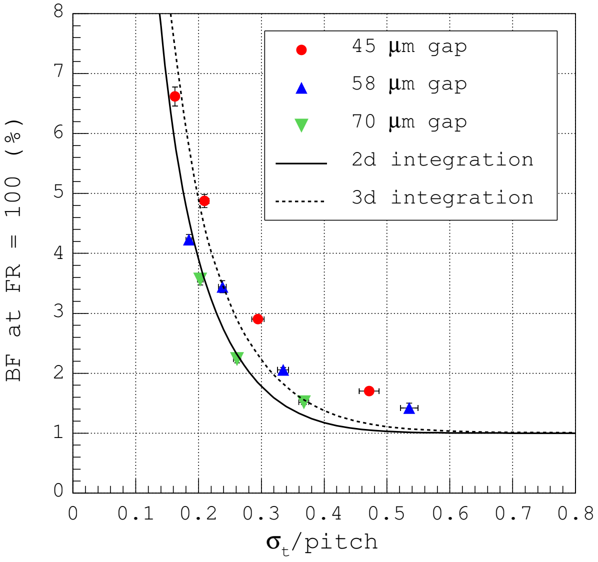

Figure 7.6: *Backflow fraction extrapolated at a field ratio of 100 for various values of the ratio* σ_t/p.

7.3.5 Discussion

We measured that the backflow fraction *BF* of most of the tested InGrids is an inverse function of the field ratio *FR*. For some geometries still, the fitted trends show only a rough agreement: the measured trends are decreasing faster or slower than the $1/FR$ behaviour. Actually, the fit quality improves if the following parametrization is used:

$$BF = p_0/FR^{p_1} \tag{7.18}$$

where p_1 is an additional parameter. When fitting Equation 7.18 to the measured points, one obtains $p_1 \sim 1$ for half of the InGrids. The other half of the detectors shows p_1 between 1.1–1.2 or close to 0.9. These slopes (-p_1) are not predicted by our model and we discuss below some likely causes for this different behaviour.

Parameter $p_1 < 1$

Slopes of -0.90 and -0.96 are obtained with the InGrids F6 and F9 of 45 μm gap. They could be explained by the following arguments.

1. The gain may depend on the drift field and slightly decrease with the field ratio, affecting the longitudinal development of the avalanche. As a result, the width of the ion density distribution shrinks with the field ratio (instead of remaining constant) and the backflow fraction decreases less rapidly than expected.

   The hole pitches and diameters of these detectors are (32,23) and (45,32) μm respectively which yields a grid optical transparency of about 40 % each. Due to the small gap size, the gain should be sensitive to the drift field and the effect presented in the first argument could be at work. This effect is not included in the simulation where the amplification field depends only on the grid voltage.

2. The entrance distribution of the electrons inside the holes depends on the field ratio. If the electron diffusion is small enough, its width should reduce when the field ratio increases. If the electrons enter uniformly in the hole (at a low field ratio for instance), the average ion density distribution will be several times broader than if they would enter at the center of the hole. Hence, while increasing the field ratio the width of the ion distribution shrinks and the backflow fraction decreases less rapidly than expected.

   The entrance distribution of the electrons in the hole depends on the shape of the field above the grid and the transverse diffusion and can not be precisely predicted. For this reason, it was assumed in our model that all electrons enter at the center of the hole.

Parameter $p_1 > 1$

Slopes steeper than -1 are obtained with all the 58 μm pitch and 70 μm gap prototypes. The 58 μm pitch InGrids have a hole diameter of 22 μm, and hence a low grid optical transparency of about 11 %. InGrids of 70 μm gaps have a lower amplification field than those of smaller gaps and, at a given field ratio, a lower drift field too. We propose below some mechanisms that could be responsible for these observations.

1. The ion diffusion would reduce the fraction of ions inside the funnel.

   Let's assume that the ion density distribution is a two-dimensional gaussian centered around the funnel. The ions drift towards the grid in a uniform amplification field. At the grid, the distribution width will have increased and the fraction of backflowing ions will be reduced.

   The ion diffusion would be equivalent to having a larger electron diffusion as the width of distribution would be given by:

   $$\sigma_\mathrm{t} = (D_\mathrm{t}^\mathrm{e} + D_\mathrm{t}^\mathrm{ion})\sqrt{g} \tag{7.19}$$

   The backflow fraction therefore would still decrease with the inverse of the field ratio and ion diffusion should not be responsible for the steep slopes.

2. The second argument is similar to that used to explain the slopes with $p_1 < 1$. If the electron entrance distribution gets wider at high field ratio, so is the average ion density distribution in the amplification region. As a result, we have the double effect that the funnel radius shrinks and the ion distribution spreads out at high field ratio. In this case, the backflow fraction would decrease faster than the inverse of the field ratio.

   As mentioned earlier, the entrance distribution is not known. At high field ratios, still, the electric field in the region where the field line compression starts, decreases. That might result in an increased electron transverse diffusion and a broader entrance distribution.

3. The electron collection efficiency could drop at lower drift fields due to an increased ion space charge or an increased transverse diffusion at the entrance of the holes. As a result, while all primary ions are collected at the cathode, some primary electrons do not reach the amplification region.

   These electrons would not contribute to the backflow current nor to the anode current. Therefore the backflow fraction calculated from Equation 7.16 would not be affected by a limited electron collection efficiency.

4. If some primary electrons recombine with some backflowing ions, Equation 7.16 is not valid anymore. The probability R that an electron recombines with a backflowing ion could increase at low drift fields as the ion drift velocity in the drift region would decrease.

   In this case, the ratio in Equation 7.16 would be proportional to:

   $$\frac{I_\mathrm{C} - I_\mathrm{P}}{I_\mathrm{A}} \propto (1-R)BF - \frac{1}{G(1-R)} \sim (1-R)BF \tag{7.20}$$

   and the trend of the measured backflow fraction with the field ratio would depend not only on $BF(E_\mathrm{D})$ but also on $R(E_\mathrm{D})$.

In order to ensure that the recombination probability was low, the exponential dependence of the anode current on the grid voltage was verified. This was done once at the beginning of the measurements with one InGrid at a drift field of a few hundred volts per centimeter. It is hence possible that the measurements done with other InGrids or at high field ratios are affected by the recombination.

7.4 Conclusion

The ion backflow properties of integrated Micromegas detectors of various geometries have been measured in a P10 gas mixture. At gains of 200–400 and at drift fields of a few hundred volts per centimeter, backflow fractions of the order of one percent were measured, which agrees with previous measurements performed with standard Micromegas. At fields of a few tens of volts per centimeter, this fraction drops to the per mil level.

A three-dimensional version of the model proposed in [147] was used to investigate the dependence of the ion backflow on the grid geometry, the field ratio and the electron transverse diffusion in the avalanche. A good agreement between the model predictions and the measurements was found, the largest absolute errors being 0.7 %.

For the tested geometries, the backflow fraction decreases with the gap size as the avalanche spread increases. It also decreases at smaller hole pitches because the field line funnel shrinks.

The backflow fraction of half of the tested geometries is an inverse function of the field ratio. This is not accurately verified with the second half of the prototypes which shows a slightly different behaviour. We think that the discrepancies are due to the recombination of the primary electrons with the backflowing ions or to the variation of the entrance position distribution of the electrons in the grid hole, with the drift field. In the latter case, the entrance distribution should depend on the three-dimensional field and the gas composition which determine how strongly the electrons are focused and how they diffuse. A full three-dimensional Monte Carlo simulation that includes the effect of diffusion, avalanche growth and the field should give a more precise estimate of the backflow fraction, however, this is beyond the scope of this thesis.

At the ILC, the number of backflowing ions per primary electrons should be about one. In other words, the backflow fraction should be equal to the inverse of the gain ($BF{\cdot}G \leq 1$). For a fraction of one per mil, the TPC should hence be operated at a low gain of 10^3. In a GridPix TPC with no dead area, the single electron detection efficiency could be lowered to 50 % while still measuring enough points for the track fit. In this case, a gain of 10^3 or less could be used depending on the exact trend of the efficiency w.r.t. the gain. That trend is measured in the next chapter.

Chapter 8

X-ray conversion signals in a GridPix TPC

In this chapter, I present measurements of the mean energy per ion pair W and the Fano factor F of 2.9 keV photo-electrons in Ar/iC$_4$H$_{10}$ 95/5 by single electron counting with the TimePix chip. I first give a short introduction on the various techniques used for measuring the Fano factor in gas. The principle of measuring W and F by means of a pixel readout chip is then explained. Some aspects of the operation of the TimePix chip are detailed and I then present the experimental set-up and comment on the choice of gas mixture, chamber geometry and photo-electron energy. A detailed account is then given on the single electron detection efficiency followed by the presentation of the results.

8.1 Introduction

8.1.1 Techniques to measure the Fano factor

The techniques used for measuring the Fano factor in gas are listed below. Depending on the technique used, the mean energy per ion pair is also measured or used as input for the determination of F.

- Ionization chamber. This technique is used for large primary ionizations such as the ones produced by α particles ([104], [107], [109] and [116]). The primary charge is read out by sensitive electronics and the measured charge distribution width directly relates to the Fano factor.

- Proportional counter. Here, each primary electron is multiplied and the signal from the total charge signal is read out. The contribution to the line width from the avalanche fluctuations can be estimated or measured, yielding information on the primary fluctuations [113, 117].

- Proportional scintillation. This technique consists in drifting the primary electrons in a region of moderate electric field. In such fields, the electrons take part in excitation of the gas molecules but do not have enough energy to ionize. The emitted UV light is read out by photo-sensitive detectors. Because the energy resolution is a decreasing function of the light yield, the contribution from primary fluctuations is derived from the extrapolation of the resolution to infinite light yields ([108], [110], [111] and [112]).
- Single electron counting. The primary electrons drift towards the readout electrode(s) where they are multiplied and counted with a certain efficiency. The values of W and F are then determined from the mean and variance of the electron number distribution. If only one electrode is available, the counting efficiency critically depends on the time between two avalanches. For this reason, the detector is filled with a low pressure gas to increase the range of the photo-electron. Also, the drift field is set in order to minimize the electron drift velocity and to have the longest time between the single electron avalanches. This technique was used for X-ray energies up to 1.5 keV by Pansky *et al.* [114].

The proportional counter and single electron counting techniques are based on the multiplication of the primary electrons and therefore can not be applied to gas mixtures without a quencher gas. Moreover, the proportional counter technique requires to measure the single electron response of the counter which is generally a difficult task. Oppositely, the scintillation technique will not work in gas mixtures containing organic molecules because the UV scintillation light would be readily absorbed. The ionization chamber method can in principle be applied to any gas mixture but only for measuring large energy deposits such as those from α particles.

Accordingly, the primary ionization statistics from soft X-rays in mixtures of a noble and a quencher gas should be best measured with the single electron counting technique. If one electrode is used to collect the charge, this technique can be used for energy deposits below 1.5 keV and at low gas pressures. If more than one electrode is available (*e.g.* with a pixel readout chip as collecting anode) it should be suitable for measuring larger X-ray energy deposits at NTP.

8.1.2 Measuring the Fano factor with Gridpix detectors

GridPix detectors combining a pixel readout chip with a Micromegas-like amplification grid have a single electron detection capability. In typical operating conditions, a detection efficiency of the order of 90 % is expected. With a TimePix chip, the high granularity of the detector ($\sim$ 65 thousand channels) should be well suitable for measuring W and F by the single electron counting technique.

An almost point-like cloud of primary electrons from a few-keV photo-electron drifts towards the chip while undergoing diffusion. Depending on the collection efficiency a certain fraction of the primary electrons reach the amplification gap where they are multiplied and detected with a high efficiency.

The dead time of a pixel of the TimePix chip is about 1 μs (for input charges of roughly 20 thousand electrons). This is larger than the time spread of the cloud due to longitudinal diffusion and hence, only one primary electron can be detected per pixel. The probability to collect two electrons on the same pixel can be reduced by insuring sufficient transverse diffusion of the cloud during the drift.

Eventually, the number of hits recorded on the pixel matrix depends on the collection and detection efficiencies and the transverse size of the cloud. Assuming that the diffusion is sufficient to collect at most one primary electron per pixel and that any detected electron produces one hit on the pixel matrix, the mean number of detected electrons N_d is equal to the mean number of hits:

$$N_\mathrm{d} = \kappa N_\mathrm{c} = \kappa\eta N_\mathrm{p} = \kappa\eta\frac{E_0}{W} \tag{8.1}$$

where E_0 is the energy of the photo-electron, N_c and N_p are the mean number of collected and primary electrons and η and κ the collection and detection efficiencies. The numbers of collected and detected primary electrons follow a binomial distribution, therefore the relative variance of N_d can be written as:

$$\left(\frac{\sigma_{N_\mathrm{d}}}{N_\mathrm{d}}\right)^2 = \frac{F}{N_\mathrm{p}} + \frac{1-\eta}{\eta N_\mathrm{p}} + \frac{1-\kappa}{\eta\kappa N_\mathrm{p}} = \frac{1}{N_\mathrm{p}}\left(F + \frac{1-\eta\kappa}{\eta\kappa}\right) \tag{8.2}$$

From Equations 8.1 and 8.2, one obtains respectively:

$$W = \kappa\eta\frac{E_0}{N_\mathrm{d}} \tag{8.3}$$

and

$$F = \left(\frac{\sigma_{N_\mathrm{d}}}{N_\mathrm{d}}\right)^2 \frac{E_0}{W} + \frac{\eta\kappa - 1}{\eta\kappa} \tag{8.4}$$

Equations 8.3 and 8.4 can be used to measure W and F if η, κ, E_0 and the distribution of the number of detected electrons are known. They are valid if the distribution of the number of hits is governed by primary, collection and detection fluctuations only. In practice, other effects such as pixel threshold and gain variations across the chip surface, electronic noise, electron attachment in the gas and multi-pixel hits due to the silicon protection layer can affect the distribution. These effects, still, can be neglected or corrected for as it will be shown in the coming sections.

8.2 The TimePix chip

8.2.1 Counting modes

A short description of the TimePix chip can be found in section 4.6.3. The TimePix chip is activated by a binary signal of adjustable duration called the shutter signal. During the shutter time, a signal crossing the threshold of a pixel produces a hit and triggers the counting of the shift register of this pixel. The number of counted clock cycles depends on the counting mode:

- Time-over-threshold (or TOT) mode. The number of counts is equal to the number of clock cycles elapsed during the time the pulse was above the threshold. This time, and thus the number of counts, is a rising function of the input charge;

- Timepix (or TIME) mode. The number of counts is equal to the number of clock cycles counted during the time between the first hit and the end of the shutter time. This time is shorter for hits recorded at the end of the shutter time than hits recorded at the beginning.

8.2.2 Threshold equalization

The pixel discriminator thresholds are set globally by means of the low-threshold Digital to Analog Converter (so-called THL DAC). Ideally, this would result in a uniform detection threshold across the pixel matrix. There are, however, pixel to pixel threshold variations and the thresholds are locally adjusted (by means of 4 adjustment bits) to minimize the spread and eventually improve the uniformity of the detection efficiency across the chip surface. This adjustment is called the threshold equalization and result in threshold variations across the chip area of about 5 %.

8.2.3 Data acquisition

The interface between the chip and the computer is realized by the MUROS readout system [215]. The MUROS supplies the bias voltages to the chip and also provides the clock. The clock frequency can be adjusted by a potentiometer inside the MUROS up to 100 MHz.

The Windows software used to control TimePix is called Pixelman [216]. It handles various tasks like frame display, threshold equalization, testing and setting the DACs, writing frame to files ... Also, it permits to make various cuts on the number of hits when writing a frame to file.

8.3 Single electron detection efficiency

The single electron detection efficiency depends on the pixel threshold and the gain distribution. After equalization, the threshold variations are of about 5 %. Also the InGrid fabrication techniques permit an accurate control of the amplification gap thickness and hence a very good gain uniformity. As a result, the detection efficiency should be uniform across the chip surface.
If one calls t the pixel threshold and $p(g)$ the normalized gain distribution (or single electron response), the detection efficiency can be written as:

$$\kappa = \int_t^{\infty} p(g)dg \tag{8.5}$$

which is actually the fraction of avalanches that contains a number of electrons larger than the threshold. Using the Polya parametrization $p(m,g)$ of the gain distribution (cf. chapter 2), Equation 8.5 becomes:

$$\kappa(m,G,t) = \int_{\mathrm{t}}^{\infty} \frac{m^m}{\Gamma(m)} \frac{1}{G} \left(\frac{g}{G}\right)^{m-1} \exp\left(-m\frac{g}{G}\right) dg \tag{8.6}$$

where G is the mean gain and m relates to the gain relative variance b through $m = 1/b$. Equation 8.6 can be calculated exactly for $m = 1$ and $m = 2$. When $m = 1$, the Polya distribution simplifies to an exponential distribution with a most probable gain of 1 and relative fluctuations of 100 % r.m.s.. The case of $m = 2$ yields a most probable gain of $(m\text{-}1)/m{\cdot}G = 1/2{\cdot}G$ and relative fluctuations of about 71 % r.m.s.. Calculating Equation 8.6 for Polya-like fluctuations ($m = 2$), the detection efficiency can be expressed as:

$$\kappa(G,t) = (1 + 2t/G)\exp\left(-\frac{2t}{G}\right) \tag{8.7}$$

and for exponential gain fluctuations ($m = 1$):

$$\kappa(G,t) = \exp\left(-\frac{t}{G}\right) \tag{8.8}$$

The trends of the detection efficiency with gain for exponential and Polya-like fluctuations are illustrated in Figure 8.1 where the gain is expressed in units of threshold. Clearly, at gains larger than the threshold, Polya-like fluctuations yield larger detection efficiencies.

The dependence of G with the grid voltage V_{g} was measured in several gas mixtures (cf. chapter 6). In Ar/iC$_4$H$_{10}$ 95/5, the contribution of photons to the gain was found to be small and the following parametrization can be used:

$$G = A\exp(BV_{\mathrm{g}}) \tag{8.9}$$

Moreover, for a given grid geometry, gas mixture and drift field, the collection efficiency should vary very little with the amplification field. This is supported by the gain measurements presented in chapter 6 which, in Ar-based mixtures with quencher fractions larger than 5% show an accurate exponential dependence of the gain on the grid voltage. Accordingly, the variations of the detected number of electrons N_d with V_g follows the variations of the detection efficiency and can be predicted:

$$N_\mathrm{d} = \eta\kappa(m, t, G)N_\mathrm{p} = \eta\kappa(m, t, V_\mathrm{g})N_\mathrm{p} \tag{8.10}$$

which, in case of Polya-like fluctuations with $m = 2$ gives:

$$N_\mathrm{d} = \eta \cdot (1 + 2t/(A\exp(BV_\mathrm{g})))\exp\left(-\frac{2t}{A\exp(BV_\mathrm{g})}\right) \cdot N_\mathrm{p} \tag{8.11}$$

Using the parameters $p_0 = \eta N_\mathrm{p}$, $p_1 = t/A$ and $p_2 = B$, Equation 8.11 becomes:

$$N_\mathrm{d} = p_0 \cdot (1 + 2p_1\exp(-p_2V_\mathrm{g}))\exp\Big(-2p_1\exp(-p_2V_\mathrm{g})\Big) \tag{8.12}$$

In the case of exponential fluctuations, one obtains:

$$N_\mathrm{d} = p_0 \cdot \exp\Big(-p_1\exp(-p_2V_\mathrm{g})\Big) \tag{8.13}$$

If the collection efficiency is close to one, the detection efficiency $\kappa(V_\mathrm{g})$ and the number of primary electrons N_p can be determine from a fit of the parameters of Equations 8.12 or 8.13 to $(V_\mathrm{g}, N_\mathrm{d})$ data points. In practice, the absolute value of the collection efficiency is not known and only a lower limit on N_p can be determined.

8.4 Experimental setup

8.4.1 The detectors

The measurements were performed in two times with different TimePix chips. In the first measurement period, the D08 TimePix chip was used. It is covered with a 15 μm thick layer of amorphous silicon (so-called SiProt layer) and equipped with an InGrid. The grid geometry is adapted to the chip pixel pattern: 55 μm hole pitch, 40 μm hole diameter and a square pattern of holes. The SU-8 supporting pillars are 30 μm diameter and also placed according to a square pattern with a pitch of 110 μm. The amplification gap thickness is about 50 μm. The grid is supported on the chip edges by a 100 μm wide dike of SU-8 which blinds the pixels underneath. The InGrid design is such that the top left corner of the chip is covered with a continuous layer of SU-8, resulting in a dead area of ~ 7.6 mm^2 (50 pixels × 50 pixels). This pad is intended for contacting the grid.

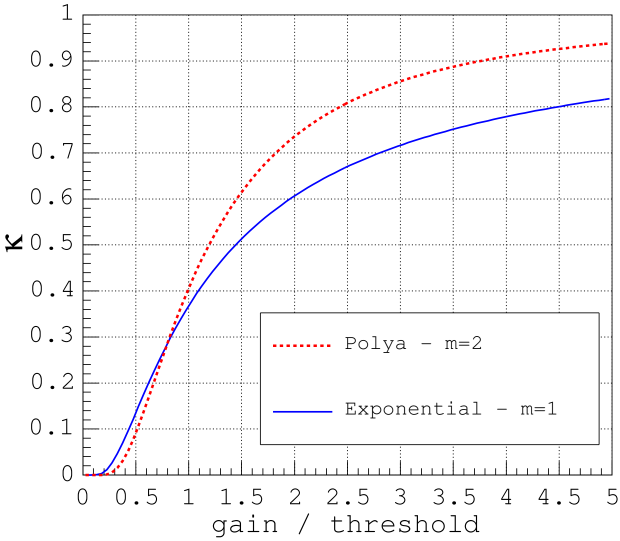

Figure 8.1: *Detection efficiency κ as a function of gain expressed in units of threshold for exponential and Polya-like gain fluctuations.*

The G06 TimePix chip was used for the second measurement period. It is covered with a 20 μm thick SiProt layer and equipped with an InGrid. The grid geometry is similar to that of the D08 chip but with a slightly smaller hole diameter of 30 μm. Also, the supporting structures were not formed by pillars but by a 50 μm thick SU-8 grid with a square pattern of holes of 30 μm diameter. In this InGrid design, the pad previously used for contacting the grid is absent. SEM images of the two detectors are shown in Figure 8.2.

8.4.2 Gas mixture

For the measurement of the photo-electron statistics, it is desirable to have a large transverse diffusion to separate the primary electrons. Also, the primary electrons should be produced close to the cathode such that they drift over the largest distance. This motivated the choice of argon as a carrier gas where 63 % of the 5.9 keV photons entering the chamber are absorbed over a distance of 2.3 cm. For its good quenching properties, we chose isobutane as a quencher. Because the transverse diffusion coefficient decreases with the isobutane concentration, the latter should be as low as possible. From energy resolution measurements (cf. chapter 6) the quenching properties of $\mathrm{Ar}/i\mathrm{C}_4\mathrm{H}_{10}$ mixtures are expected to degrade for isobutane fractions below 5 %. For this reason, a mixture of $\mathrm{Ar}/i\mathrm{C}_4\mathrm{H}_{10}$ 95/5 was adopted. In this mixture, the transverse diffusion coefficient D_t calculated by MAGBOLTZ at 500 V/cm is equal to 483 $\mu\mathrm{m}/\sqrt{\mathrm{cm}}$.

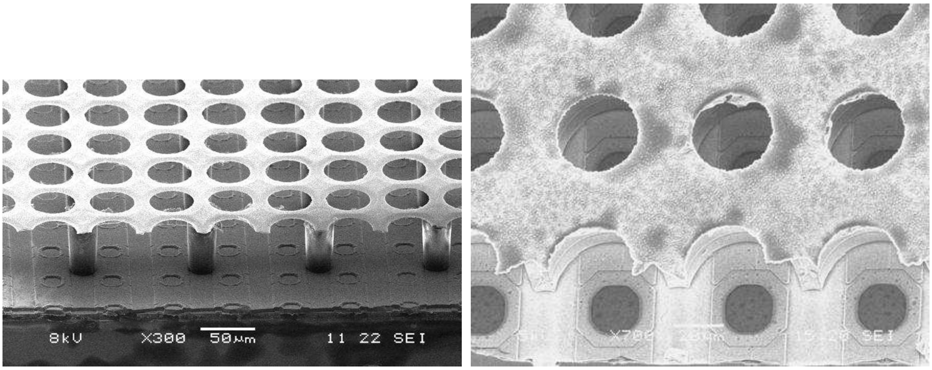

(a) (b)

Figure 8.2: *SEM images of the TimePix chips used (D08 chip (a) and G06 chip (b)).*

8.4.3 Chamber geometry

The easiest way to separate the primary electrons is to have a large drift gap. Due to the finite dimensions of the chip, however, the drift gap should not exceed a certain value. Taking $D_{\mathrm{t}} = 483\ \mu\mathrm{m}/\sqrt{cm}$ and requiring that the primary charge distribution should be contained inside the chip area up to 3 σ, we find that the drift gap should not exceed 24 cm. For practical reasons, we eventually chose a drift gap of 10 cm. The chamber consists of a $10 \times 10 \times 10\ \mathrm{cm}^3$ field cage (so-called drifter) and the chip-board (Figure 8.3).

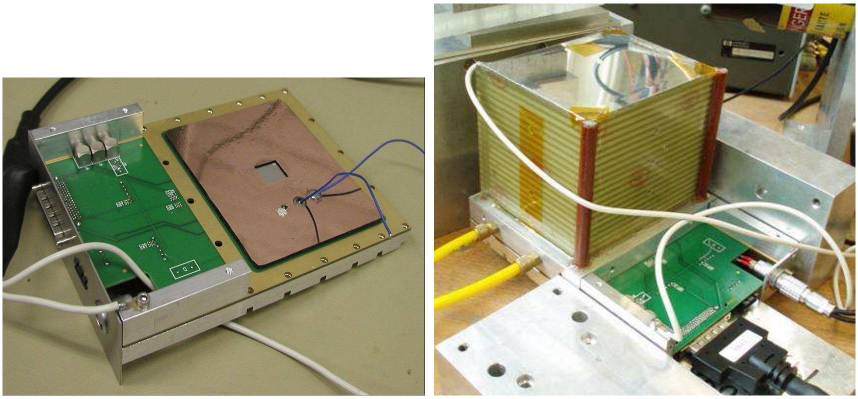

(a) (b)

Figure 8.3: *Test chamber with the field cage removed (a) and mounted on the chip board (b).*

The drifter is formed by a thin cathode foil glued on a folded printed circuit board (PCB). Nineteen parallel copper strips separated by a distance of 0.5 cm are printed on the board, inter-connected by 10 MΩ resistors. The top strip is connected to the cathode. The cathode foil and the bottom strip are connected to high voltage supplies which are used to set the drift field.

The field uniformity is obtained by a planar guard electrode placed parallel to the chip plane at a distance of 1 mm from the grid. This electrode consists of a 9×9 cm^2 copper foil stretched on a 2 mm thick PCB frame. The foil is cut on its center to a 13×13 mm^2 area and placed above the chip-board and is shown in Figure 8.3 (a).

8.4.4 The radiation source

The probability that two primary electrons are collected on the same pixel decreases with the number of primary electrons. It is therefore desirable to use an X-ray source which emits photons with an energy as low as possible.

We used an ^{55}Fe source which emits 5900 eV (Mn K$_\alpha$) and 6492 eV (Mn K$_\beta$) X-rays in the ratio 8.5:1. As detailed in chapter 6, in 13.5 % of the K$_\alpha$ quanta photo-electric absorptions, two electrons are emitted resulting in an energy deposit of 2897 eV (escape peak). In the other 86.5 %, the number of emitted electrons varies resulting in an average energy deposit of 5760 eV (photo-peak).

The structure of the escape peak is thus simpler than that of the photo-peak and less primary electrons are produced. For these reasons, the mean energy per ion pair W and the Fano factor F are measured from the distribution of the number of primary electrons produced in escape peak events. Doing so, it should be assumed that these quantities are the same for the photo-electron and the Auger electron, although they have an energy of 2694 and 203 eV respectively. Under this assumption, the mean and variance of the number of primary electrons are given by:

$$N_{\mathrm{p}} = 2897/W \tag{8.14}$$

$$\sigma^2_{N_{\mathrm{p}}} = 2897 \cdot F/W \tag{8.15}$$

In the first measurement period, the K$_\alpha$ and K$_\beta$ photons were collimated by means of a 15 mm thick plexiglas block in which a 1 mm hole was drilled. In the second period, a thin chromium foil was placed between the source and the detector and the collimator diameter was enlarged to 4 mm in order to compensate for the reduced event rate. The K-edge of chromium is at 5989 eV resulting in an absorption 7 times larger at 6492 eV than at 5900 eV. Hence, mostly 5900 eV photons entered the detector and the off-line determination of the K$_\alpha$ peak position was more straightforward.

8.5 Measurements

The first measurements performed with the D08 TimePix chip were meant to derive W and F from the mean and variance of the distribution of the number of detected electrons. After analysis of the data, it appeared that the mean, and thus W, could be accurately determined. Still, it was difficult to determine the variance and F because of the K_α and K_β peaks that merged in the distribution and the small number of recorded events. As a result, a second measurement was later performed to improve the precision on F. In the mean time, the D08 chip was damaged and the G06 chip was used instead. A larger number of events was recorded and a chromium foil was used to strongly attenuate the K_β line. In what follows, we shortly present the chip settings and explain how the event selection is done.

8.5.1 Chip settings

Noise level

At low detection efficiencies ($V_\mathrm{g} < 330$ V), the escape peak and the photo-peak slightly merge. For a proper determination of the mean position of the escape peak, it is desirable to have a clear separation. Hence, at a given grid voltage, the detection efficiency should be as high as possible, that is: the pixel threshold should be as low as possible. For this reason the threshold is set just above the noise level.

Acquisition time

The acquisition time is set in order to benefit from the full time range of the chip which, at a clock frequency of 100 MHz, is 118 μs. When a photo-electron is produced in the gas, the standard deviation σ_T of the arrival times of the primary electrons at the chip depends on the drift distance z_0, the longitudinal diffusion coefficient D_l and the drift velocity v_d:

$$\sigma_\mathrm{T} = \frac{\sigma_\mathrm{l}}{v_\mathrm{d}} = \frac{D_\mathrm{l}}{v_\mathrm{d}}\sqrt{z_0} \tag{8.16}$$

At 500 V/cm in Ar/iC$_4$H$_{10}$ 95/5, $D_\mathrm{l} = 210\ \mu\mathrm{m/cm}^{1/2}$ and $v_\mathrm{d} = 3.6$ cm/μs. Using the average drift distance z_0 = 10.0-2.3 = 7.7 cm, a point-like cloud of electrons should arrive at the chip with a time dispersion of $\sigma_\mathrm{T} = 16$ ns. This means that on average 95 % of the primary electrons of a given cloud are collected in a time of $4\sigma_\mathrm{T} = 64$ ns.

This time being much smaller than the acquisition time, the noise hits if present can be easily suppressed. With the threshold setting used, the probability that a noise hit is identified as a signal hit is about 1–2 %. A noise hit not suppressed with the time information can still be rejected if it is recorded sufficiently far from the cloud in the pixel plane. The hit selection is detailed further in the data analysis section.

Pixelman event filtering

Photo-peak events are 6–7 times more frequent than escape peak events and are not useful for our study. They should not be recorded, hence a specific routine of the software is used to record frames containing a number of hits within a user defined range. The lower limit of this range is set to 20 hits to avoid recording empty frames or frames with only a few noise hits. The upper limit is adjusted at each grid voltage such as to reject frames containing a photo-peak event or more than one photon conversion.

8.5.2 Event example

A typical event is shown in Figure 8.4 (a) where one sees the primary electrons from a quantum conversion after drifting over several centimeters. The clock cycle distribution is shown in Figure 8.4 (b) where one distinguishes a high peak due to the signal hits and a few single noise entries randomly distributed over time.

When looking at the detailed time structure of the signal (Figure 8.4 (d)), the gaussian shape expected from the longitudinal diffusion is not observed. The distribution is asymmetric with a tail at small number of clock cycles, or at late arrival times. This is due to the fact that small pulses cross the threshold later than large pulses and eventually generate a smaller number of counted clock cycles (so-called time-walk). For input charge larger than a few thousand electrons, the time to cross the threshold is constant.

Small pulses are due to small avalanche sizes but also to the resistive SiProt layer: when an avalanche develops above a pixel pad, a small fraction of the total charge is induced on the neighbouring pads which may record a hit. The charge on those pixels is smaller than that induced on the central pixel and the resulting hits are recorded later than the central hit.

This also implies that one single electron can produce adjacent hits (a hit cluster) on the pixel matrix. This effect reduces the single electron counting capability of the detector. Yet, if the diffusion is large enough the number of hit clusters should be equal to the number of detected electrons.

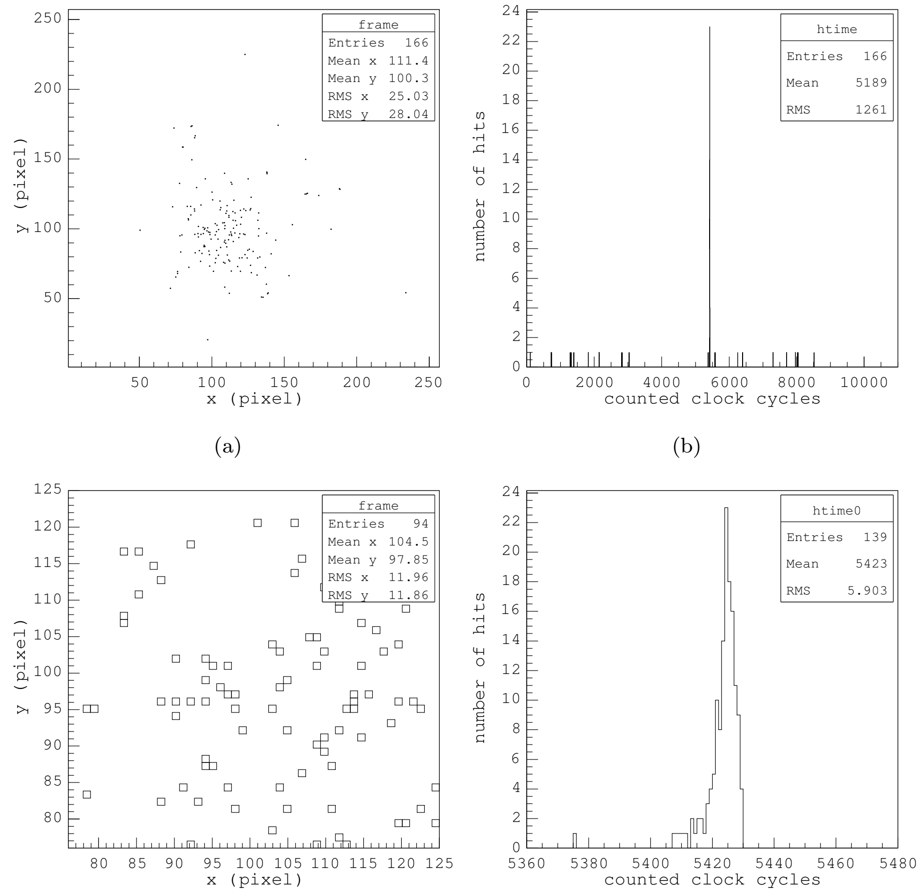

(a)

(b)

(c)

(d)

Figure 8.4: *Typical escape peak event recorded at a grid voltage of -350 V with the D08 TimePix chip (a). The clock cycle distribution exhibits a peak that corresponds to the signal hits (b). Magnified view of the pixel matrix (c) and of the distribution where one clock cycle is equal to 10 ns (d).*

8.6 Data analysis

8.6.1 Event and hit selection

The selection of events and hits proceeds as follows:

- rejection of events which are not centered using the spatial hit distribution. This is realized by imposing that at least 75 % of the hits (of a particular event) are contained inside a square of 128 times 128 pixels;

- suppression of noise hits using the time distribution. One first searches for the maximum in the clock cycle distribution and rejects hits outside a 60 clock cycle wide window centered at the maximum. A gaussian is then fitted to the distribution of the selected hits and hits within three standard deviations are kept.

  Moreover, hits in the pixel plane outside a circle of radius equal to

  $$\frac{3}{\sqrt{2}} \cdot \sqrt{\sigma_{\mathrm{x}}^2 + \sigma_{\mathrm{y}}^2} \tag{8.17}$$

  with σ_{x}^2 (resp. σ_{y}^2) the variance of the hit coordinates along the pixel rows (resp. columns) directions, are rejected.

The mean and variance of the selected hits along the x and y directions are stored for later analysis, together with the number of hit clusters.

8.6.2 Counting of the mean number of detected electrons

After a drift over a certain distance, a cloud of primary electrons has diffused sufficiently so that the number of hit clusters is equal to the number of detected electrons. At the pixel plane, the coordinates (x,y) of the electrons from a cloud produced at a distance z from the anode plane is distributed according to the following two-dimensional gaussian (cf. section 2.3.3):

$$G(x, y, z) = \frac{1}{2\pi D_{\mathrm{t}}^2 z} \exp\left(-\frac{1}{2}\frac{x^2 + y^2}{D_{\mathrm{t}}^2 z}\right) \tag{8.18}$$

which implies that the projected distributions against the x and y axes are a one-dimensional gaussian of same width as $G(x,y,z)$. Hence, the variances of the coordinates of the hits σ_x^2 and σ_y^2 relate to the expected transverse diffusion σ_{t}^2. Actually, the quantity:

$$1/2(\sigma_{\mathrm{x}}^2 + \sigma_{\mathrm{y}}^2) \tag{8.19}$$

is an estimate of σ_{t}^2 and the drift distance z_0 of the electrons can be estimated by:

$$z_{\mathrm{e}} = \frac{\sigma_{\mathrm{x}}^2 + \sigma_{\mathrm{y}}^2}{2D_{\mathrm{t}}^2} \tag{8.20}$$

It is expected that the number of hit clusters increases with z_{e} and eventually reaches a constant value equal to the number of detected electrons.

A scatter-plot of the number of hit clusters N_{hc} and z_{e} as measured with the G06 chip at -350 V is shown in Figure 8.5. The profile of this scatter-plot along the x-axis is also shown. The profile is obtained by slicing the x-axis and calculating the mean number of hit clusters in each slice.

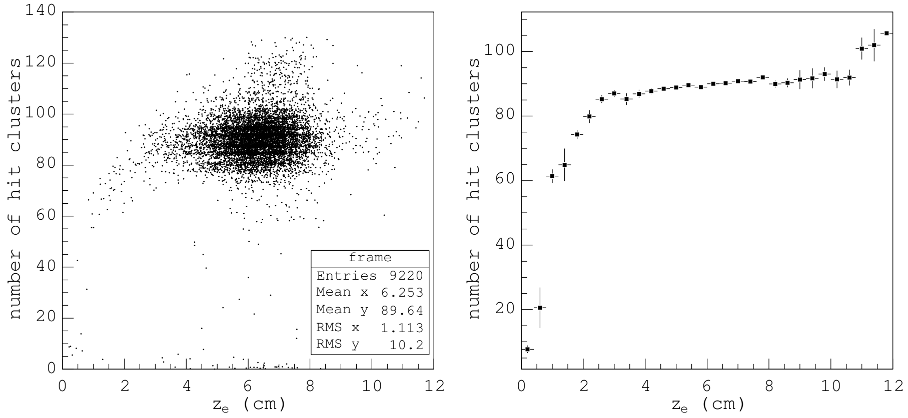

(a) (b)

Figure 8.5: *Scatter-plot of the number of hit clusters and the estimated drift distance* z_{e} *as measured at -350 V with the G06 TimePix chip (a). Profile of the scatter-plot along the x-axis (b).*

At -350 V, it is observed that N_{hc} reaches an almost constant value for $z_{\mathrm{e}} \geq 5$ cm. Therefore the mean number of detected electrons at this voltage is precisely determined by fitting the spectrum of N_{hc} of events for which $z_{\mathrm{e}} \geq 5$ cm. When raising the grid voltage and hence the gain, however, the cluster hit multiplicity increases and this minimum distance (that we will call $z_{\mathrm{e}}^{\mathrm{cut}}$) depends on the grid voltage. As a result, every spectrum is fitted several times for increasing values of $z_{\mathrm{e}}^{\mathrm{cut}}$. For the D08 chip data, the fit function is a double gaussian:

$$f = \frac{h_\alpha}{\sqrt{2\pi}\sigma_\alpha} \exp\left(-\frac{1}{2}\left(\frac{x-\mu_\alpha}{\sigma_\alpha}\right)^2\right) + \frac{h_\beta}{\sqrt{2\pi}\sigma_\beta} \exp\left(-\frac{1}{2}\left(\frac{x-\mu_\beta}{\sigma_\beta}\right)^2\right) \tag{8.21}$$

where the free parameters of the fit are h_α, μ_α and σ_α and the other parameters are constrained by:

$$\mu_\beta = \mu_\alpha \frac{3.5}{2.9} \tag{8.22}$$

and

$$\sigma_\beta = \sigma_\alpha \sqrt{\frac{3.5}{2.9}} \tag{8.23}$$

The calculated ratio between K_α and K_β conversions is:

$$h_\beta = h_\alpha / 7 \tag{8.24}$$

For the measurements done with the G06 chip, a Cr foil strongly reduced the fraction of K_β conversions in the gas and therefore a single gaussian function is used. Two fitted spectra are shown in Figure 8.6.

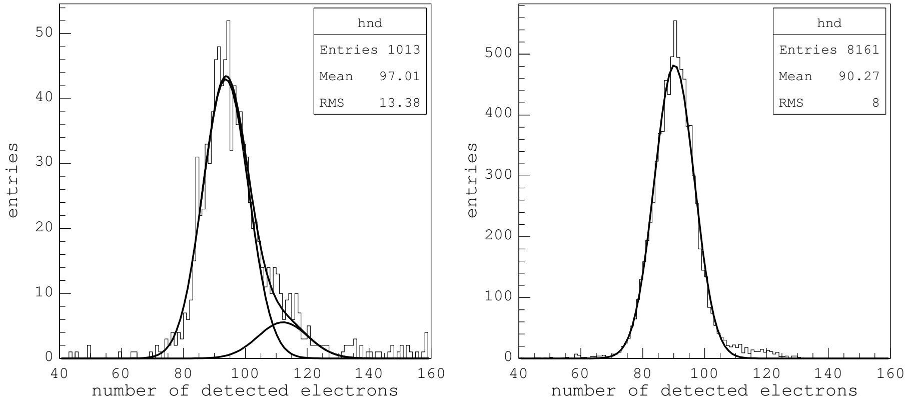

(a) (b)

Figure 8.6: *Spectra of the number of detected electrons recorded with the D08 TimePix chip at -330 V (a) and with the G06 chip at -350 V (b). In the latter case, a chromium foil was used to absorb the K_β line. The absorption is actually not complete and some remnants of this line can be seen.*

The trends of μ_α and σ_α are shown in Figure 8.7 together with that of the number of entries in the spectrum. μ_α slightly increases with $z_\mathrm{e}^\mathrm{cut}$ as the hit clusters separate. The expected plateau is not reached, still the measured variation is smaller than two clusters. Similarly, σ_α changes little, showing variations smaller than 0.2. This is also the case at other voltages and may be due to a worse noise hit suppression for events of large drift distance which have broader clock cycle and spatial distributions. Also, when a photon converts very close to the aluminium cathode, the resulting trail of excited gas molecules produces UV-photons that could liberate a few electrons from the metal by the photo-electric effect. We therefore think that the true mean and variance are obtained at values of $z_\mathrm{e}^\mathrm{cut}$ before the rise of μ_α.

The mean N_d and r.m.s. σ_{N_d} of the number of detected electrons are thus deduced from the fit parameters μ_α and σ_α at $z_\mathrm{e}^\mathrm{cut} = 3$–$5$ cm (depending on the dataset). The errors are taken to be 2 and 0.2 electrons respectively.

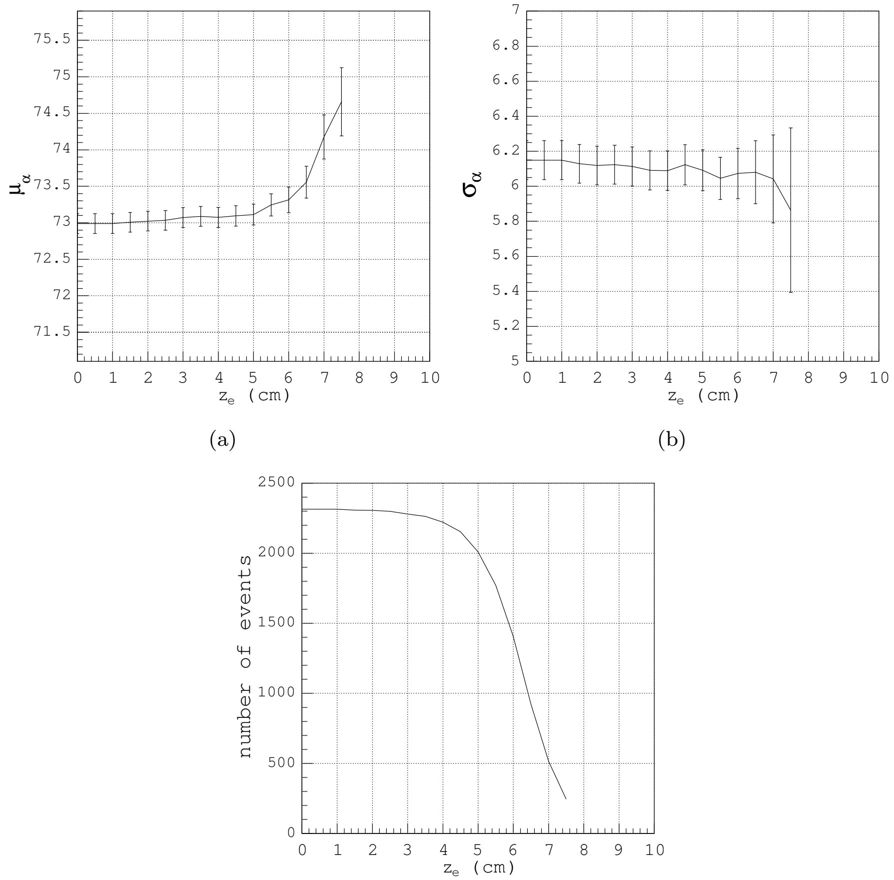

(a) (b)

(c)

Figure 8.7: *Position (a) and r.m.s. (b) of the K_α peak as a function of the minimum estimated drift distance $z_\mathrm{e}^\mathrm{cut}$ and number of entries in the spectrum (c). The data were measured with the G06 chip at -330 V.*

The means and r.m.s. of the number of detected electrons as measured at different grid voltages with the D08 and G06 chips are listed in Table 8.1. The number of entries in each spectrum is also quoted.

$-V_\mathrm{g}$ (V)	D08 chip			G06 chip		
	N_d	σ_{N_d}	Entries	N_d	σ_{N_d}	Entries
300	42.2	7.0	797			
310	63.9	5.7	880	40.3	5.6	2799
320	81.8	6.1	909	58.3	6.1	2735
330	94.0	7.0	1013	73.1	6.1	2250
340	103.3	5.9	934	82.2	6.1	2469
350	108.8	6.7	1431	90.2	6.3	8157

Table 8.1: *Means and r.m.s. of the number of detected electrons and number of entries in the fitted spectra.*

8.6.3 Single electron detection efficiency

The efficiency for single electron detection is derived by fitting the parameters of Equation 8.12 or 8.13 to the trend of N_d with the grid voltage. Doing so, it is assumed that the collection efficiency is constant over this range of grid voltage. The fitted lines with Polya-like fluctuations are shown in Figure 8.8.

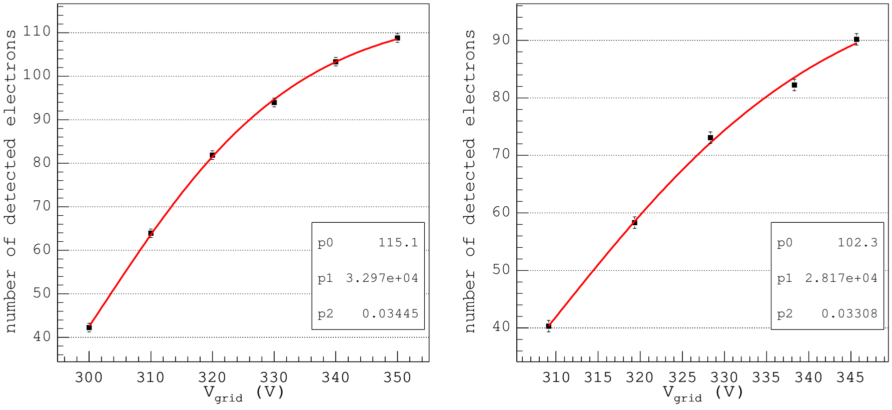

(a) (b)

Figure 8.8: *Mean number of detected electrons and grid voltage measured with the D08 (a) and G06 (b) chips. The fitted lines are obtained with Polya-like gain fluctuations. The grid voltages are corrected for pressure variations.*

With exponential fluctuations, almost the same lines are obtained (not shown) but with different fit parameters (Table 8.2). In particular, the value of $p_2 = B$ differs significantly for the two fits: between 0.033–0.035 for Polya-like fluctuations and 0.052-0.053 for exponentially distributed gains. From the gain measurements presented in chapter 6, B is close to 0.035 in Ar/iC$_4$H$_{10}$ 95/5. This is a clear indication that the gain fluctuations are more precisely described by a Polya distribution than by an exponential distribution. In what follows, the Polya-like fit parameters are used.

Chip	m	$p_0 = \eta\ N_\mathrm{p}$	$p_1 = t/A$	$p_2 = B\ (\mathrm{V}^{-1})$
D08	1	117.6 ± 1.0	5064780 ± 1855420	0.0513 ± 0.0012
	2	115.1 ± 1.9	32966 ± 18508	0.0344 ± 0.0019
G06	1	105.7 ± 7.6	2887610 ± 6994700	0.0482 ± 0.009
	2	102.3 ± 4.1	28166 ± 28853	0.0330 ± 0.004

Table 8.2: *Parameters of the fit of the number of detected electrons as a function of grid voltage for exponential (m = 1) and Polya-like (m = 2) gain fluctuations.*

The mean number of collected electrons $N_\mathrm{c} = \eta N_\mathrm{p}$ is obtained from the parameter p_0 and is equal to 115 and 102 for the D08 and G06 chip respectively. We think that this difference is due to a different collection efficiency of the two detectors. This interpretation is compatible with the larger hole diameter of the InGrid of the D08 chip (40 μm while 30 μm for the G06 chip InGrid) which could result in a higher collection efficiency (at same hole pitch and pattern, gas mixture and fields).

From the mean number of collected electrons, the detection efficiency is calculated as $N_\mathrm{d}/N_\mathrm{c}$. At -350 V, a detection efficiency of about of 95 % is derived for the two detectors. This indicates that the single electron response of the two detectors are similar.

8.6.4 Mean number of primary electrons and *W*

The mean number of primary electrons N_p is not directly accessible in this measurement because the collection efficiency can not be measured. Nevertheless, a lower limit on N_p and hence an upper limit on W can be obtained. In this case, N_p is deduced from N_d. The D08 chip InGrid should have the highest collection efficiency and we thus take $N_\mathrm{p} = 115 \pm 2$. This yields a mean energy per ion pair at 2897 eV in Ar/iC$_4$H$_{10}$ 95/5 of:

$$(W \pm \Delta W) = (25.2 \pm 0.5)\ eV \tag{8.25}$$

which is compatible with the value of 25.0 ± 0.6 eV measured by Pansky *et al.* [114] in Ar/iC$_4$H$_{10}$ 20/80 with 1253 eV X-rays (K$_\alpha$ fluorescence of Mg). At this same energy, Pansky *et al.* also measured 25.6 ± 0.3 eV in pure isobutane. This good agreement supports our assumption that the collection efficiency of the InGrid of the D08 chip is close to one.

8.6.5 Variance of the number of primary electrons and F

The calculation of the Fano factor F is performed by correcting the variance of the number of detected electrons $\sigma^2_{N_\mathrm{d}}$ for fluctuations due to limited collection and detection efficiencies.

The detection efficiency was calculated in section 8.6.3. The collection efficiency of the D08 InGrid is assumed to be equal to one. As a result, that of the G06 InGrid should be equal to 102/115 = 87 % and should contribute to 3.6 % of the measured peak relative r.m.s..

The Fano factor is then calculated from Equation 8.4. Values of F as measured with the G06 TimePix chip at various grid voltages are plotted in Figure 8.9 and listed in Table 8.3. The contribution of the detection efficiency to the peak relative r.m.s. is also quoted.

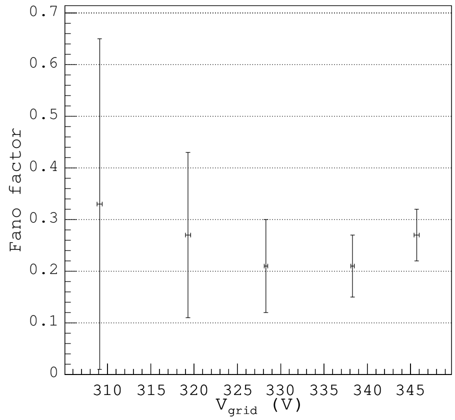

Figure 8.9: *Fano factor deduced from measurements at various grid voltages with the G06 TimePix chip.*

The measured Fano factor varies between 0.2 and 0.3. The lowest value is obtained at -330 and -340V. Taking the value with the smaller error, we obtain a Fano factor at 2897 eV in Ar/iC$_4$H$_{10}$ 95/5 of:

$$(F \pm \Delta F) = (0.21 \pm 0.06) \tag{8.26}$$

This value compares well with that measured by Pansky *et* al. who found 0.250 ± 0.010 in Ar/iC$_4$H$_{10}$ 20/80 with 1253 eV X-rays and 0.255 ± 0.009 in pure isobutane.

-V$_g$ (V)	N_d	RMS$_{N_d}$ (%)	κ	RMS$_\kappa$ (%)	RMS$_{N_p}$ (%)	F
309.1	40.3	13.8	0.40	12.2	5.38	0.33
319.3	58.3	10.5	0.57	8.6	4.88	0.27
328.3	73.1	8.3	0.72	6.2	4.26	0.21
338.3	82.2	7.4	0.81	4.9	4.27	0.21
345.7	90.2	7.0	0.88	3.6	4.82	0.27

Table 8.3: *Mean and relative r.m.s. of the number of detected electrons N_d, detection efficiency κ and corresponding fluctuations RMS$_\kappa$, primary fluctuations RMS$_{N_p}$ and Fano factor at various grid voltages. At each voltage, the contribution from the collection efficiency is equal to 3.6 %.*

8.7 Conclusion

We presented a new method to measure the mean energy per ion pair and Fano factor in gas by means of a pixel segmented readout anode. This method consists in the direct counting of the primary electrons produced by the absorption in the gas of a given energy and can be applied at normal conditions to several mixtures of a noble gas and a quencher gas.

The counting capability depends on the number of primary electrons, the transverse diffusion and the hit multiplicity. Ideally, the hit multiplicity would be equal to one, however, it increases with the gain because of the amorphous silicon (SiProt) layer. In our experimental conditions: a 10 cm drift gap, a transverse diffusion coefficient of 483 μm/$\sqrt{cm}$, 115 primary electrons and a 15–20 μm thick SiProt layer, results compatible with measurements found in literature were obtained: at 2897 eV in Ar/iC$_4$H$_{10}$ 95/5, $(W \pm \Delta W) = (25.2 \pm 0.5)$ eV and $(F \pm \Delta F) = (0.21 \pm 0.06)$.

Besides the interest of this new technique for studying the behaviour of W and F in various gas mixtures, it also provides a simple way to measure precisely the detection efficiency of GridPix detectors. This quantity would be important for instance in a pixel readout TPC to measure the dE/dx by single electron counting.

Chapter 9

Cosmic ray tracking in a GridPix TPC

One of the main applications foreseen for GridPix is to read out a Time Projection Chamber. It should hence be demonstrated that its tracking and particle identification performance is similar or superior to that achieved with standard pad readout. This task is beyond the scope of this thesis, nevertheless a first step in this direction was made by measuring the performance of a small GridPix TPC with cosmic particles.

The TPC has a sensitive volume of 1 cm^3 and its readout plane consists of a TimePix chip covered with an amorphous silicon layer and equipped with an InGrid. In a He/iC$_4$H$_{10}$ 77/23 gas mixture, a few thousand tracks of cosmic particles were recorded. Using the arrival time information from the TimePix chip, the three dimensional trajectories were reconstructed. I will report on a first estimate of the point resolution in the pixel plane and a measurement of the number of electron clusters per unit length. Also, some implications for an ILC TPC will be shortly discussed.

9.1 Introduction

The ionization from relativistic particles consists of clusters of electron/ion pairs distributed along the trajectories (cf. chapter 3). TPCs read out with pads of several mm^2 area are used to measure the charge produced along segments of tracks. In a pixel-readout TPC, almost all primary electrons are individually detected and if the diffusion is not too large, the cluster structure may be preserved during the drift and studied.

This study was conducted by means of a small TPC read out by a SiProtected and InGrid-equipped TimePix chip. In order to have a good separation between clusters, a mixture of He/iC_4H_{10} 77/23 was used for low primary ionization density and a small drift gap of 1 cm was adopted for small transverse diffusion.

The measurement of the drift lengths of the primary electrons requires the time at which the particles cross the detector. For this purpose, a coincidence set-up provides the detector with a trigger signal. Another task of the coincidence set-up is to ensure that the primary ionization density is the lowest and similar for all recorded tracks.

9.2 Experimental set-up

9.2.1 The chamber

The chamber consists of a 12 × 16 cm^2 printed circuit board (or PCB) and a 12 × 10 × 1 cm^3 cover. A TimePix chip is glued and wire-bonded to the PCB and the cover is formed by a metal square frame and a kapton foil with a thin metal layer on one side which is used as the cathode. A 6 × 8 cm^2 thin metal layer is printed on the PCB and etched in its middle to a 2 × 2 cm^2 square area where the chip is glued. This layer acts as a guard electrode and is set at the same voltage as the grid to improve the electric field uniformity.

Two holes were drilled into the metal frame for the gas circulation. The grid, guard and cathode are connected to high voltage supplies through the PCB. For the measurements, the chamber is placed vertically to record tracks oriented predominantly parallel to the pixel plane.

9.2.2 The TimePix chip

The TimePix chip (E09-W0014) is equipped with a 20 μm layer of amorphous silicon and an InGrid of about 50 μm gap. The dimensions of the grid are similar to those of D08 chip InGrid and can be found in section 8.4.1. The spread of the pixel thresholds was minimized by the equalization procedure. After equalization, the detection efficiency is uniform across the chip area except in the top left corner, on the edges, along one dead column and on a localized spot were the grid was damaged. The sensitive area is visible in Figure 4.13 (b). The chip is operated in the TIME mode in order to record the relative arrival time of the primary electrons. The clock frequency is set to 100 MHz and the active time of the detector (given by the duration of the shutter signal) to 13 μs.

9.2.3 Cosmic MIP trigger

Cosmic rays

The cosmic ray spectrum above the earth atmosphere includes all stable charged particles and nuclei with life-times of order 10^6 years or longer [217]. When entering the atmosphere, cosmic particles interact with the nuclei of nitrogen and oxygen molecules and produce charged and neutral nuclear particles. The latter rapidly decay into secondary particles (muons, neutrinos, electrons, positrons and photons) producing cascades of particles called air showers.

The secondary particles lose some energy in the atmosphere and at sea level, muons are the most numerous charged particles with an integral intensity of roughly 1 $\mathrm{cm^{-2}min^{-1}}$ in an horizontal plane. They have a mean energy of about 4 GeV and an energy spectrum almost flat below 1 GeV which steepens gradually between 10 and 100 GeV to reflect the primary spectrum in $E^{-2.7}$. At energies much larger than 1 TeV, the spectrum becomes one power steeper [218]. Muons have an overall angular distribution proportional to $\cos^2\theta$ where θ is the angle between the trajectory and the vertical [217].

Trigger signal

The trigger signal results from the time coincidence of signals from three scintillators. Two 4 × 12 $\mathrm{cm^2}$ scintillators are placed horizontally above the chamber, with an overlap area of about 4 × 4 $\mathrm{cm^2}$. Lead plates of 30 × 30 $\mathrm{cm^2}$ area for a total thickness of 10 cm are placed below the chamber and the third scintillator (1 $\mathrm{m^2}$ area) is installed below the plates. The total lead thickness corresponds to 113.5 $\mathrm{g/cm^2}$ which is equal to the mean range of 250–300 MeV/c muons in this material [195]. As a result, the third scintillator is traversed mainly by muons on the minimum of ionization or with larger energies, the lower energy part of the muon spectrum being vetoed. The coincidence setup is shown in Figure 9.1.

The scintillators are read out by photo-multiplier tubes (so-called PMTs). The PMT signals are fed to discrimators and to a coincidence unit. Upon coincidence, a trigger signal is sent from the coincidence unit to the chip through the MUROS (so-called shutter signal). The time between the passage of a particle through the three scintillators and the arrival of the shutter signal at the chip was measured to be about 100 ns. This delay is the result of the scintillator and PMT response times, the cable lengths and the processing times of the discriminators, the coincidence unit and the MUROS.

The trigger geometrical acceptance is slightly too large and some tracks may trigger the detector without traversing the sensitive volume. In the first measurement period, however, the software version would not permit to disregard empty frames and their content would be written to file. To decrease the probability to write empty files, the acquisition consisted in integrating the recorded frames over a period of 12 min. In this case, some frames contained more than one track and the analysis of those data requires a track finding algorithm. Later on, empty frames could be filtered out and single acquisitions were used: the recorded frames likely contain only one track and the need for such algorithm is less justified.

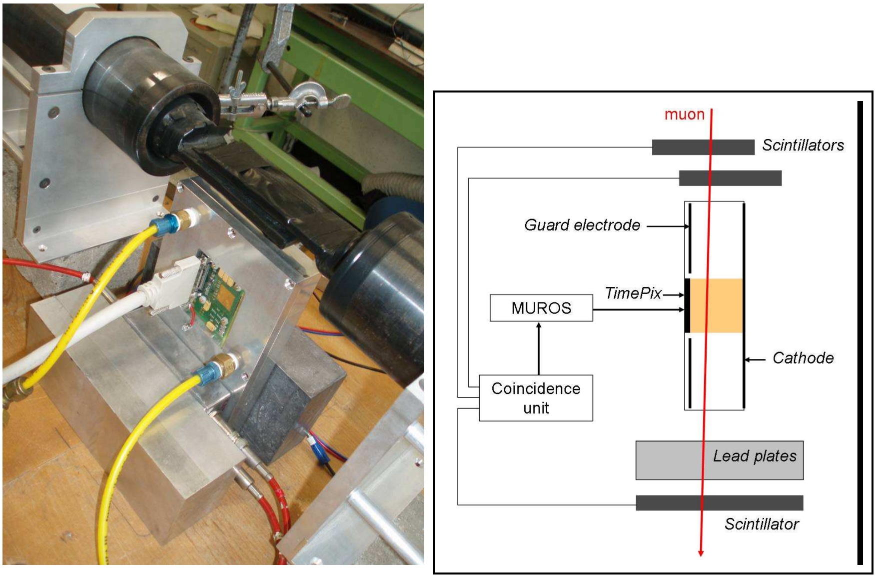

(a) (b)

Figure 9.1: *Photograph (a) and sketch (b) of the coincidence set-up. The lead plates and the third scintillator are not visible in the photograph.*

9.3 Measurements

9.3.1 Operating conditions

A series of measurements was performed at six values of grid voltage between -380 and -450 V in a gas mixture of He/iC$_4$H$_{10}$ 77/23. The trend of the gas gain G with the grid voltage V_g was measured and obeys the following relation:

$$G = 0.0231 \cdot \exp(0.030 V_\mathrm{g}) \tag{9.1}$$

The drift field was kept at 670 V/cm. The expected drift velocity and diffusion coefficients calculated by MAGBOLTZ are listed in Table 9.1.

9.3.2 Event example

An event is shown in Figure 9.2 together with the drift time distribution. Due to the time-walk input signals smaller than a few thousand electrons are detected

v_d (cm/μs)	D_t (μm/$\sqrt{cm}$)	D_l (μm/$\sqrt{cm}$)
2.4	195	144

Table 9.1: *Electron drift parameters calculated by MAGBOLTZ at 670 V/cm in He/iC$_4$H$_{10}$ 77/23. The chamber drift gap is 1 cm.*

later than larger ones (cf. chapter 8). This effect explains the right tail of the drift time distribution in Figure 9.2 (b).

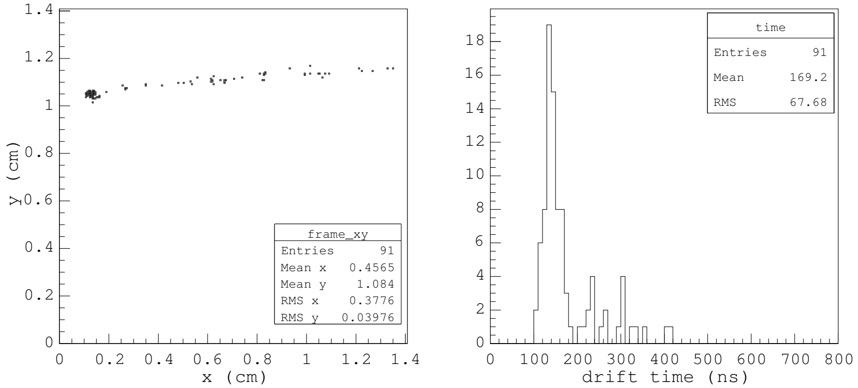

(a) (b)

Figure 9.2: *A cosmic track recorded in He/iC$_4$H$_{10}$ 77/23 at a grid voltage of -450 V (a) and the corresponding drift time distribution (b).*

The drift time of each detected electron is derived from the number of counted clock cycles C_hit. The latter is proportional to the time between the hit and the end of the shutter signal. Hence, the time Δt between the arrival of the shutter signal at the chip and the hit is:

$$\Delta t = (C_\mathrm{max} - C_\mathrm{hit}) \cdot \delta t \tag{9.2}$$

where $\delta t = 10$ ns is the duration of a clock cycle and C_max is the maximum number of clock cycles that can be recorded by a pixel during the shutter time. C_max is determined from the clock cycle distribution of all hits. Eventually, the drift time is obtained by adding to Δt the 100 ns delay due to the coincidence set-up.

9.3.3 Drift time distribution of all hits

At the various grid voltages, the drift time distributions of all hits have a similar shape: a tail on the right side and a peak on the left side. The sums of all distributions, corrected and not corrected for the effect of time-walk, are plotted in Figure 9.3. For a given track, the drift times corrected for time-walk are obtained by projecting all the hits onto the reconstructed track; this procedure is detailed in section 9.4.5.
The tail can be explained by the electron longitudinal diffusion and the time-walk while the peak is due to the primary electrons that arrive at the chip before the shutter signal. A pulse that crosses the threshold during the 100 ns delay may still be above threshold when the shutter signal arrives. In this case, the pixel counts during the full shutter time and the measured drift time is 100 ns.

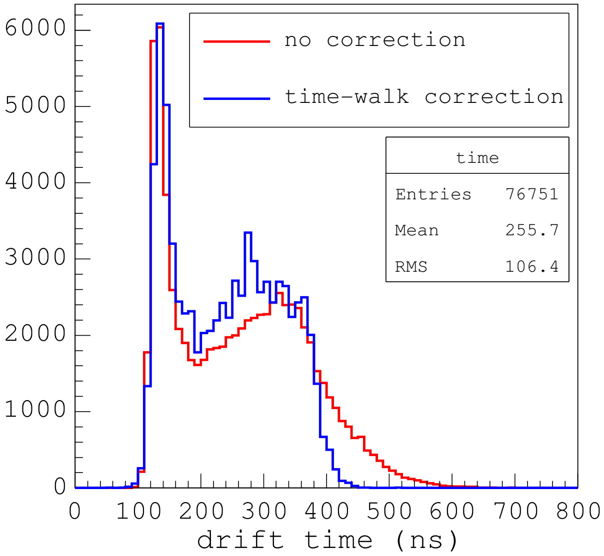

Figure 9.3: *Raw and time-walk corrected time distributions of all hits.*

The time distribution corrected for time-walk extends up to 400 ns which yields a drift velocity of 2.5 cm/μs. This agrees well with the prediction from MAGBOLTZ of 2.4 cm/μs.

9.4 Data analysis

Our goal is to measure the point resolution and the mean number of electron clusters per unit length (so-called cluster density). The analysis should hence reconstruct the initial positions of the detected electrons, group them into clusters. The cluster density is then determined from the distribution of the distances between clusters as will be explained in section 9.6. In the following, the various steps of the track reconstruction are detailed.

9.4.1 Definition of the axes

The track reconstruction is realized using a cartesian coordinate system with the x and y axes parallel to the chip rows and columns and with the origin at the bottom left corner of the pixel matrix. The projection of a track in the xy-plane defines the s-axis whose origin is at the intersection of the projected track with the y-axis. The four axes are drawn in Figure 9.4.

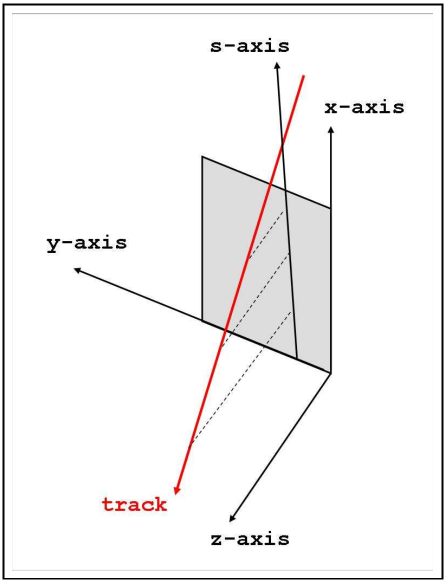

Figure 9.4: *Coordinate system used for the track reconstruction.*

9.4.2 Hit selection

The hit selection is intended for suppressing eventual noise hits. The time distribution of a typical event has a width of about 500 ns and a main peak when most of the hits are recorded. Hence, hits recorded 500 ns before or after this peak are likely noise hits and are removed from the distribution. Although the probability that the distribution still contains noise hits is very small, a second cut is applied to the time distribution. The r.m.s. of the distribution is used to suppress hits outside a window centered at the distribution maximum and with a half width of three times the r.m.s..

If a noise hit is still identified as a signal hit, it has a large probability to be located far from the track and likely will be rejected during the track fit.

9.4.3 Track finding

Some frames contain more than one track and a dedicated algorithm is used to separate them. The algorithm is based on the Hough transform and identifies straight lines in a given pattern of points [219].

The idea of the Hough transform in two dimensions is the following. A line passing through a hit is defined by two parameters, for instance the distance of closest approach to the origin ρ and an angle θ. When the line is rotated around the hit, these parameters change and eventually all the lines passing through this hit correspond to a curve in the $\rho\theta$-plane (so-called Hough plane). Hence, all hits distributed along a line (ρ_0,θ_0) in the xy-plane yield curves in the Hough plane which cross at the point (ρ_0,θ_0). In practice, the Hough plane is a two-dimensional histogram and estimates of the projected track parameters are obtained by searching for the position of the maximum in this histogram.

This technique is illustrated in Figure 9.5 where a pattern of hits from two tracks is shown, together with a top view of the two-dimensional histogram in the Hough space. Two main intersections corresponding to two peaks in the histogram are seen in the Hough space. The selected track is the one that corresponds to the highest peak.

The selection of the hits belonging to the track is done by first calculating the shortest distances between the hit positions (taken at the center of the pixels) and the Hough line: these distances are called the residuals. The mean and r.m.s. of the residuals to the Hough line are then used to reject hits with residuals three times the r.m.s. larger than the mean.

The Hough track is a good approximation of the true projected track. As it will be shown in section 9.5.1, the distribution of the hits w.r.t. to the projected track is governed primarily by the transverse diffusion. Hence, 99 % of the hits should be at a distance smaller than 3 σ from the track (and from the Hough track) and mainly noise hits or δ-rays are removed when such cut is made on the residuals.

9.4.4 Track fit in the xy-plane

The parameters of the projected track in the xy-plane are precisely determined by fitting a straight line to the hit pattern [43]. The line parameters are determined by a linear regression method which consists in minimizing the quantity:

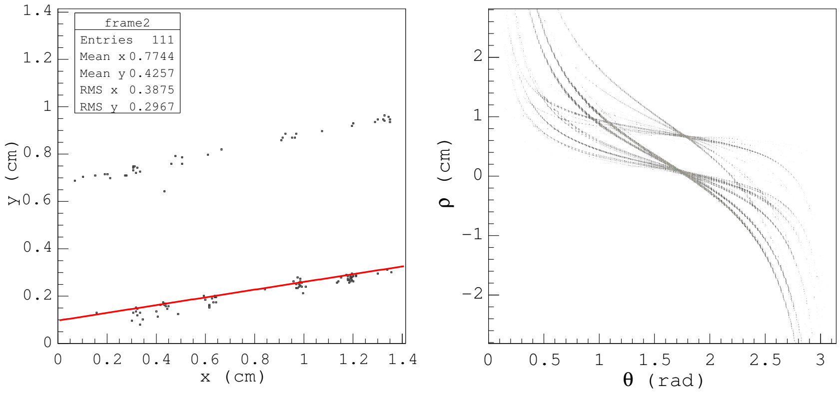

(a) (b)

Figure 9.5: *Hit pattern showing the Hough line (a) and a top view of the corresponding histogram in the Hough space (b).*

$$S = \Sigma_1^N (y_\mathrm{i} - a x_\mathrm{i} - b)^2 \tag{9.3}$$

where (a,b) are the parameters of the line and N the number of hits. If S is to be minimum, these parameters should be equal to:

$$a = \frac{1/N \cdot \Sigma(x_\mathrm{i} - \overline{x}) \cdot (y_\mathrm{i} - \overline{y})}{1/N \cdot \Sigma(x_\mathrm{i} - \overline{x})^2} \tag{9.4}$$

and

$$b = \overline{y} - a \cdot \overline{x} \tag{9.5}$$

with $\overline{x}$ and $\overline{y}$ the means of the hit coordinates along the pixel rows and columns respectively. The goodness of the fit is estimated by means of the correlation coefficient:

$$R = \frac{1/N \cdot \Sigma(x_\mathrm{i} - \overline{x}) \cdot (y_\mathrm{i} - \overline{y})}{\sigma_x \sigma_y} \tag{9.6}$$

which is equal to 1 if all points are aligned (σ_x and σ_y are the hit coordinates r.m.s. along the pixel rows and columns respectively).

This procedure is illustrated in Figure 9.6 (a) where a pattern of hits and the fitted line are shown. Using the fit parameters, one calculates the residuals of the hits coordinates w.r.t the line and the coordinates along the s-axis.

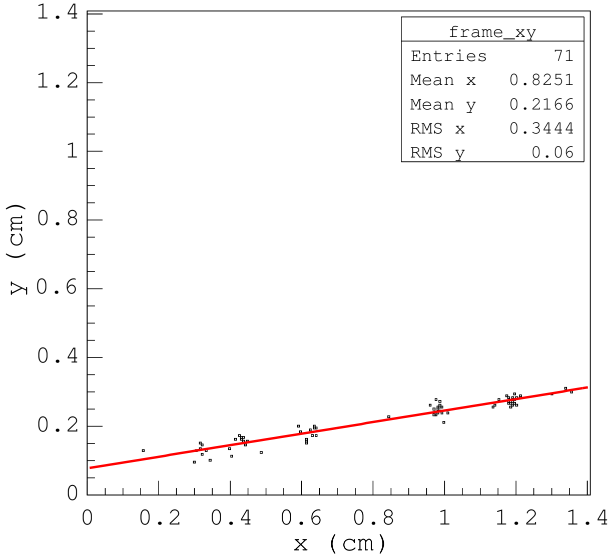

(a)

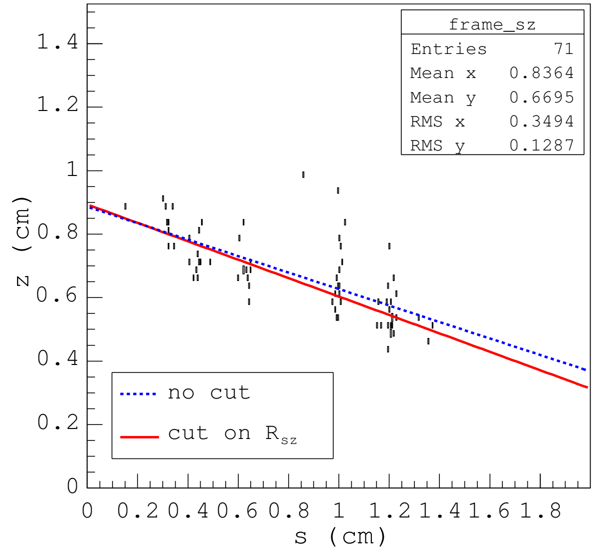

(b)

Figure 9.6: *Track fit in the xy-plane (a) and the sz-plane (b).*

9.4.5 Track fit in the sz-plane

The coordinates of the hits along the z-axis are determined from:

$$z_{\mathrm{i}} = ((C_{\mathrm{max}} - C_{\mathrm{i}}) \cdot \delta t + t_{\mathrm{delay}}) \cdot v_{\mathrm{d}} \tag{9.7}$$

where $v_{\mathrm{d}} = 2.5$ cm/μs is the measured drift velocity.
The fit of the track in the sz-plane is done with the method described in the previous section. Due to the time-walk, a significant fraction of hits has a number of clock cycles lower than expected which leads to over-estimated drift lengths. As a result, the hits in the sz-plane exhibit a large spread (Figure 9.6 (b)) and the track parameters in this plane are not accurately determined.

In order to improve the precision on the track parameters, the fit is done twice. First, all the hits are included and their residuals to the fitted line are calculated. This time, the residuals are calculated as the distances from the hits to the fitted line at constant s. In the second fit, only hits with residuals within one sigma from the mean are used. The two fitted lines are drawn in Figure 9.6 (b). Finally, the reconstructed initial positions of the primary electrons are the positions of the hits projected onto the fitted line.

9.5 Spatial resolution study

A TPC is intended for measuring the momentum of particles and what matters eventually is the resolution on the helix parameters that are fitted to the curved tracks. This resolution depends on the point resolutions σ_{xy} and σ_z and on the number of measured points along the tracks (Equations 4.9 and 4.11).

The spread of the hits w.r.t. to the reconstructed tracks in the xy and sz-plane is an indication of the point resolution of the detector. Ideally, the resolution should be derived from the spread of the hits w.r.t. the track measured by precise external detectors (*e.g.* silicon pixel detectors). Our experimental setup does not provide such information and the fitted track is used instead.

9.5.1 Hit residuals in the xy-plane and drift length

Introduction

In the xy-plane, the residuals r_{xy} of the hit coordinates w.r.t. to the fitted projected track are governed by the following effects:

- the electron transverse diffusion in the gas. At a given distance from the anode, the coordinates of an electron in a plane perpendicular to the drift field are distributed according to a two-dimensional gaussian;
- the segmentation of the readout plane. The position of a detected electron is uniformly distributed over the pixel area;

- the range of the primary electrons.

  Delta-rays with sufficient energy generate some hits far from the projected track and hence increase the variance of the residual distribution. In pure helium, the probability that an ejected electron covers an effective distance (or practical range) larger than 100 μm is about 2 % ([53] and Equation 3.17). Assuming a cosmic path length of 14 mm and 25.6 primary interactions per centimeter, the probability per track is 60 % [119]. We thus expect the δ-rays to impact on the shape of the residual distribution;

- the signal induction on neighbouring pixels (enhanced by SiProt) which produces indirect hits next to direct hits.

  Let's assume that the gain distribution, the pixel thresholds and the SiProt thickness and composition are uniform across the chip area and consider a pixel above which no electron multiplication takes place.

  In this case, the probability that this pixel records an indirect hit is proportional to the number of avalanches that develop above the neighbouring pixels. Because of the transverse diffusion, this number decreases with the distance from the projected track. Accordingly, the number of indirect hits per direct hit also decreases with this distance and the residual distribution of all hits should be slightly more peaked than that of the direct hits.

  We think that this effect has little impact on the residuals and will check this statement by comparing the shape of the residual distributions of hits of short and large drift lengths;

- the error on the fit parameters biases the measured residuals.

  The effect on the residual distribution should be very little because the track projected on the pixel plane is accurately measured. Nevertheless, to ensure a precise estimation of the projected track parameters, only tracks with a minimum length of 0.4 cm are used in the analysis.

In what follows, only the effects of diffusion and segmentation are considered.

Variance of the residuals

At the pixel plane, the coordinates (x,y) of an electron produced at a distance z from the anode plane is distributed according to the following two-dimensional gaussian (cf. section 2.3.3):

$$G(x, y, z) = \frac{1}{2\pi D_{\mathrm{t}}^2 z} \exp\left(-\frac{1}{2} \frac{x^2 + y^2}{D_{\mathrm{t}}^2 z} \right) \tag{9.8}$$

which implies that the projected distributions against the x and y axes are a one-dimensional gaussian of same width as $G(x,y,z)$. Because the orientation of the x and y axes is arbitrary, the residuals r_{xy} are also gaussian distributed:

$$G(r_{\mathrm{xy}}, z) = \frac{1}{D_{\mathrm{t}}\sqrt{2\pi z}} \exp\left(-\frac{1}{2}\frac{r_{\mathrm{xy}}^2}{D_{\mathrm{t}}^2 z}\right) \tag{9.9}$$

by definition, the variance of the residual is then:

$$\sigma_{\mathrm{xy}}^2 = D_{\mathrm{t}}^2 \cdot z \tag{9.10}$$

The coordinates (x,y) of a detected electron are uniformly distributed over the pixel area and are determined with a precision of:

$$\sigma_{\mathrm{xy},0} = p/\sqrt{12} \tag{9.11}$$

which is valid if the grid holes and pixels are arranged in a square pattern and have the same pitch p. With a pitch of 55 μm, a point resolution at zero drift length of 16 μm is expected. The two contributions to the variance are not correlated and add up quadratically:

$$\sigma_{\mathrm{xy}}^2(z) = p^2/12 + D_{\mathrm{t}}^2 \cdot z \tag{9.12}$$

If the other effects previously listed can be neglected, it should be possible to measure D_{t} and $\sigma_{\mathrm{xy},0}$ by fitting a linear function to $(\sigma_{\mathrm{xy}}^2, z)$ points.

Measurements

The two-dimensional histogram of the measured hit residuals r_{xy} with the reconstructed drift length z is shown in Figure 9.7 (a).

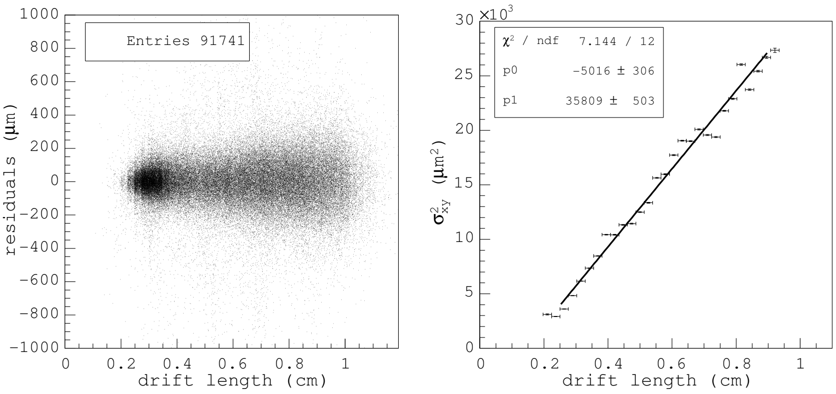

(a) (b)

Figure 9.7: *Two-dimensional histogram of the hit coordinate residuals in the xy-plane and the drift length (a). Variance of the residuals and drift length (b).*

The variance of the residuals at a given z is determined by dividing the two-dimensional histogram in slices along the z-axis. The entries in each slice (or in one-dimensional histogram) have similar drift lengths. Afterwards, a gaussian function is fitted to each one-dimensional histogram and the function parameters are stored. This slicing-fitting routine is available within the ROOT data analysis program [220].

The trend of the variance of the residuals with drift length is illustrated in Figure 9.7 (b). Due to the 100 ns delay and the 2.5 cm/μs drift velocity, the variance is not measured at drift lengths below 0.25 cm. Also, the points between 0.25 and 0.5 cm correspond to the peak of the drift time distribution and might be wrongly measured. Still, this effect seems small as the observed trend is fairly linear up to $z \sim 0.9$ cm. At larger distances, the statistics are too low and the points are not shown.

A straight line is then fitted to the points. From the line slope, the measured transverse diffusion coefficient is $189 \pm 2\ \mu\text{m}/\sqrt{cm}$, in good agreement with the MAGBOLTZ prediction of $195\ \mu\text{m}/\sqrt{cm}$. The extrapolation to zero drift length yields an unphysical negative value which could be attributed to a systematic error on the drift time (error on the 100 ns delay or drift velocity).

Effect of the SiProt

As previously mentioned, the residual distribution at short drift length should be slightly more peaked than at larger distances. This is illustrated in Figure 9.8 where a gaussian function was fitted to the distributions at $z = 0.3$–0.4 cm and $z = 0.7$–0.8 cm.

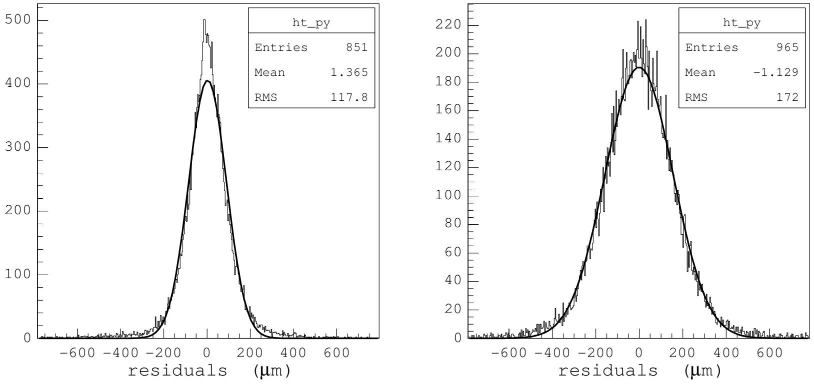

(a) (b)

Figure 9.8: *Residual distributions in the xy-plane at $z = 0.3$–0.4 cm (a) and $z = 0.7$–0.8 cm (b).*

In the latter case, the distribution is gaussian while at $z = 0.3$–0.4 cm the relative number of hits with small residuals increases. In both cases, a tail on the two sides of the distributions are observed and can be attributed to the δ-rays.

9.5.2 Hit residuals in the *sz*-plane

The distribution of the residuals in the sz-plane is also governed by the effects listed in section 9.5.1. In this case, however, the point resolution at zero drift length should be limited by the clock frequency. At 100 MHz and for a drift velocity of 2.5 cm/μsec, 70 μm are expected.

Projections of the residual distribution at $z = 0.3$–0.4 cm (a) and $z = 0.7$–0.8 cm are shown in Figure 9.9. Long tails that correspond to late detection times are observed due to the effect of the time-walk. Furthermore, the distributions are not centered at zero which shows that the residuals were not accurately measured. Accordingly, the point resolution σ_{z} is very poor.

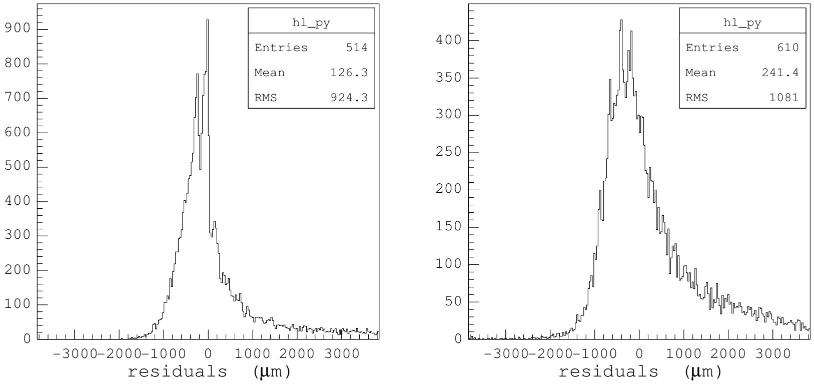

(a) (b)

Figure 9.9: *Residual distributions in the sz-plane at z = 0.3–0.4 cm (a) and z = 0.7–0.8 cm (b).*

9.5.3 Discussion

The measured point resolution in the pixel plane is compatible with the diffusion limit. In a GridPix TPC, this should improve the tracking performance for particles traversing the endplates, in particular those emitted at a small angle w.r.t. to the beam pipe (forward direction). In standard TPCs, the tracking performance degrades in the forward region because of a limited granularity close to the beam axis. With pixels, the performance could in principle be maintained down to very small angles because most primary electrons would be collected on individual pixels. In this case, the point resolution along the drift direction would be very important. Our measurements show that it is rather poor due to the effect of the time-walk. Nevertheless, it could be improved with a thinner SiProt (or without SiProt, *e.g.* with multi-stage grids) or by a design of the electronics that would minimize the time-walk or allow to correct for it (*e.g.* if both the time and charge information are available at the pixel).

9.6 Study of the number of clusters

A motivation for a GridPix TPC is the possibility to measure the cluster density along the tracks and use this information for particle identification. In order to identify a cluster, the electron diffusion should be as small as possible. In this respect our experimental conditions (small gap, large distance between clusters) are well suited. The study is realized with data recorded at a grid voltage of -450 V in order to have the highest detection efficiency for single electrons ($\sim$ 95 %).

The hits are grouped into clusters by comparing the distances between two consecutive hits along the reconstructed track to a certain step. If the distance between two hits is larger than the step, the hits belong to different clusters, otherwise to the same. Afterwards, the position of each cluster is calculated as the centre-of-gravity of the hits belonging to this cluster.
The distribution of the distances l between two adjacent clusters, determined with a step size of 275 μm (*i.e.* 5 pixels), is shown in Figure 9.10 (a). The number of clusters per unit length is then derived by fitting a decreasing exponential function to the distribution:

$$f(l) = p_0 \exp(-p_1 l) \tag{9.13}$$

where p_0 and p_1 are the function parameters and p_1 is an estimate of the number of clusters per unit length n_c (Equation 3.19). Because the shape of the distribution departs from that of an exponential for distances close to the distribution maximum, the fit is performed from a given distance d^* to 5000 μm. For 1000 $\mu\mathrm{m} \leq d^* \leq 2000$ μm, the absolute variation of p_1 is smaller than 0.5 and the value of n_c is taken as the mean value of p_1 over that range.

The advantage of this counting technique w.r.t. to the one used in [176] is that the tail of the distribution (and hence p_1 and n_c) is relatively insensitive to the step size because it corresponds to hits separated by large distances (w.r.t. the mean distance between clusters).

The obtained number of clusters per unit length n_c depends on the step size as illustrated in Figure 9.10 (b). In the same plot, the prediction from the HEED program of 25.6 clusters/cm for 300 MeV muons is indicated by a dashed line. Also, the counting algorithm was applied to HEED generated tracks and the resulting trend is also shown (the number of tracks in both cases is similar). Detection inefficiency, charge sharing between pixels and the effect of time-walk were neglected. The tracks are oriented parallel to the pixel plane with a uniform

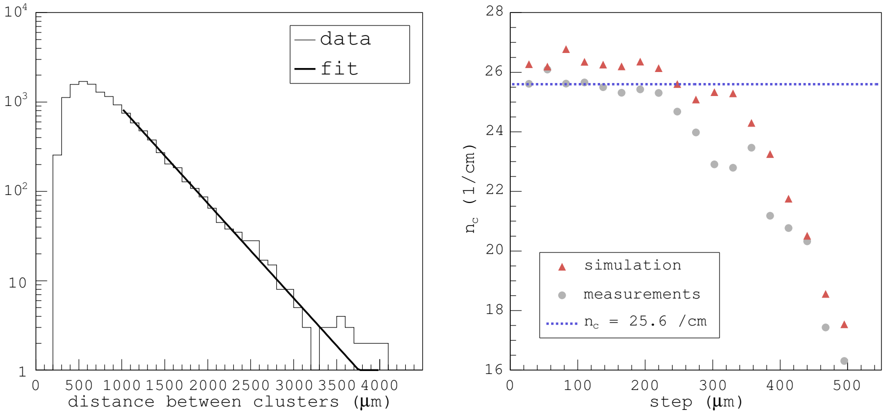

Figure 9.10: *Distribution of the distances between adjacent clusters obtained with a step size of 275 μm (i.e. 5 pixels) (a). Number of clusters per centimeter as a function of the step size (b).*

distribution along the drift direction and an angle w.r.t. to the x-axis uniformly distributed between -$\pi/4$ and $\pi/4$.

For step sizes of 20–200 μm, the values of n_c derived from the simulated distributions is about 26 clusters/cm, close to the input value of 25.6 clusters/cm. This supports the validity of our counting technique. In the same range of step sizes, the measured value of n_c is close to 25.5 clusters/cm which is in good agreement with the HEED prediction. For larger step sizes, the probability to count different clusters as a single cluster increases such that the distribution tail is not exponential anymore. The counting technique yields inaccurate results, in particular n_c drops.

9.7 Conclusion

A small TPC read out by a SiProtected and InGrid-equipped TimePix chip was built and used to record tracks of cosmic particles. During one month, the TPC was continuously operated in a mixture of He/iC$_4$H$_{10}$ 77/23 until it was stopped and a few thousand tracks were recorded.

The data analysis consisted in reconstructing the tracks in three dimensions and studying the distribution of hits along the tracks. Doing so, the drift velocity and transverse diffusion coefficient could be measured and showed a good agreement with MAGBOLTZ calculations.

The estimated point resolution in the pixel plane σ_{xy} is close to the diffusion limit. Accordingly, with a diffusion coefficient of 20 μm/$\sqrt{cm}$ (at 40 V/cm and 4 T in an Ar/CH_4 95/5 gas mixture), a point resolution of 200 μm could in principle be achieved for radial tracks (averaged over a drift length of 2 m). The ILC performance goal for a pad readout TPC is $\sigma_{\mathrm{xy}} \sim 100$ μm. With a pixel TPC the number of points measured along the track would be much larger (*e.g.* 40 times larger in argon-based mixtures for radial tracks) and the final precision on the track parameters in the readout plane should be equivalent or better, matching the ILC requirement.

The point resolution along the drift direction σ_{z} is severely affected by the time-walk and exceeds by far the expectation from the longitudinal diffusion limit (by a factor seven). It might be improved with a thinner SiProt thickness or a different design of the electronics.

The numbers just quoted give a first impression on the detector performance and more tests with external tracking information will be necessary to draw a final statement.

An electron cluster density along the tracks of 25.5 clusters/cm was measured, compatible with simulation results. This agreement tends to prove the cluster counting capability of a GridPix chamber of 1 cm drift gap in He/iC_4H_{10} 77/23. The extrapolation to other gas mixtures, larger drift gaps and different particle types and energies remains to be done. In this perspective, data have recently been collected at the CERN test beam facilities and their analysis is ongoing.

In view of a possible application at ILC, if a diffusion-limited point resolution can be achieved, a pixel TPC might show a better performance than standard readout TPCs in some respects. In particular, the tracking performance of GridPix in the forward regions should be superior because of the larger statistics and a few very accurately measured points close to the endplates. The dE/dx resolution should be comparable if the energy loss is measured by electron counting and may be improved by cluster counting.

These conclusions assume a full coverage of the TPC endplates with GridPix detectors. Several practical aspects *e.g.* detector assembly, powering and cooling are not considered and would impact on the final design and performance of a pixel TPC.

Chapter 10

Résumé de thèse

Cette thèse fut effectuée en cotutelle avec l'Université d'Amsterdam et de Paris Sud XI. Elle comporte donc un résumé substantiel en langue française où sont présentés les principaux résultats. De plus amples détails sont fournis dans le texte anglais.

Cette thèse traite de la fabrication et des tests d'un nouveau détecteur gazeux à très grand nombre de canaux de lecture. Ce détecteur appellé GridPix permet de localiser un électron liberé dans le gaz avec une grande précision et une efficacité proche de 100 %. Il est consitué d'une grille de multiplication d'électrons Micromegas et d'une puce électronique à pixels pour lire les signaux. GridPix pourrait être utilisé comme trajectographe à haute résolution pour des expériences de physique des particules au futur collisionneur linéaire ILC.

L'ILC est un accélérateur à électrons qui devrait fonctionner en parallèle avec le grand collisionneur de hadrons LHC bientôt opérationel au CERN à Genève. Les motivations pour sa construction ainsi que ses principales caractéristiques techniques sont presentées dans le premier paragraphe. Le fonctionnement des détecteurs gazeux à lecture électronique est expliqué dans le paragraphe suivant.

La sensibilité d'un détecteur GridPix aux radiations ionisantes est supérieure lorsque la grille Micromegas est fabriquée directement sur la puce à pixels. Cette grille "intégrée" est appellée InGrid et fut d'abord fabriquée sur des galettes de silicium pour étudier son gain, sa résolution en énergie et sa transparence ionique. La fabrication et les mesures de ces propriétés sont presentées dans le troisième paragraphe. Avec une InGrid, la sensibilité du détecteur dépend principalement du gain et de ses fluctuations. Ce sujet est examiné au moyen de simulations informatiques dans la section suivante.

Des petites TPC formées d'une InGrid et de la puce à pixels TimePix ont été construites. L'étude de leur réponse aux rayons X mous et aux particules cosmiques est détaillée dans le dernier paragraphe. Sur la base de mesures de l'efficacité de détection d'électrons uniques et de la résolution spatiale dans le plan de pixels, nous discuterons les avantages d'une TPC à lecture pixels à l'ILC.

10.1 Le futur collisionneur linéaire à électrons

L'ILC permettra de réaliser des collisions entre électrons et positrons à une énergie de 500 GeV dans le centre de masse et à une luminosité de $2{\cdot}10^{34}$ $\mathrm{cm}^{-2}\mathrm{s}^{-1}$ [1]. Les particules seront accélérées par paquets de $2{\cdot}10^{10}$ à des vitesses proches de celle de la lumière. Les faisceaux seront composés de trains de 1000–5000 paquets d'une durée de 0.95 ms et qui se rencontreront toutes les 200 ms. La mise en route de cet accélérateur de 31 km pourrait débuter dans la décennie 2020.

Contrairement à un accélérateur de hadrons qui sont des particules composites, un accélérateur électron/positron fait entrer en collision des particules ponctuelles. Ainsi toute l'énergie des particules est mise en jeu lors des collisions et l'état initial est bien défini. Cette particularité facilite l'analyse des résultats des collisions et permet d'effectuer des mesures de grande précision.

Si le boson de Higgs est découvert au LHC, l'ILC sera un outil unique pour mesurer ses propriétés et ainsi étudier en détail les mécanismes responsables de la masse des particules élémentaires et de la brisure de symétrie électrofaible. Il permettra aussi de tester les prédictions du Modèle Standard, la théorie actuelle des particules élémentaires et de leurs interactions, avec une précision supérieure à celle des accélérateurs actuels. Si des déviations sont décelées, différentes extensions du Modèle Standard comme les modèles super-symétriques et les modèles à dimensions supplémentaires pourront être mise à l'épreuve de l'expérience.

10.2 Détecteurs gazeux à lecture électronique

Les détecteurs utilisés dans les expériences de physique des particules permettent de mesurer la position et l'energie des particules produites lors des collisions. Ils sont composés d'un milieu sensible (gaz, liquide ou solide) et d'un système de lecture. Une particule traversant le milieu sensible y depose de l'énergie sous forme de chaleur, de lumière ou de charge électrique. Ce signal est détecté par le système de lecture et renseigne sur le temps de passage de la particule et sur l'energie déposée. Si la particule est totalement absorbée dans le milieu sensible son énergie totale peut être mesurée. Si le mileu sensible est lu en différent endroits (avec plusieurs voies de lecture) sa position peut être précisément mesurée.

10.2.1 Principe de fonctionnement

Le fonctionnement d'un détecteur gazeux est fondé sur l'ionisation des molécules du gaz, la dérive et la multiplication des électrons primaires et la lecture du signal. Dans les détecteurs récents la lecture est électronique. Dans le cas de particules chargées traversant le gaz, l'ionisation est engendrée le long de la trajectoire. Un trajectographe permet de mesurer la position de ces électrons primaires: ceux-ci dérivent sous l'influence d'un champ électrique jusqu'aux électrodes de lecture où ils sont détectés. En général la charge primaire est trop faible pour être mesurée par l'électronique de lecture et les électrons primaires sont donc multipliés dans le gaz. La multiplication se déroule dans une région de fort champ electrique où l'énergie acquise par les électrons entre deux collisions avec les molécules de gaz est parfois suffisante pour libérer de nouveaux électrons. Ces derniers à leur tour ionisent le gaz: une avalanche électronique se développe jusqu'à ce que tous les électrons soient collectés sur l'électrode de lecture. Le signal induit sur l'électrode est détecté par un circuit électronique.

10.2.2 La Chambre à Projection Temporelle

La Chambre à Projection Temporelle ou TPC est une chambre cylindrique emplie de gaz et fermée à ses extrémités par deux plans de lecture et divisée en deux volumes égaux par un plan central porté à haute tension, l'électrode de dérive. Les plans de lecture sont équipés d'un système de multiplication d'électrons et sont segmentés en damiers. Ces derniers sont connectés à des circuits électroniques placés sur les plans de lecture à l'extérieur de la chambre. A l'intérieur de la TPC règne un champ électrique axial uniforme.

Les électrons primaires libérés par une particule chargée dérivent vers un des plans de lecture où ils sont multipliés puis détectés. Ainsi une projection de la trace sur le plan de lecture est obtenue. La vitesse de dérive des électrons est constante, ce qui permet de déduire la troisième coordonnée du temps de dérive. Un champ magnétique parallèle au champ électrique courbe les trajectoires des particules chargées. La courbure est proportionelle à l'impulsion qui peut ainsi être mesurée. Ce champ permet aussi d'améliorer la précision spatiale en réduisant la diffusion transverse des électrons.

10.2.3 Le système de multiplication d'électrons Micromegas

Micromegas (Micro Mesh Gaseous Structure) est une grille conductrice d'une épaisseur de 5–20 μm, au pas de 20–50 μm maintenue par des plots isolants à 50–150 μm d'un plan de lecture [146]. Lorsque la grille est portée à un potentiel de quelques centaines de volts, un fort champ électrique est généré entre la grille et le plan de lecture. C'est la région d'amplification, où les électrons sont multipliés. Entre la grille et l'électrode de dérive règne un champ faible. C'est l'espace de dérive où les électrons primaires sont libérés. Le passage des électrons primaires de l'espace de dérive à l'espace d'amplification est favorisé par la compression des lignes de champ à proximité des trous de la grille.

10.2.4 Lecture à pixels d'une TPC Micromegas

Dans Micromegas les avalanches électroniques se développent sur des distances de quelques dizaines de microns. Les signaux sont donc très rapides et l'extension transverse des avalanches limitée à 10–20 μm, ce qui est petit par rapport à la taille des damiers (quelques mm^2). En conséquence, une avalanche est collectée sur un damier et la résolution spatiale est limitée par la taille des damiers.

La résolution peut être améliorée en étalant le signal sur plusieurs damiers et en mesurant le centre de gravité des signaux. Cette approche nécessite le dépôt d'une couche résistive sur le plan de lecture et donne de très bons résultats [31]. Une seconde solution consiste à utiliser des damiers plus petits, ce qui implique une augmentation du nombre de voies d'électronique et un encombrement conséquent des plans de lecture à l'extérieur de la TPC. Toutefois, l'utilisation de puces à pixels comme anodes collectrices permet d'intégrer une grande partie de l'électronique sur de petites surfaces et donc d'augmenter considérablement le nombre de canaux.

Le faible bruit électronique à l'entrée des pixels ainsi que leur petite taille (*e.g.* 55×55 μm^2 pour la puce TimePix [175]) permet la détection d'électrons uniques avec une efficacité proche de 100 %. Une TPC à pixels bénéficierait des avantages suivants:

- très grand nombre de points de mesure le long des traces ($\sim$ 90 /cm dans l'argon) ce qui améliorerait la précision sur l'impulsion;
- pour des traces traversant un plan de lecture, quelques points seraient en principe mesurés avec une précision de l'ordre de 20 μm;
- mesure du dE/dx par comptage des électrons primaires et donc peu affectée par les fluctuations de gain. Si la diffusion est suffisamment petite, la précision peut être améliorée par comptage des paquets d'électrons;
- identification et exclusion des électrons delta lors des mesures de trajectoire et de dE/dx, celles-ci seraient alors plus précises;
- fonctionnement à bas gains et donc à faible retour d'ions, en particulier si une efficacité de détection réduite est acceptable: un gain de 500 est en principe suffisant pour obtenir une efficacité de 50 %.

L'efficacité de détection est la probabilité que la charge induite sur la surface conductrice du pixel (ou pad) lors de la multiplication d'un électron primaire soit supérieure au seuil de détection de l'électronique du pixel. La charge induite dépend principalement du nombre de paires électron/ion formées dans l'avalanche et de la position relative de l'avalanche par rapport au pad. Pour un nombre de paires donné, l'efficacité est maximale lorsque l'avalanche se développe au-dessus du pad. L'alignement des trous de la grille avec les pads est donc très important mais est difficilement réalisable avec des grilles Micromegas standard.

En revanche la fabrication de la grille directement sur la puce par des techniques de microélectronique permet un alignement de l'ordre du micron.

10.3 InGrid, un Micromegas intégré sur silicium

InGrid fut d'abord fabriquée sur des gallettes de silicium afin d'améliorer le procédé de fabrication et de mesurer ses propriétés d'amplification et de retour d'ions. Le premier paragraphe décrit la fabrication, les résultats des tests sont présentés dans les quatre suivants.

10.3.1 Fabrication

InGrid est formée d'une anode, de pillers isolants et d'une grille. Elle est fabriquée sur des galettes de 100 mm de diamètre. Pour étudier l'impact de la géométrie de la grille sur les performances, chaque galette contient 12 InGrids d'une surface de 3.14 cm^2 et de pas et diamètres de trous differents (cf. chapitre 5). Les étapes principales de la fabrication sont décrites ci-dessous:

- dépôt par "sputtering" d'une couche mince de 200 nm d'aluminium sur la galette. La couche est gravée par photolithographie;
- dépôt d'un film photosensible d'épaisseur variable entre 20 et 100 μm. Au moyen d'un masque, certaines regions du film sont exposées à un rayonnement UV et deviennent insolubles dans une solution propre au film. Les régions exposées deviendront les pilliers;
- dépôt d'environ 1 μm d'aluminium sur le film photosensible. La couche est gravée de manière à définir 12 grilles rondes de 2 cm de diamètre;
- dissolution à travers les trous des régions du film non exposées.

Afin de faciliter les tests, la galette est découpée de manière à obtenir des InGrids individuelles qui sont ensuite montées sur des supports isolants. Les variations sur la surface des grilles de l'épaisseur du film (et donc de la distance anode-grille) et du diamètre des trous sont inférieures à 1 % et 1 μm r.m.s. respectivement.

10.3.2 Efficacité de collection des électrons

L'efficacité de collection est la probabilité qu'un électron libéré dans l'espace de dérive atteigne l'espace d'amplification. Elle dépend principalement de la configuration des lignes de champ électrique et de la diffusion des électrons dans la région où les lignes se compressent. C'est à dire des champs d'amplification et de dérive, de la géométrie de la grille et du mélange gazeux.

Mesures

L'influence des paramètres cités ci-dessus a été étudiée en mesurant la position du pic photo-électrique du fer en fonction du champ de dérive. La position est proportionelle au produit du nombre d'électrons primaires résultant de l'absorption d'un quantum du fer dans le gaz, de l'efficacité de collection et du gain. Ses variations nous renseignent donc sur le gain effectif. Cette mesure fût répétée avec des grilles de différentes géométries (épaisseur de 1 μm, distance anode-grille de 90 μm environ) et dans différents mélanges à base d'argon.

Influence de la géométrie de la grille

Les variations de la position du pic avec le rapport des champs sont présentées dans la Figure 10.1. A un rapport donné la position du pic varie significativement d'une grille à l'autre. Cette observation peut être expliquée par les différences de distances anode-grille (et donc de gain) et d'efficacités de collection.

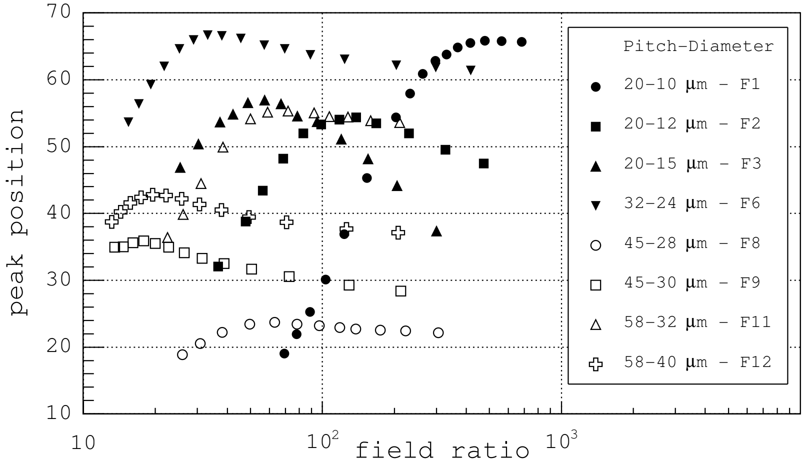

Figure 10.1: *Position du pic du fer et rapport des champs d'InGrids de géométries différentes dans l'Ar/*iC_4H_{10} *95/5. La tension de grille est de -368 V et la distance anode-grille de 90* μ*m environ.*

Pour une InGrid donnée, la position du pic augmente d'abord avec le rapport des champs, atteint un maximum et décroît ensuite. Cette tendance est interprétée comme résultant des effets opposés de la compression des lignes de champ et de la diffusion. Le premier tend à diriger de plus en plus d'électrons dans les trous tandis que par diffusion, des électrons peuvent arriver sur la grille et ne pas participer au signal. De plus, le champ d'amplification d'une grille à forte transparence optique dépend du champ de dérive. Ainsi le gain peut diminuer à hauts rapports des champs.

L'efficacité des grilles à petits trous (10–15 μm) ne semble pas très bonne, le signal étant maximum à très haut rapport de champ (grille F1 dans la figure 10.1) ou chutant fortement une fois le maximum atteint (F2 et F3). Pour des diamètres supérieurs le maximum du signal est atteint à un plus petit rapport de champ et sa décroissance, moins prononcée, pourrait être causée par une baisse de gain seulement. En effet, la diminution est corrélée à la transparence optique: le signal des grilles F8 et F11 est presque constant tandis que celui des grilles F6, F9 et F12 diminue progressivement.

Influence du mélange gazeux

Les variations de la position du pic ont été mesurées avec la grille F11 dans des mélanges Ar/CO_2 et Ar/iC_4H_{10}. Le rapport des champs auquel la position est maximale décroît avec la concentration du gaz poly-atomique (appellé quencher) car les coefficients de diffusion diminuent. A concentrations égales le maximum est atteint pour un même rapport de champ. Cette observation est en accord avec le fait que pour des champs supérieurs à quelques kV/cm, les coefficients de diffusion dépendent peu du quencher mais principalement de sa concentration.

Conclusion

Dans une TPC avec une lecture à damiers les barycentres de segments de traces sont mesurés et la précision sur un barycentre (et finalement sur les paramètres de la trace) dépend du nombre d'électrons qui contribuent au signaux. Egalement, avec des pixels le nombre de points de mesure est directement proportionnel au nombres d'électrons collectés. Dans les deux cas l'efficacité de collection doit contribuer à la résolution spatiale. Il est donc souhaitable d'avoir une efficacité la plus élevée possible.

Nos mesures montrent que l'efficacité chute au-dessus d'un certain champ de dérive $E_{\mathrm{D}}^{\mathrm{M}}$ qui dépend principalement de la géométrie de la grille. Parce que le champ d'une TPC est choisi de manière à obtenir la plus grande vitesse ou la plus petite diffusion, $E_{\mathrm{D}}^{\mathrm{M}}$ doit être le plus petit possible pour ne pas ajouter de contraintes supplémentaires sur le choix du champ. Cette condition semble être le mieux réalisée avec des InGrids dont le pas est supérieur à 32 μm.

10.3.3 Gain

Le gain dépend principalement du mélange gazeux, du champ d'amplification et de la distance anode-grille. Les deux premiers paramètres déterminent le nombre d'ionisations par unité de longueur, appellé le coefficient de Townsend α. Différents processus d'ionisation contribuent à α en fonction du mélange et l'on distingue l'ionisation directe par un électron, l'ionisation indirecte par un état excité du gaz (appellé effet Penning) ou encore la production de photo-électrons sur la grille par des photons UV de fluorescence produits dans l'avalanche.

Mesures

Le gain est calculé comme le rapport du nombre mesuré d'électrons après amplification et du nombre attendu d'électrons primaires résultant de la conversion d'un quantum du fer dans le gaz. Le nombre d'électrons primaires est déduit de l'energie moyenne par paire electron/ion et de l'energie déposée dans le gaz. Le nombre d'électrons après amplification est déterminé à partir de la position du pic photo-électrique du fer et de la constante de calibration de l'électronique. Les mesures sont effectuées dans l'argon et dans des mélanges Ar/CO_2 et Ar/$i$$C_4H_{10}$ avec une grille de 58 μm de pas, 32 μm de diamètre et dont la distance anode-grille est de 86 μm. Elles sont présentées dans la Figure 10.2 (a).

Influence du mélange gazeux

Dans la plupart des mélanges le gain est une fonction exponentielle du champ d'amplification et atteint une valeur maximale d'environ 10^4 et $2{\cdot}10^4$ dans les mélanges à base de CO_2 et d'isobutane respectivement. A un champ et dans un mélange donnés, le gain décroît avec la concentration de quencher car l'energie des électrons d'avalanche et donc le coefficient de Townsend diminuent. Il est interéssant de noter que le gain diminue lorsque du CO_2 est mélangé à une base d'argon tandis qu'il augmente lorsque le gaz ajouté est de l'isobutane.

Influence des photons

Les courbes de gain mesurées dans l'argon et dans les mélanges contenant moins de 5 % de quencher présentent à des gains proches du maximum un comportement sur-exponentiel. Cette tendance résulte du mécanisme de "photon feedback" [202]: une petite fraction des photons UV produits dans l'avalanche initiale libère des photo-électrons de la grille. Ces derniers se multiplient produisant des avalanches secondaires qui augmentent le gain. L'augmentation relative du gain due aux photons est importante dans l'argon et dans les mélanges contenant moins de 5 % de quencher. A un gain de $5{\cdot}10^3$, elle est de 20 et 50 % dans les mélanges Ar/$i$$C_4H_{10}$ 97.5/2.5 et 99/1 respectivement.

Influence de l'effet Penning

L'augmentation relative du coefficient de Townsend α due à l'effet Penning se déduit du gain mesuré et du gain calculé par le programme MAGBOLTZ [37]. Dans les mélanges Ar/CO_2 utilisés, la contribution de l'effet Penning au gain augmente avec la concentration de CO_2. L'augmentation de α reste cependant modeste (inférieure à 10 % dans Ar/CO_2 80/20) car un seul état excité de l'atome d'argon peut ioniser une molécule de CO_2. En revanche plusieurs réactions Penning sont permises dans les mélanges Ar/$i$$C_4H_{10}$ car le potentiel d'ionisation de l'isobutane est très bas (10.67 eV contre 13.77 eV pour le CO_2). En conséquence, l'effet Penning contribue de manière importante au gain: l'augmentation relative

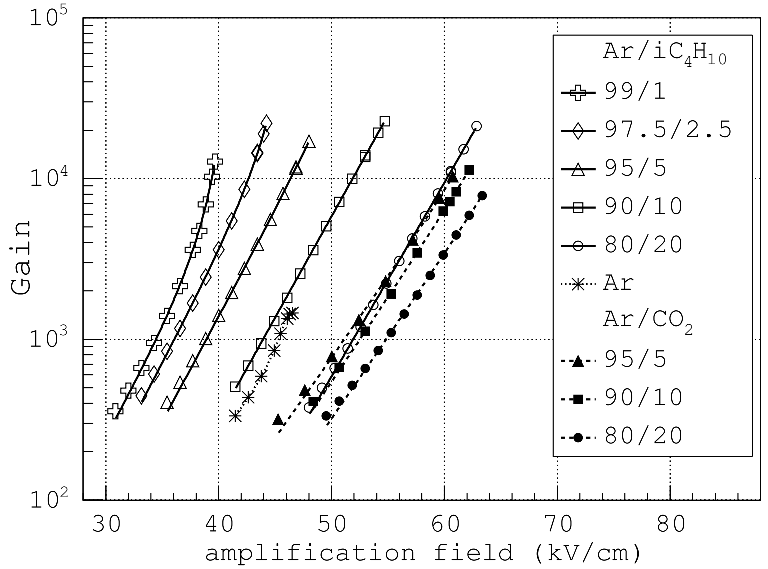

(a)

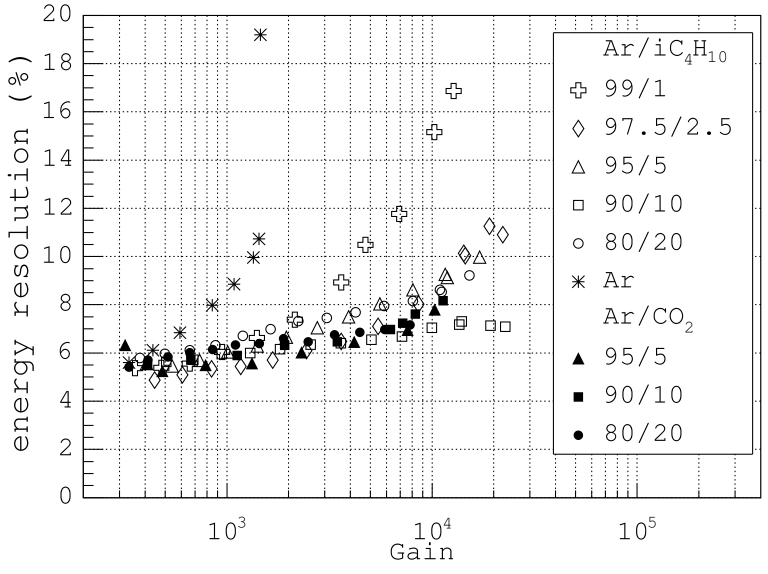

(b)

Figure 10.2: *Gain (a) et résolution à 5.9 keV (b) dans les mélanges à base d'argon.*

de α est autour de 65 % dans Ar/iC$_4$H$_{10}$ 99/1 et 97.5/2.5 et décroît à 40, 20 et 5 % dans les mélanges 95/5, 90/10 et 80/20 respectivement.

Influence de la distance anode-grille

Dans un mélange gazeux et à une tension de grille donnés, il est prédit que le gain des détecteurs Micromegas est maximum pour une distance anode-grille comprise entre 10 et 100 μm. Si la distance est telle que le gain est maximum, ce dernier est alors relativement insensible à de petites variations locales de la distance anode-grille. Cet effet de compensation du gain fut étudié avec trois InGrids de différentes distances anode-grille à une tension de grille de -390 V dans un mélange Ar/CH$_4$ 90/10. La distance pour laquelle le gain est maximum est estimée à 53 μm en ajustant les paramètres d'une parabole aux mesures. Cette valeur dépend principalement du gaz porteur et devrait donc être similaire dans d'autres mélanges à base d'argon [206].

Conclusion

Les mesures de gain des InGrid dans les différents mélanges gazeux utilisés sont en accord avec celles effectuées avec des Micromegas standard. Toutefois le gain maximum des InGrids dans les mélanges Ar/iC$_4$H$_{10}$ est inférieur d'un facteur 2–5 [62]. Ceci n'est pas un inconvénient car dans une TPC à pixels un gain de 10^4 permet en principe d'obtenir une efficacité de détection au minimum de 90 %.

Les photons de fluorescence et l'effet Penning contribuent au gain du détecteur. Il est cependant préférable de minimiser la contribution des photons car ils augmentent la probabilité de décharge. A cet effet un pourcentage de quencher d'au moins 5 % est necéssaire. Les mélanges à effet Penning permettent d'obtenir des gains maximums plus élevés que les mélanges réguliers. De plus, la tension de grille nécéssaire pour un certain gain est réduite tout comme les dommages éventuels des décharges sur les éléments du détecteur (grille, puce). Les mélanges Ar/iC$_4$H$_{10}$ bénéficient d'un fort effet Penning, spécialement à des pourcentages d'isobutane inférieurs à 10 %. Ce n'est pas le cas des mélanges Ar/CO$_2$ qui nécessitent des tensions de grille plus élevées.

Une propriété importante pour la fabrication d'un détecteur Micromegas de grande surface ou d'une TPC à pixels est la relative insensibilité du gain envers de petites variations de la distance anode-grille. Dans les mélanges à base d'argon la distance anode-grille doit être d'environ 53 μm pour bénéficier de cet effet.

10.3.4 Résolution en énergie

La résolution en énergie des détecteurs gazeux basés sur la multiplication des électrons est limitée par le processus d'ionisation primaire et par les fluctuations de gain. Le premier est décrit par l'energie moyenne par paires electron/ion W et le facteur de Fano F tandis que les fluctuations de gain sont quantifiées par la variance relative du gain b. Les valeurs de W, F et b rapportées dans la littérature permettent de calculer la résolution minimale: 5 % r.m.s. à 5.9 keV.

Mesures

La résolution en énergie est mesurée comme la largeur relative du pic photoélectrique du fer. Les mesures sont effectuées dans les même mélanges et avec la même InGrid utilisés pour les mesures de gain. Ses variations en fonction du gain apparaissent dans la Figure 10.2 (b). Dans tous les mélanges la résolution se dégrade avec le gain, de manière très abrupte dans l'argon et dans les mélanges dont la concentration de quencher est inférieure à 5 %. A des gains inférieurs à 10^3 la résolution mesurée est proche de 5 % r.m.s., sa limite théorique.

Conclusion

L'abrupte dégradation de la résolution dans les mélanges à faibles concentrations de quencher suggère que celle-ci est causée par le mécanisme de “photon feedback”. Des résultats de simulation de ce mécanisme présentés dans le paragraphe 10.4 soutiennent cette hypothèse. Ils montrent que b augmente avec le gain car la queue de la distribution de gain (normalisée à un gain de 1) s'allonge. Dans une TPC à pixels l'efficacité de détection bénéficierait de ces fluctuations à hauts gains mais au prix d'une probabilité de décharge plus élevée.

10.3.5 Retour des ions

Le retour des ions est la dérive des ions positifs produits dans les avalanches électroniques de la région d'amplification à l'électrode de dérive. Dans une TPC fonctionnant à haut flux de particules la charge d'espace des ions traversant la TPC est suffisante pour modifier localement le champ électrique et donc la dérive des électrons primaires. En règle générale le nombre de ces ions doit être le plus petit possible. Pour une TPC à l'ILC l'objectif est d'avoir environ un ion traversant la TPC par électron primaire, c'est à dire $G{\cdot}BF \sim 1$ où G est le gain et BF la fraction de retour d'ions (“backflow fraction”).

Fraction de retour d'ions du détecteur Micromegas

La diffusion des ions dans l'espace d'amplification est négligeable et donc le nombre d'ions remontant dans l'espace de dérive est égal au nombre d'ions produits dans l'entonnoir des lignes de champ. La fraction de retour d'ions dépend donc de la distribution spatiale des avalanches (diffusion transverse des électrons σ_{t} et coefficient de Townsend) et du volume de l'entonnoir dans la région d'amplification (rapport des champs, pas des trous p et distance anode-grille).

Avec des Micromegas standard, il a été mesuré que la fraction de retour d'ions BF décroît comme l'inverse du rapport des champ et diminue avec le pas des trous. Ces mesures sont publiées dans [147] où il est aussi prédit que BF est une fonction décroissante du rapport σ_{t}/p jusqu'à $\sigma_{\mathrm{t}}/p = 0.5$. Au-dessus de cette valeur BF est constant et égal à l'inverse du rapport des champs.

Mesures avec des Micromegas intégrés

Le champ électrique près des trous des InGrids et donc les propriétés de retour d'ions peuvent être différents de ceux des Micromegas standard car la grille est très fine. Pour une TPC à l'ILC il est important de connaître ces propriétés à l'avance. De plus, il est facile de fabriquer des InGrids de géométries différentes et ainsi d'étudier plus en détail la relation entre le retour d'ions et la géométrie.

Les mesures sont effectuées avec un canon à rayons X dans un mélange Ar/CH_4 90/10. Les InGrids utilisées ont des pas de 20–58 μm et des distances anode-grille de 45–70 μm. La fraction de retour d'ions est déterminée à différents champs de dérive en mesurant les courants à travers l'anode et la cathode.

Influence du rapport des champs

Les variations de BF avec le rapport des champs FR ("field ratio") mesurées avec des InGrids dont la distance anode-grille est de 58 μm sont présentées dans la Figure 10.3 (a). Pour chaque InGrid la fonction p_0/FR est aussi tracée dans le graphique, p_0 étant un paramètre ajusté aux mesures. Dans la plupart des cas l'ajustement est bon: BF est une fonction inverse de FR car la surface transverse de l'entonnoir est inversement proportionnelle au rapport des champs.

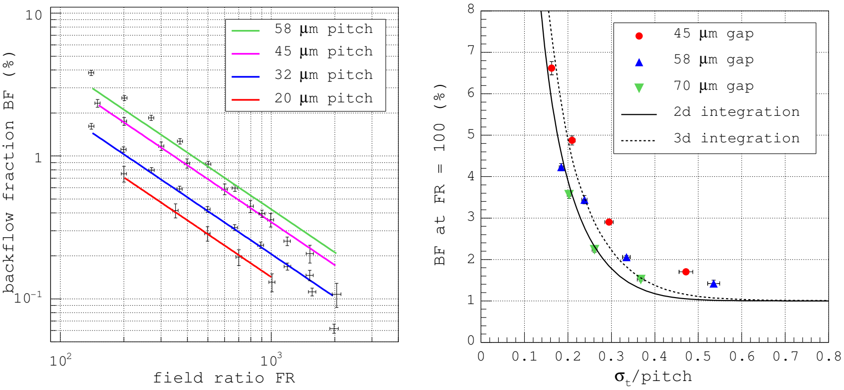

(a) (b)

Figure 10.3: *Fraction de retour d'ions en fonction du rapport des champs (a). Fraction à un rapport des champs de 100 en fonction du rapport de la diffusion transverse σ_{t} et du pas des trous p (b).*

Influence de la géométrie du détecteur

Il apparaît dans la Figure 10.3 (a) qu'à un rapport des champs et une distance anode-grille donnés, la fraction de retour d'ions diminue avec le pas des trous p. Ceci s'explique par le fait que la surface transverse de l'entonnoir est inversement proportionnelle au carré du pas (pour un agencement carré de trous). En comparant les mesures effectuées avec des grilles de même pas mais de différentes distances anode-grille, nous constatons que BF diminue avec cette distance car l'étalement transversal de l'avalanche σ_t devient plus important.

En fait le pas et l'étalement devraient agir de manière opposée sur la fraction de retour d'ions [147]. Cette prédiction est confirmée dans la Figure 10.3 (b) où apparaît la valeur de BF extrapolée à un rapport de champ de 100 en fonction du rapport σ_t/p. Les lignes sont les résultats de l'intégration numérique de la distribution spatiale des ions en deux et trois dimensions. Les points de mesure sont un peu dispersés mais la tendance générale est bien reproduite. Le plateau à $\sigma_\mathrm{t}/p \geq 0.5$ est suggéré bien que des mesures supplémentaires avec des InGrids de plus petits pas ou de plus grandes distances anode-grille soient nécéssaires pour conclure sur ce point.

Conclusion

Les InGrids montrent des performances de retour d'ions similaires à celles des Micromegas standard. Pour une géométrie donnée la fraction de retour d'ions est une fonction inverse du champ de dérive. A des champs de quelques dizaines de volts et avec une géométrie optimisée ($\sigma_\mathrm{t}/p \geq 0.5$), seul un ion sur mille environ remonte dans l'espace de dérive ($BF \sim 10^{-3}$). L'objectif pour une TPC à l'ILC imposerait alors un gain de 10^3 auquel l'efficacité d'un détecteur GridPix devrait être de l'ordre de 50 %. Cette efficacité réduite affecterait de manière limitée la résolution spatiale si toute la surface des plans de lecture est sensible. En effet, le nombre de points de mesure le long des traces serait toujours suffisant pour déterminer précisément les trajectoires des particules.

10.4 Simulation des fluctuations de gain

Le nombre total d'électrons produits dans une avalanche électronique fluctue d'une avalanche à l'autre. Ces fluctuations nous intéressent car pour un seuil donné elle détermine l'efficacité de détection. Trois causes de fluctuations de gain sont étudiées: les fluctuations intrinsèques, les avalanches secondaires et la non-uniformité du champ d'amplification.

Fluctuations intrinsèques

La distribution du gain peut être obtenue par simulation Monte Carlo en utilisant le modèle simple de développement d'avalanche proposé par Legler [70]. Selon ce modèle chaque électron libéré a d'abord une probabilité nulle de ioniser le gaz. Au-delà d'une certaine distance de dérive x_0 cette probabilité devient significative. La forme des distributions simulées dépend du rapport $\chi = x_0/\lambda$ où $\lambda = 1/\alpha$ est la distance moyenne entre ionisations. A bas champ (10–20 kV/cm), $x_0 \ll \lambda$ et la distribution est proche d'une exponentielle décroissante. A des champs plus élevés, x_0 augmente plus rapidement que λ et les deux deviennent comparables. Le nombre d'ionisations est alors contraint par x_0 et la distribution peut être décrite par le produit d'une exponentielle et d'une puissance (distribution de Polya de paramètre m).

Le maximum de la distribution de Polya est proche de sa valeur moyenne. Du point de vue de l'efficacité de détection, cette distribution est donc plus avantageuse qu'une exponentielle. Pour un gain donné, le champ d'amplification doit alors être le plus élevé possible. En pratique le champ varie entre 40–100 kV/cm et la variation du gain est de 60–80 % r.m.s. ce qui correspond à un paramètre m de la distribution de Polya entre 1.5 et 3.

Influence des photons

L'effet des avalanches secondaires sur la distribution du gain a été simulé. Les paramètres du model sont le nombre de photons et d'électrons produits par unité de longueur, le libre parcours moyen des photons dans le gaz, la géométrie du détecteur et l'efficacité de la grille pour l'effet photo-électrique. Par souci de simplicité, l'énergie des photons est unique et la distance x_0 est nulle.

Le model montre que la forme de la distribution de gain est en fait gouverné par un seul paramètre: le nombre moyen de photo-électrons N libérés dans l'avalanche initiale. Pour $N = 0$ la distribution est de type exponentiel car une seule avalanche se développe et $x_0 = 0$. Lorsque N augmente les avalanches secondaires étendent la queue de la distribution: à $N = 0.6$, la r.m.s. relative du gain double.

Non-uniformités du champ électrique

Lorsque que le diamètre des trous d est comparable à la distance anode-grille g le champ d'amplification près de la grille n'est pas uniforme. En conséquence, le gain doit dépendre de la position d'éntrée des électrons dans le trou. La variation du gain avec la position d'entrée a été calculée par le programme GARFIELD au moyen d'un modèle du champ électrique en deux dimensions [221, 81]. La distribution de la position d'entrée des électrons n'étant pas connue, elle est supposée uniforme.

La r.m.s. relative du gain est une fonction décroissante du rapport g/d: pour $g/d = 1$ elle est égale à 25–30 % et décroît sous 5 % pour $g/d \geq 4$. En réalité les électrons sont dirigés vers le centre des trous et ces variations sont des limites supérieures. Néanmoins, pour des grilles telles que $g/d \geq 4$ les fluctuations liées à la non-uniformité du champ sont négligeables quelque soit le rapport des champs.

10.5 Tests de petites TPC à pixels GridPix

Des détecteurs GridPix formés d'une InGrid et de la puce TimePix ont été fabriqués. Dans un premier temps l'efficacité de détection est mesurée au moyen d'une source de fer. Nous montrerons qu'à hauts gains celle-ci est proche de 95 % ce qui permet la mesure de la statistique de l'ionisation primaire. La réponse du détecteur aux particules cosmiques est ensuite étudiée. Des résultats sur la résolution spatiale et sur la possibilité de compter les paquets d'électrons le long des traces sont présentés.

10.5.1 La puce TimePix

TimePix est une puce électronique fabriquée en technologie CMOS 0.25 μm [175]. Elle est formée d'une matrice de 256 × 256 pixels d'une taille de 55 × 55 μm^2, la surface active est égale à 14 × 14 mm^2. Chaque pixel est équipé en surface d'une électrode octogonale de 10 μm de côté entourée d'une couche isolante. Le circuit électronique d'un pixel est divisé en une partie analogue connectée à l'électrode et une partie digitale. Le rôle de la première est d'amplifier et de discriminer les signaux en fonction d'un seuil de détection réglable. La partie digitale synchronise les signaux à une horloge interne et contient un compteur de cycles d'horloge.

Les modes de comptage principaux sont les modes charge et temps. En mode charge le comptage s'effectue durant le temps au-dessus du seuil du signal, le nombre de cycles comptés est alors une fonction croissante de la charge induite sur l'électrode. En mode temps le comptage s'effectue à partir de la détection du signal jusqu'à la fin du temps d'acquisition. Pour un temps d'acquisition donné, le nombre de cycles permet donc de mesurer le temps de détection.

10.5.2 Réponse aux rayons X du fer

Spectre du fer dans les mélanges à base d'argon

L'isotope ^{55}Fe se transforme en manganèse par capture électronique. La vacance électronique induit un ré-arrangement des électrons avec émission de photons de fluorescence d'énergie 5900 eV (transition K_α) et 6492 eV (K_β) selon le rapport 8.5:1. Dans les mélanges gazeux à base d'argon un quantum du fer est absorbé le plus souvent par effet photo-électrique sur un atome d'argon. Un photo-électron est alors éjecté de l'atome. Dans près de 86 % des cas le photo-électron est suivi d'un nombre variable d'électrons Auger. L'énergie moyenne déposée dans le gaz par les électrons est alors égale à 5760 eV et correspond au pic photo-électrique. Dans les autres cas un photon de fluorescence est émis, suivi d'un électron Auger. Le photon s'échappe du détecteur et l'énergie déposée dans le gaz est de 2897 eV. Ce second pic est appellé le pic d'échappement. Une fraction de l'énergie déposée est dissipée en ionisation du gaz résultant en un certain nombre d'électrons primaires.

Mesure de l'efficacité de détection

Les électrons primaires dérivent jusqu'à la grille où ils sont détectés avec une certaine efficacité κ. Si la distance de dérive est suffisante ils sont détectés sur des pixels différents et leur nombre N_{d} peut être déterminé par comptage. Ce dernier est proportionel à $\kappa(G)$ et augmente donc avec la tension de grille V_{g}. La forme théorique de $\kappa(G)$ est connue pour une distribution de gain de type Polya avec $m = 2$ et une distribution exponentielle ($m = 1$). La forme de $G(V_{\mathrm{g}})$ étant aussi connue il est possible à partir de points de mesures $(N_{\mathrm{d}}, V_{\mathrm{g}})$ de déterminer la valeur assymptotique de N_{d} pour un gain infini et donc l'efficacité de détection.

Cette mesure a été réalisée avec une petite TPC dont le volume actif est égal à $14 \times 14 \times 100$ mm^3 dans un mélange Ar/iC$_4$H$_{10}$ 95/5. A différentes tensions de grille plusieurs centaines d'événements d'échappement sont enregistrées. A partir des évènements suffisamment diffus le spectre du nombre d'électrons détectés est reconstruit (Figure 10.4 (a)). N_{d} est alors déduit de la position du pic. Les variations de N_{d} avec la tension de grille apparaissent dans la Figure 10.4 (b). La valeur asymptotique est égale à 115 électrons. A -350 V l'efficacité de détection est donc de 95 %.

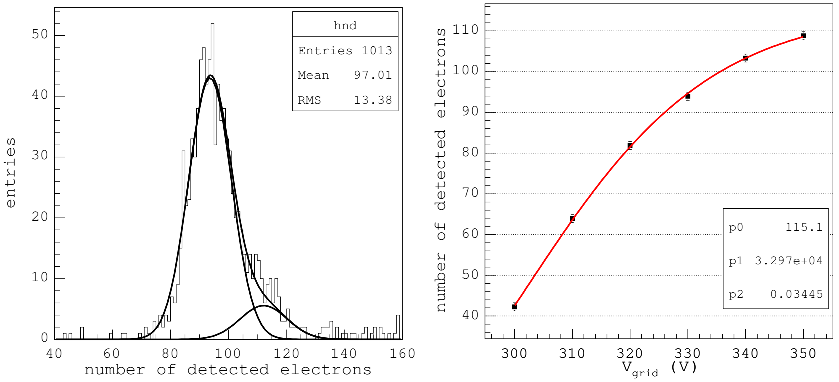

(a) (b)

Figure 10.4: *Spectre du nombre d'électrons détectés à -330 V (a). Nombre d'électrons détectés et tension de grille (b).*

Mesure de la statistique d'ionisation

Pour une énergie fixe dissipée dans le gaz E_0 le nombre d'électrons primaires fluctue. Il obéit à une distribution de moyenne E_0/W et de variance $F \cdot W/E_0$ où W est l'énergie moyenne par paire électron/ion et F le facteur de Fano.

L'énergie moyenne par paire est déduite du nombre d'électrons détectés. Nous trouvons dans l'Ar/iC$_4$H$_{10}$ 95/5 à 2897 eV $(W \pm \Delta\ W) = (25.2 \pm 0.5)$ eV.

L'efficacité de collection de la grille n'étant pas connue cette valeur est une borne supérieure. Le bon accord avec des mesures publiées suggère néanmoins que la collection est proche de 100 % [114]. Le facteur de Fano est déterminé à partir de la largeur du pic en corrigeant pour les contributions des efficacités de collection et de détection limitées: $(F \pm \Delta\ F) = (0.21 \pm 0.06)$.

10.5.3 Réponse aux particules cosmiques

Introduction

Les particules chargées produisent des paquets d'électrons le long de leurs trajectoires. Grâce au mode temps de la puce TimePix les positions des électrons et donc la trace peuvent être reconstruites en trois dimensions. La distribution des électrons le long des traces nous renseigne alors sur la résolution spatiale. Si la diffusion et la densité d'ionisation n'est pas trop grande la structure en paquets est préservée et peut être mesurée pour améliorer la mesure du dE/dx. Nous utilisons donc une TPC dont la distance de dérive maximale est égale à 10 mm et un mélange He/iC$_4$H$_{10}$ 77/23. De plus, un dispositif de coïcidence est utilisé pour déclencher l'acquisition du détecteur lors du passage de particules cosmiques au minimum ionisant seulement. Une trace de particule projetée sur le plan de pixels est présentée dans la Figure 10.5 (a).

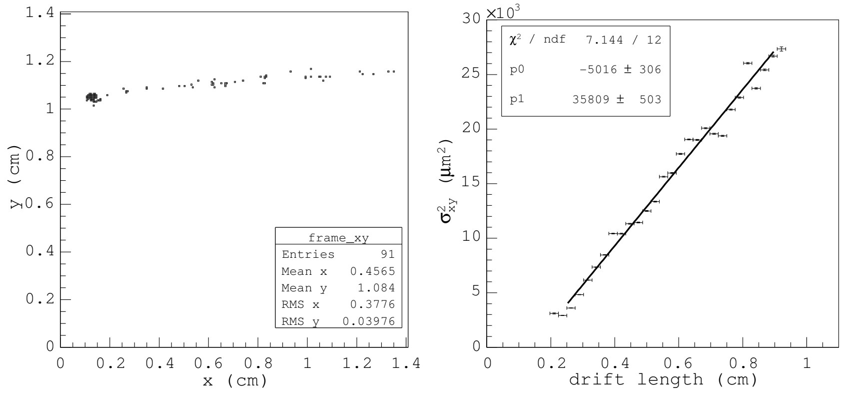

(a) (b)

Figure 10.5: *Trace de particule cosmique dans le plan de pixels (a). Variance des résidus dans le plan de pixels et distance de dérive (b).*

Résolution spatiale

Les positions des électrons dans le plan de pixels xy et suivant la direction de dérive z sont mesurées différemment. Nous distinguons donc la résolution σ_{xy} de la résolution σ_{z}. L'analyse d'un évènement consiste à identifier une trace et à déterminer ses paramètres, d'abord dans le plan xy et ensuite dans le plan sz où s est la direction de la trace projetée. Dans chaque plan les distances entre les positions reconstruites des électrons et la trace (appellés résidus) sont calculées.

Pour une certaine distance de dérive les résolutions sont déduites des largeurs des distributions des résidus. Les variations du carré de la résolution σ_{xy} en fonction de la distance de dérive sont présentées dans la Figure 10.5 (b). A une distance de 1 cm du plan de pixels la résolution est d'environ 175 μm, proche de la limite imposée par la diffusion transverse. La résolution σ_{z} est moins bonne. D'une part la granularité suivant l'axe z est inférieure à celle des pixels (250 μm contre 55 μm). D'autre part le temps auquel un signal est détecté dépend de la charge d'entrée dans le circuit électronique: sous quelques milliers d'électrons le signal de sortie du préamplificateur croît plus lentement et passe donc le seuil plus tard. La distribution des résidus est fortement asymétrique et la résolution σ_{z} ne peut être correctement estimée.

Mesure du nombre de paquets d'électrons par unité de longueur

Les positions reconstruites des électrons primaires sont projetées sur la trace tridimensionelle. Les électrons sont alors groupés en comparant la distance entre deux électrons voisins à un certain pas. Si la distance est inférieure au pas les électrons appartiennet au même paquet, dans le cas contraire à deux paquets différents. La position d'un paquet est définie comme le centre de gravité des positions des électrons qu'il contient. Le nombre de paquets d'électrons par unité de longueur, déduit de la distribution des distances entre deux paquets voisins, est égal à 25–26 paquets par centimètre. Le très bon accord avec la prédiction du programme HEED (25.6 paquets/cm) démontre la possibilité de compter les paquets d'électrons dans nos conditions expérimentales [119].

10.6 Conclusion

GridPix permet la détection d'électrons uniques avec une efficacité de 95 % et une précision dans le plan de lecture proche de la limite imposée par la diffusion. Ces performances jusqu'à présent inégalées par d'autres trajectographes gazeux nécessitent la fabrication de la grille d'amplification Micromegas sur la puce à pixels. Les InGrids permettent d'atteindre un gain de 1–$2{\cdot}10^4$ dans les mélanges Ar/CO$_2$ et Ar/iC$_4$H$_{10}$, une résolution en énergie proche de la limite théorique et une fraction de retour d'ions de 10^{-3}–10^{-1}.

Une TPC à lecture GridPix répondrait à certaines exigences expérimentales du programme de recherche du futur collisionneur à électrons ILC. A un gain de 10^3 et avec une géométrie de grille optimisée le nombre d'ions remontant dans l'espace de dérive peut être égal au nombre d'électrons primaires tout en conservant une efficacité de détection de 50 %. La résolution sur l'impulsion bénéficierait de la haute statistique primaire et de la trés bonne précision dans le plan de pixel. Dans un mélange Ar/CH_4 95/5 à 4 T et 40 V/cm l'objectif de $\sigma_{p_\mathrm{t}}/p_\mathrm{t} \sim 5{\cdot}10^{-5}p_\mathrm{t}$ est théoriquement atteignable car la diffusion transverse est de 20 μm/$\sqrt{cm}$. De plus, pour des traces traversant un plan de lecture quelques points seraient mesurés avec une précision de l'ordre de 20 μm.

Summary

This thesis reports on the fabrication and test of a pixel readout gaseous detector formed by a Micromegas amplification grid integrated on a CMOS pixel readout chip by microelectronic techniques. This very high granularity low-mass detector called GridPix provides single electron sensitivity and can be fabricated by post-processing of pixel chip wafers.

For the first time, the track of a charged particle can be measured electron by electron, providing all the information about the three-dimensional particle trajectory and its energy loss in the gas. Such a performance makes GridPix very attractive for tracking at actual and next-generation high luminosity colliders. In particular, it could be applied as the readout of a Time Projection Chamber at the future International Linear Collider.

Chapter five described the fabrication process of the Micromegas grid (InGrid) on silicon wafers. The microelectronic techniques used give freedom in the choice of the grid geometrical parameters and several 314 mm^2 area prototypes with various hole diameters, pitches and amplification gap thicknesses were made. Systematic measurements of those parameters over the grid areas show that the hole dimensions can be controlled to a 1 μm precision and that the gap size varies by less than 1 %.

Measurements of collection efficiency, gain and energy resolution of the InGrid prototypes in various Ar/CO$_2$ and Ar/iC$_4$H$_{10}$ gas mixtures were presented in chapter six. Also, some measurements were done in an Ar/CH$_4$ mixture. The performance is comparable with that of standard Micromegas, although the InGrids exhibit a smaller maximum gain of about $2{\cdot}10^4$ and are less robust against gas discharges. Due to the uniform amplification gap, a very good energy resolution of 5.2 % r.m.s. at 5900 eV ^{55}Fe X-rays was measured in Ar/CH$_4$ 90/10, close to the primary ionization and gas amplification limit.

I studied the impact of the Penning effect on the measured gains and found that it is more important in Ar/iC$_4$H$_{10}$ than in Ar/CO$_2$ mixtures. This can be explained by the larger number of Penning reactions energetically allowed in Ar/iC$_4$H$_{10}$ mixtures. It was observed that the number of Penning ionizations in binary Ar-based mixtures increases with the CO$_2$ fraction while it decreases with that of iC$_4$H$_{10}$.

The contribution of secondary avalanches (initiated by UV photons) to the gain was estimated by fitting a specific function to the gain curves. It increases with the gain and is especially important at low quencher fractions. At a gain of 10^4 in Ar/iC$_4$H$_{10}$ 99/1, secondary avalanches contribute to 75 % of the total gain which drops to 20 % in Ar/iC$_4$H$_{10}$ 95/5 and 35 % in Ar/CO$_2$ 95/5.

A model of avalanche development with UV photon feedback was proposed and strongly supports that the energy resolution of Micromegas-like detectors in the gas mixtures used depends on the quenching of the UV photons. When the gain increases, a larger number of photo-electrons is released from the grid which adds to the gain fluctuations and hence degrades the energy resolution. This finding should be applicable to other gas mixtures.

The capability of GridPix detectors to detect single primary electrons is determined by the shape of the gain distribution and the pixel noise level. Simulation results suggest that the distribution is better parametrized by a Polya function than by an exponential. If no photon feedback takes place, the simulated distribution (normalized to a gain of one) exhibits a maximum that increases with the amplification field and has a relative gain variation between 50–70 % r.m.s.. Photon feedback mainly changes the distribution tail. In gas mixtures with more than 5 % quencher, measurements indicate that the effect of photons on the avalanche statistics is very small. In such mixtures, the shape of the gain distribution should therefore depend mainly on the field.

The field non-uniformities at the entrance of the grid holes should affect the shape of the gain distribution too. When the amplification gap size is about four times larger than the hole diameter, however, this effect should be negligible.

The number of backflowing ions in the ILC Time Projection Chamber should be at most equal to the number of primary electrons (*i.e.* $BF{\cdot}G \leq 1$). The backflow fraction of standard Micromegas can reach a few per mil or even less. Moreover, the low noise at the input of the pixels allows operation of the detector at small gains, especially if the gain distribution is closer to a Polya than an exponential function. In the future, it is expected that the noise level at the pixel inputs will be even lower and the operating gain will be reduced further. As a result, the ion backflow density in a pixel readout TPC should be very small. With a gain of 10^3 and a backflow fraction of the order of 0.1 %, the ILC figure of merit of $BF{\cdot}G \sim 1$ would be achieved. That would be an unprecedented performance for a TPC operated without gating grid.

I was involved in the measurement of the ion backflow fraction of InGrids of various grid geometries in an Ar/CH_4 90/10 gas mixture. The results are well compatible with previous measurements done with standard Micromegas, between 0.1 and 1 % depending on the drift field. The large number of available prototypes permitted the test of the model proposed by the group of Orsay-Saclay which predicts that for a given gap and field, the backflow fraction decreases with the hole pitch squared and eventually reaches a plateau. Although the plateau could not be reached, this trend was measured and showed a good agreement with simulation results.

The single electron detection capability of Gridpix detectors can be exploited to measure the mean energy per ion pair and Fano factor. This study was realized by counting the number of primary electrons created by ^{55}Fe conversions in an Ar/iC_4H_{10} 95/5 mixture. I found $W = 25.2 \pm 0.5$ eV and $F = 0.21 \pm 0.06$, these are in line with values found in literature. This study illustrates the application of GridPix as a soft X-ray digital detector with an almost Fano-limited energy resolution.

The measured trend of the number of detected electrons with the grid voltage (or gain) gives information on the shape of the gain distribution. It completely rules out the assumption of exponentially distributed gains and strongly supports a Polya-like shape. Furthermore, the measured energy resolution and the value of F quoted above set an upper limit on the gain relative variance of about 70 %. This value is incompatible with exponential fluctuations but in agreement with our Monte Carlo estimations. Due to the shape of the Polya distribution, the operation of GridPix detectors at gains of a few thousands should be permitted, resulting in small discharge probability and low ion backflow. Operating at low gain is also an advantage for the long-term irradiation behaviour of GridPix detectors. This conclusion should also be valid for standard Micromegas, although for large area grids (*e.g.* 30×30 cm^2), the gain fluctuations may be dominated by the gap non-uniformities.

An important motivation for a pixel readout TPC is the possibility to identify a particle from the number of electron clusters produced along a given length of track. The precision with which the clusters are counted should depend mainly on the primary ionization density and the electron diffusion.

I examined the possibility of cluster counting with a set of cosmic ray data recorded at NIKHEF with a He/iC_4H_{10}-filled small TPC. After three-dimensional track reconstruction, the mean number of clusters per centimeter was derived from the distribution of the measured distances between clusters. That number shows an excellent agreement with the simulated value which demonstrates the possibility to accurately count clusters in those conditions.

Still, important studies remain to de done such as the extrapolation of the counting capability to larger gaps and in argon-based mixtures. Also, the precision on the measured cluster density as a function of the available track length and the impact of this precision on the particle identification efficiency should be assessed.

Samenvatting

Dit proefschrift handelt over het construeren en testen van gasgevulde detectoren met een pixel-uitlezing, samengesteld uit een Micromegas gasversterkingsrooster dat is geïntegreerd, met behulp van micro-elektronica technieken, op een CMOS pixel chip. Deze GridPix detector is fijnmazig, bevat weinig materiaal en is gevoelig voor individuele elektronen en kan worden vervaardigd met behulp van het nabewerken van *chip wafers*.

Voor het eerst is het hiermee mogelijk om het spoor van elektronen, gevormd door een passerend geladen deeltje, per apart elektron te meten. Hiermee komt alle beschikbare informatie over de baan en energieverlies van het deeltje, in drie dimensies, beschikbaar. De GridPix detector is daardoor uitstekend geschikt om als spoordetector te gebruiken bij de huidige en toekomstige hoge-intensiteit botsingmachines.

Hoofdstuk 5 beschrijft de realisatie van een constructiemethode voor het plaatsen van een Micromegas rooster (InGrid) op *chip wafers*. Deze micro-elektronica techniek biedt vrijheid in het kiezen van een aantal geometrische parameters: diverse prototypen, met een oppervlak van 314 mm^2, zijn vervaardigd met verschillende diameter en steek van de gaten, en dikte van de multiplicatielaag. Uit metingen blijkt dat de gaten gemaakt kunnen worden met een afwijking van minder dan 1 μm ten opzichte van de bedoelde maat. De variatie in de dikte van de multiplicatielaag is minder dan 1 %.

De efficiëntie van het detecteren van elektronen, de versterking en de precisie van het energieverlies is gemeten met prototypen van InGrid in gasmengsels van Ar/CO$_2$ en Ar/iC$_4$H$_{10}$ met diverse concentraties van het doofgas. De kwaliteit van InGrid blijkt vergelijkbaar te zijn met die van een Micromegas, hoewel de maximaal haalbare versterking lager is ($2{\cdot}10^4$), en InGrid minder goed bestand is tegen ontladingen. Als gevolg van de uniformiteit van de multiplicatielaag is

het energieverlies heel precies meetbaar met een standaardafwijking van 5–6 %, voor 5.9 keV Röntgenquanta uit een ^{55}Fe bron. Dit benadert de statistisch best haalbare precisie.

De invloed van het Penning effect op de gemeten gasversterking is groter bij Ar/iC_4H_{10} dan bij Ar/CO_2 mengsels. Dit wordt verklaard door het grotere aantal Penningreacties die energetisch mogelijk zijn in Ar/iC_4H_{10} mengsels. Opgemerkt wordt dat het aantal Penning-ionisaties in binaire Ar mengsels toeneemt met de CO_2 fractie, terwijl dit afneemt met iC_4H_{10}.

Er is een schatting gemaakt van de bijdrage aan de gasversterking van secondaire lawines, veroorzaakt door UV fotonen, door de gemeten gasversterking te vergelijken met een hiervoor gecorrigeerde theoretische waarde. Dit effect wordt groter bij een hogere gasversterking en is van speciaal belang bij gasmengsels met weinig doofgas. Bij een gasversterking van 10^4, in een mengsel van Ar/iC_4H_{10} 99/1 is er een bijdrage van 75 % in de totale gasversterking ten gevolge van secondaire lawines. De bijdrage neemt af tot 20 % in Ar/iC_4H_{10} 95/5 en tot 35 % in Ar/CO_2 95/5.

Een eenvoudig model voor de ontwikkeling van UV-geïnitieerde lawines is uiteengezet en ondersteunt de gedachte dat de resolutie van het gemeten energieverlies met een Micromegas-detector afhangt van de absorptie van de UV fotonen. Het aantal uit het rooster losgewerkte foto-elektronen neemt toe met de gasversterking; dit voegt een fluctuatie toe aan de gasversterking waardoor de precisie van de meting van het energieverlies afneemt. Hetzelfde effect zou in andere gasmengsels moeten optreden.

Het vermogen van GridPix detectoren om individuele elektronen te kunnen detecteren wordt bepaald door de statistiek van de gasversterking en het ruisniveau van de pixels. Uit simulaties blijkt dat deze statistiek eerder een Polya verdeling volgt dan een exponentiële. Zonder terugkoppeling via UV fotonen vertoont de gesimuleerde verdeling (genormaliseerd tot gasversterking 1) een maximum waarvan de positie toeneemt met het multiplicatie-veld en die een standaardafwijking heeft van 50–70 %. Terugkoppeling via fotonen heeft vooral effect op de staart van de verdeling. Uit metingen blijkt dat in gasmengsels met meer dan 5 % doofgas het effect van fotonen op de multiplicatie-statistiek zeer klein is. In deze mengsels wordt de statistische verdeling van de gasversterking voornamelijk door het elektrisch veld bepaald.

De niet-uniformiteit van het elektrisch veld bij de ingang van de roostergaten zal ook van invloed zijn op de statistische verdeling van de gasversterking. Indien de dikte van de gasversterkingsruimte ongeveer vier keer groter is dan de diameter van de gaten dan zal dit effect verwaarloosbaar klein zijn.

Het aantal terugkerende ionen in de ILC Time Projection Chamber moet beperkt blijven tot de orde-grootte van het aantal primaire elektronen (dus $BF{\cdot}G \leq 1$). In een standaard Micromegas detector kan de fractie van de ionen die terugkeren beperkt blijven tot een paar promille, of minder. Bovendien kan de detector, met zijn lage ingangsruis, met een lage gasversterking werken, in het bijzonder als de gasversterking meer de gedaante heeft van een Polya verdeling dan die van een exponentiële functie. Het ligt in de verwachting dat het ruisniveau van toekomstige pixel chips verder zal afnemen, waardoor met een nog lagere gasversterking kan worden gewerkt. Als gevolg hiervan zal het aantal terugkerende ionen in een TPC met pixel-uitlezing zeer gering zijn. Met een gasversterking van 10^3 en een terugkeer-fractie van ongeveer 0.1 % wordt de streefconditie $BF{\cdot}G \sim 1$ bereikt. Dit zou een ongeëvenaarde prestatie zijn voor een TPC zonder poortelectrode.

Metingen van de fractie van de terugkerende ionen zijn gedaan met detectoren met diverse rooster-geometrieen in een Ar/CH_4 90/10 gasmengsel. De resultaten hiervan zijn in goede overeenstemming met eerdere metingen gedaan aan een standaard Micromegas detector, met waarden tussen 0.1 en 1 %. Dankzij het groot aantal beschikbare prototypes was het mogelijk om een model, geopperd door de Orsay-Saclay groep te toetsen. Dit model voorspelt dat voor een gegeven dikte van het versterkingsvolume en elektrisch veld de terugkeerfractie afneemt met het kwadraat van de steek van de gaten en uiteindelijk een plateau bereikt. Hoewel dit plateau niet gehaald werd is de gemeten trend in goede overeenstemming met het resultaat van de simulaties.

Het vermogen van de GridPix detectoren om individuele elektronen te meten kan worden ingezet om het gemiddeld energieverlies per elektron-ion paar en de Fano factor te meten. Deze bepaling werd gedaan door het aantal primaire elektronen te tellen dat vrijkomt bij de conversie van ^{55}Fe Röntgen-quanta in een Ar/iC_4H_{10} 95/5 gasmengsel. De gevonden waarden zijn $W = 25.2 \pm 0.5$ eV en $F = 0.21 \pm 0.06$ en zijn in overeenstemming met waarden uit de literatuur. Deze studie onderstreept de toepassing van GridPix als lage-energie Röntgendetector met een energie-resolutie die slechts beperkt is door de Fano factor.

De gemeten trend in het aantal gedetecteerde elektronen als functie van de potentiaal van het rooster, dan wel de gasversterking, geeft spectrale informatie over de gasversterking. Een exponentiële verdeling wordt totaal uitgesloten, terwijl een Polya verdeling uitstekend past. Bovendien wordt er, als consequentie van de gemeten resolutie van het energieverlies en de gevonden waarde van de Fano factor F, een bovengrens gesteld van 70 % aan de variatie van de gasversterking. Deze waarde kan niet in overeenstemming worden gebracht met een exponentiële verdeling, maar klopt wel met een schatting verkregen uit Monte Carlo simulaties. Met een Polya verdeling kunnen GridPix detectoren werken met een gasversterking van slechts een paar duizend waarbij de kans op doorslag klein is, evenals de fractie van terugkerende ionen. Het bedrijven van de GridPix detector bij een lage gasversterking is ook gunstig voor het functioneren ervan in een lange periode van bestraling. Deze conclusie zou ook moeten gelden voor een standaard Micromegas detector, hoewel bij grote roosters (bv. 30 × 30 cm^2) de variatie in de gasversterking wordt bepaald door de niet-homogeniteit van het multiplicatie-volume.

Een belangrijk argument ten gunste van een pixel-uitlezing van een TPC is de mogelijkheid om deeltjes te identificeren door het aantal elektron-groepjes te bepalen langs een bepaalde lengte van het spoor. De precisie waarmee deze dichtheid kan worden bepaald hangt voornamelijk af van de dichtheid van de primaire ionisatie en de diffusie van elektronen.

De mogelijkheid om deze dichtheid te bepalen werd onderzocht aan de gegevens van kosmische straling, geregistreerd op het Nikhef met een kleine TPC gevuld met een $\text{He}/i\text{C}_4\text{H}_{10}$ gasmengsel. Na het reconstrueren van sporen in drie dimensies werd de gemiddelde dichtheid van elektron-groepjes per centimeter bepaald aan de hand van de verdeling van de gemeten afstanden tussen de groepjes. Die dichtheid stemt zeer goed overeen met de gesimuleerde waarde, en laat daarmee zien dat het goed mogelijk is om op deze manier het aantal groepjes te tellen.

Desalniettemin moeten er nog belangrijke studies worden uitgevoerd, zoals het extrapoleren van het tellen van groepjes naar grotere driftvolumes, en in gasmengsels gebaseerd op Argon. Verder zou de precisie van de bepaling van het aantal groepjes langs de beschikbare lengte langs het spoor, en de invloed hiervan op de efficiëntie van het identificeren van deeltjes, onder de aandacht moeten worden gebracht.

Acknowledgments

Here come, finally, the acknowledgments. The part I dreamt writing for months. From my experience, it seems that this is the firstly read part whenever someone gets a thesis in his hands. I will therefore try to write it as seriously as I would do for a chapter, quoting all names that should definitely be there as well as things that don't summarize in equations. Before proceeding to a list of names, I should first admit that these 4 years spent in the Netherlands were a profitable experience, having many opportunities to discover more about science, the world, myself and Belgian beers. I am really grateful to FOM and NIKHEF that invited me from France to the Netherlands and that offered me very good working conditions.

Starting from the beginning, I was 4 years ago in the SC group of Twente where I began fabricating detectors under the supervision of Jurriaan Schmitz. There, most of my memories are intact and my thanks go to the most brilliant fellows of the group: Ihor, Arjen, Tom, Natalie, Sander, Cora, Joost, Jiwu and last but far not least Victor the Spanish poet and also the only person able to survive with only fruits! Hola, que tal? Hablo un poco de español. La vida sin ti hubiera sido tan aburrida. Mucha suerte con tu tesis y mucha suerte en la vida.

After a while I went back to NIKHEF with a testable detector and enjoyed, most of the time, measuring operational characteristics. I have to admit that even today, getting ^{55}Fe X-ray signals on the scope, rising above the noise is still a kind of excitement. I'd like to say that I did everything myself but of course, during that time, many people helped me and contributed to the work reported in that thesis. The main at NIKHEF are called Jan Timmermans and Harry van der Graaf. Beside your scientific contributions, thanks Jan for your availability when I had questions and for the discussions in French which made me feel like Amsterdam is part of France. Harry, great lute player, bedankt for your contribution too. I will miss for sure your enthusiasm and the whistled melodies gliding in the ground floor corridor. Friendly thoughts go to several colleagues, the brightest stars from NIKHEF. In order of appearance: Sipho, Marten, Elmaar, Martin, Lucie and may I should not forget Yevgen, the greatest tennis player and hiker of all, the Ukranian smuggler who always brought the finest products from Kiev! You are simply a great person, I will miss you for sure.

It is impossible that I don't mentioned here the decisive part taken by my french promotor Paul Colas in the realization of this thesis. Thanks Paul for your advices, guidance and commitment in the Amsterdam/Orsay cotutelle. On the same occasion, I'd like to express my warm greetings to the French scientists I met from time to time in Saclay: Ioannis, Fabien, Ester and of course David who always provided me with some practical solutions to any hardware/software problems!

I'd like now to acknowledge my Dutch friend, de koning van Zeeburg: Bastian de Vries. It was more than nice to have him in the neighbourhood. Bastian, Netherlands would have been different without you. Maybe you will succeed where I always failed: getting a Palm beer for free at the Badhuis bar!

A mes parents Jeanne et Robert et mon frère Emmanuel de Clermont Ferrand, cette thèse est aussi la votre. Les arrivées et départs ont rythmé ces quatres ans: revenir au pays était toujours une grande joie, en repartir difficile. Vous avez toujours été au rendez-vous et à mes côtés. Merci pour votre soutient indéfectible.

The last name that should have appeared here will not. Instead I would like to conclude these acknowledgments with the most beautiful poem I found about Amsterdam. Unfortunately it is in French and would lose all its charm if translated. I have no choice but to write it in its original language.

Amsterdam
Dans les retours enchantés,
Je me pavane dans les rues de
Amsterdam,
La circulaire, la ronde, la concentrique
Qui concentre en elle la vie des mes amours,
Amsterdam,
Qui retient dans son ventre le fruit passionné de mes amours absentes,
Devant toi spectateur éloquent,
Amsterdam,
Matrice ou tu m'observes, m'attises et me desires
Où dans notre Ronde de nuit,
Tu abolis la solitude des heures perdues,
Amsterdam,
Spectaculaire sein qui recueille les sons des souffles des cris,
Cette fois à deux.

Bibliography

[1] ILC Reference Design Report, Executive Summary (2007).

[2] R. Brinkmann *et al.*, TESLA Technical Design Report, DESY-2001-011 (2001).

[3] P.W. Higgs, *Phys. Rev. Lett.* **13** (1964) 508.

[4] G.S. Guralnik, C.R. Hagen and T. Kibble, *Phys. Rev. Lett.* **13** (1965) 585.

[5] LEP WG for Higgs boson searches, R. Barate *et al.*, *Phys. Lett. B* **565** (2003) 61.

[6] The LEP collaborations and the LEP electroweak working group, hep-ex/0612034.

[7] T. Hambye and K. Riesselmann, *Phys. Rev. D* **55** (1997) 7255.

[8] B.W. Lee, C. Quigg and H.B. Thacker, *Phys. Rev. D* **16** (1977) 1519.

[9] A. Djouadi, J. Kalinowski and M. Spira, *Comput. Phys. Commun.* **108** (1998) 56.

[10] A. Djouadi, J. Kalinowski and P.M. Zerwas, *Z. Phys. C* **70** (1996) 435.

[11] M. Lüscher and P. Weisz, *Phys. Lett. B* **212** (1988) 472.

[12] J. Ellis, M.K. Gaillard and D.V. Nanopoulos, *Nucl. Phys. B* **106** (1976) 292.

[13] R.N. Cahn and S. Dawson, *Phys. Lett. B* **136** (1984) 196.

[14] W. Kilian, M. Kramer and P.M. Zerwas, *Phys. Lett. B* **373** (1996) 135.

[15] ILC Reference Design Report, Physics at the ILC (2007).

[16] ACFA Linear Collider Working Group, K. Abe *et al.*, hep-ph/0109166.

[17] A. Djouadi, hep-ph/0503172, to appear in *Phys. Rept.*.

[18] C. Castanier, P. Gay, P. Lutz and J. Orloff, hep-ex/0101028.

[19] J. Wess and B. Zumino, *Nucl. Phys. B* **70** (1974) 39.

[20] Yu. A. Gol'fand and E.P. Likhtman, *JETP Lett.* **13** (1971) 323.

[21] E. Witten, *Nucl. Phys. B* **188** (1981) 513.

[22] E. Witten, *Nucl. Phys. B* **202** (1982) 253.

[23] J.A. Aguilar-Saavedra *et al.*, *Eur. Phys. J. C* **46** (2006) 43.

[24] H. Goldberg, *Phys. Rev. Lett.* **50** (1983) 1419.

[25] ILC Reference Design Report, Detectors (2007).

[26] Proposal to the ILCSC R&D Panel on Tracking for the ILC. SiLC collaboration, http://silc.in2p3.fr.

[27] SiD Tracker R&D Report. SiD Tracking Group, http://ilcdoc.linearcollider.org/record/6320.

[28] The LCTPC collaboration, http://www.lctpc.org.

[29] EUDET: an integrated infrastructure initiative, http://www.eudet.org.

[30] D. Karlen, P. Poffenberger and G. Rosenbaum, *Nucl. Instr. and Meth. A* **555** (2005) 80.

[31] M. Dixit *et al.*, *Nucl. Instr. and Meth. A* **581** (2007) 254.

[32] N. Akchurin *et al.*, *Nucl. Instr. and Meth. A* **537** (2005) 537.

[33] The SiD concept group: T. Abe *et al.*, SiD Detector Outline Document, http://hep.uchicago.edu/ oreglia/siddod.pdf (2006).

[34] GLC project: Linear Collider for TeV physics, KEK-REPORT-2003-7.

[35] LDC working group: D. Kiseilewska *et al.*, Detector Outline Document for the Large Detector Concept, http://www.ilcldc.org/documents/dod/ (2006).

[36] The 4th concept group: P. Le Du *et al.*, Detector Outline Document for the Fourth Concept Detector at the International Linear Collider, http://www.4thconcept.org/4doc.pdf (2006).

[37] S.F. Biagi, *Nucl. Instr. and Meth. A* **421** (1999) 234.

[38] E.W. McDaniel, *Collision phenomena in ionized gases*, John Wiley and sons, New York (1964).

[39] L.G.H. Huxley and R.W. Crompton, *The diffusion and drift of electrons in gases*, Wiley, New York (1974).

[40] P. Langevin, *C. R. Acad. Sci. (Paris)* **146** (1908) 530.

[41] D.S. Lemons and A. Gythiel, *Am. J. Phys.* **65** No 11 (1997) 1079.

[42] K. Kleinknecht, *Detectors for particle radiation, 2nd edition*, Cambridge University Press, Cambridge (1998).

[43] W. Blum and L. Rolandi, *Particle detection with drift chambers*, Springer-Verlag Berlin Heidelberg (1993).

[44] C. Ramsauer, *Ann. Phys.* **66** (1921) 546.

[45] W.P. Allis and P.M. Morse, *Z. Phys.* **70** (1931) 567.

[46] G. Schultz, *Etude d'un détecteur de particules à trés haute résolution spatiale*, Thèse, Univ. Louis-Pasteur, Strasbourg (1979), unpublished. Also: CERN EP Internal Report 76-19 (1976).

[47] G. Schultz, G. Charpak and F. Sauli *Rev. Phys. Appl. (France)* **12** (1977) 67.

[48] Landolt and Börnstein, vol. IV/3, *Eigenschaften des Plasmas, no 44315, 6th edition*, Springer-Verlag Berlin Heidelberg (1957).

[49] C.J. Martoff *et al.*, *Nucl. Instr. and Meth. A* **440** (2000) 355.

[50] E.B.Wagner, F.J. Davies and G.S. Hurst *J. Chem. Phys.* **47** (1967) 3138.

[51] A.J.P.L. Policarpo, *Physica Scripta* **23** (1981) 539.

[52] *Handbook of Chemistry and Physics*, R.C. Weast (C.R.C. Press, Bica Raton, Fl. (1981) 205.

[53] F. Sauli, *Principles of operation of Multiwire Proportional and Drift Chambers*, CERN Yellow Reports 77-09 (1977).

[54] M. Suzuki and S. Kubota, *Nucl. Instr. and Meth. A* **164** (1979) 197.

[55] R.I. Schoen, *J. Chem. Phys.* **17** (1962) 2032.

[56] Yu.N. Pestov *et al.*, *Nucl. Instr. and Meth. A* **456** (2000) 11.

[57] B.D. Ramsey and P.C. Agrawal, *Nucl. Instr. and Meth. A* **273** (1988) 326.

[58] B.D. Ramsey and P.C. Agrawal, *Nucl. Instr. and Meth. A* **273** (1988) 331.

[59] B.D. Ramsey, P.C. Agrawal and M.C. Weisskopf, *Nucl. Instr. and Meth. A* **277** (1989) 557.

[60] B.D. Ramsey and P.C. Agrawal, *Nucl. Instr. and Meth. A* **278** (1989) 576.

[61] B.D. Ramsey and P.C. Agrawal, *IEEE Trans. Nucl. Sc.* **36** (1989) 866.

[62] D. Attié *et al.*, EUDET-Memo-2006-010, http://www.eudet.org (2006).

[63] H. Raether, *Electron avalanches and breakdown in gases*, Butterworth, London (1964).

[64] V. Palladino and B. Sadoulet, *Nucl. Instr. and Meth. A* **128** (1975) 323.

[65] M.E. Rose and S.A. Korff, *Phys. Rev.* **59** (1941) 850.

[66] R.A. Wijsman, *Phys. Rev.* **75** (1949) 833.

[67] W. Legler, *Z. Phys.* **140** (1955) 221.

[68] L. Frommhold, *Z. Phys.* **144** (1956) 396.

[69] A.H. Cookson, B.W. Ward and T.G. Lewis, *Brit. J. Appl. Phys.* **17** (1966) 891.

[70] W. Legler, *Z. Naturforschung* **16a** (1961) 253.

[71] W. Riegler, *Nucl. Instr. and Meth. A* **500** (2003) 144.

[72] H. Schlumbohm, *Z. Phys.* **151** (1958) 563.

[73] W. Legler, *Br. J. Appl. Phys.* **18** (1967) 1275.

[74] G.D. Alkhazov, *Nucl. Instr. and Meth. A* **75** (1969) 161.

[75] G.D. Alkhazov, *Nucl. Instr. and Meth. A* **89** (1970) 155.

[76] J. Byrne, *Proc. R. Soc. Edinburgh XVI A* **33** (1962).

[77] A.H. Cookson and T.G. Lewis, *Brit. J. Appl. Phys.* **17** (1966) 1473.

[78] P. Fonte *et al.*, *Nucl. Instr. and Meth. A* **433** (1999) 513.

[79] J. Derré and I. Giomataris, *Nucl. Instr. and Meth. A* **477** (2002) 23.

[80] J. Schmitz, *The Microstrip Gas Counter and its application in the ATLAS tracker* PhD. Thesis (1994), NIKHEF Institute, Amsterdam, The Netherlands.

[81] M. Chefdeville *et al.*, *Nucl. Instr. and Meth. A* **591** (2008) 147.

[82] W. Schockley, *J. Appl. Phys.* **9** (1938) 635.

[83] S. Ramo, *Proc. IRE* **27** (1939) 584.

[84] W. Riegler, *Nucl. Instr. and Meth. A* **491** (2002) 258.

[85] W. Riegler, *Nucl. Instr. and Meth. A* **535** (2004) 287.

[86] XCOM: Photon Cross Sections Database, NIST Standard Reference Database 8 (XGAM), http://physics.nist.gov/PhysRefData/Xcom/Text/XCOM.html.

[87] C. Grupen and B. Shwartz, *Particle Detectors, 2nd edition*, Cambridge University Press, Cambridge (2008).

[88] K.D. Childs *et al.*, in C.L. Hedberg, Ed., *Handbook of Auger Electron Spectroscopy*, Physical Electronics, Eden Prairie, MN (1995).

[89] L. Asplund *et al.*, *Phys. Scr.* **16** (1977) 268.

[90] C.D. Brogles, D.A. Thomas and S.K. Haynes, *Phys. Rev.* **89** (1953) 715.

[91] M.O. Krause, *J. Phys. Chem. Ref. Data* **8** (1979) 307.

[92] J.A. Bearden, *Rev. Mod. Phys.* **39** (1967) 78.

[93] W.R. Leo, *Techniques for Nuclear and Particle Physics Experiments*, Springer-Verlag (1993).

[94] M. Inokuti, *Radiat. Res.* **64** (1975) 6.

[95] L.G. Christophorou, *Atomic and Molecular Radiation Physics*, Wiley, London (1971).

[96] D. Combecher, *Proceedings of the 3rd Symposium on Neutron Dosimetry in Biology and Medicine*, ed. by G. Burger and H.G. Ebert, held at Neuherberg, (1977) 97.

[97] W.P. Jesse and J. Sadaukis, *Phys. Rev.* **100** (1955) 1755.

[98] G.G. Meisels, *J. Chem. Phys.* **41** (1964) 51.

[99] U. Fano, *Phys. Rev.* **72** (1947) 26.

[100] T.H.V.T. Dias *et al.*, *Appl. Phys.* **82** (1997) 2742.

[101] I. Krajcar Bronić, *Nucl. Instr. and Meth. B* **71** (1992) 366.

[102] M.M.F Ribeirete *et al.*, *Nucl. Instr. and Meth. A* **214** (1983) 561.

[103] B. Grosswendt, *Proc. 8th Symposium on Microdosimetry*, eds. J. Booz and H.G. Ebert Harwood, Academic for the Commission of the European Communities, London (1983) 165.

[104] G.D. Alkhazov, A.P. Komar and A.A. Vorob'ev, *Nucl. Instr. and Meth.* **48** (1967) 1.

[105] A.A. Vorob'ev, A.P. Komar and V.A. Korolev, *Sov. Phys. - Doklady* **6** (1961) 219.

[106] G.D. Alkhazov, *Sov. Phys. - Tech. Phys.* **16** (1972) 1540.

[107] A.P. Komar, A.A. Vorob'ev and V.A. Korolyov, *Dokl. Akad. Nauk SSSR* **136** (1961) 795.

[108] A. Hashiba *et al.*, *Nucl. Instr. and Meth. A* **227** (1984) 305.

[109] H. Mamyoda *et al.*, *Nucl. Instr. and Meth. A* **227** (1984) 311.

[110] E.P. de Lima and al., *Nucl. Instr. and Meth.* **192** (1982) 575.

[111] A.J.P.L. Policarpo *et al.*, *Nucl. Instr. and Meth. A* **118** (1974) 221.

[112] D.F. Anderson *et al.*, *Nucl. Instr. and Meth. A* **163** (1979) 125.

[113] D. Srdoč, B. Obelić and I. Krajcar Bronić, *J. Phys. B* **20** (1987) 4473.

[114] A. Pansky, A. Breskin and R. Chechik, *J. Appl. Phys.* **79** (1996) 8892.

[115] W. Neumann, *Proc. 7th Symposium on Microdosimetry*, Harwood Academic Publisher Ltd. for the Commission of the European Communities, (1981) 1067.

[116] M. Kase, J. Kikuchi and T. Doke, *Nucl. Instr. and Meth. A* **163** (1979) 289.

[117] G.S. Hurst *et al.*, *Nucl. Instr. and Meth. A* **155** (1978) 203.

[118] E.J. Kobetich and R. Katz, *Phys. Rev.* **170** (1968) 391.

[119] I.B. Smirnov, *Nucl. Instr. and Meth. A* **554** (2005) 474.

[120] R. Veenhof, *Nucl. Instr. and Meth. A* **563** (2006) 291.

[121] E. Fermi, *Phys. Rev.* **57** (1940) 485.

[122] M. Hauschild, *Nucl. Instr. and Meth. A* **379** (1996) 436.

[123] H. Fischle, J. Heintze and B. Schmidt, *Nucl. Instr. and Meth. A* **301** (1991) 202.

[124] M. Matoba *et al.*, *IEEE Trans. Nucl. Sci. NS* **32** (1985) 541.

[125] J. Dubbert, *Nucl. Instr. and Meth. A* **581** (2007) 507.

[126] G. Charpak *et al.*, *Nucl. Instr. and Meth. A* **148** (1978) 471.

[127] The ALEPH TPC Collaboration, *Nucl. Instr. and Meth. A* **306** (1991) 446.

[128] D. Delikaris *et al.*, *Nucl. Instr. and Meth. A* **283** (1989) 567.

[129] P. Glässel, for the ALICE TPC Collaboration, *Nucl. Instr. and Meth. A* **572** (2007) 64.

[130] C. Garabatos *et al.*, *MWPC rate capability measurements with an X-ray tube* Scientific Report, FAIR-QCD-CBM-13 (2005).

[131] J. Schmitz, NIKHEF preprint (1991) 14.

[132] A. Bahri *et al.*, *Nucl. Instr. and Meth. A* **349** (1994) 274.

[133] S.F. Biagi and T.J. Jones, *Nucl. Instr. and Meth. A* **361** (1995) 72.

[134] E. Christophel and M. Dracos, *Nucl. Instr. and Meth. A* **398** (1997) 195.

[135] B. Adeva *et al.*, *Nucl. Instr. and Meth. A* **435** (1999) 402.

[136] M. Bouianov *et al.*, *Nucl. Instr. and Meth. A* **535** (2004) 236.

[137] L. Dick, R. De Oliveira and D. Watts, *Nucl. Instr. and Meth. A* **535** (2004) 347.

[138] F.D. van der Berg *et al.*, *Nucl. Instr. and Meth. A* **453** (2000) 530.

[139] R. Bellazzini *et al.*, *Nucl. Instr. and Meth. A* **423** (2000) 125.

[140] A. Oed, *Nucl. Instr. and Meth. A* **263** (1988) 351.

[141] F. Angelini *et al.*, *IEEE Trans. Nucl. Sci. NS* **37** (1990) 112.

[142] R. Bouclier *et al.*, *Nucl. Instr. and Meth. A* **332** (1993) 100.

[143] F. Angelini *et al.*, *CERN 90-10* (1990) 222.

[144] J.E. Bateman *et al.*, *Energy Resolution of X-ray Detecting Gas Microstrip Detectors* RAL-TR-2000-022 (2000), Rutherford Appleton Laboratory, Chilton, UK.

[145] F. Sauli and A. Sharma, *Annu. Rev. Nucl. Part. Sci.* **49** (1999) 341.

[146] I. Giomataris *et al.*, *Nucl. Instr. and Meth. A* **376** (1996) 29.

[147] P. Colas, I. Giomataris and V. Lepeltier, *Nucl. Instr. and Meth. A* **535** (2004) 226.

[148] I. Giomataris *et al.*, *Nucl. Instr. and Meth. A* **419** (1998) 239.

[149] F. Jeanneau *et al.*, *Nucl. Instr. and Meth. A* **461** (2001) 84.

[150] J. Derré *et al.*, *Nucl. Instr. and Meth. A* **412** (1998) 47.

[151] B. Peyaud, *Nucl. Instr. and Meth. A* **535** (2004) 247.

[152] E. Ferrer Ribas *et al.*, *Nucl. Instr. and Meth. A* **581** (2007) 217.

[153] F. Kunne *et al.*, *Nucl. Instr. and Meth. A* **536** (2005) 61.

[154] Y. Kudenko, *Nucl. Instr. and Meth. A* In Press.

[155] F. Sauli, *Nucl. Instr. and Meth. A* **386** (1997) 531.

[156] R. Bellazzini *et al.*, *Nucl. Instr. and Meth. A* **419** (1998) 429.

[157] J. Benlloch *et al.*, *Nucl. Instr. and Meth. A* **419** (1998) 410.

[158] M. Ziegler *et al.*, *A Triple GEM detector for LHCb* TRAC **99-024** (1999).

[159] T. Zeuner, *Nucl. Instr. and Meth. A* **446** (2000) 324.

[160] K. Sachs *et al.*, *Nucl. Instr. and Meth. A* **538** (2005) 372.

[161] W. Riegler, *Nucl. Instr. and Meth. A* **535** (2004) 79.

[162] T. Zeuner, *Nucl. Instr. and Meth. A* **446** (2000) 324.

[163] B. Ketzer *et al.*, *Nucl. Instr. and Meth. A* **535** (2004) 314.

[164] D. Raspino *et al.*, *Nucl. Instr. and Meth. A* **581** (2007) 283.

[165] G. Ruggiero, The TOTEM Detectors, *Proc. of the XI*$^{\text{th}}$ *International Conference on Elastic and Diffractive Scattering Towards the High Energy Frontiers*, Blois, France (2005).

[166] I. Tserruya *et al.*, *Nucl. Instr. and Meth. A* **523** (2004) 345.

[167] M. Hauschild, *Proceedings of the International Workshop on Linear* e^+e^- *Colliders*, Jeju, Korea (2002).

[168] H. van der Graaf *et al.*, *Nucl. Instr. and Meth. A* **560** (2006) 131.

[169] R. Bellazzini *et al.*, *Nucl. Instr. and Meth. A* **576** (2007) 183.

[170] D. R. Nygren, *Journal of Physics: Conference Series* **65** (2007) 012003.

[171] A. Bamberger, *Nucl. Instr. and Meth. A* **572** (2006) 157.

[172] A. Bamberger, *Nucl. Instr. and Meth. A* **581** (2007) 274.

[173] P. Colas *et al.*, *Nucl. Instr. and Meth. A* **535** (2004) 506.

[174] X. Llopart and M. Campbell, *Nucl. Instr. and Meth. A* **509** (2003) 157.

[175] X. Llopart *et al.*, *Nucl. Instr. and Meth. A* **581** (2007) 485.

[176] M. Campbell *et* al, *Nucl. Instr. and Meth. A* **540** (2005) 295.

[177] J. Schmitz, *Nucl. Instr. and Meth. A* **576** (2007) 142.

[178] M. Chefdeville *et al.*, *Nucl. Instr. and Meth. A* **556** (2006) 490.

[179] N. Wyrsch *et al.*, *Proceedings of the MRS Symposium* **869** (2005) 3.

[180] H. van der Graaf *et al.*, *Nucl. Sc. Symp. Conf. Rec., IEEE* **6** (2007) 4631.

[181] R.L. Glückstern, *Nucl. Instr. and Meth.* **24** (1963) 381.

[182] M.J. Madou, *Fundamentals of Microfabrication*, 2nd edition, CRC press, Boca Raton (2002).

[183] S.A. Campbell, *The Science and Engineering of Microelectronic Fabrication*, 2nd edition, Oxford University press (2001).

[184] Oxford Plasmalab 400.

[185] H. Lorenz et al, *J. Micromech. Microeng.* **7** (1997) 121.

[186] E.H. Conradie and D.F. Moore, *J. Micromech. Microeng.* **12** (2002) 368.

[187] M. Key, V. Cindro and M. Lozano, *Radiation Physics and Chemistry* **71** (2004) 1003.

[188] M. Key *et al.*, *Nucl. Instr. and Meth. A* **525** (2004) 49-52.

[189] M. Nordstrom *et al.*, *Microelectronic Engineering* **78** (2005) 152.

[190] S. Wolf and R.N. Tauber, *Silicon Processing for the VLSI Era, Vol. 1: Process Technology*, 2nd edition, Lattice press (1999).

[191] Veeco Dektak 8.

[192] V.M. Blanco Carballo, Twente Univ., presentation given at the MPGD Workshop, Amsterdam, The Netherlands (2008).

[193] ORTEC, Research amplifier 450.

[194] AMPTEK, Multi Channel Analyzer, Pocket MCA, MCA8000A.

[195] Particle Data Group, *Particle Physics Booklet*, (2004).

[196] M. Cardona and L. Ley, Eds., *Photoemission in Solids I: General Principles*, Springer-Verlag, Berlin (1978).

[197] J.C. Fuggle and N. Martensson, *J. Electron Spectrosc. Relat. Phenom.* **21** (1980) 275.

[198] J.-J. Yeh and I. Lindau, *At. Data Nucl. Data Tables* **32** (1985) 1.

[199] K. Ueda *et al.*, *J. Phys. B* **24** (1991) 605.

[200] S. Hedman *et al.*, *J. Phys. B* **15** (1982) 799.

[201] T. Kylli *et al.*, *Phys. Rev. A* **59** (1999) 4071.

[202] I. Krajcar Bronić and B. Grosswendt, *Nucl. Instr. and Meth. B* **142** (1998) 219.

[203] I. Giomataris *et al.*, *Nucl. Instr. and Meth. A* **560** (2006) 405.

[204] P. Fonte, V. Peskov and F. Sauli, *Nucl. Instr. and Meth. A* **305** (1991) 91.

[205] R. Veenhof, presentation given at the RD51 collaboration meeting at NIKHEF, Amsterdam, The Netherlands (2008).

[206] J. Martin, *Study of a Micromegas TPC for the future linear collider*, Master Thesis (2002), IRFU/CEA/SPP, Saclay, France.

[207] D.F. Cowen *et al.*, *Nucl. Instr. and Meth. A* **252** (1986) 403.

[208] J.H. Thomas *et al.*, *Nucl. Instr. and Meth. A* **499** (2003) 659.

[209] A. Bondar *et al.*, *Nucl. Instr. and Meth. A* **478** (2002) 225.

[210] D. Bloch *et al.*, *Nucl. Instr. and Meth. A* **516** (2004) 315.

[211] Ansoft, Maxwell Parameter extractor 3D.

[212] HAMAMATSU Handy type soft X-ray source C4870.

[213] TENMA multimeter 72-2040.

[214] PREMA 5000 DMM/Scanner, SN 1702.

[215] D. San Segundo Bello *et al.*, *Proceedings of the 4th International Workshop on Radiation Imaging Detectors*, Amsterdam, The Netherlands, (2002).

[216] T. Holy *et al.*, *Nucl. Instr. and Meth. A* **563** (2006) 254.

[217] Nuclear and Particle physics, *J. of Phys. G* **33** (2006) 247.

[218] Review of Particle physics, S. Eidelman *et al. Phys. Lett. B* **592** (2004) 1.

[219] R.K. Bock and W. Krischer, *The Data Analysis BriefBook*, Springer-Verlag (1998).

[220] ROOT, An Object-Oriented Data Analysis Framework, http://root.cern.ch/.

[221] R. Veenhof, *Nucl. Instr. and Meth. A* **419** (1998) 729.